Ultra-Lightweight Energy Harvesting Devices Based on $FeCl_3$ Intercalated Few Layer Graphene Electrodes

Departments of Physics and Engineering

Submitted by Kieran Kane Walsh, to the University of Exeter as a thesis for the degree of Doctor of Philosophy in Physics, March 2021.

Kieran Kane Walsh

March 2021

Abstract

This thesis examines for the first time, the integration of $FeCl_3$ Intercalated Few Layer Graphene (i-FLG) materials in energy harvesting devices. i-FLG has shown excellent promise in the field of optoelectronic devices, such as photodetectors and light emitting devices, thanks to its high charge carrier concentration ($\approx 9{\times}10^{14}$ cm^{-2}), low sheet resistance ($< 10\ \Omega$/sq) and high transmittance ($> 84\%$). However, its integration into energy harvesting devices has not been previously explored. This thesis introduces a novel method of scaling up the i-FLG manufacture from 1 cm^2 to wafer scale (36 cm^2). This involved the development of a method for transferring large areas of graphene from their growth substrate (Ni) to a glass substrate, followed by the demonstration of large area functionalization of graphene by $FeCl_3$ intercalation. Raman spectroscopy mapping of 300 μm $\times$ 300 μm areas is used to calculate a metric (PosG), related to the frequency of the G band, by which the level of intercalation in a sample can be assessed. Additional functionalization by UV/Ozone treatment is also investigated and shown to improve surface wetting of i-FLG films by the introduction of oxygen containing groups on the i-FLG surface. This was used to improve the deposition of organic layers on i-FLG, and successfully fabricate Organic Photovoltaic (OPV) devices from solution processed methods.

Two types of energy harvesting devices, OPV and Triboelectric Nanogenerators (TENG), were fabricated as the first examples of energy harvesting devices with i-FLG electrodes. i-FLG based OPV devices demonstrated superior device stability under both continuous and periodic illumination, and comparable efficiencies to commercially available Indium Tin Oxide (ITO) electrode based devices. i-FLG TENG devices outperformed pristine graphene devices in terms of both their short

circuit current and open circuit voltage response. This improvement is a direct result of functionalization through intercalation with $FeCl_3$. These results indicate that i-FLG has potential advantages for use in energy harvesting devices compared to alternative electrode materials. Further work with this material shows promise in applications as a flexible electrode for use in flexible energy harvesting devices.

Dedication

This thesis is dedicated to the many excellent teachers I have had the fortune to be taught by throughout my life. Andy Troupe of Mounts Bay School, Pete Wilkins of Truro College, Richard Thompson of the materials science department at Durham University, and of course my supervisors, Monica Craciun and Saverio Russo. More than anyone though, this thesis is dedicated to my parents, whose teaching during my time in home education and afterwards allowed me to discover my own interests and learning style. Without this, I would not have been able to complete this PhD. All my love and thanks for your continued support.

Declaration

I declare that all work contained within this thesis was completed by myself. All contributions by other authors are noted and declared where relevant.

Kieran K. Walsh

Acknowledgements

Firstly, I would like to thank my supervisors, Prof. Monica Craciun and Prof. Saverio Russo for their conception of the project, along with giving me endless advice and feedback on my progress. Without their continued support none of this work would have been possible. Additionally, I would like to thank the members of my research group who have contributed to my knowledge and understanding throughout my PhD. Matt, Gareth, Jake, Adolfo, Elias, Shin and Dimitar; you were all instrumental to my progress, especially in the early days when I was still finding my feet with the processes of intercalation, Raman measurements and device fabrication in the cleanroom. Conor, Jonas, Ioannis, Agnes and Konstantinos; thank you for always helping me when needed, even if it was just to lend a hand in the lab or discuss ideas. I would also like to thank those who have directly assisted with carrying out experimental work where I could not. Again, Adolfo, many thanks for your help with taking magneto-transport measurements. Likewise, thank you to Christos Melios and Vishal Panchal from the National Physical Laboratory and Bruker, respectively, for their help with SKPFM measurements. I would like to thank the members and staff of the CDT in Metamaterials for their support throughout my PhD, particularly Harry for the unlucky task of proof reading this document. I would like to acknowledge the help and support of my housemates and friends; Francis, Cam and all the members of the Swordgang Adventuring Party for diligently distracting me from my work and keeping me sane for the past 4 and a half years. Lastly, I would like to thank my parents and sister for always supporting me, and guiding me through the many years of education. I could not have done it without you.

Acronyms

2D 2 Dimensional

AC Alternating Current

AFM Atomic Force Microscopy

AM1.5G Air Mass 1.5G

BHJ Bulk Heterojunction

BS Beam Splitter

CCD Charge Coupled Device

CNP Charge Neutrality Point

CT Charge Transfer

CVD Chemical Vapour Deposition

DC Direct Current

DCB Dichlorobenzene

DI De-Ionized

DiF Drop in Filter

DIO Diiodooctane

DoS Density of States

DSSC Dye Sensitized Solar Cell

EPBT Energy Pay Back Time

ETL Electron Transport Layer

FF Fill Factor

FLG Few Layer Graphene

FM Flip Mirror

HCl Hydrochloric Acid

HOMO Highest Occupied Molecular Orbital

HOPG Highly Orientated Pyrolitic Graphite

HOPV Hybrid Organic-Inorganic Photovoltaics

HTL Hole Transport Layer

i-FLG Intercalated Few Layer Graphene

IoT Internet of Things

IPA Isopropyl Alcohol

IR Infrared

ITO Indium Tin Oxide

IV Current Voltage

LED Light Emitting Diode

LO Longitudinal Optical

LUMO Lowest Unoccupied Molecular Orbital

NMP N-Methyl-2-pyrrolidone

MPP Maximum Power Point

OLED Organic Light Emitting Diode

OPV Organic Photovoltaics

PC70BM [6,6]-Phenyl-C71-butyric acid methyl ester

PCE Power Conversion Efficiency

PDMS Polydimethylsiloxane

PEDOT:PSS Poly(3,4-ethylenedioxythiophene) Polystyrene Sulfonate

PEN Polyethylene Naphthalate

PET Polyethylene Terephthalate

PMGI Polymethylglutarimide

PMMA Polymethylmethacrylate

PPY Polypyrrole

PTB7 Poly [[4,8-bis[(2-ethylhexyl)oxy]benzo[1,2-b:4,5-b']dithiophene-2,6-diyl][3-fluoro-2-[(2-ethylhexyl)carbonyl]thieno[3,4-b]thiophenediyl]]

PTFE Polytetrafluoroethylene

PVD Physical Vapour Deposition

RIE Reactive Ion Etching

RMS Root Mean Square

SEM Scanning Electron Microscopy

SPG Solution processed Graphene

SKPFM Scanning Kelvin Probe Force Microscopy

TCNQ Tetracyanoquinodimethane

TENG Triboelectric Nanogenerator

TO Transverse Optical

UV Ultraviolet

Contents

List of Figures

Chapter 1

Introduction

Over the last hundred years there has been an unprecedented surge in technological development that has lead to dramatic improvements to almost every aspect of society. People now live longer, experience greater social mobility, suffer lower rates of illiteracy and infant mortality, and are better educated than any generation that preceded them. However, the vast majority of the planet's energy produced during this time has been generated through the burning of fossil fuels [1], mostly in the form of gas, oil or coal. These sources of energy have long been known to be key contributors to greenhouse gas emissions. Thanks to the efforts of climate scientists, we now have a greater understanding of the effect our means of energy production has on the Earth's climate, and the need for alternative means of fueling our energy demands. Given that the population of the Earth is growing, so too is our need for ever greater amounts of energy [2]. This increase in energy demand is what is currently leading humanity towards what has been dubbed a "climate disaster". However, the prospect of this energy crisis has seen a renewed interest in alternative means of energy production, namely renewable methods that exploit and harvest energy from surrounding environment, such as mechanical energy, wind power, solar energy, thermal energy and chemical energy. This thesis will focus on two specific energy harvesting methods, solar energy harvesting through photovoltaic devices, and mechanical energy harvesting through Triboelectric Nanogenerator (TENG) devices.

Photovoltaic technology in particular has seen an explosion of research over the past decades, partly due to the discovery of new materials for photovoltaics and partly due to how synonymous photovoltaics are with renewable energy harvesting. Photovoltaic devices, also referred to as solar cells, produce energy by converting sunlight into electrical energy. As such, they provide us with a source of practically limitless energy, and an appealing solution to many of the energy concerns facing humanity. However, they are not without drawbacks. Photovoltaic devices are expensive to manufacture and install in large scale projects, and tend to require the use of scarce or toxic materials in their fabrication. There are many varieties of photovoltaic devices, the most popular in commercial use being silicon based photovoltaics [3, 4]. Other photovoltaic technologies of interest include Hybrid Organic-Inorganic Photovoltaics (HOPVs) such as Perovskite solar cells [5, 6, 7], Dye Sensitized Solar Cells (DSSCs) [1] and Organic Photovoltaics (OPVs) [8, 9, 10]. It is the latter variety, OPVs, that will be the focus of much of the discussion in this work.

OPVs are made from organic materials, typically chemicals specifically synthesized for use as active compounds in OPV technology. These materials are generally classed as either polymer or small molecule donors or acceptors (dependent on whether they donate or accept electrons). Historically, these types of solar cells suffer from very low Power Conversion Efficiencies (PCEs) [11] due to narrow absorption bands [12] and low charge mobility [13] compared to other photovoltaic technologies. However, recent developments in the field of OPV donor and acceptor synthesis has lead to significant advancements being made, not only to OPVs but also to Organic Light Emitting Diodes (OLEDs). Where OPVs long had a target efficiency of just 10% [14], less than half that of other photovoltaic technologies, their record efficiency is now greater than 17% [15]. One of the most appealing advantages of using OPVs for energy harvesting is their low cost. Compared to other photovoltaic materials, the production of organic photovoltaic donor and acceptor compounds is very cheap. In addition, unlike many other types of photovoltaic technology, OPV devices are fabricated almost entirely through solution processable means[16]. This

leads to a much lower device cost per area than other PV technologies such as Si or Perovskite solar cells [17]. Therefore, the energy required to fabricate OPVs is much less than for any other variety of photovoltaic technology. This gives OPVs a reduced Energy Pay Back Time, i.e. the time required for an energy system to generate the amount of energy equivalent to the amount that took to produce the system.

Two main applications of OPV devices have been identified as potential industry disruptors; namely their use as energy harvesting devices for Internet of Things (IoT) applications and their use in semitransparent energy harvesting coatings for buildings. The IoT is another concept that has seen great interest in recent years, particularly with the developments made in the fields of artificial intelligence and big data handling. The IoT is made up of multiple systems, each made up of many sensors, receivers and transmitters, collecting data on whatever process the system undertakes [18]. This data can then be analysed and used to make the system run more efficiently, or to inform the operation of the system in another way. For example, the first system connected in an IoT fashion was a vending machine that was capable of monitoring the stocks of different consumable items stored inside, and sending out a signal when it required restocking. This lowers the operation cost as it reduces the amount of human interaction that is required.

The reason OPV technology is so appealing to use in IoT applications is that it is a low cost means of energy harvesting, and crucially, it is inherently flexible. The sensors, receivers and transmitters needed in IoT systems do not require large amounts of power to run. However, in many cases, such as remote medical diagnostic devices, they are required to be flexible. The development of flexible energy harvesting devices is a crucial field of research currently under much investigation. Few energy harvesting devices can compete with OPVs at this stage, but despite this OPVs are yet to see commercial success for two primary reasons. Firstly, other photovoltaic technologies far surpass the efficiencies achievable by OPVs, leading to greater research interest. Secondly, the vast majority of OPV, and photovoltaic

devices in general, are fabricated using Indium Tin Oxide (ITO) electrodes. ITO is a transparent electrode known for its high transmission (comparable to glass) and very low sheet resistance. However, the use of ITO in OPV devices comes with a number of drawbacks. ITO is extremely brittle, and quickly increases in sheet resistance if bent. This makes the fabrication of flexible OPV devices with ITO electrodes extremely difficult. Furthermore, ITO has been shown to contribute to device degradation and instability due to the diffusion of Indium ions into the active layers of the device [19], causing damage to the device and the ITO itself. Lastly, ITO is fabricated through high temperature processes, and as such requires a lot of energy to manufacture. This in turn increases the energy required in the fabrication of the OPV device, to such an extent that over 80% of the total energy required to fabricate the device is used in the fabrication of the ITO electrode [20]. This highlights the need for development of low cost, transparent electrodes for use in energy harvesting devices. This will be the focus of the work presented in this thesis.

For an electrode to be suitable for use in flexible OPV applications, it requires three key material properties: low sheet resistance, high transmission and flexibility to mechanical deformation. Finding a material that possesses all of these qualities to the required degree has long presented researchers with a challenge. However, a number of possible candidates are now known to scientists, each achieving different levels of success. Some conductive polymers such as PEDOT:PSS [21, 22, 23], polypyrrole (PPY) [24, 25] and polyaniline (PANI) [26, 27, 28] have shown excellent promise for their flexibility. However, the sheet resistance of these polymers remains orders of magnitude higher than other alternative electrodes, with PEDOT:PSS falling in the range of 2 – 3000 kΩ/sq, PPY falling in the range of 2 – 10 kΩ/sq, and PANI having a sheet resistance of around 600 Ω/sq – 600 kΩ/sq. Significant variation in sheet resistance of polymer films is seen due to variation in film thickness, method of film fabrication, sample crystallinity and substrate used. It is also common for dopants or different polymer blends to be added to improve the sample conductivity, however these have been avoided in the selection of data provided here.

Metal nano-wire electrodes are another area of research currently under investigation for OPV energy harvesting applications. Such electrodes are made from a metal film (typically copper, silver or gold) [29, 30, 31], that is been patterned into a nano-wire mesh using lithographic techniques. While these electrodes have excellent sheet resistance and transmittance, they are also costly to fabricate and posses an inherent roughness that can negatively impact photovoltaic device performance. Although this technology shows great promise, it is too early to determine whether metal nano-wire electrodes will develop into a scalable technology due to their expensive fabrication process.

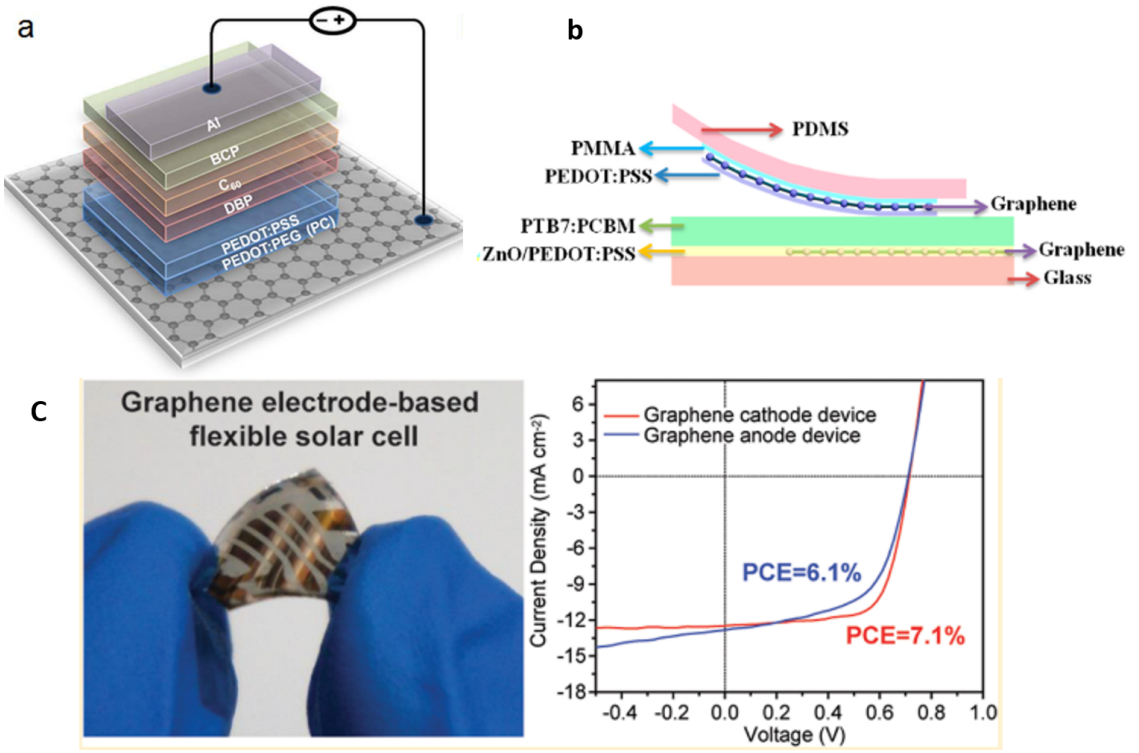

Figure 1.1: Examples of OPV devices fabricated with graphene electrodes. Figures reproduced from literature, ***a*** [36], ***b*** [35] (Reprinted with permission from ACS Nano 2015, 9, 12, 12026–12034, Copyright 2015 American Chemical Society) and ***c*** [37] (Reprinted with permission from Nano Lett. 2014, 14, 9, 5148–5154. Copyright 2014 American Chemical Society).

One material that has perhaps shown the most promise for use in energy harvesting is graphene. Graphene is a single layer of carbon atoms, arranged in a hexagonal

lattice, known for its impressive material properties and being the first of the new family of 2D materials to be discovered [32, 33, 34]. Since its discovery, graphene has been the focus of an unprecedented number of studies, with many researchers investigating ways to integrate graphene into optoelectronic devices, with a strong focus on energy harvesting devices such as solar cells. This is due to a number of factors, graphene's low sheet resistance ($\approx$ 1 kΩ/sq) making it a fantastic conductor, it's atomic thickness giving it excellent transmission across the visible range ($\approx$ 97% at 550 nm) [35], and it's inherent flexibility [36]. These properties make it a prime candidate for use as a transparent electrode in OPV devices, some examples of which can be seen in figure 1.1 [37, 38, 39]. However, as time has progressed, it has become apparent that integrating graphene into photovoltaic devices is more difficult than first anticipated.

There are numerous examples of graphene being integrated into OPV devices [40, 39, 41, 42]; with the most popular variety being single layer graphene grown on Copper (Cu) by Chemical Vapour Deposition (CVD) [40, 43, 37]. These devices show many appealing properties, such as their flexibility or low cost fabrication process [44, 45]. However, graphene also has a number of properties that have hindered progress in this field. Although graphene has a low sheet resistance, it remains much higher than that of the current industry standard for transparent electrodes, ITO. This causes device efficiencies to be lower than those of ITO based devices. In addition, graphene's hydrophobic surface makes it challenging to fabricate devices that contain layers made from aqueous solutions, such as those used in the field of organic optoelectronics [46]. However, these set-backs have lead to the field of functionalized graphene research, which seeks to improve the material properties of graphene through the chemical/physical modification of the graphene itself [47, 48, 49, 50, 51, 52, 53]. This has been shown to be effective with a large range of doping methods and chemicals. One such method is that of intercalation, a process by which a chemical/atom is inserted between the planes of a layered material [54, 55]. This thesis will focus on the role of $FeCl_3$ intercalated Few Layer Graphene (i-FLG)

as a transparent electrode for use in energy harvesting systems.

Many strategies have been used to dope graphene in an effort to improve its material properties. Surface chemical functionalization [56], chemical doping [57], and physical doping [58] have all been shown as effective methods of lowering the sheet resistance of graphene. However, intercalation with species such as $FeCl_3$ have a number of advantages over other methods of doping, such as there being no covalent bonds formed with the graphene [59], the high level of doping achievable [58, 60], and the stability of the i-FLG to temperature and humidity[61]. This highly doped form of i-FLG has a number of properties that make it more appealing to use as an electrode for energy harvesting applications than pristine graphene. Firstly, it has a reduced sheet resistance, with mechanically exfoliated i-FLG samples reaching resistances as low as 8 Ω/sq at room temperature [62]. While the intercalation massively reduces the sheet resistance, it does not significantly impact the transmittance of the material, allowing a large portion of light in the visible range to pass through the electrode [63]. Additionally, these properties are retained after significant mechanical deformation, making this material suitable for use as a transparent electrode in flexible device applications [64]. Previous examples of optoelectronic devices fabricated from i-FLG include nanoscale photodetectors [65], which showed a vast improvement to their linear dynamic range compared to standard graphene photodetectors [66], and flexible electroluminescent devices with increased efficiency [64]. These devices are displayed in figure 1.2.

Energy harvesting can take a wide range of forms, from photovotaic energy harvesting generating electricity from sunlight [67, 68, 69], to thermoelectric generators that can harvest energy from excess heat [18, 70]. These methods allow energy to be collected from natural processes that would otherwise see the energy dispersed as heat. One form of energy harvesting that taps into this same principle and has only recently seen significant research interest is that of the triboelectric energy harvesting [71, 72]. This is the process by which mechanical energy is converted into electrical energy through the contact (pressure or friction) between two materials

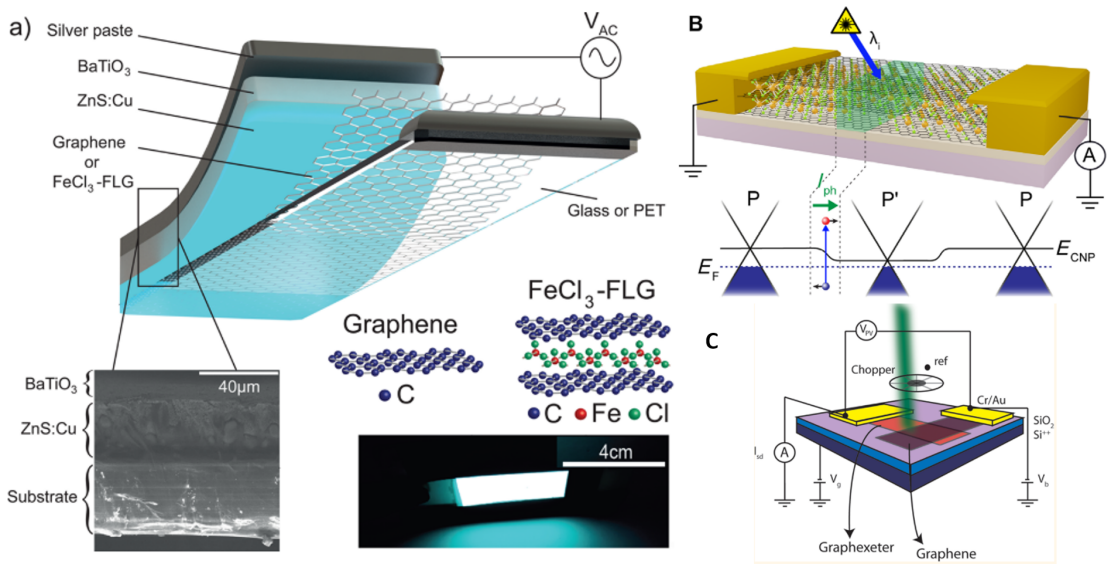

Figure 1.2: i-FLG devices fabricated in previous investigations. ***a*** shows a flexible electroluminescent device made with an i-FLG electrode [58] (Reprinted with permission from ACS Appl. Mater. Interfaces 2016, 8, 26, 16541–16545. Copyright 2016 American Chemical Society) ***b*** and ***c*** show examples of i-FLG being used in photodetectors [60] (Reprinted with permission from Science Advances 26 May 2017:Vol. 3, no. 5, e1602617. Copyright 2016 AAAS) [59] (Reprinted with permission from ACS Nano 2013, 7, 6, 5052–5057. Copyright 2013 American Chemical Society).

[73]. This occurs through a charge transfer between the two materials, known as contact electrification. Although this phenomena has been known of for hundreds of years [74, 75], it has only been in the last decade that researchers utilize this effect in the field of energy harvesting [76, 77]. More specifically, the manufacture of low cost devices capable of powering small electronic devices such as sensors, receivers and transmitters could revolutionise the fields of wearable electronics and remote medical monitoring [78], allowing them to be integrated into IoT systems [79, 80, 81].

The intercalation of FLG with $FeCl_3$ has been previously shown to increase both the work function (as high as 5.2 eV) and charge carrier concentrations (up to 9×10^{14} cm^{-2}) [60]. These properties make i-FLG an appealing material for use in TENG devices, with the potential to increase electrical outputs of the devices as a result of the doping from $FeCl_3$ adjusting the position of i-FLG in the triboelectric series [82].

Despite the impressive properties of i-FLG, it is yet to be investigated as a material for energy harvesting, with its most obvious application being to photovoltaic devices. This thesis will investigate the use of i-FLG as a transparent conductive electrode for energy harvesting purposes, examining different fabrication and characterization methods needed to design functioning devices. I will start by developing a large area transfer and intercalation process to produce satisfactory electrodes for energy harvesting devices (Chapter 4). I will then go on to use UV/Ozone treatment to further functionalize the electrodes by improving their surface wetting properties, required for the fabrication of working OPV devices (Chapter 5). I then demonstrate the first example of i-FLG electrodes being used in photovoltaic devices of any kind, showing superior stability compared to ITO based devices (Chapter 6). Finally, I produce Triboelectric Nanogenerator (TENG) devices capable of harvesting energy from friction. I will attempt to determine the position of i-FLG in the triboelectric series, and demonstrate its superior triboelectric energy harvesting capabilities compared to pristine graphene devices (Chapter 7).

Chapter 2

Theory and Background

2.1 Introduction

The aim of this chapter is to set out, in clear terms, the underlying physics that govern the processes in energy harvesting devices, as well as the background to understand the effects of replacing components such as the electrode. This entails summarising a monumental body of research on graphene, photovoltaics, organic electronics and triboelectric devices. As such, I will not devote as much attention to each section as would be provided in a literature review. However, sufficient detail will be provided to allow the reader to follow all subsequent discussions in further chapters.

2.2 Graphene

As mentioned in chapter 1, Graphene was first discovered in 2004 [32] after being first theoretically described in the 1940's [83]. The initial findings on graphene inspired a fervor of research that quickly went about characterising the unique properties of graphene [84], developing manufacturing methods [85, 86], and investigating applications through test devices.

2.2.1 Structure and properties

Graphene is the first of the realised 2 dimensional (2D) materials, being the 2D variant of the Graphitic allotrope of carbon. It is, as such, comprised of a single sheet of carbon atoms arranged in a hexagonal lattice. Carbon atoms have 1s and 2s orbitals filled, and a further 2 electrons singly occupying two of the 3p orbitals. The 2s and p orbitals lie sufficiently close in energy to allow for the hybridisation of orbitals in either sp, sp^2 or sp^3 hybridisation, formed by the mixing of 1, 2 or 3 p orbitals with the s orbital, respectively. sp^3 hybridised orbitals, such as those in diamond, form a tetrahedral structure, with each atom able to form 4 sigma (σ) bonds with adjacent carbon atoms. In sp^2 hybridised atoms, the three sp^2 atomic orbitals are arranged in a trigonal planar structure, with one p_z orbital orientated perpendicular to the plane. This gives rise to the hexagonal planar structure found in graphitic materials, with each carbon atom forming 3 σ bonds with adjacent carbon atoms. The remaining singly occupied p_z orbital is then able to form a pi (π) bond with adjacent carbon atoms. This forms a sea of delocalized electrons above and below the plane of carbon atoms.

This structure is a result of the hybridisation of 2s and 2p atomic orbitals for each of the carbon atoms in the lattice, forming 3 sp^2 hybridised orbitals, and leaving the p_z orbital unchanged. Figure 2.1 shows the hybridization of carbon atomic orbitals into sp^2 molecular orbitals, as well as the formation of the σ and π bonds. The bonding structure of graphene then arises from the overlap of these sp^2 orbitals, forming strong covalent bonds with adjacent in-plane carbon atoms. The overlap of adjacent p_z orbitals then allows for the delocalization of electrons above and below the whole sheet of carbon atoms, as seen with aromatic carbons but on a much larger scale. It is this combination of strength from hybridised covalent bonds, and electrical conductivity from delocalized electrons above and below the plane of carbon atoms that gives graphene many of its attractive properties for energy harvesting, such as its low sheet resistance and high transmission across the visible spectrum. It is also this delocalization of charges into π bonds that allow for the

Van der Waal's forces that hold sheets of FLG together.

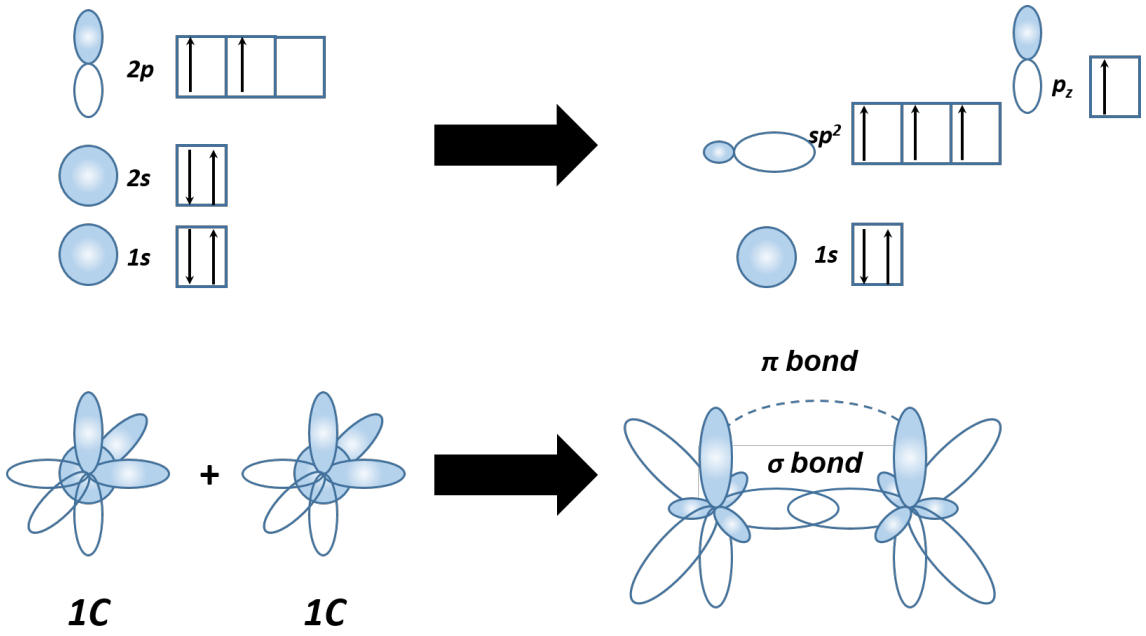

Figure 2.1: sp^2 hybridisation in graphene. The top diagram shows how the rearrangement of the 2s and 2p atomic orbitals in carbon leads to the formation of 3 sp^2 hybridised orbitals, leaving a single p_z orbital. The overlap of sp^2 orbitals leads to the formation of a sigma (σ) bond, while the overlap of adjacent p_z orbitals leads to the formation of a π bond, as shown in the bottom diagram.

Graphene's hexagonal lattice is made up of two overlapping trigonal planar sublattices, A and B. Fom this knowledge, the electronic band structure of graphene was derived, using the tight binding approximation and considering only interactions between nearest neighbouring atoms. This gives rise to an upper energy band (conduction band) and a lower energy band (valence band) which overlap precisely at $E(k) = 0$. This is known as the K point, and is at the edge of the first Brillouin zone. The Gamma (Γ) point lies at the centre of the first Brillouin zone, as shown in figure 2.2. The dispersion of valence and conduction bands at the K points (also known as Dirac points or Charge Neutrality Points (CNPs)) is linear for small energy excitations, allowing charge carriers to behave as massless Dirac fermions and attain Fermi velocities up to $c/300$ (one 300^{th} the speed of light) [87].

The Fermi energy level (E_f) of undoped graphene sits at the CNP, but can be

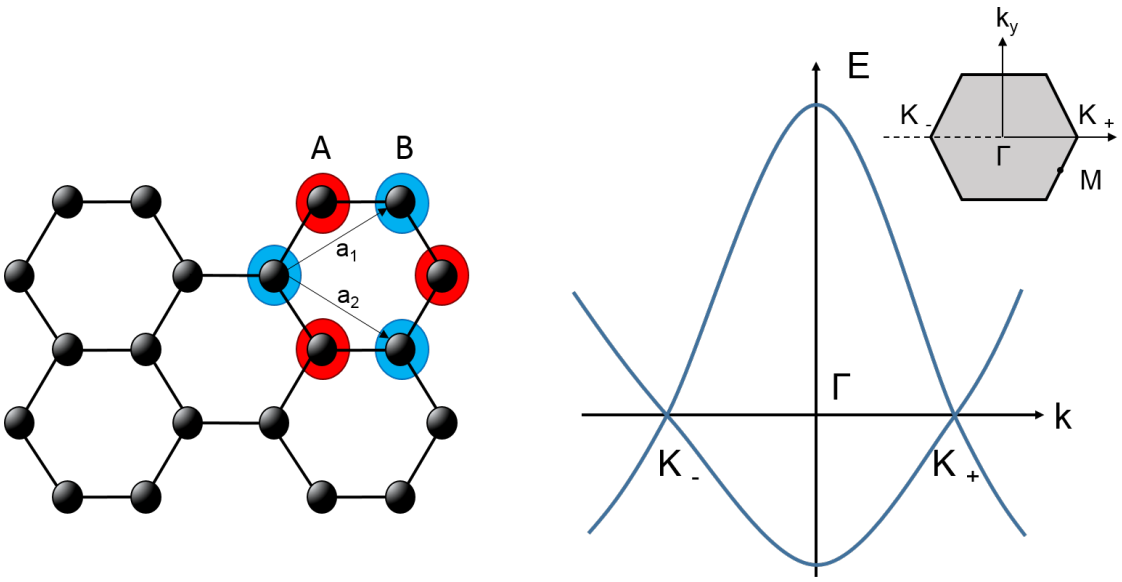

Figure 2.2: (Left) Bonding structure of monolayer graphene, showing the two overlapping trigonal planar sublattices (A and B) and the two equivalent primitive lattice vectors (a_1 and a_2). (Right) 2D representation of the band structure of graphene, plotting the energy bands as a function of wavevector (k_x) along the line $k_y = 0$. K and Γ points are shown and related to their positions on the edge of graphene's first Brillouin zone.

adjusted by various methods to be above or below the CNP. This allows for the tuning of the majority charge carriers in graphene from electrons ($E_f >$ CNP) to holes ($E_f <$ CNP) in what is known as the ambipolar field effect [32], shown in figures 2.3a, 2.3b and 2.3c. This can be achieved through application of a backgate voltage or through chemical functionalization of the graphene, which is of key relevance to the application of graphene as an anode/cathode in photovoltaic devices. The Density of States (DoS) in graphene is zero at the K points and increases in a linear fashion with increasing energy. The effect of this is that undoped graphene has a high resistivity, due to there being no states for electrons/holes to occupy at the CNP. Once doping drives the Fermi energy above or below the CNP, graphene's resistivity drops dramatically due to the increase in allowed states accessible for electrons and holes to occupy.

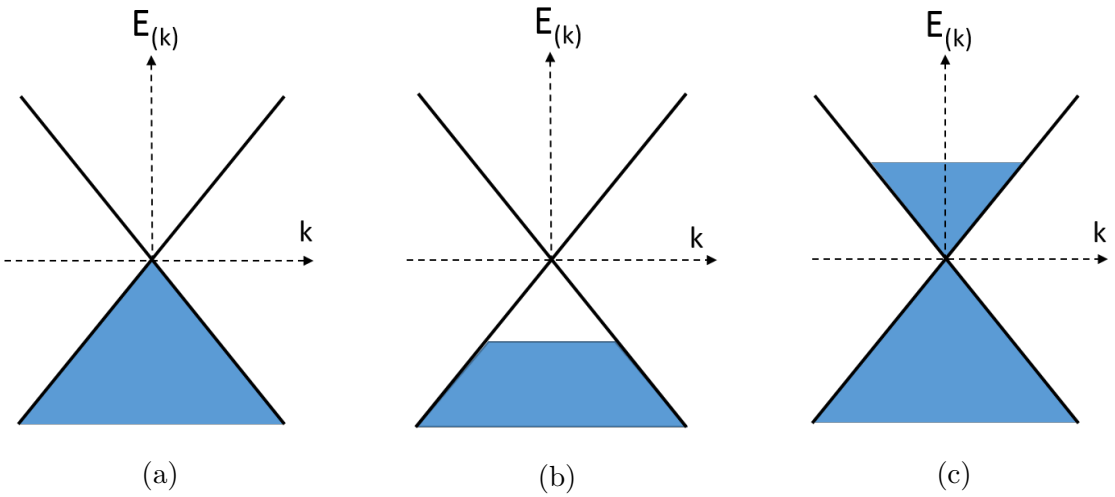

(a) (b) (c)

Figure 2.3: Showing the band structure of graphene at the K point for three distinct regimes of doping. Blue area denotes the filling of the valence/conduction bands to the respective Fermi level. Figure 2.3a undoped graphene, where the valence band is filled and the Fermi level sits at the CNP. Figure 2.3b shows graphene that has been p-doped by holes, dropping the Fermi level below the CNP. Figure 2.3c shows the Fermi level being lifted into the conduction band by n-doping.

2.2.2 Methods of fabrication

As previously mentioned, the earliest form of graphene to be successively isolated was produced from flakes of graphite that were mechanically exfoliated from one another by what has become known as the scotch tape method. Since then, a wide variety of other methods for producing graphene have been explored, with a number showing great promise. Broadly, these can be separated into 'top down' and 'bottom up' approaches.

Top Down Methods

Top down approaches, like mechanical exfoliation and liquid phase exfoliation rely on starting from a sample of graphite before separating the graphite sheets to produce individual flakes of graphene. While mechanical exfoliation uses adhesive tape to achieve this, liquid phase exfoliation relies on dispersing graphene flakes into solution, usually through a combination of high shear mixing or sonication and the use

of solvents or surfactants to stabilise the resulting suspension of flakes [88, 89, 90]. These two approaches have very different resulting outcomes in terms of the quality of graphene produced. Mechanically exfoliated graphene has the highest carrier mobility achieved to date [91]. This is due to the controlled manner in which it is produced, and the large domain sizes of graphene produced from single crystal sources. Graphene produced by liquid phase exfoliation, however, tends to have much smaller domain sizes (< 1 μm) and a much higher density of defects due to damage and contamination of the graphene during exfoliation. The scale on which these two methods of graphene production function, however, is completely different. Mechanical exfoliation can only produce flakes at best hundreds of microns in diameter, which is clearly not usable for large scale devices. In contrast, liquid phase exfoliation is capable of producing graphene suspensions that can be printed or sprayed to produce films meters in diameter, suitable for large scale industrial applications.

Bottom Up Methods

Bottom up methods take a different approach to graphene fabrication, relying instead on progressively building graphene films from smaller precursor molecules. These methods, including Chemical Vapour Deposition (CVD), Physical Vapour Deposition (PVD) and other variants, typically involve flowing a precursor gas of methane and hydrogen over a catalytic substrate, such as copper or nickel.

The methane molecules will then break apart under interaction with the catalytic substrate. For Copper catalysts, the carbon atoms then arrange themselves on the surface of the catalyst, forming a graphene film. For Nickel catalysts, the carbon atoms are absorbed into the catalyst and precipitate out upon cooling, forming a multilayered graphene film. Therefore, the structure of the graphene film being grown is dependent on the catalyst and conditions used. Typically, copper catalysts are used for growing monolayer graphene films with large domain sizes, while nickel catalysts produce multilayer graphene films with much smaller domain sizes. The

effect of this is that copper grown CVD graphene films tend to have a lower sheet resistance and greater transmission than nickel grown CVD graphene films, leading them to be far more extensively studied for use in optoelectronic devices, including solar cells. However, nickel grown CVD graphene has its own advantages, which will be examined later. The two varieties of graphene examined in this thesis will be nickel grown CVD FLG and liquid phase exfoliated graphene dispersed in aqueous solution by sodium cholate.

2.2.3 Characterisation by Raman Spectroscopy

Since the discovery of graphene in 2004, Raman spectroscopy has been an invaluable method of characterising the properties of graphene samples; from their number of layers [92] to the density of defects in the sample [93, 94]. In this section I will explore the theory behind Raman spectroscopy, and how it can be used as such an effective tool in the characterisation of graphene electrodes.

Raman spectroscopy is a non-destructive spectroscopic technique that relies on the scattering of incident light, and its conversion to vibrational energy in the form of phonons. After the discovery of this effect in 1928 [95], it has become invaluable to the characterization of the structure of materials. When a photon of sufficient energy interacts with a material, it can promote an electron of that material to be in a higher virtual energy state [96]. This state is extremely short lived, however, and quickly decays back to the electronic ground state, re-emitting a photon as it does so. Both the upper electronic states and the ground state are comprised of multiple vibrational energy levels, with much closer separation than the electronic states. This allows the conversion of the incident light energy to vibrational energy by the electron finishing in a higher/lower vibrational state than it originally started (as shown in figure 2.4). This change in vibrational state only occurs for a very small fraction of the incident photons ($\approx$ 1 in every 1,000,000 absorption events) with the rest undergoing Rayleigh scattering, where a photon is rapidly absorbed and re-emitted with the same wavelength. Photons that undergo Stokes/anti-Stokes Raman

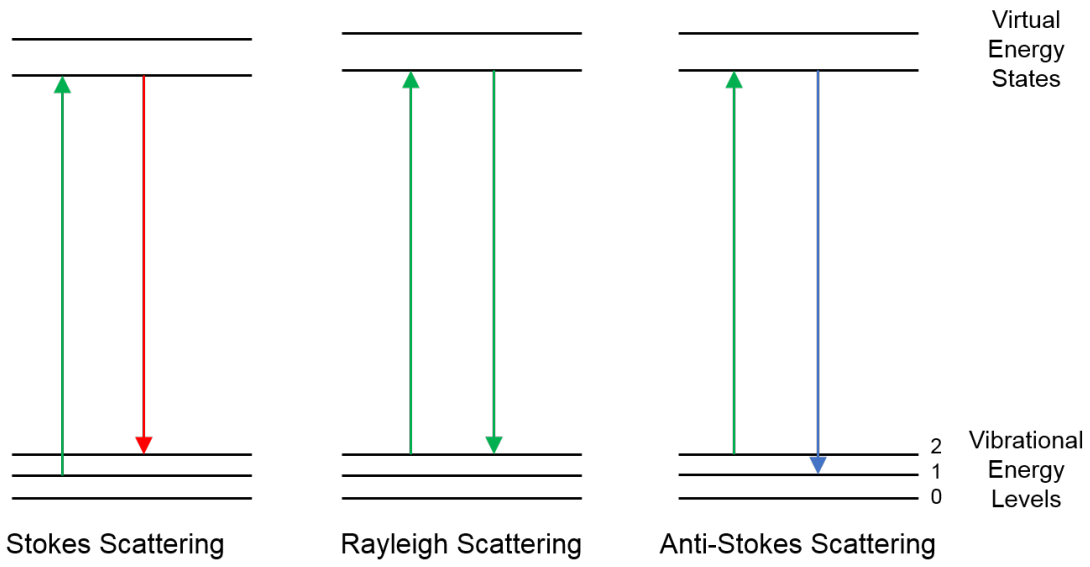

Figure 2.4: Energy transitions for light undergoing Rayleigh, Stokes and Anti-Stokes Scattering. The red arrow represents a scattered photon of lower energy than the incident photon, and the blue arrow represents a scattered photon of greater energy than the incident photon. Rayleigh scattering is elastic and so the re-emitted photon has the same energy, and hence wavelength, as the absorbed photon. For both Stokes/Anti-Stokes scattering, the re-emitted photon has lost/gained energy, and so is re-emitted at a longer/shorter wavelength.

scattering lose/gain a small amount of energy to/from the vibrational energy in the sample. As such the re-emitted photon has a slight shift in wavelength, redshifted for Stokes and blueshifted for anti-Stokes. The subsequent change in wavelength (or Raman Shift) is used to gain information about the separation of vibrational energy levels in the sample, and as such, information about its structure, chemical environments and much more. The energy level transitions associated with Stokes, Anti-Stokes and Rayleigh scattering are detailed in figure 2.4.

Not all vibrational modes are Raman active, with some only accessible by direct transition between vibrational energy levels by Infra-Red (IR) absorption. IR active modes are vibrational modes where the vibrations cause a change in the dipole moment of the sample. Raman active modes produce a change in the polarisabilility ellipsoid of the material. This is determined by the point group of the material and

the irreducible representations of its vibrational modes. Vibrational modes that involve the in-phase motion of all atoms of the unit cell are known as acoustic phonons, where as vibrations where atoms are out of phase are called optical phonons. For graphene, these vibrations can either be in plane (i) or out of plane (o) in relation to the atomic lattice.

The Raman shift value seen in Raman spectra is calculated from the shift in energy experienced by the scattered photon. This can be calculated from the shift in wavelength after Stokes/Anti-Stokes scattering, given by equation 2.1. Where E_2 and E_1 are the energies of the re-emitted and absorbed photons, h is Plank's constant, c is the speed of light, and λ_2 and λ_1 are the wavelengths of the re-emitted and absorbed photons.

$$\Delta E = E_2 - E_1 = \frac{hc}{\lambda_2} - \frac{hc}{\lambda_1} = hc\left(\frac{1}{\lambda_2} - \frac{1}{\lambda_1}\right) \tag{2.1}$$

The total shift in energy is displayed on the x-axis of a Raman spectrum in reciprocal centimeters (cm^{-1}).

In the Raman spectrum of pristine graphene (figure 2.5), there are a number of characteristic peaks that provide information on the structure of the sample. These peaks originate from different scattering mechanisms and vibrational modes in the graphene film [92]. These peaks are the G-peak, the 2D-peak and the D-peak. The G peak is common to all graphitic materials and is caused by a transition within the same Dirac cone, around the Γ point, and as such is an intra-valley transition (shown in figure 2.6a).

After absorption of a photon the electron scatters from the asymmetric in plane stretching of sp^2 hybridised carbon atoms, known as the E_{2g} phonon mode. This mode is comprised of two degenerate phonon modes, the Transverse Optical (TO) and Longitudinal Optical (LO) at the centre of the first Brillouin zone [97]. After scattering, the electron and hole will undergo radiative recombination, re-emitting a scattered photon with a different energy. The shift in energy of the re-emitted photon produces a peak with a Raman shift of approximately 1580 cm^{-1}. The intensity of the G-peak is proportional to the number of carbon environments that

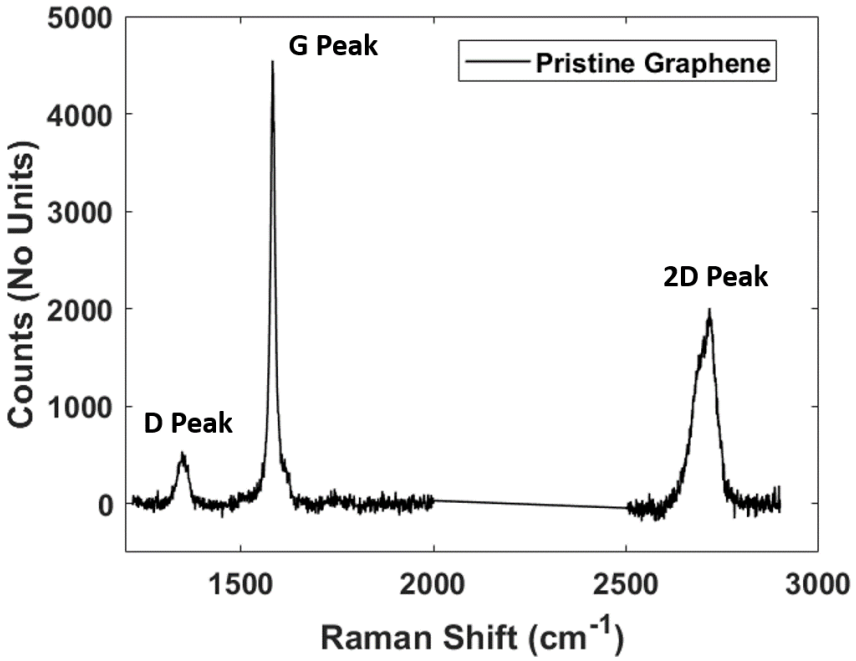

Figure 2.5: Raman spectrum of pristine FLG, measured with a 514 nm laser. The figure shows the positions and relative intensities of the three primary Raman peaks for graphene; the D, G and 2D peaks.

undergo this vibration, and so is proportional to the amount of graphene in the sample. As such, the intensity of the G-peak decreases when approaching monolayer graphene. In addition to this, the position of the G-peak can vary depending on the conditions of the graphene sample. Both doping [93, 98, 99] of the graphene and strain [100] in the graphene sheet can be causes of a shift/splitting of the G and 2D peaks, respectively. The contributions to peak shift can be separated into doping and strain contributions by correlation analysis of the G and 2D peaks, with more advanced analysis methods existing for determining the precise nature of the strain [101].

The most intense peak in the Raman spectrum of monolayer graphene is the 2D-peak. This peak originates from a second order process and can occur in either a double or triple resonance fashion [102], as detailed in figure 2.6c. First, a photon is absorbed promoting an electron near the vicinity of the K point to the conduction band. The electron then scatters from a TO phonon to the K' point. For the

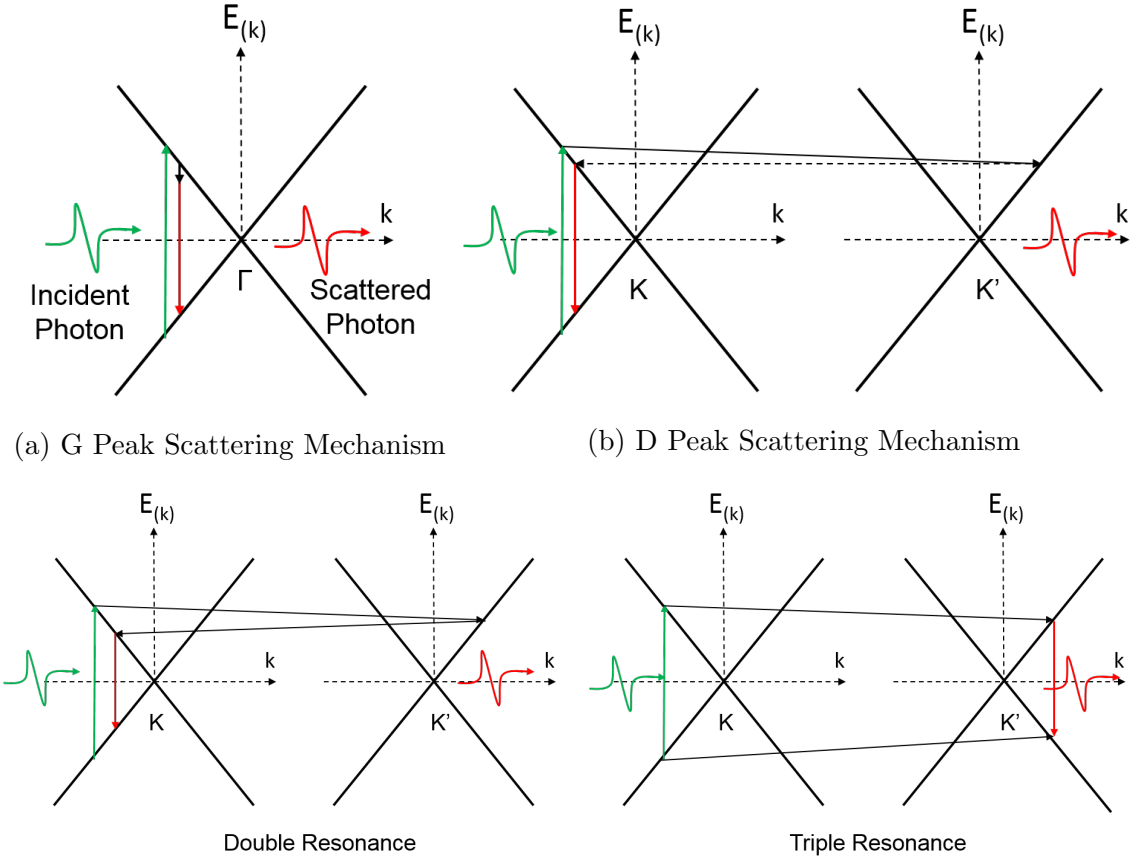

(a) G Peak Scattering Mechanism

(b) D Peak Scattering Mechanism

(c) Double and Triple Resonant 2D Peak Scattering Mechanisms

Figure 2.6: Illustration of the scattering processes that lead to the separate G, D and 2D peaks that are present in the majority of monolayer graphene samples. Green and red arrows represent the electronic transition of a charge carrier before and after scattering respectively. The black arrows represent inelastic scattering processes that occur when the charge carriers scatter from phonons in the graphene. Finally, the dashed black arrow represents the scattering from a defect in the graphene and is, as such, an elastic process.

doubly resonant case, the electron scatters from another TO phonon with opposite momentum to the first, back to the K point of the original Dirac cone, where it can recombine with a hole and re-emit a scattered photon. For the triply resonant case, the scattering of an electron by the first TO phonon is followed by a hole scattering from a TO phonon with opposite momentum to the first. This causes the electron and hole to recombine in the vicinity of the K' point. For monolayer graphene, the 2D peak is comprised of a single Lorentzian peak, however, as the number of graphene layers increases, so too does the complexity of the peak [93]. This is because the band structure of graphene changes with increasing layers, increasing the number of transitions that can occur. For bilayer graphene, two more energy bands are present above and below the Dirac cone, allowing for transitions that cause the 2D peak to be formed of 4 Lorentzian subpeaks. This allows vital information about the structure of graphene to be gained from examining the structure of the 2D peak.

The D-peak, named because it necessitates the presence of a defect in order to be active, originates from a doubly resonant inelastic scattering process, similar to the 2D-peak (shown in figure 2.6b). This occurs via as an inter-valley transition at the K and K' points of the first Brillouin zone [102]. A photon is first absorbed, promoting an electron to the conduction band near the K point, where it scatters from a TO phonon to the K' point. The electron is then backscattered from a defect, back to the K point, where it can recombine with a hole. As this process involves back scattering from a defect, instead of a second phonon with opposite momentum (as seen for the 2D-peak, the second overtone of the D peak) the Raman shift observed is half that for the 2D-peak, centred around 1350 cm^{-1} [93]. Because this peak is triggered by the presence of defects, the intensity of the D-peak is proportional to the density of defects in the sample, and so is vital for investigating the quality of a graphene sample.

2.2.4 Methods of functionalization

While graphene has excellent properties in terms of mechanical strength, electrical conductivity and transparency, for use as a transparent conducting electrode it must compete with the properties of the current industry leader, Indium Tin Oxide (ITO). This has lead many researchers to investigate methods of doping graphene using a range of chemicals and methods which I shall now discuss. The principle behind these methods being that the charge carrier concentration, and hence the sheet resistance of the graphene film can be tailored to the desired application by varying the doping concentration. Some of the most studied methods of doing this are as follows:

Chemical doping

The simplest method of doping graphene is simply by applying a chemical dopant to the surface of a graphene film, either by spin coating the chemical in solution or by another method such as vapour deposition. This allows the dopant molecules to interact with graphene's delocalized π bonding structure. The transfer of electrons from the dopant to graphene (n-doping) or from graphene to the dopant (p-doping) can then take place through the overlap of the dopant molecule's molecular orbitals with those in graphene. While this method is very scalable and easy to perform, it also has limited benefits as the doping can only be applied to the surface of the graphene film. Additionally, the dopant molecules are susceptible to removal through many solvent cleaning procedures, such as those used in the fabrication of many optoelectronic devices. This method has been used effectively, in cases where successive graphene films were doped and transferred on top of one another, producing an FLG film with dopant molecules in between each layer. This leads to improved levels of doping as the dopant can donate/withdraw charge to/from two graphene layers at once. However, this removes any advantage this method had in terms of scalability due to the work intensive process of manually transferring each graphene layer successively. Commonly studied chemical dopants, such as tetra-

cyanoquinodimethane (TCNQ), have been shown to substantially reduce the sheet resistance of graphene films by approximately one order of magnitude, while also increasing both the carrier concentration and work function [48]. Other examples of chemicals used in the doping of graphene films include tetracyanoethylene (TCNE) [59], gold chloride ($AuCl_3$) [103], nitric acid (HNO_3) [104]. Additionally, covalent doping of graphene with nitrogen atoms (leading to n-doping) can occur through reactions with species such as ammonia (NH_3), catalysed by electrothermal heating [105]. Other varieties of covalent doping can cause the addition of boron atoms to the graphene lattice (leading to p-doping), through pyrolytic synthesis [106, 107].

Surface doping with metal particles

Similar to doping graphene by means of chemical treatment, the addition of metal nanoparticles onto the surface of graphene has been shown to be effective at reducing sheet resistances. This functions in a similar manner to chemical doping, with the charge transfer between the metal and the graphene occurring due to the proximity of their outermost orbitals [108, 109]. Typically, gold and silver are used for this, as they have exceedingly high charge carrier concentrations, and so can easily dope graphene. One additional effect of this is that if the metal nanoparticles are arranged in the correct manner and are of the correct size and shape, their presence can lead to the plasmonic enhancement of incident electric fields around the particles. This has been used in photovoltaics to enhance device efficiency by concentrating the electric field of the incident light around the metal nanoparticles, close enough to the active layer to lead to enhanced photocurrent generation [110, 111].

While this method leads to a reduced sheet resistance for the resulting electrode, and increased device efficiencies when employed in photovoltaic devices, it also has the effect of increasing the surface roughness of the electrode. The dimensions of the metal nanoparticlles used in plasmonic arrays are on the scale of a few hundred nanometers. This causes the surface of the graphene electrode to have a roughness on the same scale. For many varieties of photovoltaic device this has little impact,

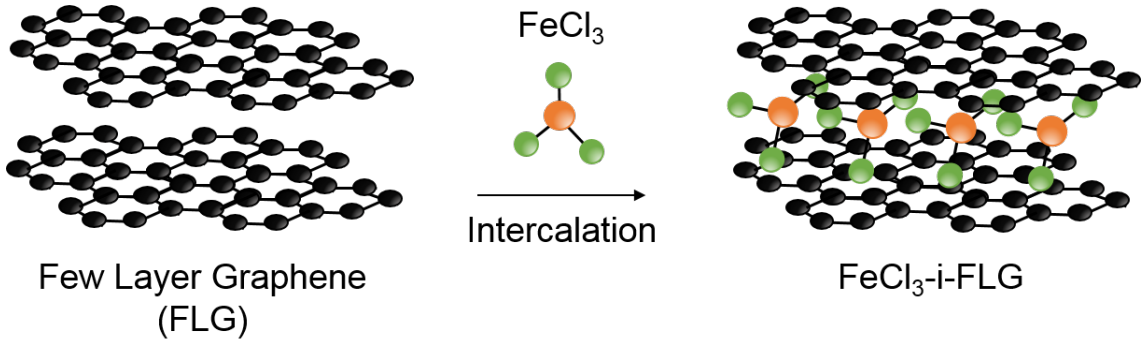

Figure 2.7: Illustration of the process of intercalation; where molecules of $FeCl_3$ penetrate between the sheets of graphene in a few layer sample (two sheets shown). The resultant i-FLG is strongly p-doped, leading to a significant drop in sheet resistance.

but due to the thin nature of Organic Photovoltaic devices, this roughness will lead to device failure and so is not an effective method of doping graphene.

Intercalation

Intercalation has been shown to be a very effective method of doping few layer graphene systems, producing the highest charge carrier concentrations reported in functionalized graphene electrodes and reducing sheet resistance values by up to three orders of magnitude [62]. The process of intercalation works by inserting atomic or molecular species between a layered structure. This was first performed on graphite long before graphene was first isolated [112]. In the case of intercalated graphene, FLG grown by CVD on Nickel is used. This has the advantage of the graphene being multilayer in nature, while also possessing relatively small domain size compared to copper grown CVD graphene. This means that there are a large number of edge sites from which the intercalant can enter between the graphene sheets. Many species have been used to intercalate graphene, including Li atoms [113], Ca [114], $FeCl_3$ and many others [115, 116]. This is carried out by a number of methods, broadly broken down into intercalation facilitated by heating or sonication. When intercalating by heating, a furnace must be used to heat the intercalant to the point of sublimation in close proximity to the graphene sample. This causes

the intercalant to vaporise and penetrate between the sheets of graphene, as shown in figure 2.7. This can be carried out either in an inert atmosphere or under high vacuum depending on the precise intercalant being used. Intercalation by sonication is typically carried out in solution, where a low power ultrasonic vibration is used to partially separate the layers of graphene and allow the penetration of small atoms/molecules in solution. By the nature of this method, it is primarily used on graphene dispersed in solution already, and is normally applied to the fabrication of hydrogen storage materials, and as such will not be described further.

Once intercalated with $FeCl_3$, the intercalant acts as a dopant molecule, p-doping the graphene and reducing its sheet resistance due to the large increase in charge carrier concentration. Samples with charge carrier concentrations as high as 9×10^{14} cm^{-2} and sheet resistances as low as 8 Ω/sq have been achieved in mechanically exfoliated samples comprised of 5 layers of graphene with intercalant between each layer [62]. This is a larger charge carrier concentration than what has been achieved in graphene samples surface doped by chemicals, due to the doping from intercalation affecting two layers of graphene simultaneously. This doping also increases the work function of the i-FLG, raising it to as high as 5.1 eV [60]. Further properties of i-FLG, such as transmittance and carrier mobility, can be found in figure 2.8. However, the intercalation of graphene is not always complete, and can lead to different staging conditions. This occurs when some but not all layers have been intercalated. The staging is defined by the number of graphene layers between each successive layer of intercalant, stage 1 being fully intercalated, stage 2 having two graphene layers between each intercalant layer, and so on. The increased spacing between the graphene layers in an intercalated sample leads to the decoupling of the graphene layers, as can be seen from the change in the structure of the 2D Raman peak from a multipeak in FLG to a single Lorentzian peak in i-FLG [62].

In addition to the massive reduction in sheet resistance seen in $FeCl_3$ intercalated graphene, a number of other studies have highlighted its applicability to the field of photovoltaic electrodes [47, 117, 118]. Firstly, despite the insertion of numerous

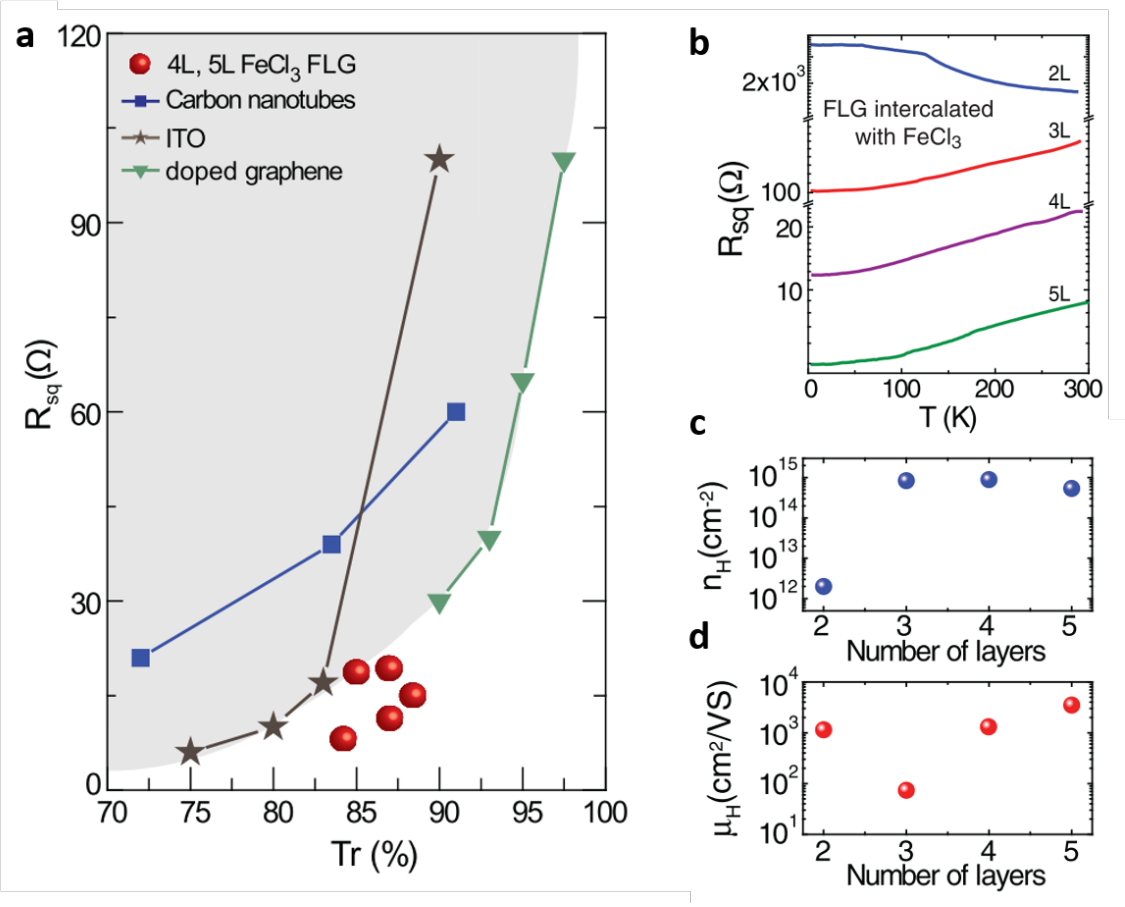

Figure 2.8: ***a.*** The sheet resistance and transmittance of a number of transparent conductive electrodes. Best performing electrodes are located in the bottom right of the graph, for the highest transmittance and lowest sheet resistance. Here, i-FLG shows superior performance to ITO and other forms of doped graphene. ***b.*** The sheet resistance of i-FLG samples of different numbers of layers across a range of temperatures. ***c.*** Change in i-FLG charge carrier concentration with number of graphene layers. ***d.*** Change in i-FLG carrier mobility with number of graphene layers (Reproduced with permissions from Adv. Mater. 2012, 24, 2844–2849. Copyright 2012 John Wiley and Sons).

other layers of atoms into the graphene structure, the transmission properties of the resulting i-FLG sample are largely unchanged. This allows for highly conductive electrodes to be produced with excellent transmission across the full range of the visible spectrum [63]. Secondly, $FeCl_3$ i-FLG have been demonstrated to be highly resistant to atmospheric contamination/degradation. $FeCl_3$ is aggressively hygroscopic, and will absorb water molecules from the air in ambient conditions. Once intercalated between graphene sheets, however, the resulting material shows excellent resistance to atmospheric humidity over a large temperature range [61]. This makes intercalation the most appealing of all currently examined doping strategies, as it produces highly conductive electrodes that are resistant to environmental factors.

2.3 Energy Harvesting

Energy harvesting is the collection of energy from processes that occur naturally and require no fuel source. These include the harvesting of mechanical energy through wind, wave, tidal and vibrational energy harvesting; as well as the harvesting of energy from sunlight and heat. These methods of energy harvesting have long been investigated and researched, but have regained interest in recent years due to the drive for renewable methods of energy production. Additionally, the recently emerging IoT requires methods to continually power large numbers of low energy cost devices, and energy harvesting devices can fulfil this requirement. As there are such a large variety of energy harvesting methods, this thesis will focus on only two: Photovoltaic energy harvesting and triboelectric energy harvesting.

2.3.1 Photovoltaic Energy Harvesting

The photovoltaic effect was first observed by Becquerel in the late 1830's, and since then has been expanded upon by countless researchers. There are many varieties of photovoltaic cells, with the most recent efficiencies achieved by each variety dis-

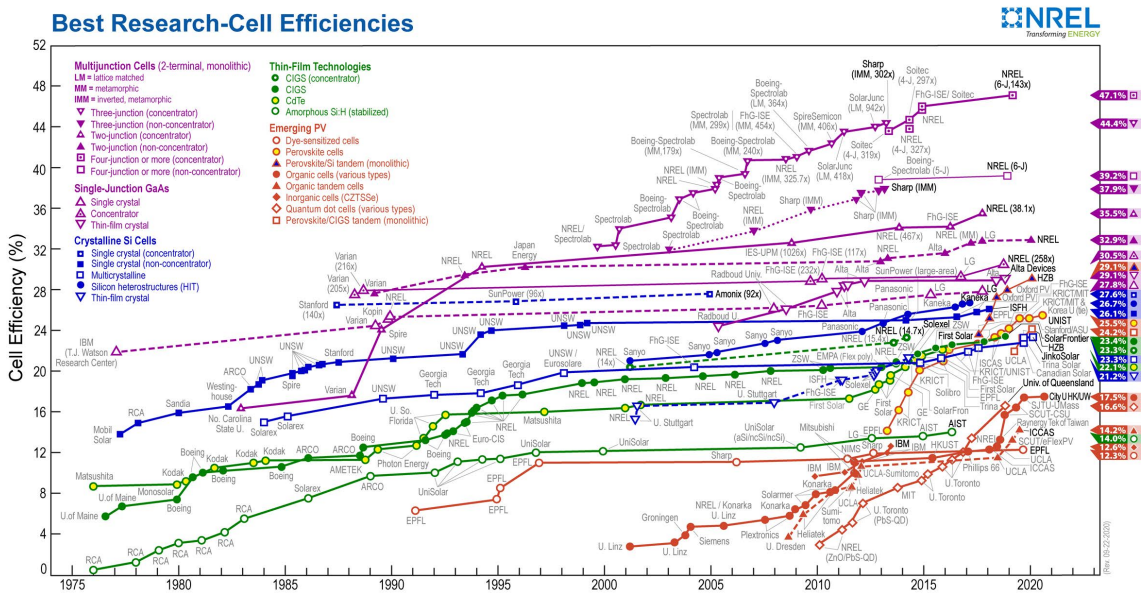

Figure 2.9: Chart of solar cell efficiency progress from 1975 to 2020 for certified solar cells of different varieties. Data collected by the National Renewable Energies Laboratory (NREL) and made freely available on their website: https://www.nrel.gov/pv/cell-efficiency.html

played in figure 2.9. In its most basic form, the photovoltaic effect functions as follows: A sample of semiconducting material is irradiated with light of some wavelength, λ. Semiconducting materials possess a bandgap, that is, a gap in energy between their valence and conduction bands. If the energy carried by that light ($E = \frac{hc}{\lambda}$) is equal or greater than the bandgap of the material being irradiated, the material will absorb a photon of light, causing the transition of an electron from the valence to the conduction band. Once in the conduction band, the electrons can be extracted to the electrodes by way of a built in electric field. In silicon solar cells, this electric field is produced by the difference in charge carrier concentration across the depletion layer that forms as a result of bringing together two materials with different doping concentrations. In other types of solar cells (organic, Perovskite, etc.), this electric field is produced by the difference in work functions of the two electrodes. The greater the number of photons absorbed, the greater the number of electrons promoted to the conduction band and the larger the current produced.

Photovoltaic Device Structure

While there are many varieties of solar cells and many different structures that have been tested, the vast majority of solar cells are comprised of a similar layered structure with an absorber material sandwiched between two conductive electrodes. The top electrode must also be transparent in order to allow light to enter the solar cell, typically Indium Tin Oxide (ITO) is employed for this. In silicon solar cells, the absorber layer is made up of two layers of silicon with different dopings, one p-doped and one n-doped. When brought together charges are exchanged between these two layers, forming a depletion layer at the interface. Such a device structure is shown in figure 2.10. The difference in charge carrier concentrations across this layer produces an electric field, which allows the separation of charges (as previously mentioned). In other solar cells, such as organic solar cells, these layers are not planar, and are instead formed from a mixture of two organic compounds, one donor and one acceptor, in what is known as a Bulk Heterojuntion (BHJ).

In many types of solar cell, the excitation of an electron to the conduction band does not result in a free electron and hole, but rather a bound electron–hole pair known as an exciton. This is a neutral quasi-particle that forms due to the Coulombic attraction between the negatively charged electron and the positively charged hole. This causes the exciton to be held together with a characteristic binding energy which must be overcome in order to separate the exciton into free charges. Organic solar cells have particularly high binding energies on the order of 100s of meV, and as such require a strong electrical field to separate the exciton. This is achieved by selecting electrodes of sufficiently different work functions, as well as using electron transport layers (ETLs) and hole transport layers (HTLs) to encourage the separation of charges. This results in a slight drop in V_{oc} due to the energy cost of separating the charges.

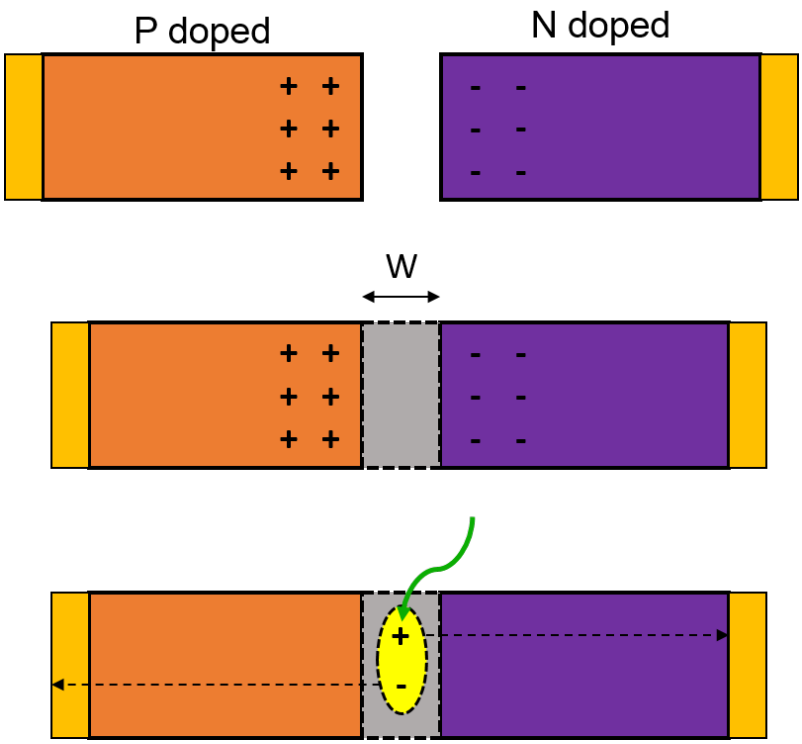

Figure 2.10: The basic structure of a photovoltaic cell formed by joining two pieces of p and n doped semiconducting material. The diagram shows the formation of the depletion layer of width W, due to migration of charges at the interface. This allows charges to be extracted when excited by an incident photon (shown in green).

Working Principle and Electrical Characteristics

Electrically, a photovoltaic cell behaves in the same manner as a diode, with an additional photocurrent term being generated from the extraction of photoexcited free charge carriers when irradiated with light. An equivalent circuit diagram (figure 2.11) can be produced to describe the behaviour observed in photovoltaic devices, and hence an equation for the current generated can be derived.

$$I = I_d + I_{sh} - I_{ph} \tag{2.2}$$

The current generated by a solar cell has three contributing factors, the current flowing through the diode (I_d), the current flowing through the shunt resistor (I_{sh}) and the photocurrent (I_{ph}). Treating the p-n junction of the solar cell as an ideal diode, we can treat the first term as simply the current through an ideal diode, given

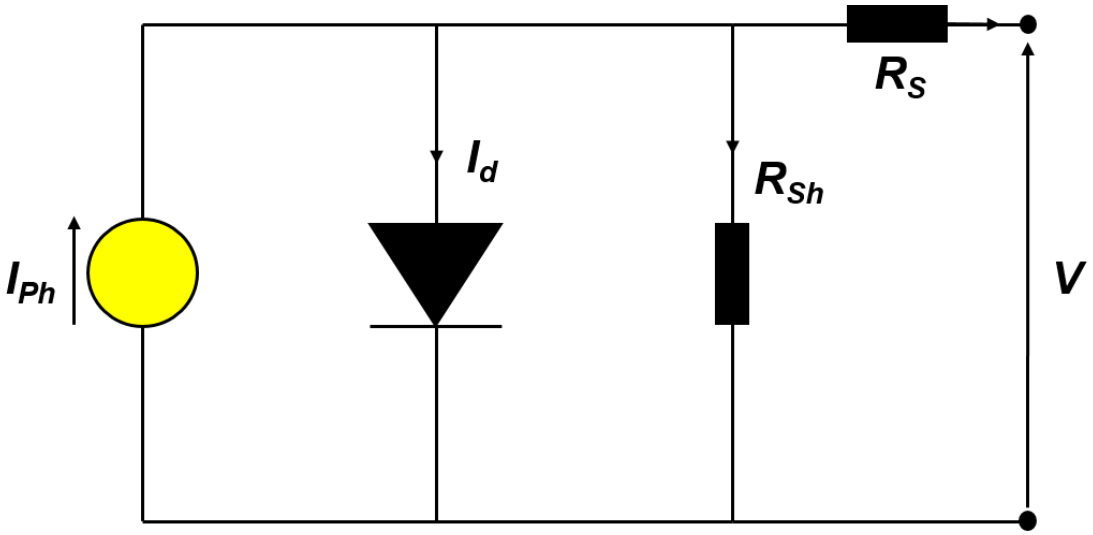

Figure 2.11: Equivalence circuit for a photovoltaic cell showing the generation of photocurrent in parallel with a diode and shunt resistor, and in series with a series resistor.

by the Shockley diode equation:

$$I_d = I_0(e^{\frac{qV_i}{k_bT}} - 1) \tag{2.3}$$

where the term V_i is the voltage across the elements in the circuit: $V_i = V + IR_s$, q is the elementary unit of charge, k_b is the Boltzmann constant and T is the temperature in Kelvin. The current through the shunt resistor can then be described by Ohm's law: $I_{sh} = \frac{V_i}{R_{sh}}$. From this, the full characteristic equation can be derived.

$$I = I_0(e^{\frac{q(V+IR_s)}{k_bT}} - 1) + \frac{V+IR_s}{R_{sh}} - I_{ph} \tag{2.4}$$

The photocurrent is negative as convention, as it opposes the contributions from the diode (I_d) and shunt. The physical significance of the shunt (R_{sh}) and series (R_s) resistors is important to note, as these heavily influence the FF of the photovoltaic device. The series resistance represents the resistance of the two electrodes extracting current, as well as the resistance of the materials current travels through while being extracted, and the contact resistance between each of the layers comprising the solar cell. The easiest of these quantities to adjust is the resistance of the electrodes, as I shall explore later. The lower the series resistance in a solar cell, the

more current can be extracted. The shunt resistance, represents the resistance to the flow of current on alternative current pathways through the solar cell, such as those created by pinholes. Such a redirection of current reduces the total current that can be extracted, as well as the voltage from the solar cell. The shunt resistance is usually determined by the presence of defects in the solar cell that form during fabrication [119, 120]. As such, it is beneficial for the shunt resistance to be as high as possible to prevent these losses.

In addition to the basic operation of a solar cell, it is important to understand how to characterise photovoltaic devices, which parameters are important and what this tells us about the performance of the solar cell. The most basic way to characterise a solar cell is through IV curve measurement. An example IV curve, labelled with relevant photovoltaic device parameters, is shown in figure 2.12. Performing this measurement involves sweeping the voltage across a solar cell and measuring the output current, in either light or dark conditions. In the dark, this characterises the diode behaviour of the solar cell, whereas under illumination the additional contribution from the photogenerated current is also characterized. By performing this measurement the user can extract the short circuit current (J_{sc}), open circuit voltage (V_{oc}), series resistance, shunt resistance, device efficiency (η) and fill factor (FF).

The short circuit current is defined as the current produced by a solar cell under illumination and short circuit conditions (zero voltage) and as such can simply be read off the IV curve where the current crosses the y-axis. Similarly, the open circuit voltage is the voltage across the device when there is zero current flowing, and can be read off where the IV curve crosses the x-axis. The maximum power output, P_{Max} (also known as the Maximum Power Point, MPP) is found using the formula $P = IV$ and multiplying together the current and voltage on the curve. The fill factor can then be found by dividing the maximum output power by the product of the open circuit voltage and the short circuit current, as follows:

$$FF = \frac{J_{MPP} \cdot V_{MPP}}{J_{sc} \cdot V_{oc}} = \frac{P_{Max}}{J_{sc} \cdot V_{oc}} \tag{2.5}$$

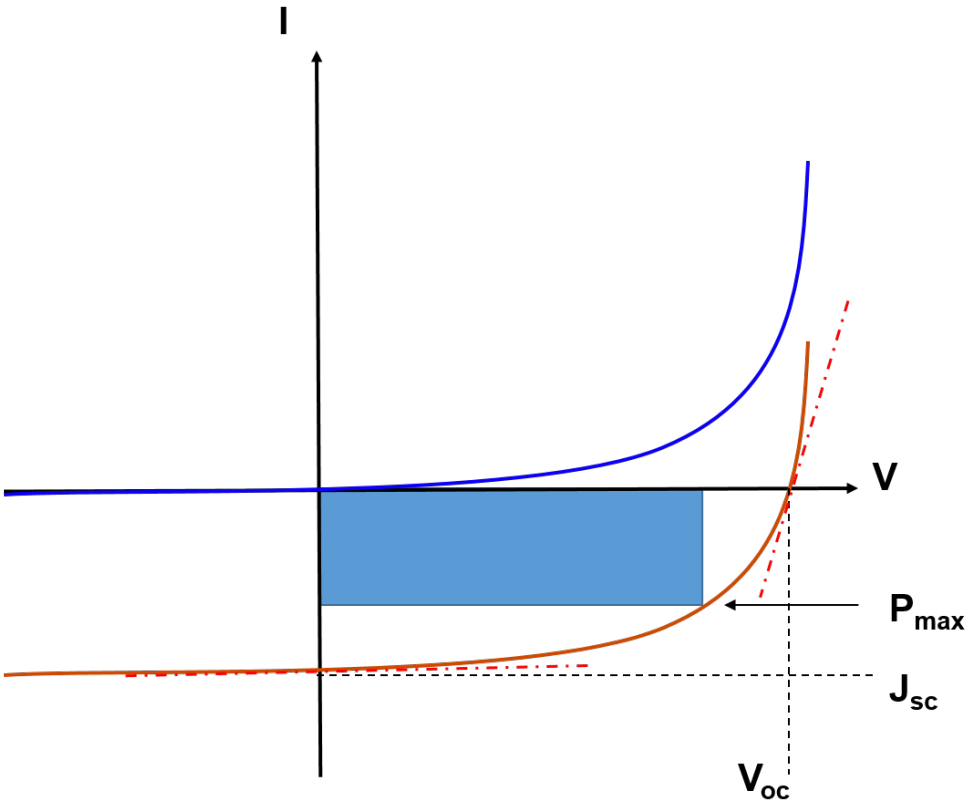

Figure 2.12: Example of a typical IV curve from a solar cell, indicating the relevant parameters that can be extracted from the curve, including the open circuit voltage (V_{OC}), short circuit current (J_{SC}) and maximum power point (P_{max}). The fill factor (FF) is calculated from the ratio between the areas of the blue rectangle and the rectangle made by black dotted lines. The red dotted lines shown are used to calculate the gradient at the J_{sc} and V_{oc}, the inverse of which provides values for the shunt (R_{sh}) and series resistances (R_{series}) respectively.

This provides a measure of the squareness of the IV curve and an indication of how effective charge generation and extraction are in the device. Device efficiency can be measured by the ratio of power produced by the device divided by the power input into the device. In the case of solar cells, the input power is simply the power of the incident light on the solar cell. Rearranging equation 2 for the maximum power term we find the expression $P_{Max} = J_{sc} \cdot V_{oc} \cdot FF$, meaning the efficiency can be expressed as:

$$\eta = \frac{J_{sc} \cdot V_{oc} \cdot FF}{P_{in}} \tag{2.6}$$

allowing all crucial device parameters to be extracted from a single measurement.

Factors Impacting Photovoltaic Power Conversion Efficiency

There are many factors that can influence the efficiency of a photovoltaic device. These can vary between different types of solar cell, but in general the following can be considered:

- **Transmission Through the Electrode**

  For light to enter the solar cell, it must first pass through the top electrode. Therefore, electrodes with high transmittance are favourable as they allow more photons to enter the device.

- **Internal Quantum Efficiency**

  The internal quantum efficiency is defined as the ratio of photons to enter a device to the number of electrons excited to the conduction band. This is a property of the absorber or active material in the solar cell.

- **Recombination rates**

  After excitation, if charges are not separated and extracted quickly enough, they may recombine, reducing the number of excited charges. There are a number of different mechanisms by which recombination can occur, including radiative recombination, trap assisted recombination [121, 122] and Auger recombination [123].

- **Charge Extraction Efficiency**

  Because solar cells are comprised of a number of layers, any energy offsets between these layers can cause barriers to charge transport. This can increase series resistance, as well as causing the IV curve to deviate from the typical diode shape.

The extent to which these factors impact the device is dependent on the type of solar cell being considered, as I shall now describe for Organic Photovoltaic (OPV) devices. However, these factors are not measured in this work, only the PCE.

2.3.2 Organic Photovoltaics

The field of organic photovoltaics began in the 1950's, with the study of organic dyes. Kearns and Calvin are widely credited with the development of the first OPV device, in their study of magnesium phthalocyanines where they achieved a photovoltage of 200 meV [124]. However, the field of OPV devices did not truly expand until the 1980's, when the first heterojunction organic solar cell was developed by Tang et al., exceeding 1% efficiency [125]. The next crucial step in the development of OPV technology was the development of the first BHJ OPV devices by Yu et al. in the 1990's [126]. Now, the field of OPV technology relies on the development of new organic donor and acceptor compounds in order to improve device efficiencies. However, some studies into alternative electrodes to ITO have been carried out, as was mentioned in chapter 1. While these alternative electrodes have shown great promise at improving device flexibility, few have produced devices that can compete with ITO based devices. For this to be achieved, the electrode requires both a low sheet resistance ($< 10\ \Omega$/sq) and high transmittance ($> 85\%$). Doped forms of graphene, such as i-FLG, have shown potential to reach these benchmark values and compete with ITO.

After the discovery of graphene, a great deal of research has been carried out to integrate graphene electrodes into OPV devices. OPV devices with graphene electrodes produced by solution processable means [127], as well as graphene electrode grown by CVD [128] have been investigated and shown to act as effective transparent electrodes. However, these devices still fell short of the efficiency values set by ITO based devices. In 2014, Park et al. produced an OPV device with a graphene anode and cathode on a polyethylene naphthalate (PEN), making a fully flexible OPV device that achieved comparable efficiencies to ITO based devices (7.1%) [39]. Doped graphene electrodes were also previously shown to lead to improved OPV performance (1.63%), and come close to exceeding the efficiency values produced by ITO based OPV devices produced alongside [49]. Hsu et al. fabricated doped graphene electrodes by sequentially stacking monolayers of CVD graphene with lay-

ers of TCNQ dopant in between each graphene layer [48]. By varying the number of graphene layers, they found that 3 layers of graphene with two layers of TCNQ produced the best performing devices, achieving an average efficiency of $\approx 2.6\%$ (1.5% lower than ITO based devices). While this strategy is effective at producing electrodes of low resistance and high transmittance, it is also labour intensive and does not easily translate to a large scale fabrication process. Intercalation achieves a similar result, with layers of dopant in between multiple graphene layers, but does not require repeated transfer of monolayer graphene. Despite the promise that both doped and undoped varieties of graphene show as transparent electrodes for OPV applications, there have been few examples of graphene based devices exceeding the efficiency values achieved by ITO devices, and those that have are likely due to a poorly optimised fabrication process leading to under-performing ITO based devices. Current leading OPV technologies can now achieve efficiencies over 17% [15]. However, the challenge for this promising technology is to now match these values in flexible devices, as rigid ITO electrodes are still used to attain the best efficiency values. In addition, OPV device stability remains a crucial issue that is still under investigation, which shall be discussed later.

Organic solar cells utilise organic semiconducting materials as the absorption layer, using donor and acceptor compounds to take the place of the positive and negatively doped regions of the semiconductor. These materials are typically conjugated polymers with additional electron donating/withdrawing groups added in order to stabilise the excited state after the absorption of a photon. Unlike in silicon photovoltaic devices, the donor and acceptor compounds in OPVs do not have conduction and valence bands, instead we must consider the Lowest Unoccupied Molecular Orbital (LUMO) and Highest Occupied Molecular Orbital (HOMO). This is because electronic excitation does not occur in the bulk of a semiconducting material, but rather at a molecular level.

The two semiconducting materials that make up the absorption layer are typically dispersed together in an organic solution where they are mixed before be-

ing deposited onto a desired electrode, usually by spin coating. This forms what is known as a Bulk Heterojunction (BHJ), where the organic donor and acceptor separate into different phases which then form a nanostructured interpenetrated bi-continuous network. This means that the two separate phases are mixed into one another as a network of long cylindrical domains of polymers, with a typical phase domain size on the order of 10 nm.

The BHJ is held between two transport layers, ETL and the HTL [129]. The materials used for these layers have higher mobilities for the carrier they are selected for (higher hole mobility for the HTL and higher electron mobility for the ETL) [130]. This prevents the transport of current in the reverse direction, reducing the leakage current. These layers are used to fix the work functions at either end of the BHJ near the levels of the HOMO of the donor at the anode, and near the LUMO of the acceptor near the cathode. This improves the charge extraction efficiency by preventing the build up of charges at the interface.

As was mentioned previously, the binding energy of excitons formed in organic solar cells is greater than those formed in many other types of solar cell, typically on the order of 0.2– 1.0 eV [131]. This is because the low dielectric constant of the organic materials limits the screening of the Coulomb attraction between the electron and hole in the exciton. The processes that govern exciton transport in OPV devices are still under investigation, and are likely to vary depending on the exact materials being used.

The processes governing the transport of excitons in the BHJ is are still under investigation, and the perspective offered here does not examine the competing theories in detail. When an exciton forms in the BHJ, it travels by diffusion to the interface between the donor and acceptor, where it loses some energy [132]. The distance an exciton can travel before recombining is known as the exciton diffusion length [133, 134]. The exciton then forms a charge transfer exciton (also known as a geminate exciton), where the exciton is no longer localised to one organic molecule (known as a Frenkel exciton), but rather split across two, bridging

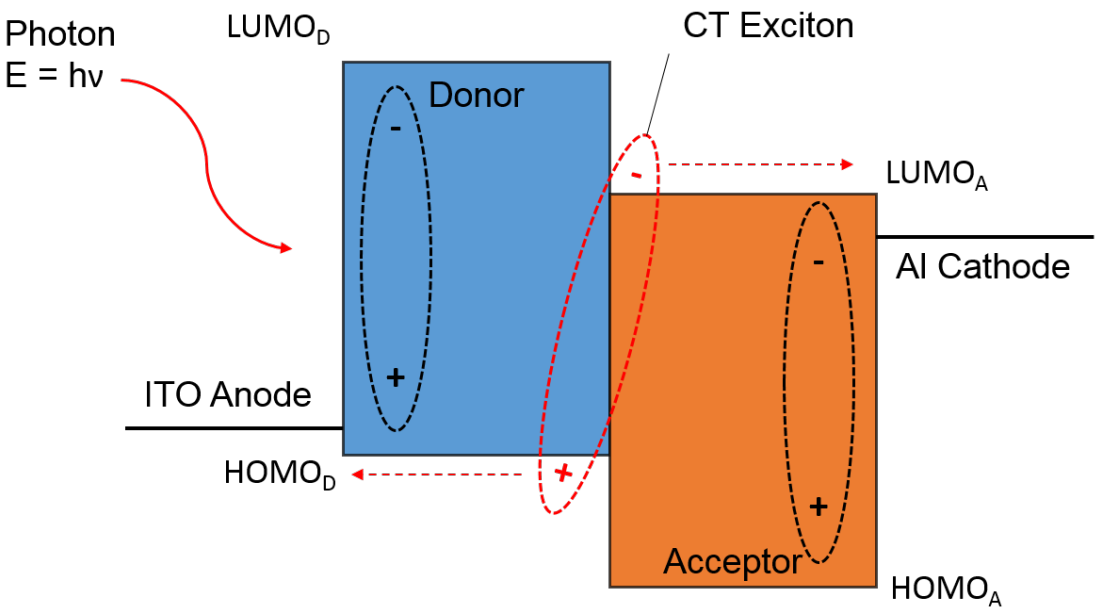

Figure 2.13: This figure shows the generation of an exciton in either the donor or acceptor material upon the absorption of an incident photon. The exciton can then diffuse to the interface between the donor and acceptor, where it forms a charge transfer (CT) exciton, shown in red, spread across the donor and acceptor interface. This allows the separation of the exciton by the in-built electric field. The electron is then extracted at the cathode and the hole is extracted at the anode (transport layers not shown for simplicity).

the donor/acceptor interface [131]. This lowers the binding energy of the exciton sufficiently that the internal electric field can separate the charges, allowing the electron to be extracted through the acceptor to the cathode, and the hole to be extracted through the donor to the anode. A simplified diagram of this process is shown in figure 2.13. The process of the exciton traveling from one organic molecule to another is facilitated by Forster resonance energy transfer[135], where the exciton is able to hop between molecules by a dipole-dipole coupling interaction between organic molecules [136, 137].

The diffusion of the exciton to the interface between donor and acceptor compounds is crucial to the generation of free charges in OPV devices. Therefore, the diffusion length of the exciton, governed by the exciton recombination time is

a crucial parameter [138]. Typically, excitons in organic material have very brief lifetimes, allowing them to diffuse over distances on the order of 10s of nm before recombination occurs. This is one of the reasons that the BHJ structure has become ubiquitous for OPV devices, because the domain size within the BHJ matches that of the diffusion distances achieved by the excitons. This means that the domain size and structure of the BHJ is key to the design of efficient OPV devices.

Charge Recombination in OPV devices

As was outlined in the previous section, recombination of charges is a key factor impacting device efficiency. In OPV devices there are many causes of charge recombination competing with charge generation through absorption, the result dictating the current that can be extracted from the junction under different bias conditions. Recombination can occur both before or after the charge separation at the donor/acceptor interface, and can be either radiative (releasing a photon) or non-radiative. The simplest form of recombination is band-to-band recombination that occurs due to the relaxation of the free electron back into the valence band from the conduction band. This usually occurs as a bimolecular process [139]. Recombination may also occur via geminate recombination, where the exciton has formed but has not yet dissociated into free charges. This predominantly happens while the exciton is localised to one molecule, but can also occur while the exciton is in its charge transfer state. This type of recombination tends to dominate when the domains in the BHJ are larger than the diffusion length of the exciton and occurs over very short timescales ($\approx$ 100 ns). Recombination can also occur at the interface between the donor and acceptor, or in the bulk of the heterojunction[140], where the charges (either free or in a CT state) recombine across separate molecules. This is known as bimolecular or Langevin recombination [141]. This type of recombination is particularly strong in low mobility organic solar cells, where electrons and holes travel slowly, giving more time to encounter one another and recombine via coulombic attraction. In addition to this, traps formed in the BHJ (either from manufacturing

defects or from the degradation of the organic constituents) allow for trap assisted recombination [13, 142]. This is where an electron or hole falls into a trap state with an energy inbetween the HOMO and LUMO level. This trapped charge can then attract surrounding free charges and recombine when they encounter one another. This type of recombination is known as Shockley-Read-Hall (SRH) recombination, and is particularly dominant under high trap concentrations in the BHJ.

Limiting the impact of these different recombination mechanisms is a key area of research in the OPV community. However, some level of recombination is always present in OPV devices and cannot be mitigated. Instead, many works focus on increasing the number of charges generated to offset the recombination. This can be achieved through many different methods, but instead I shall focus on the replacement of the electrode with a better suited transparent conducting material to improve charge extraction.

Organic Photovoltaic Devices Based on Graphene Electrodes

The vast majority of OPV devices employ an ITO electrode. This is a highly conductive and transparent form of glass that is well suited for use in most solar cells, along with many other types of optoelectronic devices. In recent years, however, graphene has received much interest in its application as a transparent conductive electrode in solar cells. Directly comparing the two materials, one can see that ITO has a lower sheet resistance and higher transmission than pristine graphene. This has not dissuaded many researchers from testing the functionality of graphene electrodes in OPV devices. Many successful devices have been characterised, with efficiencies generally falling slightly short of those achieved by ITO based devices. Undoped graphene is not well suited to this, as it possesses a relatively high sheet resistance and low work function. This leads to poor charge extraction and causes excess recombination at the electrode. Therefore, the use of previously mentioned doping methods is required in order to lower the sheet resistance and adjust the work function. Where these methods have been employed, device efficiencies have

been improved but still rarely exceed those of ITO based devices.

It may be inevitable that ITO devices outperform graphene based solar cells in terms of efficiency. However, another advantage offered by graphene is that it is highly flexible and mechanically robust. ITO on the other hand is extremely brittle and is subject to large increase in sheet resistance when bent. This is because the ITO forms cracks after the application of relatively little stress, inhibiting the flow of charges. Efforts have been made to develop flexible forms of ITO but these tend to be limited to very small bending angles and are not suitable for repeated bending cycles. Therefore, the development of graphene electrodes for OPV devices is crucial for the fabrication of flexible OPV devices. In this thesis I shall examine the use of $FeCl_3$ intercalated FLG (i-FLG) as a transparent electrode for OPV technology.

2.3.3 Triboelectric Energy Harvesting

Another form of energy harvesting that has received a lot of interest in recent years is triboelectric energy harvesting. This is the harvesting of energy through the friction or contact between two materials. While this is a relatively new addition to the selection of energy harvesting methods, it has been shown to exceed both thermoelectric and pietzoelectric energy harvesting in terms of the power output.

Perhaps the simplest example of the triboelectric effect that many people are familiar with is the build up of static charge that is observed when you rub two objects together. For example, a person rubbing a balloon on their hair builds up a static charge between the two, forming an electrostatic attraction that causes their hair to stick to the balloon. The process by which the charges are transferred from the hair to the balloon is known as the triboelectric effect. Similar demonstrations can be made with a cotton cloth and a PVC pipe, or on a larger scale, a Van de Graaff generator [74].

There are a number of competing theories as to the exact mechanism by which the triboelectric effect occurs, whether the charge transfer occurs by transfer of material, ions or electrons. However, recent work by Xu et al [143] gives strong evidence that

electron transfer between the two materials is the governing mechanism by which the effect occurs, though this may not be the case for all triboelectric systems. The origin of the effect lies in the chemical and material properties of the two materials in question. When the two materials, A and B, are brought into contact as in figure 2.14a, one material (A) may hold electrons more strongly than the other material (B). This is because the electrons of material A lie at a lower energy relative to the vacuum level than in material B. When material A and B come into contact, there are vacant energy levels present in material A that are lower in energy than the current occupied energy levels in material B. This causes material B to lose some of its electrons, transferring them to material A in the process. This produces an excess of electrons, and hence a negative charge on material A, and a deficit of electrons and a positive charge on material B. This in turn causes an electric field between the two materials, which can be used to drive a current and extract energy from the system. This is the principle that all Triboelectric Nanogenerator (TENG) devices operate by, although there are a number of different types of TENG that will be discussed later. The performance of TENG devices is largely determined by the choice of materials used, which is informed through the triboelectric series.

The Triboelectric Series

The propensity for a material to donate or receive electrons from another material when the two are brought into contact, has a number of contributing factors. These include the material's surface free energy, work function, and chemical composition along with others [144]. These factors are all summarised in the triboelectric series, a qualitative order of materials based on whether they donate or accept electrons when brought into contact with another material [145]. Figure 2.14b shows the position of a select number of common materials in the triboelectric series. Materials that give up electrons are known as positive triboelectric materials, and are placed at the top of the list, whilst materials that gain electrons are known as negative triboelectric materials and are placed at the bottom of the list. The further apart two materials

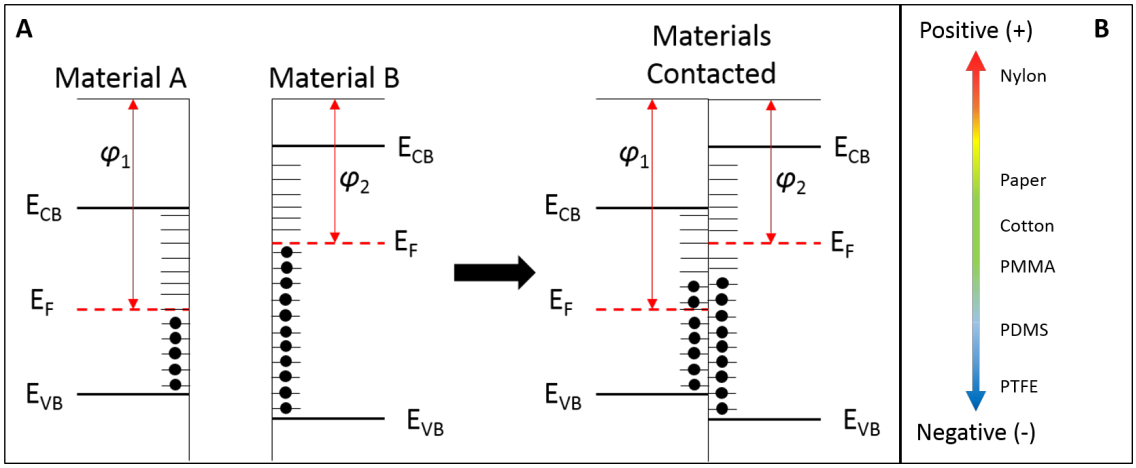

Figure 2.14: ***a***: Triboelectric charge transfer diagram where E_{CB}, E_{VB} and E_F are the conduction band, valence band and Fermi energies, and $\phi_{1,2}$ are the work functions of materials A and B respectively. Here the two materials (A and B) start separated with offset Fermi levels. When brought into contact, electrons can transfer from one material to the other due to the vacant energy levels on Material A being of lower energy than the filled states of Material B. This charge transfer can be observed in the form of voltage produced when the materials are contacted and separated. ***b***: The triboelectric series for a number of commonly used materials in triboelectric devices.

are in the triboelectric series, the greater the triboelectric charge transfer between the two of them when they are brought into contact. It is therefore crucial to the operation of efficient TENG devices that the appropriate materials are selected for the triboelectric layers. However, as is shown in figure 2.14, the doping level and Fermi energy are also key factors, meaning that the position of a material in the triboelectric series can be adjusted by either positive or negative doping. Graphene is an excellent candidate for this as there are numerous methods available to dope graphene.

Triboelectric Nanogenerator Devices

The simplest design for a triboelectric nanogenerator (TENG) is that of a single electrode coated with a dielectric material. Another material is then brought into

contact with the dielectric and triboelectric charge transfer takes place. As the materials are separated, the charges on the surface of the dielectric induce charges in the underlying electrode. As the dielectric and contact triboelectric material are repeatedly contacted and separated, the device will produce both a current and voltage response that can be used to power small electrical devices such as basic sensors and LED lighting [72].

While other more complicated architectures for TENG devices have been investigate, the devices fabricated in this investigation are all limited to a single dielectric layer that is brought into contact with the graphene based electrode. However, it should be noted that large improvements to device performance are observed when fabricating devices with multiple stacked triboelectric layers.

2D Materials

Thanks to the growing interest in the field of research into 2D materials and their properties, a number of recent studies have examined a range of 2D materials and their triboelectric properties. Work by Seol et al. used the triboelectric response of different 2D materials when combined with a range of polymers to determine their relative positions in the triboelectric series [82]. This work also demonstrated that chemical doping of MoS_2 can be used to alter the position of the material in the triboelectric series by changing the work function of the material. In a similar manner, the doping achieved by intercalation shifts the work function of i-FLG, potentially changing its position in the triboelectric series.

Graphene has already been the focus of a number of investigations to the use of 2D materials in triboelectric energy harvesting devices. Solution processed graphene has shown promising use in TENG devices due to its ease of processing and fabrication [72, 79, 146], while reduced graphene oxide based TENG devices have seen interest for similar reasons [147, 80]. This investigation will instead focus on CVD graphene, which has seen much less interest for TENG devices.

Triboelectric Nanogenerator Devices with Graphene Electrodes

As the development of TENG devices is still in its infancy there is a relatively small pool of research to draw from. Nonetheless, TENG devices have been fabricated with Graphene electrodes, with the aim being to make use of Graphene's flexible nature and highly appealing conductive properties. Shin et al. [148] developed a method of Graphene electrode fabrication through exfoliation in solution before filtering and transfer of the electrode to a desired substrate. The TENG devices fabricated as a result used a Polydimethylsiloxane (PDMS) polymer layer as the triboelectric material. Using Graphene from a solution processable source is a very appealing method of fabricating TENG devices as it allows for the easy fabrication of large area devices with a relatively low material cost. Reduced Graphene oxide has been used by a number of groups in TENG devices explicitly for this purpose [147, 80]. However, for devices designed to be integrated into wearable on-skin devices, such as those used in medical diagnostic monitoring, CVD Graphene holds the advantage as it is much thinner due to being comprised of single or FLG as opposed to many layers on top of one another [79, 146].

These two methods of Graphene production give exceptional choice to researchers seeking to design TENG devices for different applications. Low cost, large area devices (such as those used in harvesting energy from pedestrian or vehicular motion under pavements or roads) can be easily fabricated from solution processed Graphene or Graphene oxide. Where devices are used for medical sensing, higher sensitivity is required, therefore a more conductive electrode is required in the form of CVD Graphene. This also allows the entire device to be made with an extremely low thickness, on the order of 100 nm, making them seamlessly wearable by patients. The performance of such devices and the factors affecting the devices will be examined in more detail in Chapter 7.

Chapter 3

Experimental Methods

3.1 Introduction

Understanding the methods used in the fabrication and characterization of materials and devices is crucial in understanding how best to apply those materials to real world applications, as well as what conclusions can be drawn from the results presented. Throughout this work, I have strived to follow the fabrication and characterization procedures set out by the research communities in academia and industry. These can differ depending on the type of device or material being tested due to specific material requirements limiting the generality of characterization methods. Therefore, before presenting my results I will give an in-depth look into the fabrication and characterization methods used throughout. I will begin by discussing the methods of preparation used in producing graphene electrodes, including the cleaning and transfer procedures used throughout this work for both small and large area graphene samples. I will then discuss the fabrication methods used to produce the devices, including Hall bars for electrical characterisation, organic solar cells, and triboelectric nanogenerators. Finally, I will discuss the characterisation techniques that are used, both for the characterisation of graphene's material properties (such as Raman spectroscopy and resistance measurements), and for device characterisation of the energy harvesting devices produced in this work. Any methods specifically developed for the work carried out in this thesis, however, are covered in their own

respective chapters.

3.2 Fabrication - Graphene Electrode Preparation

The preparation of graphene for intercalation and subsequent device fabrication follows the same strategy, with slight differences depending on the type of graphene being used, the device being fabricated and the purpose of its fabrication. In general, the process is as follows: Transfer of graphene from growth substrate to a suitable substrate for intercalation, intercalation with $FeCl_3$, fabrication of devices. Two types of CVD grown FLG films were purchased from Graphene Supermarket, 1 cm $\times$ 1 cm graphene samples and 4 inch diameter wafers of graphene, both grown on $Ni/Si/SiO_2$ substrates.

To intercalate a sample of graphene, it must first be transferred from its growth substrate. This is because the Ni growth catalyst is corroded by the $FeCl_3$ vapour produced during intercalation [149]. Therefore, the graphene film is first transferred to a glass or quartz substrate, as these can withstand the temperatures of intercalation and remain unaffected by the $FeCl_3$ gas. These substrates also allow for the use of the intercalated graphene as a transparent electrode . Once intercalated, the i-FLG film can be transferred to flexible substrates, as I shall discuss later.

3.2.1 Substrate Cleaning and Preparation

Rigorous substrate cleaning was employed to ensure as little contamination as possible before intercalation, as the results of intercalation can be heavily dependent on the sample being free from contaminants. Substrates were cleaned by sonication in De-Ionized (DI) water inside a heated sonication bath for 30 minutes. An N_2 gun was then used to dry the substrates, before they were placed in heated Acetone (70°C) for 30 minutes. Substrates are then removed and dried with an N_2 gun again, before being placed in heated Isopropyl Alcohol (IPA), also at 70°C for a further 30

minutes. The substrates are then removed and dried for one final time, before being cleaned using Reactive Ion Etching (RIE).

A moderate strength Oxygen plasma was used for substrate cleaning. The primary function of this plasma is to removes chemical residues that may be present on the surface of the substrate, leading to a clean surface for the transfer of graphene. However, RIE treatment with Oxygen plasma also introduces Oxygen containing groups onto the surface of the substrate, improving the adhesion between the graphene and substrate upon transfer.

Graphene films are first protected by spin coating a layer of Polymethylmethacrylate (PMMA, A4 495k) of approximately 300 nm thickness onto the graphene. The sample is then desiccated for 30 minutes to ensure the Anisole solvent in the PMMA film has dried. The edges of the sample are then scraped with a scalpel, damaging the edges of the PMMA film such that the etchant solution can penetrate underneath the graphene and etch the Ni catalyst. The samples are then blow dried with N_2 to remove any particles of Ni or Si/SiO_2 generated from this scraping from the surface of the sample. The sample is now ready for chemical etching of the Ni catalyst and transfer to a suitable intercalation substrate.

3.2.2 Small Area Graphene Transfer

The following method of graphene film transfer was first developed and used to transfer graphene grown by Chemical Vapour Deposition (CVD) from its growth substrate to a desired substrate [150, 151]. It has become one of the most widely used methods of graphene preparation due to the ease in which it can be carried out, the range of substrates that can be used and the quality of graphene that can be retained through its use. However, there are a number of drawbacks to this method that will be discussed later.

Once a graphene sample has been coated in PMMA, a 1M solution of $FeCl_3$ is made up to etch the Ni catalyst layer. This solution is prepared by mixing crystals of hydrated iron chloride with DI water and mixing with a magnetic stirrer bar

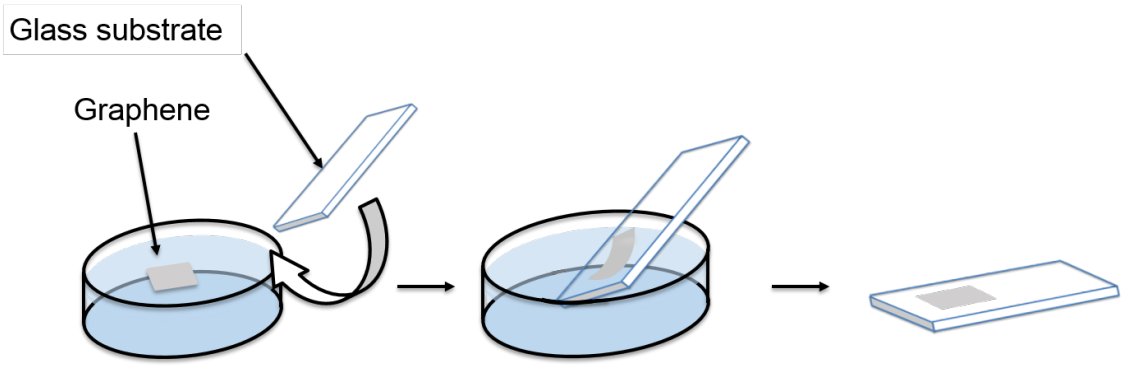

Figure 3.1: Flotation aided transfer: a process by which suspended graphene films are lifted from the surface of a DI water bath in order to transfer them to a desired substrate (xy)

for 24 hours. The solution is then vacuum filtered through filter paper (Whatman, 5.5 cm diameter) to remove any undissolved particles of iron chloride from solution. Graphene samples are placed on the surface of the etchant solution, a pair of tweezers are used to press the corners of the sample into the solution, ensuring the solution is contacting the Ni layer along the whole of the perimeter of the sample. As the Ni film is very thin it does not take long to etch, for 1 cm $\times$ 1 cm samples the process takes as little as a couple of hours but can take much longer for larger samples. Once the etch is fully completed the underlying Si/SiO_2 substrate will detach from the floating graphene/PMMA film and fall to the bottom of the etchant solution. At this point, the etchant solution can be diluted with DI Water to aid in cleaning the graphene samples, and make their removal from the surface of the solution easier. The graphene sample is then removed from the etchant solution and floated on the surface of a beaker of DI Water, using a small container to scoop up the floating graphene film and deposit it in the new beaker. This step is repeated 5 times to ensure all $FeCl_3$ contaminants have been removed from the sample.

The graphene can now be transferred from the surface of the DI water to the freshly cleaned substrate. This is carried out by flotation aided transfer, where the etched graphene film is floated on the surface of a DI water bath and a clean substrate used to lift the graphene from underneath [150, 152, 153]. A schematic

of this process is shown in figure 3.1. The adhesion between the graphene and the substrate allows the graphene film to readily stick to the substrate. However, care must be taken when lifting the graphene from the surface of the DI water, as lifting the substrate too quickly can cause damage to the sample. Once the graphene is on the glass substrate it is left to dry in air before being desiccated. At this stage there is a thin film of water between the substrate and the graphene, it is important to ensure this water is completely dried before desiccation as any droplets of water that remain under the film will cause damage to the graphene film during desiccation. After 30 minutes of desiccation, the sample can be annealed, which is carried out at 150˚c for 10 minutes. This serves two purposes as it simultaneously bakes the PMMA film as well as ensuring the graphene adheres to the substrate. Once the sample has cooled, the PMMA is removed by washing in warm Acetone (70°C for 3 hours) before being rinsed in IPA (70°C for 30 minutes). The clean graphene sample is then desiccated until it is loaded into the intercalation tube.

3.2.3 Intercalation of Few Layer Graphene with $FeCl_3$

Intercalation is the process by which a chemical or atomic species (in this case $FeCl_3$) penetrates between the layers of another material [112], leading to a doping of said material. The effect of this intercalation is a very strong doping of the graphene and a massive reduction in sheet resistance [60, 62], making the resulting material extremely appealing for use in flexible photovoltaics [154].

A three zone furnace was used to control the temperatures of both the intercalant ($FeCl_3$) and sample (FLG), a diagram for which is found in figure 3.2. The sample and intercalant are first loaded into the intercalation tube, a 3cm diameter glass tube, in zones 2 and 1 respectively. Zone three is left empty for purposes that will be explained later. Before intercalation, the furnace is pumped down using both a rotary and turbo vacuum pump, to a pressure of 1×10^{-6} mbar, ensuring all water vapour is removed before heating. This is crucial to successful intercalation as $FeCl_3$ is extremely hygroscopic, readily absorbing moisture from the atmosphere, so humid

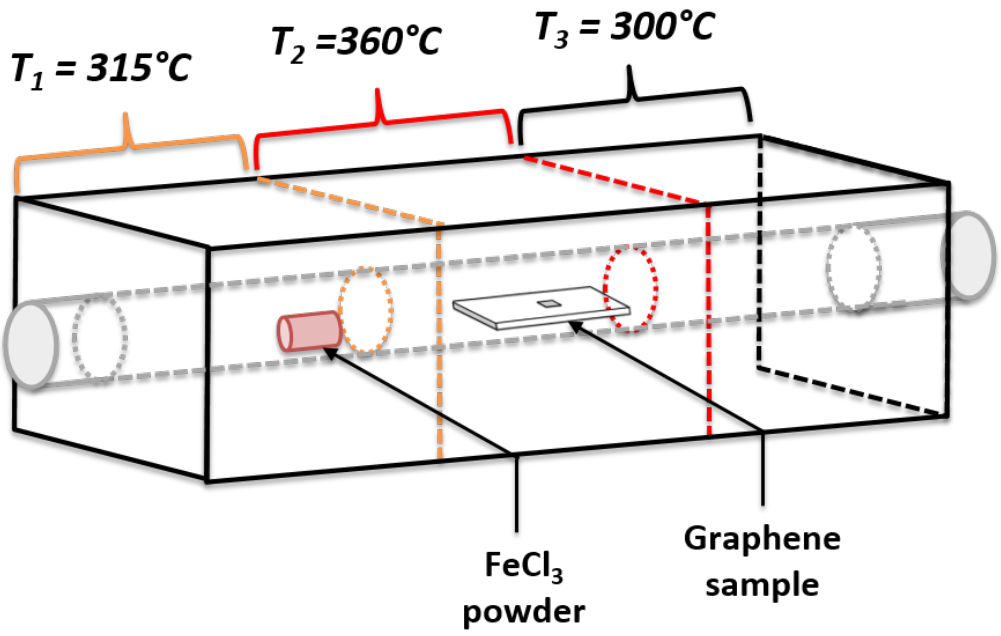

Figure 3.2: Intercalation furnace schematic labelled with the three zone temperatures used for standard intercalation procedures. The positions of the $FeCl_3$ powder and graphene sample inside the quartz tube are also shown, these positions were held fixed throughout this investigation.

conditions interfere with intercalation. All zones are then heated at a constant rate of 10°C/s, up to temperatures of 315°C (Zone 1), 360°C (Zone 2), and 300°C (Zone 3). As $FeCl_3$ sublimates at 315°C, it will remain in a gaseous state in zones 1 and 2 but will then condense in zone 3. This prevents the $FeCl_3$ vapour condensing on the sample, leading to cleaner samples with a greater degree of intercalation. This results in the majority of the $FeCl_3$ vapour condensing at the end of zone 3, where the intercalation tube is at its coolest. Samples are held at the aforementioned temperatures for 8 hours before the tube is cooled at a rate of 10°C/s. At this stage, the tube can then be vented and the sample removed.

As I shall further investigate in chapter 4, intercalation with $FeCl_3$ is a very reactive process. This means that any organic material residues or contamination of the sample or intercalation equipment can lead to unwanted reactions taking place, resulting in aggregates forming on the sample's surface. The presence of these aggregates adds to the roughness of the i-FLG film, which can negatively impact

device function, even short circuiting devices. In addition, the oxidation of these aggregates produces a thick insulating layer on the surface of the i-FLG. To mitigate the risk of this occurring, graphene samples are placed in a desiccator immediately after intercalation. After 30 minutes under vacuum the graphene is washed in warm IPA (70°C) for 5 minutes, before being dried with an N_2 gun.

3.3 Device Fabrication

A number of different devices were fabricated to investigate the impact of using graphene in energy harvesting devices. The first devices characterised were samples of i-FLG, patterned into Hall bars. These devices were fabricated to characterise the electrical properties of i-FLG samples. OPV devices with both ITO and i-FLG electrodes were fabricated to assess the utility of i-FLG as a flexible transparent electrode. Finally, Triboelectric Nanogenerators (TENGs) were fabricated using both large area i-FLG samples and solution processed graphene electrodes to investigate the use of graphene electrodes in triboelectric energy harvesting.

3.3.1 Hall Bar Fabrication

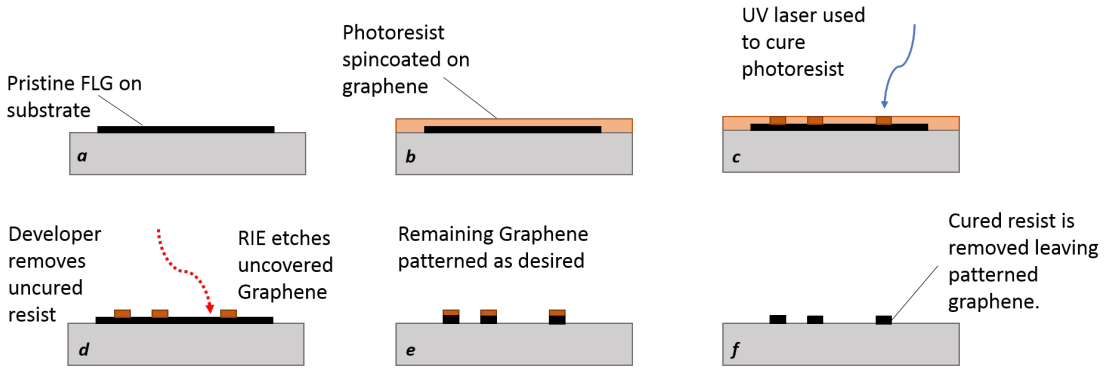

Figure 3.3: Lithographic process used in the fabrication of i-FLG Hall bar devices used in magneto-transport measurements. Running from ***a*** to ***f***, this process allows the patterning of graphene Hall bar devices, which can then be intercalated and contacted to measure the charge transport properties of the material.

FLG samples were patterned into 6 terminal Hall bars by means of UV laser writing lithography, magneto-transport measurements were then used to characterize carrier type, density and mobility by the Hall Effect [155]. Small sections of large area FLG samples were fabricated into 6 terminal Hall bars using laser writing of a polymer mask and photoresist before developing the mask and etching it using RIE (process shown in figure 3.3). First, Polydimethylglutarimide (PMGI) is spin

coated onto the graphene at 4000 rpm before being baked for 5 minutes at 150°C. The photoresist S1813 was then spin coated at 4000 rpm and baked for 1 minute at 115°C. Together, these polymers form the positive photoresist, meaning that areas of the resist exposed to UV laser (405 nm, 5 μm spot size) in the writing process are then removed in the development stage. Development was carried out by submerging samples in the developing agent MF319 for 30 seconds before transferring them to DI water for 30 seconds. Samples were then dried using a nitrogen gun. This left photoresist patterned into the desired Hall bar shape on the surface of the graphene, and uncovered graphene over the rest of the substrate. RIE was then used to remove this unwanted graphene, using a high energy O_2 plasma. Undeveloped resist was then removed by washing in N-Methyl-2-pyrrolidone (NMP) for 30 minutes at 60°C, before replacing the NMP with fresh NMP for a further 30 minutes. Finally, the samples were washed in Acetone and IPA, each for 10 minutes at 70°C.

Once FLG samples had been patterned into Hall bars they were intercalated following the procedures previously outlined. Once intercalated, another photoresist is applied in the same manner as before and the laser writer used again, this time to pattern a shadow mask to apply Cr/Au contacts by thermal evaporation. After patterning, the photoresist was developed, leaving holes over the graphene contact pads. The sample was then loaded into a HVV thermal evaporator and the chamber pumped down to a pressure of 10^{-6} mbar. 5 nm of chromium followed by 50 nm of gold were then deposited onto the graphene by thermal evaporation. At this stage, the device can be contacted to the chip carrier and characterized.

3.3.2 Organic Photovoltaic Device Fabrication

Fabrication of organic photovoltaic devices was carried out in a glovebox with a supply of nitrogen to provide an inert atmosphere for the organic materials being used in fabrication. The glovebox used, however, did not hold the nitrogen atmosphere for long, and regular measurements of both the oxygen and water content of the glovebox were made. Nitrogen purges and regenerations were used to manage

the O_2 and water content, and devices were only fabricated when O_2 concentration was below 50ppm, and water content having a boiling point of -70°C (equating to an internal pressure of 1 Bar below atmospheric pressure). However, between fabrication steps the nitrogen atmosphere would not hold and the level of both water and oxygen content would increase. Therefore, many of the devices produced for this investigation were not produced under ideal conditions which is likely to impact the results gained from them. In addition, although fabrication in an inert atmosphere prevents a number of degradation mechanisms OPV devices are susceptible to, there remain a number of processes that can still lead to reduction in device performance and even complete device failure [156] such as photo-induced degradation mechanisms.

Towards the end of the fabrication process for these devices, the glovebox was repaired such that it would hold a N_2 atmosphere for much longer without increasing concentrations of O_2 and water. This made the conditions inside the glovebox much easier to control and reduced the incidence of devices being prepared under poor conditions.

Materials

Materials used in the fabrication of organic solar cells were purchased from Ossila Ltd. with the exception of ZnO and the aluminium and gold used in metal contact evaporation. Poly[[4,8-bis[(2-ethylhexyl)oxy]benzo[1,2-b:4,5-b']dithiophene-2,6-diyl][3-fluoro-2-[(2-ethylhexyl)carbonyl]thieno[3,4-b]thiophenediyl]] (PTB7) from batch 214 and [6,6]-Phenyl-C71-butyric acid methyl ester (PC70BM,95%) from batch 113 were used as the organic donor and acceptor compounds respectively [140]. The chemical structures for these two materials are shown in figures 3.4a and 3.4b respectively. Poly(3,4-ethylenedioxythiophene) polystyrene sulfonate (PEDOT:PSS, HTL Solar 1) was purchased from Ossila but was manufactured by Heraeus Clevios^{TM} and used as the HTL. PEDOT:PSS was selected as a hole transport layer for use in both ITO and i-FLG based devices so that the only difference between the devices was

the electrode. This allows the performance of the electrode to be directly compared. Due to the high work function of i-FLG, it is possible that PEDOT:PSS free devices would perform better than those with a PEDOT:PSS HTL. However, this would change the fraction of light that entered the BHJ of the solar cell, making it difficult to directly attribute differences in the performance of the devices to the electrodes alone. Aluminium doped ZnO solution was purchased from Avantama and was used as the ETL. ITO coated quartz substrates were purchased from Ossila, along with quartz substrates for the transfer of Ni-CVD graphene, as discussed previously. Dichlorobenzene (DCB), Diiodooctane (DIO), Acetone and Isopropyl Alcohol (IPA) were purchased from Fisher Scientific and used throughout the fabrication process.

(a) PTB7 molecular structure

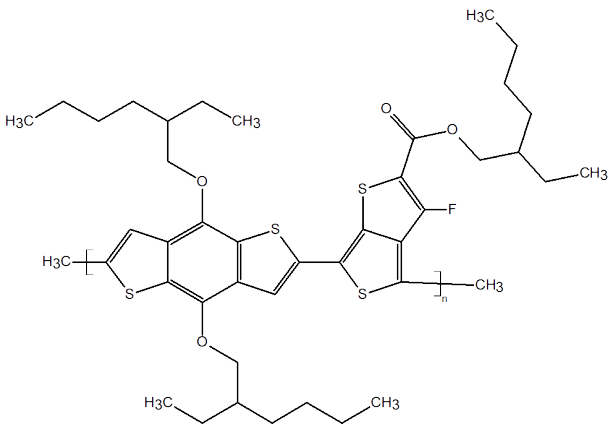

(b) PC70BM Molecular structure

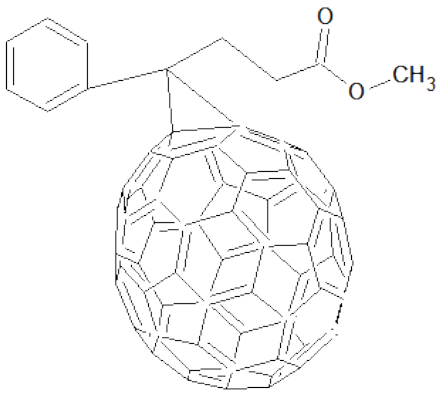

Figure 3.4: Molecular structures of the OPV materials making up the BHJ in the OPV devices produced in this investigation.

Bulk Heterojunction Solution Preparation

Before fabrication, the bulk heterojunction (BHJ) solution must be prepared. As this layer is comprised of the active photovoltaic materials in the device, it is crucial to take care during solution preparation in order to fabricate working devices. Instructions for how to prepare the solution, concentrations of each compound used, as well as spin coating and annealing parameters for each layer were taken from the Ossila website and adapted where needed. The fabrication parameters, such as

blend ratio of the donor:acceptor and concentration of DIO solvent additive, have been studied extensively and optimised in previous works [157].

Firstly, 15 mg/ml of PTB7 is added to DCB and stirred continually in the dark with magnetic stirrer bar. A slightly elevated temperature of 50°C was used to ensure all the PTB7 dissolved into solution. After 1 hour of mixing 10 mg/ml of PC70BM was added and mixed for a further hour, before adding a 1:1 mixture of DCB and DIO such that the final solution contains 3%/vol DIO. DIO has been shown to be a useful secondary solvent in the fabrication of high efficiency OPV devices. DIO preferentially solvates PC70BM, and has been shown to reduce the incidence of fullerene aggregates [10]. It has also been shown to act as a plasticising agent and coarsen domain sizes during its removal through thermal annealing [158], producing an improved BHJ morphology and leading to increased device efficiencies [130, 157, 159] and greater quantum efficiencies [9]. Once made, the BHJ solution was kept stirring in the dark at a temperature of 70°C in order to prevent the formation of polymer aggregates.

Substrate preparation

In order for good success rates of working devices, substrates must be thoroughly cleaned before being used in fabrication. Cleaning steps vary slightly between ITO and quartz substrates. Both ITO and quartz substrates were purchased from Ossila ltd., with ITO substrates having a nominal sheet resistance of 20 Ω/sq and surface roughness of 1.8 nm, and quartz substrates having a nominal surface roughness of 1 nm.

ITO substrates were first sonicated in DI water for 30 minutes to remove any dust or particulates on the ITO surface. A substrate rack was used in order to sonicate the maximum number of ITO substrates at one time without risk of damaging the substrates on each other during sonication. Substrates and rack are then transferred to a warm solution of Acetone (70°C for 30 minutes), this removes most common organic contaminants such as oils from human skin that may have residues on the

substrates. Finally, the substrates and rack are transferred to warm IPA (70°C for 30 minutes) to rinse off any acetone/organic residue remaining on the substrates. After this, the substrates are removed from the rack and are dried using N_2 gun.

Finally, ITO substrates are loaded into a JLS Reactive Ion Etcher (RIE), where they are exposed to a high power oxygen plasma (50 sccm, 100 W for 10 minutes 30 seconds). This removes any contaminants still remaining on the substrate, as well as raising the work function of the ITO by replacing any oxygen vacancies that formed on the surface. The substrates are then desiccated before being loaded into the glovebox for fabrication.

The key difference for preparation of quartz substrates is that graphene must be transferred on to the substrate and intercalated before device fabrication can take place. While the cleaning procedure is the same as for ITO, the RIE recipe used is much more mild, instead using a 30 W plasma for two 30 second periods one after the other. Graphene transfer and intercalation followed the same procedure as previously described in section 2.3. After graphene transfer and intercalation the samples are loaded into a custom built substrate holder to apply a gold contact strip down the long edge of the substrate. This allows the use of our characterization setup's push-fit test board without damaging the graphene electrode. Once in the sample holder, strips of aluminium foil are cut and taped into place over the graphene, leaving only a thin strip of graphene exposed to be contacted by the gold (discussed later). Before loading into the glovebox, the intercalated graphene electrode on quartz is first exposed to a short treatment (5 minutes) of UV/ozone exposure to aid in the spreading and coverage of the PEDOT:PSS layer.

Spin coating OPV Layers

Optimal thickness for each OPV layer were taken from the Ossila website and are not tested or compared in this work. The speed of the spin coater used in this investigation is limited to 5000 rpm, this speed was insufficient to produce PEDOT:PSS films thin enough for use in OPV devices. To achieve the desired thickness of 30-

40 nm the PEDOT:PSS solution must first be diluted with DI water, making up a 3:1 mixture of PEDOT:PSS solution and DI water. It was also found that the PEDOT:PSS layers being fabricated contained aggregates, even if the solution had been filtered (0.45μm PTFE syringe filter). Therefore, PEDOT:PSS solutions were sonicated for 1 hour before use and then filtered twice before spin coating. While this greatly reduced the occurrence of aggregates and their size, some aggregates persisted, leading to varying device success rates. Optimal thickness was obtained with a spin speed of 2400 rpm, which is used throughout this study. After spin coating a high purity cotton swab dipped in DI water is used to clean PEDOT:PSS off the ITO/Au contact strip. The sample is then annealed at 150°C for 5 minutes to remove any water trapped within the PEDOT:PSS layer, before being allowed to cool.

An hour before spin coating the active layer, the stirring temperature of the BHJ solution was increased to 80°C, as this helped disperse aggregates formed in the solution. Organic BHJ layers were spun at 1200 rpm to achieve a desired thickness of 90 nm. 25 μl of solution was pipetted onto the spinning substrate and was left to spin for 2 minutes to allow the film to dry. Once dried, the cathode strip was again wiped with a high purity cotton swab, this time wetted with IPA to remove excess OPV solution. Care was used to ensure no solvent from the swab penetrated into the film or wiped the active area of the device. Samples were then left in the glovebox to further dry for at least 2-3 hours before the ETL was applied.

A solution of Al doped ZnO in IPA was used as the ETL, and was spun at 2700 rpm to achieve the desired thickness of 30 nm. After spin coating a high purity cotton swab that had been wetted with IPA was used to clean excess ZnO from the contact strip, again taking care not to damage the active layers of the device. Once wiped, the device was annealed at 140°C for 10 minutes. This annealing stage not only anneals the ZnO layer, but also aids in removing any remnant DIO solvent from the active layers of the device. Once annealing is complete the samples are left to cool before being moved to a desiccator for at least 1 hour prior to evaporation

of metal contacts.

Metal Contact Evaporation

Metal contacts and contact strips were applied to the samples and substrates using an HVV thermal evaporator. This evaporates a desired metal through Joule heating of a metal boat or ceramic crucible such that the rate of evaporation can be controlled by the user through control of the current. For standard geometry devices, a low work function metal such as Aluminium is required to act as the cathode. This is usually used in combination with a thin layer of Calcium to act as a sticking layer to aid in charge extraction. While it was possible to evaporate Aluminium in the thermal evaporator used, Calcium could not be evaporated and so was not used in any devices. This is likely to impact on the efficiency of devices produced, but is consistent for all devices. Al contacts were deposited through a custom built shadow mask at a rate of 0.5–1.0 Å/s for a total final thickness of 100 nm. It should be noted that a number of different designs of evaporation vessel were tested during this investigation, including a tungsten basket, tungsten boat, tungsten box with a perforated lid, and finally a ceramic crucible. When melting, Aluminium would commonly flow out of whatever container it was in and either corrode the container (preventing current flowing and halting the evaporation) or would short circuit the machine. This caused a number of contact evaporation procedures to end before the desired thickness of contact was reached, causing some devices to have much thinner contacts than others (in the range of 20–60 nm). Once the contacts are deposited the devices are moved back into a desiccator, ready to be characterized.

Thermal evaporation was also used for depositing a contact strip onto the i-FLG electrode so that it could still be contacted after deposition of organic layers. For this, a 100 nm Gold contact was used with a 5 nm sticking layer of Chromium to aid in adhesion to the graphene. Metals were deposited at a rate of 0.5 Å/s, none of the problems experienced with Aluminum occurred when evaporating Gold or Chromium.

OPV Device Design

Due to differences in the patterning of the ITO electrodes and i-FLG samples, two OPV device designs were used. These designs are shown in figures 3.5a and 3.5b, for ITO and i-FLG devices respectively.

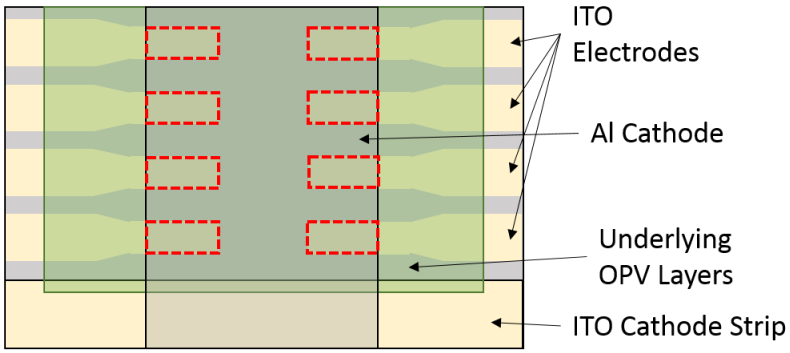

(a) ITO Device

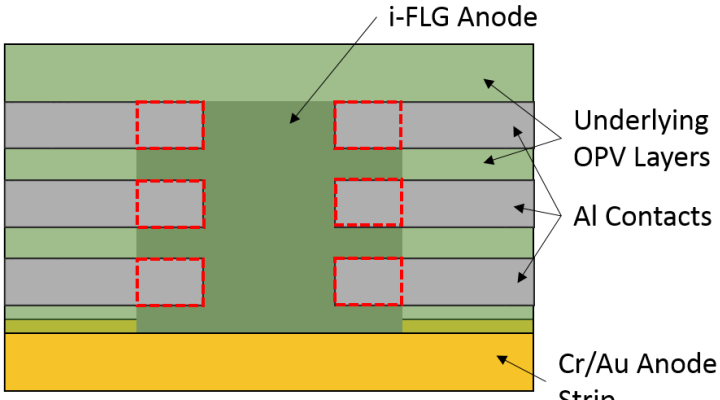

(b) i-FLG Device

Figure 3.5: OPV device designs with a. ITO electrodes, and b. i-FLG electrodes. Substrate dimensions were 2 cm × 1.5 cm but device active areas varied due to variation in overlap between anode and cathode. This was particularly necessary for i-FLG electrode devices as the position of the i-FLG electrode was subject to variation during the transfer process. As such, device dimensions were measured prior to IV characterisation for all devices.

Two types of ITO based solar cells are used, one on quartz with electrodes and contact strip pre-patterned and the other using unpatterned ITO on PET. The pre-patterned ITO samples are designed to produce 8 individual devices per sample, with the metal cathode being applied as a single strip down the centre of the sample,

overlapping with the contact strip (figure 3.5a). The active device areas are then the regions where this central metal strip overlaps with the patterned ITO underneath. For unpatterned ITO samples on PET, ITO must be removed from the edges and a contact strip applied perpendicular to the central ITO strip. The metal electrodes are then evaporated through a mask, patterning them into 8 individual contacts and defining 8 active device areas where they overlap with the ITO electrode. For i-FLG based OPV devices, the design is the same regardless of whether on quartz or PET. This is because the same 1 cm×1 cm samples were used for both, making it far easier to pattern the electrodes by evaporating the metal contacts through a mask than by first patterning the i-FLG and depositing a single metal contact strip. A schematic for the i-FLG device design is shown in figure 3.5b

3.4 Characterisation

The accurate characterization of materials and devices is crucial in developing energy harvesting devices. Here I will describe the experimental methods used to characterise the properties of graphene electrodes prepared by fishing method, large area transfer and solution processing. Methods for the characterisation of both photovoltaic and triboelectric devices fabricated using these graphene electrodes are then explained.

3.4.1 Electrical Characterisation of Graphene Electrodes

Characterising the electrical properties of graphene electrodes is key to understanding how they will perform in devices. Resistance measurements were carried out using both 2 and 4 terminal measurements. Both varieties of measurement were carried out using a Keithly 2400 source measurement unit so both source a voltage and measure the resulting current simultaneously.

2 terminal measurements were carried out using the transfer length method, where multiple contacts are placed along a conducting channel of a material at

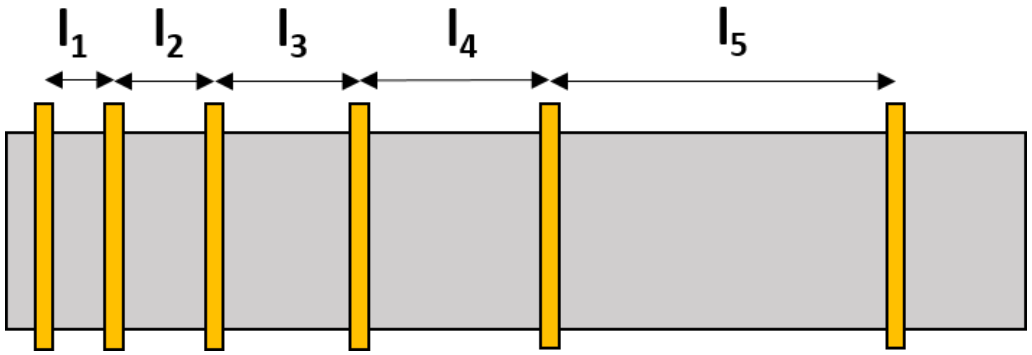

Figure 3.6: Diagram showing the measurements made for resistance measurements made with the transfer length method. Metal contacts (gold vertical bars) are applied to the sample at varying distances (l) apart. Two terminal resistance measurements are then made and are plotted against the length between the terminals, divided by the width of the sample.

varying distances, as shown in figure 3.6. A voltage is then sourced across two of these contacts and the resulting current measured. Using Ohm's law, a resistance can then be calculated.

$$V = IR \tag{3.1}$$

This is then repeated for all pairs of contacts along the conducting channel. The resistance measured can then be plotted against the distance between the two corresponding contacts. As the distance between the contacts increases, the resistance measured increases linearly following the equation,

$$R = R_s \frac{L}{w} + 2R_c \tag{3.2}$$

where R_s is the sheet resistance, L is the distance between the two contacts, w is the width of the conducting channel and R_c is the contact resistance where the two contacts meet the graphene channel. From a linear plot of resistance against length/width ($\frac{l}{w}$) both the sheet resistance and contact resistance can be found from the gradient and intercept values respectively. A conductive graphene channel was defined using a scalpel to cut a channel of known width into the graphene electrode. Silver paint (RS Components) contacts were then applied and the distances between them measured. Tungsten electrical probe tips were used to contact the silver paint

by carefully lowering them onto the silver contacts, taking care not to damage the contacts or the graphene film.

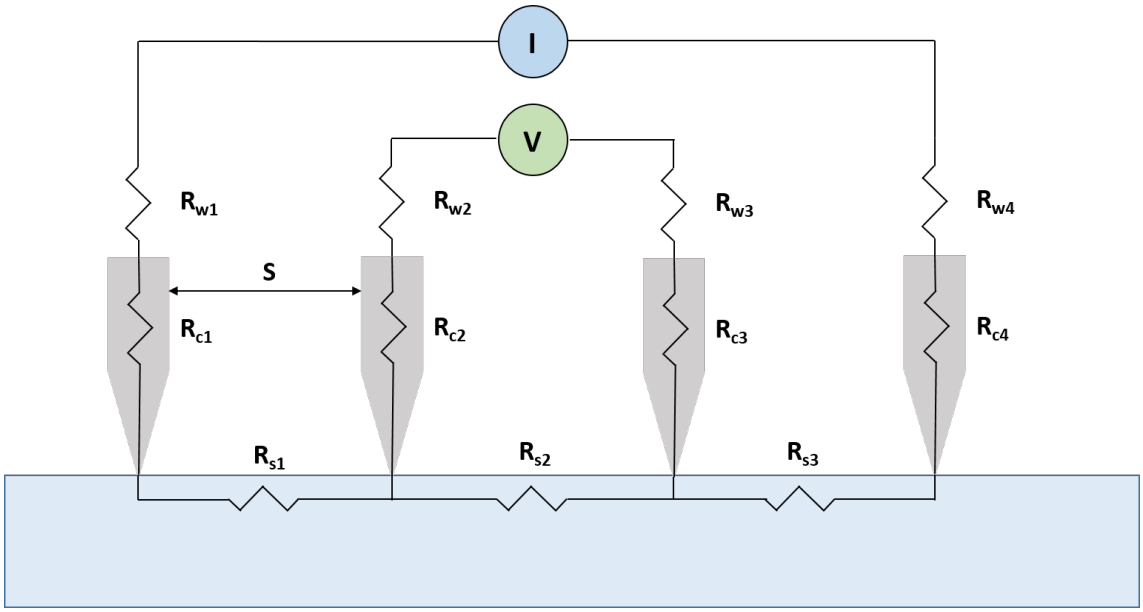

Figure 3.7: Diagram of 4 point probe resistance measurement. Here, a current is sourced between the two outer probes and the voltage is measured between the two inner probes. The contact resistance (R_c) and wire resistance (R_w) are not included in the resistance measurement.

4 terminal measurements were carried out using a Signatone S-302-4/SP4 4 point probe system. This measurement functions by placing 4 equally spaced probe contacts on the surface of the sample to be measured. A DC current is then sourced between the two outermost contacts and a potential difference measured between the two inner contacts, allowing for the measurement of resistance. This measurement is shown in figure 3.7, where R_s is the sample resistance between the probes, R_c is the resistance of the contacts, and R_w is the resistance of the wires leading to each of the 4 probes. By using this method, the contact and wire resistance can be eliminated, making this a more reliable method of sheet resistance measurement. A geometrical correction factor must then be applied to account for sample shape. For samples where the separation between the probes and sample thickness are much less than the lateral dimensions of the sample, a correction factor 4.5324 ($\frac{\pi}{\ln 2}$) is used. This is due to the

3.4.2 Magneto-transport Measurements

In addition to the resistance measurements that were also carried out on the various types of graphene electrodes produced here, magneto-transport measurements were carried out to characterise other electrical properties of the i-FLG electrodes, including the carrier mobility and charge carrier concentration of the graphene samples. Magneto-transport measurements were carried out in two different manners, one using Van der Pauw geometry (figure 3.8) and the other using the classic Hall bar geometry.

Van der Pauw Measurements

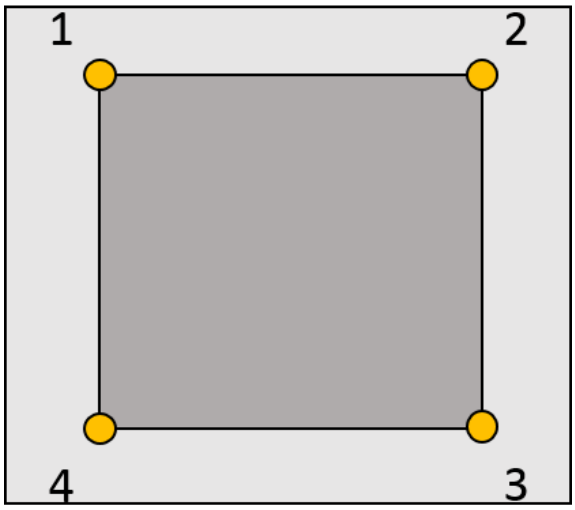

Figure 3.8: Schematic for Van der Pauw sheet resistance measurements in a square geometry. The dark grey area signifies the sample area, with the gold markers on the corners of the sample being where the contacts are positioned. Other measurement geometries are also usable, however all samples characterized by this method were 1 cm $\times$ 1 cm squares.

Van der Pauw magneto-transport measurements were made by Dr. Christos Melios using a custom built Mageto-Transport measurement set-up specifically designed for making environmental transport measurements. Using this set-up the user can measure sheet resistance, charge carrier concentration and carrier mobility. Devices

tested were limited to a 1 cm ×1 cm geometry, this was due to the positioning of the gold plated, half-sphere contacts used to contact the corners of the samples. By limiting samples to this geometry it allows Hall effect measurements to be carried out without any fabrication of Hall bars being required. This removes the possibility of doping the graphene through contamination with polymers used in fabrication procedures. Sheet resistance values were measured without the use of magnetic field, applying a current (100 μA, $f_{current}$=96 Hz) between two adjacent contacts and measuring the voltage across the other two. This is then repeated for each pair of adjacent contacts, allowing the calculation of the sheet resistance as follows:

$$R_{43,12} = \frac{V_{43}}{I_{12}} \tag{3.3}$$

$$R_a = \frac{R_{43,12} + R_{34,21} + R_{12,43} + R_{21,34}}{4}, \quad R_b = \frac{R_{32,41} + R_{23,14} + R_{41,32} + R_{14,23}}{4} \tag{3.4}$$

$$e^{\frac{-\pi R_a}{R_s}} + e^{\frac{-\pi R_b}{R_s}} = 1 \tag{3.5}$$

where equation 3.5 can then be solved numerically for R_s. Measurement of the carrier mobility and concentration must be done in the presence of a magnetic field to trigger the Hall effect. An electromagnetic coil is used to achieve this, producing a DC magnetic field and allowing the measurement of the Hall voltage (V_H). A lock in amplifier is used for measurement of the voltage for both sheet resistance and Hall effect measurements.

The charge carrier concentration and carrier mobility can then be calculated using the Hall voltage as follows:

$$R_H = \frac{V_H t}{IB} = -\frac{1}{ne} \tag{3.6}$$

$$\mu = \frac{R_H}{R_S} \tag{3.7}$$

where R_H is the Hall resistance, t is the sample thickness, B is the strength of the applied magnetic field, n is the charge carrier concentration and μ is the carrier

mobility. The Hall voltage is calculated by measuring the voltage between opposite corners of the sample (such as 1 and 3), with the current flowing between the other two corners (2 and 4). This is repeated twice for each set of opposite contacts, as well as for the magnetic field being applied in positive and negative z-directions with respect to the x-y plane made by the sample. The Hall voltage is then given by:

$$V_H = \frac{(V_{24}^+ - V_{24}^-) + (V_{42}^+ - V_{42}^-) + (V_{13}^+ - V_{13}^-) + (V_{31}^+ - V_{31}^-)}{8} \tag{3.8}$$

where the + and - signs indicate the direction of the applied magnetic field.

Hall Effect Measurements

Small sections of large area FLG samples were fabricated into 6 terminal Hall bars using laser writing of a polymer mask and photoresist before developing the mask and etching it using RIE (described in section 3.3.1). Once patterned into Hall bars, FLG were intercalated following the procedures previously outlined. After intercalation, another photoresist is applied in the same manner as before and the laser writer used again, this time to pattern a shadow mask to apply Cr/Au contacts by thermal evaporation. Once contacts are deposited the sample is mounted to a chip carrier, the Cr/Au contacts are connected to the carrier pins via bonding with gold wire. This stage, as well as the following characterisation of the magneto-transport properties of the samples were carried out with the assistance of Dr. Adolfo De Sanctis.

The sample and chip carrier were mounted into a magnetic field chamber for room temperature magneto-transport measurements. A diagram of the hall effect is shown in figure 3.9. An AC current (I) is sourced along the channel length by applying a source drain bias of 3 V, with a ballast resistor (1 MΩ) placed in series with the sample. A perpendicular magnetic field (B) is then applied, causing a Lorentz force to be applied to the electrons flowing along the channel. This causes the charges flowing in the channel to deviate from their linear path (shown by the dotted arrow in the figure), causing the build up of charges on the edges of the

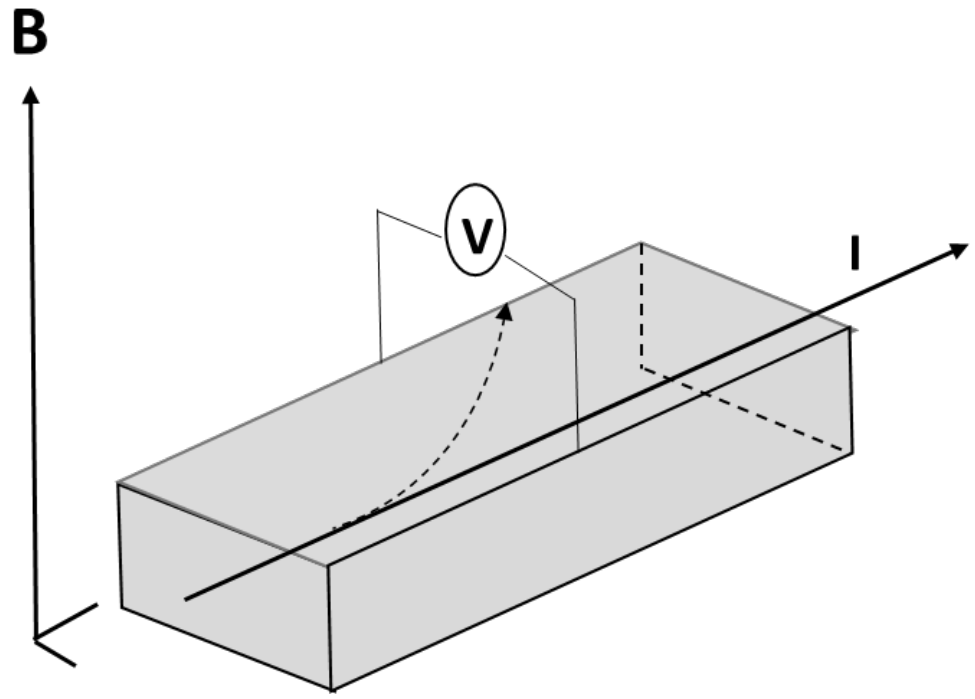

Figure 3.9: Diagram to illustrate how Hall effect measurements were carried out. The channel of material being characterized (grey) is placed in a magnetic field chamber and has a current passed through it, perpendicular to the direction of the applied magnetic field. The Lorentz force experienced by charges in the channel then causes a build up of voltage, perpendicular to both the current and magnetic field. This voltage can be used to calculate the Hall resistance and hence the charge carrier concentration, sheet resistance and carrier mobility.

channel, producing a voltage. The voltage parallel (V_{xx}) and perpendicular (V_{xy}) to the applied current are measured by means of a lock-in-amplifier. By measurement of V_{xy} and the current flowing across the sample, the Hall resistance can be calculated, which allows for the measurement of the charge carrier concentration using equation 3.6. V_{xx} is used to calculate the sample's sheet resistance using Ohm's law.

$$R_s = \frac{V_{xx}}{I} \tag{3.9}$$

3.4.3 Optical Characterization of Graphene Samples

While the electrical characterization of graphene electrodes is crucial to their applications, so too is their optical characterization. This can take many forms, but for the purposes of this work optical characterization involves optical microscopy, transmission measurements and Raman spectroscopy

Optical Microscopy

Optical microscopy was used throughout OPV device fabrication to assess the effect of changing parameters in the spin coating, solution preparation and mixing, and ozone treatment stages. These images were used to inform the changes being made to fabrication steps. Typically, a $\times 5$ magnification was used to image large areas of the films, however $\times 10$ and $\times 20$ magnifications were also used to image individual particle aggregates. A $\times 50$ magnification was used when imaging individual graphene domains or particularly small aggregates. In addition to this, optical microscopy was also used to investigate damage to OPV devices caused by repeated bending cycles, such as cracks in the ITO electrodes or delamination of OPV layers.

Raman Spectroscopy

As was discussed in chapter 2.2.3, Raman spectroscopy is a technique where vibrational energy transitions in a material are triggered by the scattering of incident photons. This causes a shift in the wavenumber of the scattered light, compared to the incident light. This is known as the Raman shift, and signifies energy level transitions between different Raman active vibrational modes. In graphene samples there are three main Raman active modes that are seen in the majority of Raman spectra; these are the G-peak (1580 cm^{-1}), the D-peak (1350 cm^{-1}) and the 2D-peak (2700 cm^{-1}). By measuring the exact position and intensity of these peaks in graphene samples it is possible to access a lot of information about the properties of the sample, such as number of layers [160], doping [161], defect density [161, 94] and many others, without risking damage to the graphene sample. In this section,

I shall describe the general method by which Raman Spectra were collected, before expanding upon this method later in Chapter 4.

Throughout this investigation, Raman spectroscopy was carried out using a multipurpose microscope, custom built specifically for the purpose of characterizing optoelectronic devices built from 2D materials (figure 3.10) [162]. A calibration spectrum is first taken from a sample of Si/SiO_2, which gives a characteristic peak at 520 cm^{-1}. This allows the exact wavelength of the laser being used to be calibrated for, as small variations in this wavelength can cause large variations in the positions of graphene's characteristic Raman peaks. A 30–50 mW, 514 nm laser was used, with a 2 second exposure time and a spot diameter of approximately 1 μm. It should be noted that most graphene samples would be somewhat damaged if exposed to this intensity, however i-FLG can withstand much higher levels of irradiation before showing any damage, making this intensity suitable. This setup was not capable of measuring the entire Raman spectrum of graphene in one measurement, and instead had to measure regions of interest of the spectrum. As such, to measure the complete spectrum, two measurements were collected over regions of interest covering the D and G peaks in one, and the 2D peak in the other.

In this thesis, Raman spectroscopy is primarily used to characterize the doping and defects in graphene samples. This is done through two similar methods for both the doping and defect densities. Doping of the graphene samples can be detected in the Raman spectrum by a shift in the G-peak. This is caused by a stiffening of the G-peak phonon caused by a shift in the Fermi energy of the graphene sample that results from the doping. In intercalated graphene, the doping is dependent on the extent of the intercalation between the layers of graphene. Each Raman spectrum samples all the graphene environments present within the laser spot area, meaning the resulting spectrum is an aggregate of the individual spectra from each layer of graphene. This results in the G-peak of intercalated graphene being a composite peak of each of the G-subpeaks created by different doping environments. As has been previously shown, pristine graphene results in a G-peak centred around 1580

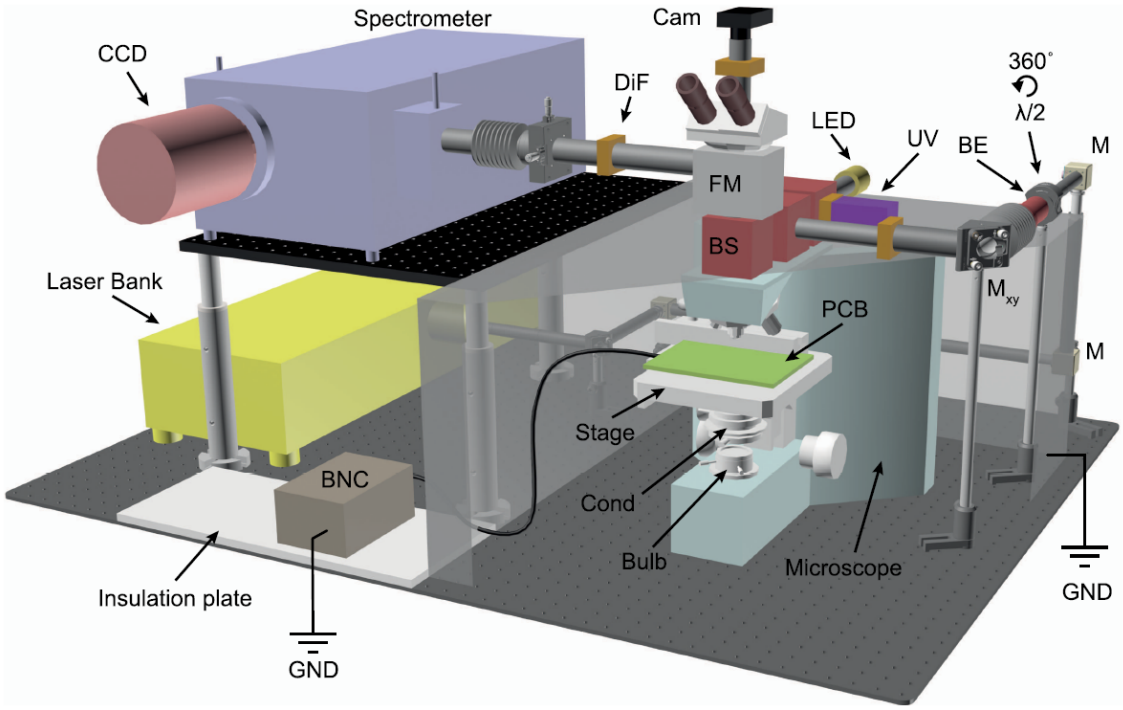

Figure 3.10: 3D model of the multipurpose microscope used for the characterization of samples by Raman spectroscopy. The 514 nm laser exits the laser bank (yellow) and is directed onto a Beam Splitter (BS). 50% of the beam is then shone on the sample mounted on the stage, the other 50% of the beam is reflected off the flip mirror (FM). The Raman light from the sample then passes back through the BS and is reflected by the FM. The source light from the laser is then filtered out using a 514 nm notch filter in the Drop in Filter (DiF) slot, while the Raman light is able to enter the spectrometer (purple). Here, the beam is collimated by a collimating mirror, before being diffracted by the diffraction grating in the spectrometer. The diffracted beam is then focused on to the Charge Coupled Device (CCD) from a focusing mirror, where signals of different wavelengths can be detected. Figure reproduced with permission (AIP Publishing)

cm^{-1}, graphene doped by a single layer of $FeCl_3$ results in G-peak around 1612 cm^{-1}, and graphene doped on either side by $FeCl_3$ results in a G-peak around 1625 cm^{-1}. The resulting doping associated with each shift value can be calculated from the work of Lazzeri et al. [98], however the sensitivity with which this can be performed reduces with increasing Raman shift values. I will go on to further expand upon this method by using Raman mapping to produce maps of the composite G-peak shift values to spatially characterize the degree of intercalation.

Another key parameter in the characterization of graphene samples is the defect density. This can have a profound impact on many properties of the graphene sample, including the electron/hole mobility, sheet resistance and, depending on the type of defect, the surface properties of the sample. The D-peak in the Raman spectrum of graphene is triggered by the presence of defects, and therefore has a smaller peak area for samples of graphene with lower defect densities. While this is difficult to accurately quantify, by calculating the ratio of peak intensities for the D and G peaks, one can estimate the ratio of active defect sites to the total number of graphene environments. This has previously been measured, showing different varieties of defects to be characterized by different D and G peak intensity ratios [94, 163]. This method is later expanded upon and used to map the defect density across large sample areas, as will be discussed in Chapter 5. Characterisation of defects was carried out using a script prepared by Miss Gabriella Prando, which analyses the intensity of the G and D peaks using peak fitting similar to what has previously been described for the characterization of the G-peak.

3.4.4 Transmission measurements

Measurements of the transmission spectra of i-FLG samples were made using the same custom built, multipurpose microscope as was used to collect Raman spectra (figure 3.10) [162]. The transmission of light from a white Light Emitting Diode (LED) through the i-FLG sample was measured across a range of wavelengths covering the visible spectrum. A calibration measurement was first made on a clean quartz

substrate, which was then subtracted from the transmission through sample and substrate. By measuring the transmission intensity through no sample, the wavelength dependent intensity of the light source is characterised. Transmittance through the substrate is then measured by recording the intensity of light passing through the substrate and dividing it by the intensity of the source ($T_{substrate} = I_{substrate}/I_{source}$, where T and I denote transmittance and intensity respectively). The transmittance of the sample is then measured in the same way, but with the light intensity of the source reduced by the transmittance of the substrate, as shown in equation 3.10.

$$T(\lambda)_{sample} = \frac{I(\lambda)_{sample}}{T_{substrate} I(\lambda)_{source}} = \frac{I(\lambda)_{sample}}{I(\lambda)_{substrate}} \tag{3.10}$$

3.4.5 Surface Characterisation of Graphene Electrodes

The surface properties of a material can greatly influence its success in device applications. Specifically, the surface roughness and the work function are two key material parameters in the fabrication of both solar cells and TENG devices. In this section I will describe the methods used to examine these properties.

Profiler Measurements

A KLA Tencor Alpha Step D-100 Profilometer was used to measure sample thickness and roughness. This functions in a similar manner to an AFM operating in contact mode, where a probe tip is brought into contact with the surface of the sample and dragged along the surface in a single direction. This defines the y direction as vertical displacement (height), the z direction as the horizontal distance over which the measurement is made (the length of the scan). As the scans are only measured in a single direction, the x direction is not used. This allows the measurement of the deflection of the tip in the y-axis for the given displacement in the z-axis. This produces a surface profile that details a line scan of the sample's topography. Both sample thickness and surface roughness are calculated from these profiles. Firstly,

a calibration sample is measured to ensure that measured heights accurately reflect the actual heights. Then the tip is placed over an area of substrate next to the region of sample to be measured. The tip is then engaged and dragged across the sample in the z direction. Starting the measurement from the substrate allows the accurate calculation of sample thickness provided a large enough distance is scanned. Multiple scans were collected across different regions of each sample and the mean thickness calculated for each sample, selecting to average only across the region of full thickness.

Root mean square (RMS) surface roughness measurements were carried out by calculating the standard deviation in height for flat regions of the profiles collected. Multiple such measurements are carried out on each sample, allowing for the calculation of the RMS roughness. As the edges of the graphene samples measured were sloped due to non-uniform detachment from the filter membrane, it is important not to include these regions in measurements of thickness or roughness.

Atomic Force Microscopy

Atomic Force Microscopy (AFM) was used to measure the roughness of substrates and electrodes being used in OPV devices. All measurements made with this technique used non-contact tapping mode, this technique (detailed in figure 3.11.a) involves a very small AFM tip, placed at the end of a vibrating cantilever, travelling over the surface of the sample being measured. A Bruker Innova AFM was used for measurement of topographical data, using a Nanosensors PPP-NCHR silicon AFM probe tip in non-contact tapping mode. This means that the cantilever is constantly oscillating up and down, bringing the tip closer and then further away from the surface. The attraction between the tip and the sample, caused by Van der Waals forces, cause the cantilever's vibrations to deviate from the natural frequency, which is calibrated for prior to measurement. By using the change in cantilever frequency, the proximity of the tip to the sample can be calculated, allowing a map of the topographical surface underneath the tip to be produced. Operation in this

mode is crucial to ensure graphene samples are not damaged by the probe tip during measurements.

Scanning Kelvin Probe Force Microscopy

Scanning Kelvin Probe Force Microscopy (SKPFM) is a similar experimental technique to AFM, but allows access to much more information about the electrical environment of a sample's surface. Similar to AFM, an oscillating probe tip is used to map the sample's surface. However, unlike AFM measurements, the probe tip used is conductive. This allows the surface potential of the sample to be analysed through the contact potential difference (CPD) between the sample and the tip [164]. Prior calibration of the probe tip potential allows the direct mapping of the work function of the material, through the equation:

$$eV_{CPD} + \phi_{Tip} = \phi_{Sample} \tag{3.11}$$

where e is the elementary charge, V_{CPD} is the contact potential difference, ϕ_{Tip} is the work function of the probe tip and ϕ_{Sample} is the work function of the sample.

The principle behind this measurement is shown in figure 3.11.b–d. When the probe and sample are close enough to establish an electrical connection, the Fermi levels of the tip and sample align, producing a contact potential difference that is defined by the difference in work functions of the two materials ($V_{CPD} = \frac{\phi_s - \phi_t}{-e}$) [165]. This allows SKPFM to accurately measure the work function of a material with similar spacial resolution to topographical AFM maps, making it an extremely powerful surface characterization technique.

Two sets of SKPFM measurements were carried during this work. The first set by Dr. Christos Melios using an NT-MDT NTEGRA Aura system using frequency-modulated SKPFM mode and conductive Bruker PFQNE tips. This was carried out at the National Physical Laboratories (NPL) on i-FLG from 1 cm × 1 cm and wafer scale samples. Topography and surface potential of the samples were both collected simultaneously. Freshly exfoliated Highly Orientated Pyrolitic Graphite (HOPG) was used to calibrate for the tip potential before each measurement. SKPFM mea-

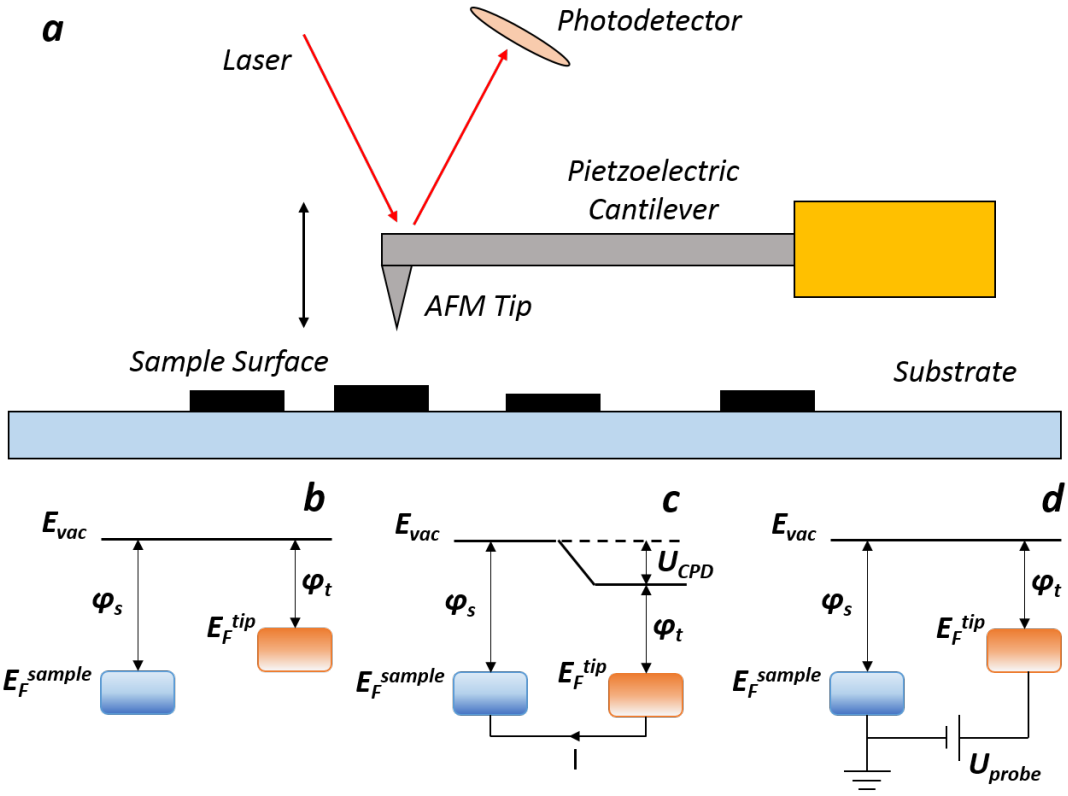

Figure 3.11: Schematic showing the operation of ***a*** an AFM functioning in tapping mode and ***b***, ***c*** and ***d*** illustration to show the working principle of SKPFM. In AFM, a pietzoelectric cantilever is used to generate oscillations that move the AFM tip towards and away from the sample surface. A laser is reflected from the back side of the tip onto a photodetector to accurately determine the position of the tip. Deviations from the natural frequency of the cantilever are caused by Van der Waal's interactions between the tip and the sample, allowing a topographical reconstruction of the sample's surface. In SKPFM, the sample and tip begin separated (***b***) before being brought close enough for an electrical connection to be established (***c***), generating a contact potential difference (U_{CPD}) which can be offset by the application of a bias voltage to the probe tip (U_{probe}) (***d***).

surements were taken over a 30 μm $\times$ 30 μm area to account for variation in the film thickness, and hence the intercalation conditions of the i-FLG samples.

The second set of SKPFM measurements were carried out by Vishan Pashal at the University of Exeter using a Bruker Dimension XR Scanning Probe Microscope in Peak Force KPFM mode. A PFQNE-Al probe tip was used (doped silicon with a 5 nm tip radius), allowing topography and surface potential to be collected simultaneously. Freshly exfoliated Highly Orientated Pyrolitic Graphite (HOPG) was again used to calibrate for the tip potential before each measurement. These measurements were carried out on freshly intercalated samples of FLG, as well as a sample of i-FLG that had been exposed with UV/Ozone treatment.

Contact Angle Measurements

A contact angle Goniometer, shown in figure 3.12, was used to measure the contact angle made between DI water droplets and the graphene/intercalated graphene surface. The setup is first calibrated by using a small spirit level to ensure the sample mount is level. The sample is then placed on the sample mount and a small droplet of water is placed in the centre of the graphene film by pipette. A camera set up on the same plane as the sample is then used to take a short video of the droplet. The droplet is back-lit by a light, allowing for good contrast in the image and for the edge of the droplet to be clearly seen. The contact angle is then measured by selecting individual frames from the video and measuring the angle made between the droplet and the surface of the graphene. The angles at either side of the droplet are averaged by calculation of the mean, to account for any slope that could not be corrected for in the setup.

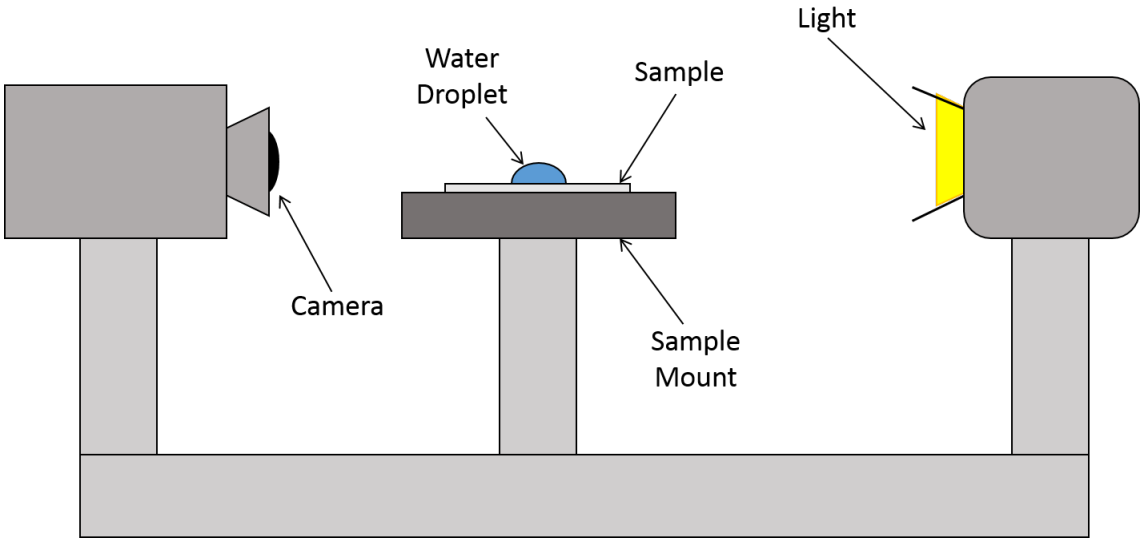

Figure 3.12: Diagram of the setup used to measure the contact angle made between water droplets and graphene samples.

3.5 Device Characterization

Throughout this thesis I will test the applicability of graphene and intercalated graphene electrodes in different devices for energy harvesting. The two types of energy harvesting devices examined and characterized are OPV devices and TENG devices. The following are the characterization methods used for each device, as well as a brief background to understand the measurements, further to what is discussed in the Chapter 2.

3.5.1 Photovoltaic Device Characterisation

Accurate characterisation of photovoltaic devices is crucial to the assessment of how different components of the photovoltaic device impact device performance. In this investigation I focus only on the benefits/drawbacks in using i-FLG electrodes as it applies to device efficiency, stability and flexibility. As such, the optimisation of each aspect of the OPV devices has not been investigated and device efficiencies are lower than for reference devices (Ossila). However, comparisons of the performances of different devices with different electrodes can still be made.

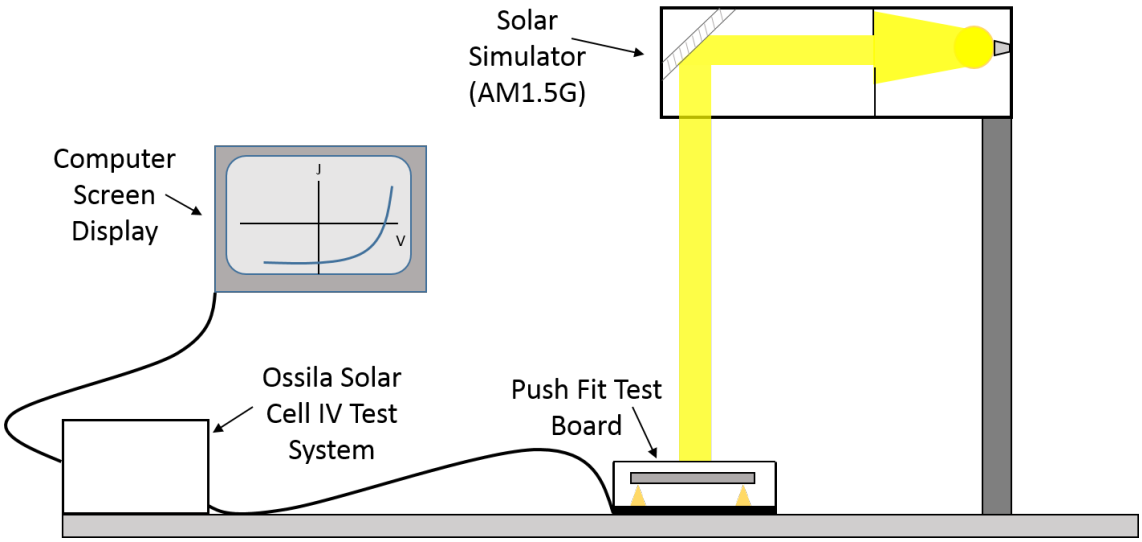

Figure 3.13: Diagram of the setup used in characterization of OPV devices. The solar simulator is fitted with an AM1.5 G filter that approximates the spectrum of the sun for standard conditions on Earth. This is used to illuminate the sample, which is fitted into the push fit test board. From here, the IV curve sweep is carried out by the Ossila Solar Cell IV Test System and displayed on the computer screen. IV Curve sweep parameters are controlled via the Ossila software, such as voltage sweep range, voltage step increment and dwell time.

Current-Voltage Curve Measurement

Current Voltage (IV) curve measurement was carried out using an Ossila Solar Cell IV Test System with push fit test board. Samples were loaded into the push fit test board where the contacts have been patterned to line up with sets of metal pins inside the test board. The pins are slightly spring-loaded so that they compress when the sample is fixed into place and do not damage the contacts. IV curve sweeps were run between -1 and 1 V, and then 1 and -1 V to assess any hysteresis between the two sweeps. Voltage step increments of 10 mV and a voltage settle time of 10 ms were used. A diagram of the setup used for photovoltaic device characterization is shown in figure 3.13.

When measuring IV response under light exposure, an appropriate solar simulator must be used to replicate the wavelength dependent light intensity that is

produced by the Sun. For this investigation a Newport 94011A class ABB solar simulator (Xenon arc lamp fitted with an AM1.5G filter) was used. The irradiance intensity is adjusted by altering the height of the solar simulator from the sample. This height was calibrated using an Oriel model 91150V Calibration Cell connected to a readout meter, giving the intensity of the solar simulator measured in Suns (1 Sun = 1kW/m^2). Before measurement of devices, the solar simulator was turned on and left for 30 minutes so that the emission would stabilize. Over that time, the calibration cell was set up and periodic readings of intensity and temperature were taken to ensure the correct intensity was being output.

For each sample, measurements were carried out under illumination and under dark conditions. For measurement of the dark curve, the shutter on the solar simulator was closed and a cover placed over the opening on the push-fit test board to prevent any ambient light from entering and giving false readings.

Once the IV curves (light and dark) have been collected for a device, performance metrics can be extracted. The metrics used to assess OPV performance in this study are efficiency, short circuit current (J_{sc}), open circuit voltage (V_{oc}), fill factor (FF) and the series and shunt resistances (R_{se},R_{sh}). These are extracted from the IV curve using the Ossila Solar Cell IV Test System software and are explained in figure 2.12 of Chapter 2.

3.5.2 Triboelectric Device Characterization

The triboelectric response of devices was characterized by means of recording the current/voltage output of the device during contact cycling of the materials being used. The motion of the device was controlled by an actuator set to run from a Labview program. The controlled variables were the set and return points of the actuator, and the frequency of the movement cycles. A load cell was also connected to the actuator, allowing the force on the TENG device on each cycle to be recorded. This investigation made use of the setup built by Dr. Zakaria Saadi, shown in figure 3.14. This setup involves two mounts on which to fix the two sides of the TENG

device. One of these mounts is connected to an electronic actuator with a load cell attached. This allowed the contact and separation of the two triboelectric layers to be controlled via a labview code running through a computer connected to the actuator and load cell. The load cell allowed for monitoring the force applied to the TENG device, which was maintained at less than 5 N throughout the experiments. This ensured minimal vibrations were present, as these can affect the results being collected.

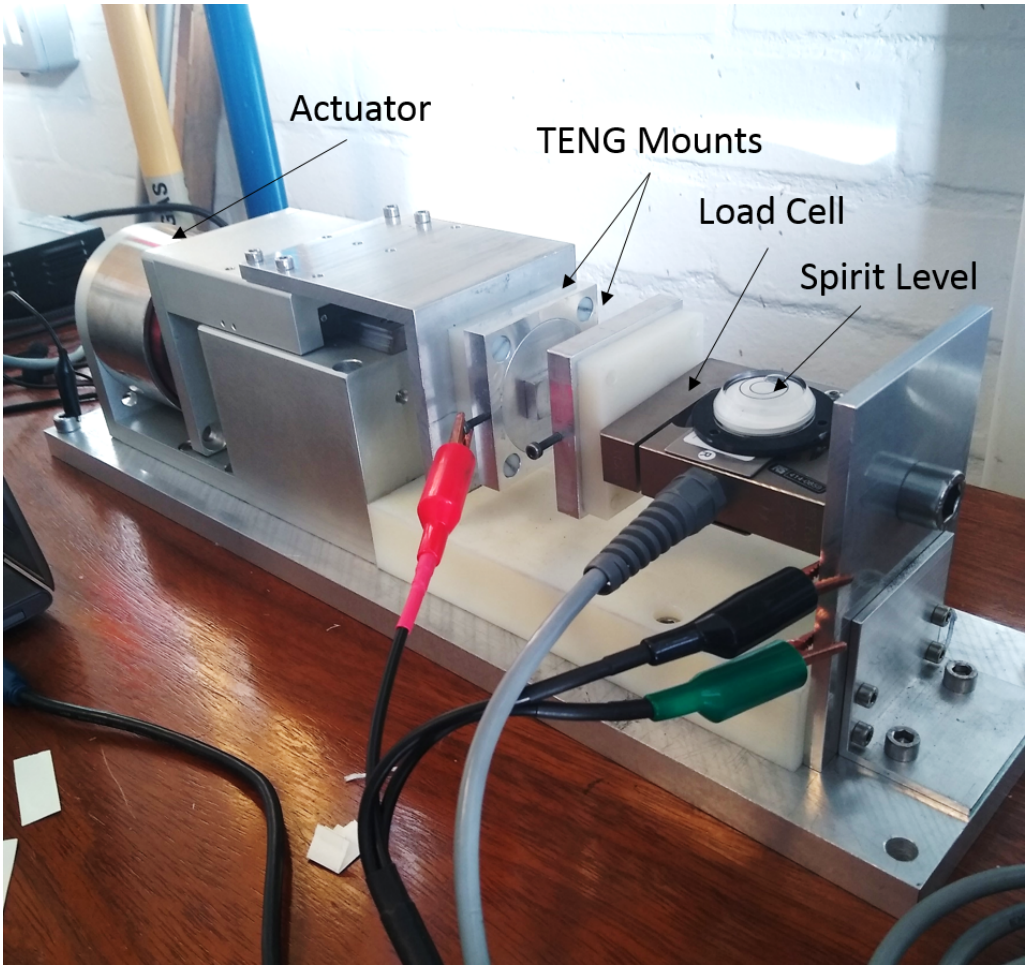

Figure 3.14: The setup used to characterize TENG devices. This setup was built by Dr. Zakaria Saadi and designed by R.D.I.G. Dharmasena from the University of Surrey, and adapted from his works (xy). The whole setup is fixed to a metal plate which is bolted to the lab bench to minimise vibrations during measurements.

Two Keithley source-measurement units were used to both control the actuator and to measure the current and voltage in short circuit and open circuit configura-

tions respectively. The dielectric material being tested against i-FLG was taped to one of the mounts using copper tape, allowing measurements to be made in double electrode configuration by connecting the Keithley source measurement unit to both the TENG device and the mount housing the dielectric material. The key difference between these two measurement configurations is that in double electrode (DE) the electrical signal being measured represents current/voltage from the two halves of the device, where single electrode (SE) only acquires a signal from one of the electrodes (in this case the i-FLG electrode). This typically means that measurements made in DE mode are approximately double the magnitude of those made in SE mode.

When measuring the devices, the alignment of the setup is first checked to ensure a planar contact between the TENG and the mounted material. A set-point is then created when the two materials are in contact, allowing the contact and separation of the materials to be cycled. The actuator then runs the cycle for over a period of approximately a minute, with the measurement of the current/voltage response running for the last 20 seconds of the cycling motion. This allows the measurement to stabilize to any unbalance of surface charges of the materials caused by contamination or remnant frictional charging that occurred during sample preparation and mounting.

Chapter 4

Wafer Scale $FeCl_3$ Intercalated Few Layer Graphene Electrodes

---

Data contained within this chapter has been subject to publication: *"Wafer scale $FeCl_3$ intercalated graphene electrodes for photovoltaic applications."* K. K. Walsh, C. Murphy, G. Jones, M. Barnes, A. De Sanctis, S. Dong-Wook, S. Russo, M. F. Craciun. Proc. SPIE 10688, Photonics for Solar Energy Systems VII, 106881C (21 May 2018); DOI: 10.1117/12.2307410.

4.1 Introduction

Graphene presents many appealing properties for use in photovoltaic technologies, particularly its excellent flexibility, transparency and conductive properties [35, 64]. However, compared to the industry leader, Indium Tin Oxide (ITO), graphene has a relatively high sheet resistance, which has lead to reduced photocurrents and device efficiencies in photovoltaic devices incorporating graphene electrodes. Intercalation of FLG with Iron Chloride ($FeCl_3$) has been demonstrated as an excellent method of doping Graphene, leading to a reduction in sheet resistance of up to 3 orders of magnitude [62]. In addition, this doping is resistant to atmospheric contamination [61], unlike many other chemical dopants such as HNO_3 [51, 166, 167], $SOCl_2$ [51] and tetracyanoquinodimethane (TCNQ) [48]. This makes intercalated FLG (i-FLG)

suitable for use in devices that make use of solution deposition procedures, such as those used in the fabrication of organic photovoltaic (OPV) devices. Another crucial factor to the use of doped graphene as a transparent conductive electrode is the scalability of the fabrication methods used in both electrode preparation and doping of the graphene. This has lead to many devices reported in literature being prepared using techniques that are not scalable and do not give an accurate indication of how the devices will perform when scaled up. As such, in this chapter I will present a method I developed for the scaling up of the manufacturing process for preparing wafer scale (7 cm $\times$ 7 cm) i-FLG samples. This process first involves the transfer of wafer scale FLG samples using a custom built transfer setup, followed by intercalation in a 9 cm diameter furnace. This required the optimisation of the intercalation temperature used. I then present a new method that I developed for the characterization of the prepared i-FLG samples using Raman spectroscopy, introducing a new metric by which to quantify the degree of intercalation within the i-FLG [117]. Measurements of sheet resistance, work function, carrier mobility and charge carrier concentration are then all used to characterise the quality of the i-FLG samples and determine their suitability for use in flexible OPV devices.

4.2 Etching and Transfer of Wafer Scale FLG Samples

Two types of FLG films were purchased from Graphene Supermarket, 1 cm $\times$ 1 cm graphene samples and 4 inch diameter wafers of graphene, both grown on Ni/Si/SiO_2 substrates. This allows the results of the newly developed intercalation conditions for wafer scale samples to be compared to the previously established method for intercalating 1 cm $\times$ 1 cm samples.

As was discussed in the methods chapter, before intercalation graphene must first be transferred to a suitable substrate that can withstand intercalation conditions. While the flotation assisted transfer method is capable of achieving this with smaller

samples, large area samples are commonly damaged or destroyed due to the difficulty of transferring them in this manner. This prevents it from being scaled up to an industrial scale process capable of manufacturing large area graphene devices. In addition, the flotation assisted transfer method is also extremely time consuming and labour intensive, highlighting the need for the development of a new transfer process that can be scaled up more easily. As such, a partially automated large area transfer setup and method were developed to improve the yield and quality of graphene samples being transferred. This process, schematically illustrated in figure 4.1, was developed by myself and Mr. Conor Murphy, with guidance from Dr. Matthew Barnes and Dr. Gareth Jones.

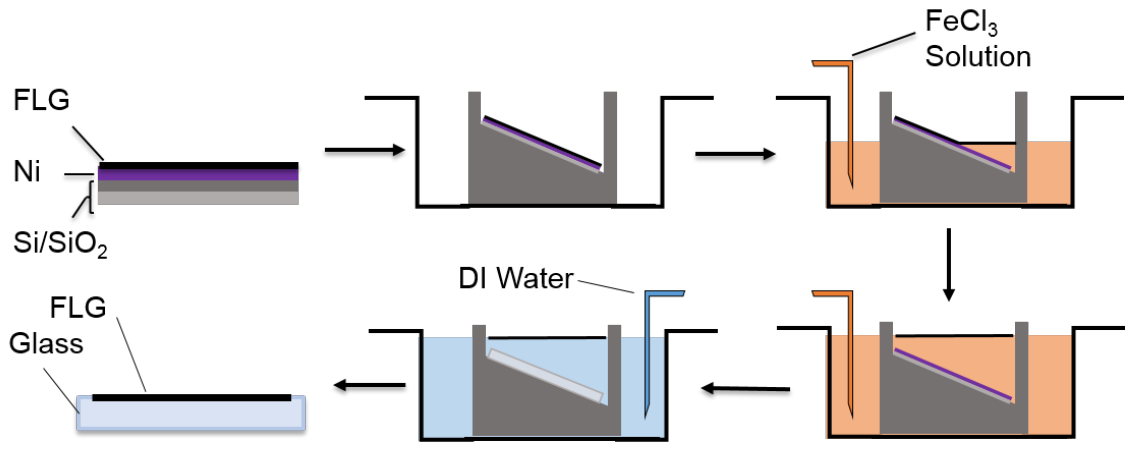

Figure 4.1: Large area graphene transfer process, detailing the etching of the Ni catalyst by $FeCl_3$ solution, floating of the graphene film, replacement of the $FeCl_3$ solution with DI water and subsequent transfer of the graphene to a clean glass substrate

This new method of graphene transfer employs a stationary wedge mount for the graphene sample to be mounted, and controls the etch and transfer of the graphene through the use of rotary pumps. Using this method it was possible to quickly and reliably transfer large area graphene samples, as is detailed below [117].

A custom built wedge mount was produced and placed inside an etching bath, shown in figure 4.2. This wedge is designed to fit samples of up to 7 × 7 cm in size, but in principle can be made to any size to fit the manufacturing need. The etching

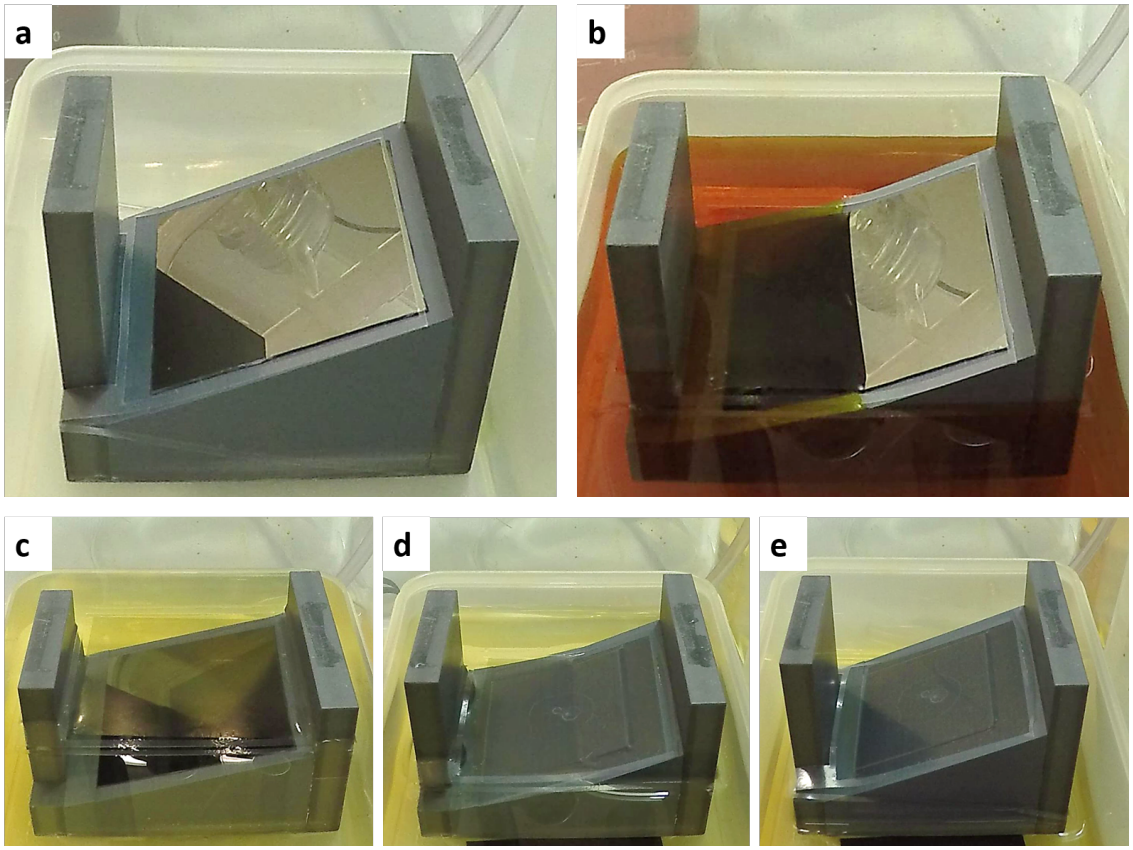

Figure 4.2: Images recorded during the etching and transfer procedure. ***a.*** Large area graphene on Ni/Si/SiO_2 growth substrate is mounted to the custom built wedge. ***b.*** 1 M $FeCl_3$ etchant solution is steadily pumped into the bath around the wedge, etching the Ni as the level of the solution rises. ***c.*** Once the etch is complete, the $FeCl_3$ solution is replaced by DI water by flooding the bath. ***d.*** Si/SiO_2 substrate is removed and replaced with a clean glass substrate. The pumps are run in reverse to pump the DI water out of the bath, lowering the level and beginning the transfer. ***e.*** Large area graphene transfer is complete with no damage to the sample.

bath is connected to two rotary pumps. These are used for both filling and draining the bath, and are controlled through a simple Labview program which allows the user to set the voltage and hence the pump rate. Once a sample of Ni grown CVD graphene has been selected and prepared for transfer, it is fixed to the wedge by placing a small spot of PMMA solution to the back of the Si/SiO_2 substrate. A custom made floating border made from a thin sheet of plastic is then placed around the wedge. The purpose of this boarder is to hold the floating graphene film in place once it has detached from the growth substrate. The pumps are then connected to a bottle of 1M $FeCl_3$ solution and are turned on. The rate of flow of $FeCl_3$ etchant solution can be controlled through the voltage (the volume of liquid transported with each pump) or the frequency (time between successive pumps). Pumps are set to pump continually until the etchant has reached the bottom of the sample. At this point the pump rate is slowed to give the solution time to etch the Ni underneath the graphene. If the rate is too high, the level of etchant inside the bath will rise too quickly, not giving the Ni a chance to etch. As the solution rises, this can lead to rips and tears in the graphene as it is being pulled away from the Ni by the surface tension of the etchant solution. By selecting the correct voltage and time delay between successive pumps ($V_{pump} = 3V$ for 2 seconds, $t_{delay} = 10s$), the full etch can be completed in between 2-3 hours with no damage to the graphene film. This full process is illustrated in figure 4.2a-e, showing each of the steps of the etching and transfer process.

Once the etch is completed, the etchant solution must be washed out of the bath. To achieve this, the pumps are disconnected from the $FeCl_3$ solution and connected to a supply of DI water. This is then continually pumped into the bath, flooding it and displacing the $FeCl_3$ solution. This is carried out until the solution in the bath is clear and has lost the distinctive orange colour of the $FeCl_3$ solution, indicating that a clean transfer can take place. A pair of tweezers are then used to remove the growth substrate from under the floating graphene sample, and replace it with the desired substrate. The pumps are then used to pump the DI Water back out

of the bath, lowering the level at a steady rate. This slowly transfers the graphene to the newly replaced substrate in a very controlled manner. Once the water level in the bath has reached the bottom of the wedge, the transfer is complete and the graphene can be dried and cleaned in the same manner described previously.

4.3 Intercalation of Wafer scale FLG samples

The three zone furnace method that is discussed in Chapter 3 was adapted to be used on larger area samples by using an intercalation tube of increased diameter, going from a 3 cm diameter to 9 cm diameter in order to accommodate samples larger than 2 cm × 2 cm. The largest sample to be transferred and intercalated

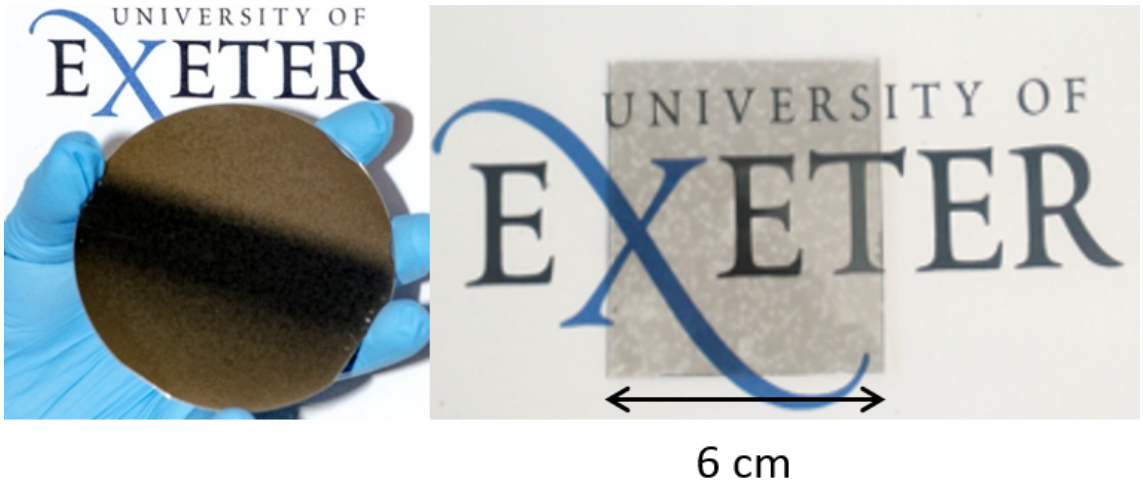

Figure 4.3: (Left) Image of a 4 inch wafer of Ni CVD grown graphene. (Right) 36 cm^2 sample of i-FLG after transfer to a glass substrate and intercalation.

using the method outlined above was 36 cm^2 (shown in figure 4.3), although larger transfers are feasible with this set-up. Using a larger intercalation tube also meant that the temperature parameters for each of the three zones must be re-optimized as the heat flow is different in the larger tube. This was attempted by raising the temperature of the intercalant zone (zone 1). A temperature range of 310 – 360 °C was chosen, as this covers the entire temperature range from the sublimation point of $FeCl_3$ to the temperature of the sample zone (zone 2). The temperatures of zones

2 and 3 were held fixed at 360 °C and 300 °C, respectively. This is because the degree of intercalation and quality of the sample greatly decreased if either of these values were changed. In addition to the re-optimization of intercalant zone temperature, the mass of $FeCl_3$ used in each intercalation was increased to 1g. This was for two reasons, firstly the sublimated $FeCl_3$ gas is filling a much larger volume in the larger tube, and so more is needed to achieve the same gaseous density as in the smaller tube. Secondly, the area of graphene being intercalated is much larger, meaning more $FeCl_3$ would be needed to achieve the same level of doping. Sample and intercalant position were also held constant throughout this investigation as it had been observed that these parameters had less of an impact on the degree of sample intercalation. The previous positions determined as optimum for intercalation using the 3 cm diameter intercalation tube were also used with the larger diameter tube, with the vial of intercalant being held in zone 1, 3 cm from the opening to zone 2, and the sample being positioned 7.5 cm away from the intercalant in zone 2. Zones were heated with the same rate of temperature increase as was described in Chapter 3, and zone 3's temperature was held fixed at 300 °C to encourage the crystallization of $FeCl_3$ vapour.

Due to the high temperatures used in intercalation, and the reactive nature of the $FeCl_3$ vapour, any contamination present on the sample or in the intercalation tube can result in the formation of $FeCl_3$ particle aggregates. These cover the surface of the i-FLG sample and can be many hundreds of nm in size. The presence of these particles gives the graphene a slightly white and cloudy appearance due to the size and density of the aggregates. The formation of these aggregates can only be avoided through cleaning of both the FLG sample and intercalation tube, prior to intercalation. When removed through cleaning, these aggregates can tear holes in the graphene film and lead to damage. In addition, aggregates that are not removed in cleaning oxidise in atmospheric conditions, leaving behind patches of insulating material. Both these effects can negatively impact the quality of the i-FLG produced (as will be seen later). Additionally, the oxidised aggregates greatly

contribute to the surface roughness of the graphene. This is particularly relevant to the field of organic photovoltaics as roughness is known to be a key factor that can reduce the short circuit current of a device, or even cause the failure of the device entirely. To mitigate these risks, i-FLG samples are placed in a desiccator for 30 minutes immediately after intercalation, at approximately 1×10^{-3} mbar. This aids in the removal of particle aggregates from the graphene surface. The graphene is washed in warm IPA (70°C) for 5 minutes, before being dried with an N_2 gun. This partially cleans any aggregates from the surface of the graphene, but is not effective at removing all aggregates from large area samples.

4.4 Raman Characterization of Large Area i-FLG

As was discussed in Chapter 3, Raman spectroscopy was carried out using a multipurpose microscope, custom built specifically for the purpose of characterizing optoelectronic devices built from 2D materials [162]. It has previously been established that the intercalation of graphene with $FeCl_3$ causes a transfer of electrons from the graphene to the $FeCl_3$. This is due to the overlap of the delocalized p-orbitals in graphene with the d-orbitals from the metal ions in $FeCl_3$ [168]. The effect of this is a strong p-doping of the graphene and subsequent drop in Fermi level. This doping can be detected through a blue shift in G-peak of the graphene's Raman spectrum, caused by a stiffening of the E_{2g} phonon mode [98]. This provides a method of assessing the degree of intercalation in a sample by measuring the doping level through Raman spectroscopy. This was used to characterize the degree of intercalation in wafer scale i-FLG samples. As such, I introduce a new metric by which to quantify the doping in intercalated graphene samples [117]. This method relies solely on comparing the mean G-peak shift values measured by Raman spectroscopy.

The precise shift in G-peak observed in the Raman spectrum relates to the number of adjacent $FeCl_3$ layers doping the graphene, with one layer shifting the G peak position from 1580cm^{-1} (pristine) to 1612 cm^{-1}, and two adjacent layers

shifting the G-peak position to 1625 cm^{-1}. These are referred to as the G_0, G_1 and G_2 peaks respectively, and are identified in figure 4.4. In fully intercalated samples prepared from exfoliated graphene flakes, full intercalation is indicated by the presence of a single peak at 1625 cm^{-1} (G_2), and no other peaks. However, in CVD grown samples, full intercalation is much more difficult to achieve. This leads to the G-peak being composed of a superposition of G_0, G_1 and G_2 peaks, as well as sub-peaks originating from partial intercalation between layers of graphene. This presents a problem for characterising intercalated CVD graphene films, as both the number of graphene layers, the staging, and hence the doping, varies across the sample. To overcome this problem of inhomogeneity, we propose the use of a metric for evaluating the degree of intercalation within a sample, taking into account both the position and relative intensity of each sub-peak. This is done by calculating an area weighted G-peak position, $\langle \mathrm{PosG} \rangle$, through the fitting of individual Lorentzian peaks to the Raman spectrum and weighting their contribution to the mean position by their relative intensity before normalising to the total intensity of the G-peak. This metric is described by equation 4.1 [117].

$$< PosG >= \frac{PosG_0 \cdot \frac{AreaG_0}{2} + PosG_1 \cdot AreaG_1 + PosG_2 \cdot AreaG_2}{\frac{AreaG_0}{2} + AreaG_1 + AreaG_2}\,, \qquad (4.1)$$

where $PosG$ refers to the Raman shift position of that respective peak in cm^{-1} and $AreaG$ is the integrated intensity of that respective peak. The factor of 1/2 in the $AreaG_0$ terms is introduced to account for the fact that G peak Full Width at Half Maximum (FWHM) reduces by approximately 1/2 when doped above $\approx 3{\times}10^{13}$ cm^{-2} [169]. This means that otherwise, the G_0 peak would be oversampled, reducing the overall $\langle \mathrm{PosG} \rangle$ value.

By calculating this $\langle \mathrm{PosG} \rangle$ metric, it allows the Raman spectrum to be assigned a mean G-peak shift value. By collecting Raman maps, the mean G-peak shift values across the area of the sample can be calculated, allowing the degree of intercalation across the area of a sample to be determined. Raman mapping was conducted on two different scales, one on a small scale covering a 30 μm $\times$ 30 μm area sampling

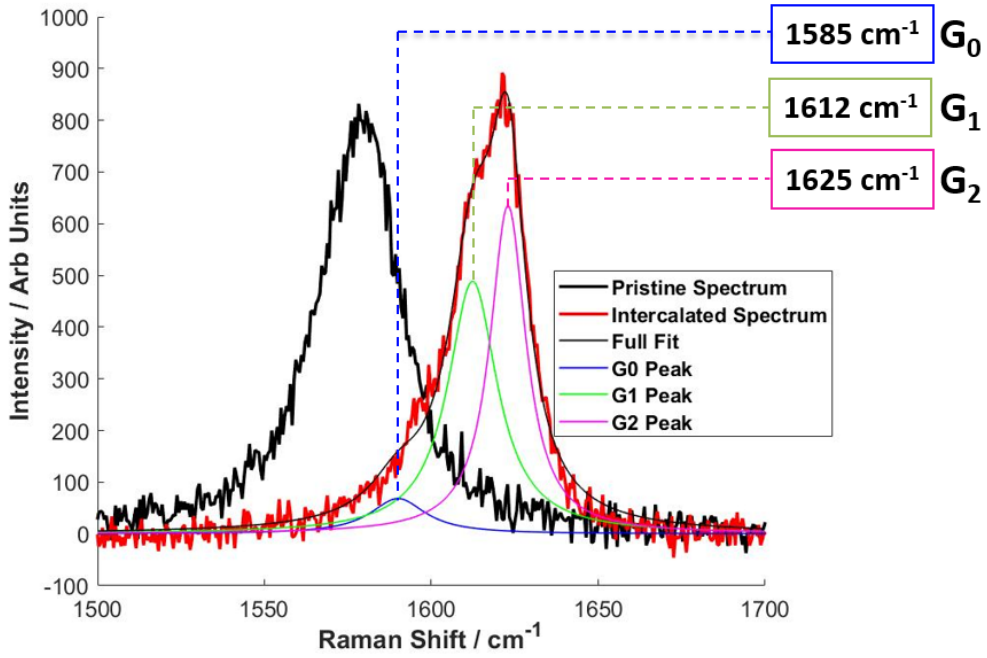

Figure 4.4: Raman spectra showing the shift in G peak caused by doping through intercalation with $FeCl_3$. The sub-peaks (G_0, G_1 and G_2) are shown here, fitted with three separate Lorentzian functions.

every point, and the other on a larger scale covering a 300 μm $\times$ 300 μm area, where spectra are only collected every 10 μm. This allows for two kinds of measurements to be made, one where the small scale variations in the sample doping caused by holes in the sample or variation in graphene layer thickness to be mapped (figure 4.5), and one where the average doping environment across a large area of the sample is calculated.

Each point sampled in a Raman map can now have the shift in G-peak fitted and a mean $\langle \text{PosG} \rangle$ value calculated. Following the work of Lazzeri [98], the shift in G-peak can be used to calculate the charge carrier concentration in the sample, allowing the direct mapping of charge carrier concentration from Raman measurements, as has been shown previously [60]. This is a very powerful technique, as other methods of measuring the charge carrier concentration require the fabrication of devices to electrically characterize, typically making the sample unusable for any other purpose. These Raman maps, such as the one shown in figure 4.5, are used in correlation with

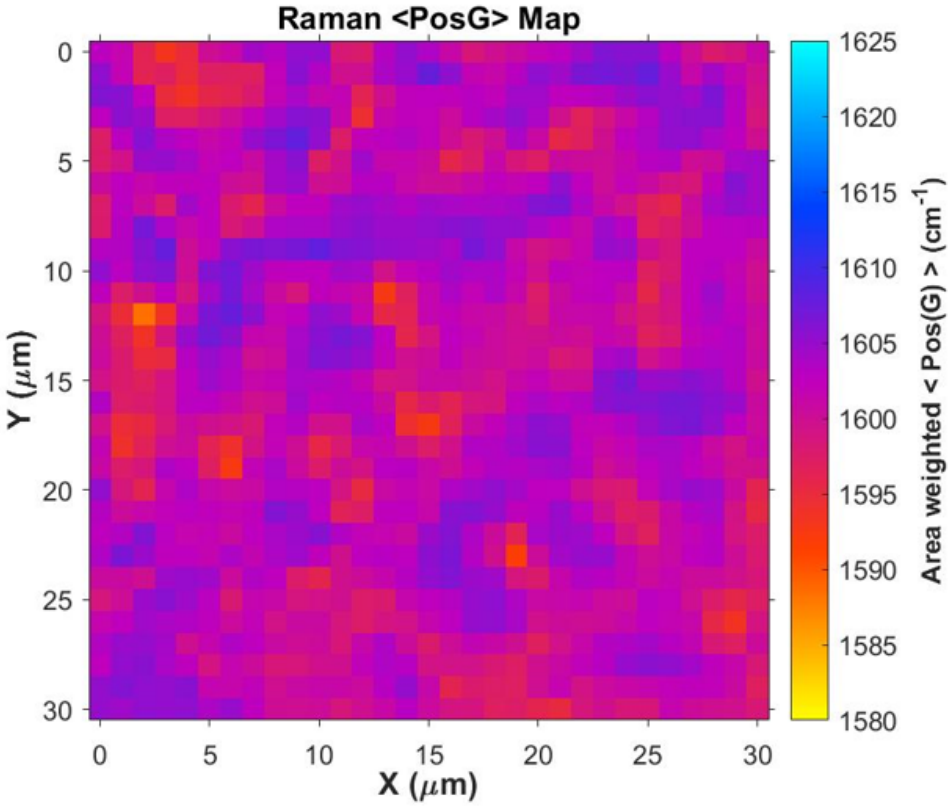

Figure 4.5: PosG map constructed by the taking point spectra across a 30 μm×30 μm area and fitting the individual point spectra with Lorentzian functions to determine the area weighted G-peak position. This allows the observation of how intercalation varies across the sample and can be correlated with changes in the sample by comparing the map to optical images

optical images to examine the variation in doping, and hence intercalation, across the sample due to changes in flake thickness, as well as the density of graphene in that area, as demonstrated previously [117]. These Raman maps can then be converted into histograms, and used to compare the degree of intercalation between samples. A comparison between a pristine sample and intercalated sample is shown in figure 4.6. The histograms for these two sets do not overlap, indicating that for all points measured in the intercalated sample, doping was higher than in the pristine sample.

The mean $\langle \text{PosG} \rangle$ value as measured from Raman mapping was calculated for samples intercalated with zone 1 temperatures ranging from 300 – 360°C. The re-

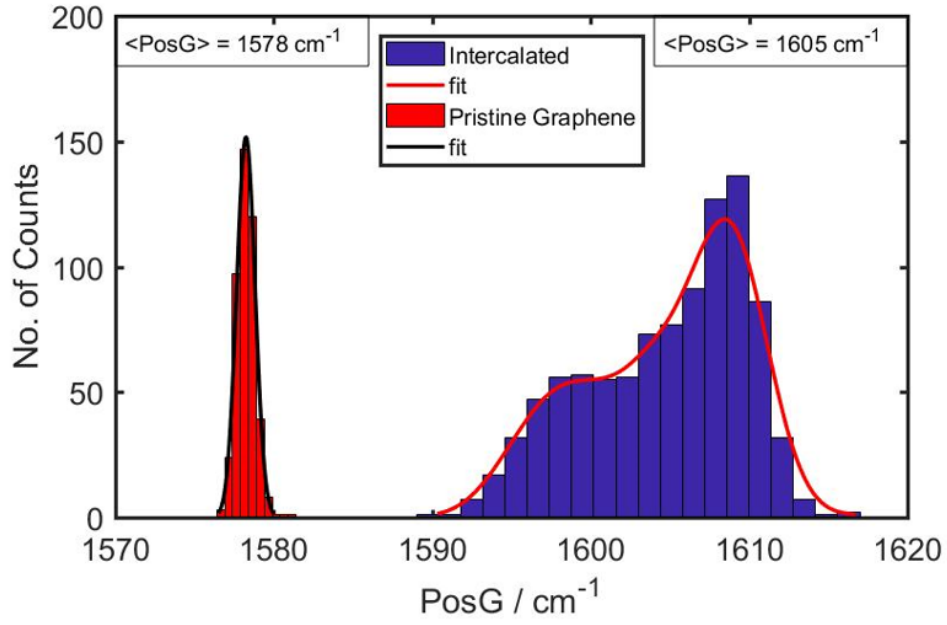

Figure 4.6: Histograms of the PosG data taken pristine and intercalated samples, detailing the distribution of PosG values collected in the map. The PosG values for an unintercalated sample of pristine graphene illustrate the significance of doping by intercalation. Mean PosG values for both sets of data are displayed above.

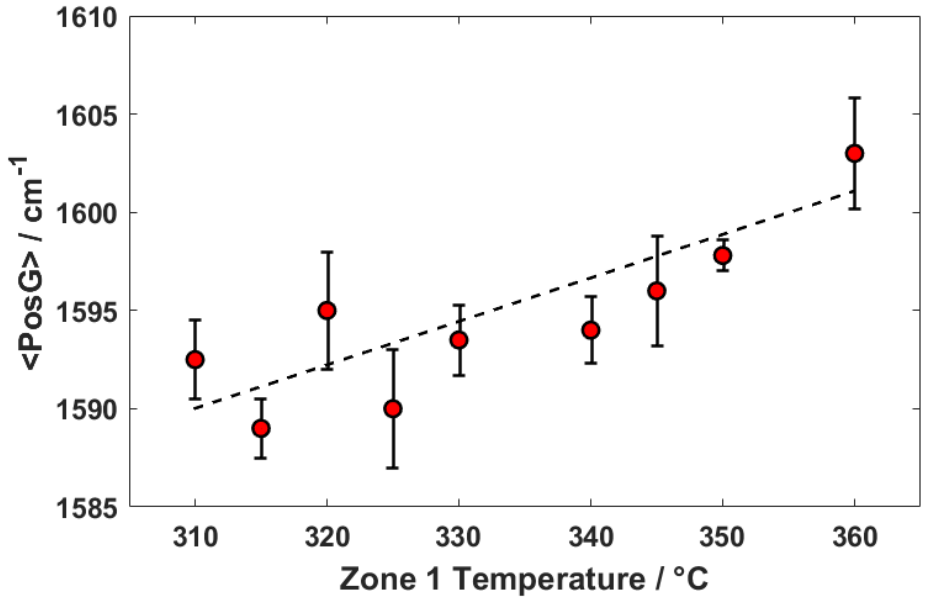

Figure 4.7: Effect of increasing zone 1 (intercalant) temperature on the degree of sample intercalation as measured by the ⟨PosG⟩ metric.

sults, displayed in figure 4.7, show increasing temperature to increase the degree of intercalation as measured by the ⟨PosG⟩ metric. Increasing the temperature of the intercalant zone increases rate of sublimation of the $FeCl_3$, and hence the vapour pressure achieved during the intercalation process. This makes it easier for the $FeCl_3$ molecules to penetrate between the graphene sheets, improving the degree of intercalation achieved. Increasing zone 1 temperature from the previously optimised conditions for the smaller tube of 315°C, to 360°C caused an increase in mean G peak position from 1590 cm^{-1} to 1603 cm^{-1}. While this is still lower than the G Peak position observed for stage 2 intercalated graphene of 1612 cm^{-1}, this metric accounts for both the positions of all peaks, as well as the area ratios between them for every point sampled across an area of the sample. By observing the ⟨PosG⟩ histograms it can be seen that the maps contain peaks composed of G_0, G_1 and G_2 peaks, indicating that full intercalation has taken place. We observe that for Ni grown CVD FLG, some flakes in the film will fully intercalate while others will not, remaining either partially intercalated or partially surface doped by the $FeCl_3$.

4 point probe measurements of sheet resistance of samples intercalated under different conditions revealed that the sheet resistance of intercalated samples did not fall below 100 Ω/sq, regardless of the ⟨PosG⟩ value measured for the sample. This is shown in figure 4.8, and was also found to be the case for smaller area samples (1 cm×1 cm). Further investigation showed that the graphene purchased for this study had numerous holes, some 10's – 100's of nm across in its surface, as shown in figure 4.9a. By mapping the area of one such hole with Raman spectroscopy and calculating the ⟨PosG⟩ values, a map of the charge carrier concentration across the area of the hole was produced (figure 4.9b). Charge carrier concentration was calculated by empirically fitting a 5^{th} order polynomial to the data in figure 2 of Lazzeri's paper [98]. This allowed the charge carrier concentration to be calculated for the relative Raman shift value of the G-peak.

These results indicate two things, firstly that the centre of the hole contains graphene, indicating the holes most likely originate from the Ni CVD growth process

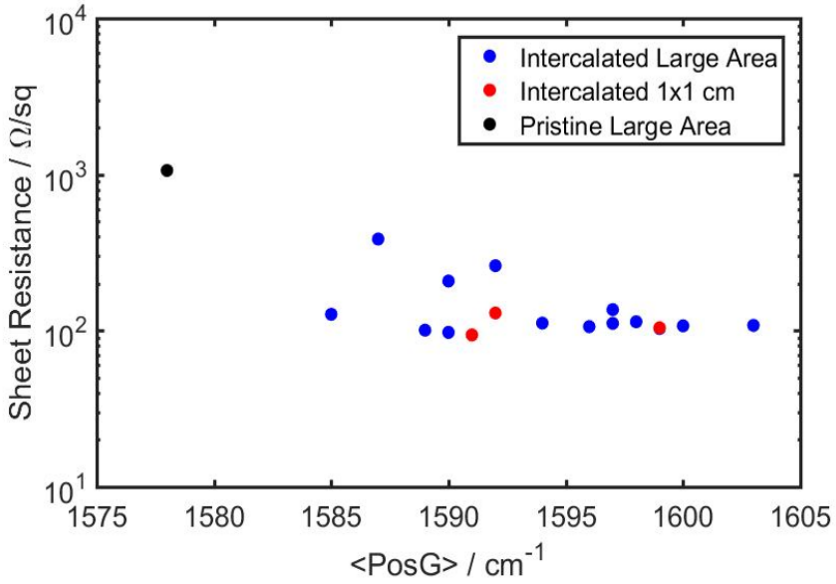

Figure 4.8: Effect of intercalation on the sheet resistance of large area i-FLG samples. A wide range of PosG values produce the same reduction in sheet resistance, indicating only partial doping is required to achieve this level of improvement to sheet resistance, and that the sheet resistance of the samples may be limited by other factors.

[170], as opposed to damage to the graphene film during transfer. Secondly, these areas of graphene are much thinner and do not intercalate as well as the thicker surrounding areas of graphene. This is because the area of graphene within the holes is comprised of a bilayer of graphene that covers the whole sample. This bilayer is very difficult to intercalate due to the lack of accessible edges for the $FeCl_3$ to penetrate from, and its proximity to the substrate. The thicker areas of graphene around this hole have a much higher level of doping (2-4 times that of the partially doped area), indicating that thicker flakes have a propensity to intercalate better. This highlights the need for better quality FLG films that are homogeneous over a large area to allow for the uniform doping of large area graphene films.

Due to the variation of flake thickness and film coverage across the sample and the presence of holes in the graphene film, it was necessary to periodically sample points across a large area to attain a representative measurement of the $\langle$PosG$\rangle$. 300 μm $\times$ 300 μm maps were taken, with a 10 μm step size between each measurement,

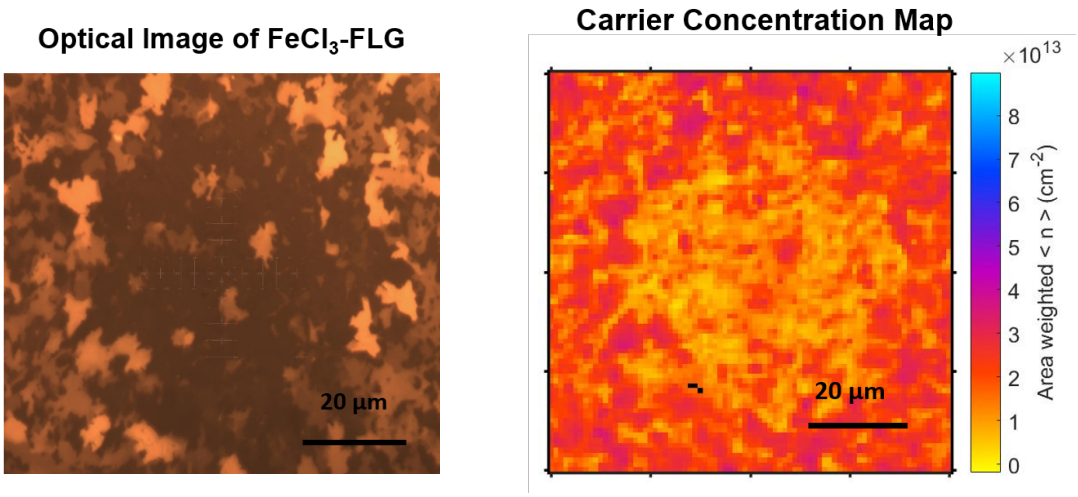

(a) (b)

Figure 4.9: Optical image (Left) and charge carrier concentration map (Right) taken over a hole in an i-FLG sample. 4.9b shows a drop in charge carrier concentration across the hole, indicating thinner regions intercalate to a lesser degree. This is ascribed to be the cause of the limited reduction in sheet resistance observed for wafer scale samples.

allowing the variation of the local doping environment to be ignored. Collecting multiple maps over different regions of the same sample showed they produce the same ⟨PosG⟩ values, indicating that this method attains a representative average of the degree of intercalation across the sample, and that sample intercalation is consistent across the area of the sample. The ⟨PosG⟩ values calculated from 30 μm × 30 μm and 300 μm × 300 μm maps also showed good agreement in the cases where large holes could be avoided in the smaller area scan.

The minimum sheet resistance values achieved in this study were around 100 Ω/sq, which was produced in a number of different FLG samples with varying ⟨PosG⟩ values. The same resistance values being achieved in samples with different values of ⟨PosG⟩ shows that only partial doping of the graphene film is required to reduce the sheet resistance by an order of magnitude. This is a significant result for scaling up the size of optoelectronic devices such graphene electrodes can be applied to. However, this value is much higher than the 8 Ω/sq that can be achieved in both mechanically exfoliated samples [62], and the 20 Ω/sq that can be achieved for 1

cm × 1 cm i-FLG samples [64]. As was previously mentioned, the presence of holes in the samples limits the sheet resistance that can be achieved. This is due to two effects; firstly the increased resistance due to the presence of the holes themselves, and secondly due to the poorer intercalation across the holes increasing the sample doping inhomogeneity. Another factor that may impact the reduction in sheet resistance observed with intercalation is the presence of iron particle aggregates on the i-FLG sample's surface. These can introduce defects into the graphene film, act as scattering sites and introduce additional resistance to the 4 point probe measurements made on graphene. As such, the removal of these particles is of key interest to making successful large area i-FLG samples.

4.5 Acid Cleaning of Wafer Scale i-FLG Samples

Optimization of intercalation conditions in the large area furnace resulted in many samples being heavily contaminated by large aggregates on the surface of the i-FLG. This has the potential to cause damage to any devices fabricated from the i-FLG produced, as surface roughness is a key parameter that leads to carrier recombination and increased risk of shorts in OPV devices [49]. To avoid this, a cleaning procedure was trialled with the aim of removing these surface contaminants from the graphene, without damaging or de-intercalating the samples. Hydrochloric acid was chosen as a cleaning agent as it is a particularly aggressive acid and is known to be very effective at removing metal particles. In addition, due to graphene's inert nature, there should be no reactions between the HCl and the graphene. A cleaning procedure was established by which the i-FLG samples were submerged (or partially submerged) in a solution of HCl for a set duration. Combinations of concentrations and cleaning times included 6M for 2 hours, 1M for 24 hours, and finally 1M for 1 hour. The sample is then removed and sequentially submerged in 3 separate baths of DI water to remove HCl residues. The sample is then washed in warm acetone and IPA (70°C, 10 minutes each). After cleaning, the sample was imaged by optical microscope to determine whether aggregates had in fact been removed. In addition, both sheet

resistance and Raman mapping measurements were taken before and after cleaning with HCl to determine if HCl causes de-intercalation of $FeCl_3$ from the graphene sheets, and the effect this has on the conductive properties of the i-FLG.

The aggregated particles produced during intercalation typically measure a few hundred nanometers in height, many times the thickness of the graphene itself. Crucially, this is also greater than the thickness of the organic layers used in OPV devices, making this a key problem if i-FLG electrodes are to be used in OPV devices. While optimisation of intercalation parameters and rigorous cleaning of samples can be used to mitigate the formation of aggregates on samples, results from intercalation of large area samples showed the aggregates to still be present (figure 4.10a). To improve the quality of large area i-FLG samples, cleaning procedures were tested in an attempt to remove these aggregates. Washing in hot IPA (70°C) is already employed after the i-FLG sample is removed from intercalation. This is due to the presence of a cloudy white colour across the surface of samples, caused by micron scale aggregates that form on the surface. While this has shown promising at removing aggregates from small area samples, it does not appear aggressive enough to remove them from the large area samples, as shown in figures 4.10b, 4.10c and 4.10d. Here, I shall investigate the effectiveness of removing iron aggregates using washes in hydrochloric acid of different concentrations and wash times.

Initial tests showed the cloudy white colour caused by dispersed particles on the i-FLG surface was removed by submerging the graphene in HCl (6M) for a prolonged period of time (2 hours). However, this exposure also damaged the graphene by delaminating certain areas from the substrate, indicating lower concentrations/cleaning times are required. A lower concentration of 1M was trialled, with a cleaning time of 24 hours to allow the lower concentration solution to take effect. However, this also caused the graphene to detach from the substrate, damaging the electrode beyond use. Finally, a concentration of 1M was used with a cleaning time of 1 hour was tested. This combination of HCl concentration and cleaning time showed promise, as it could remove Iron aggregates without completely removing

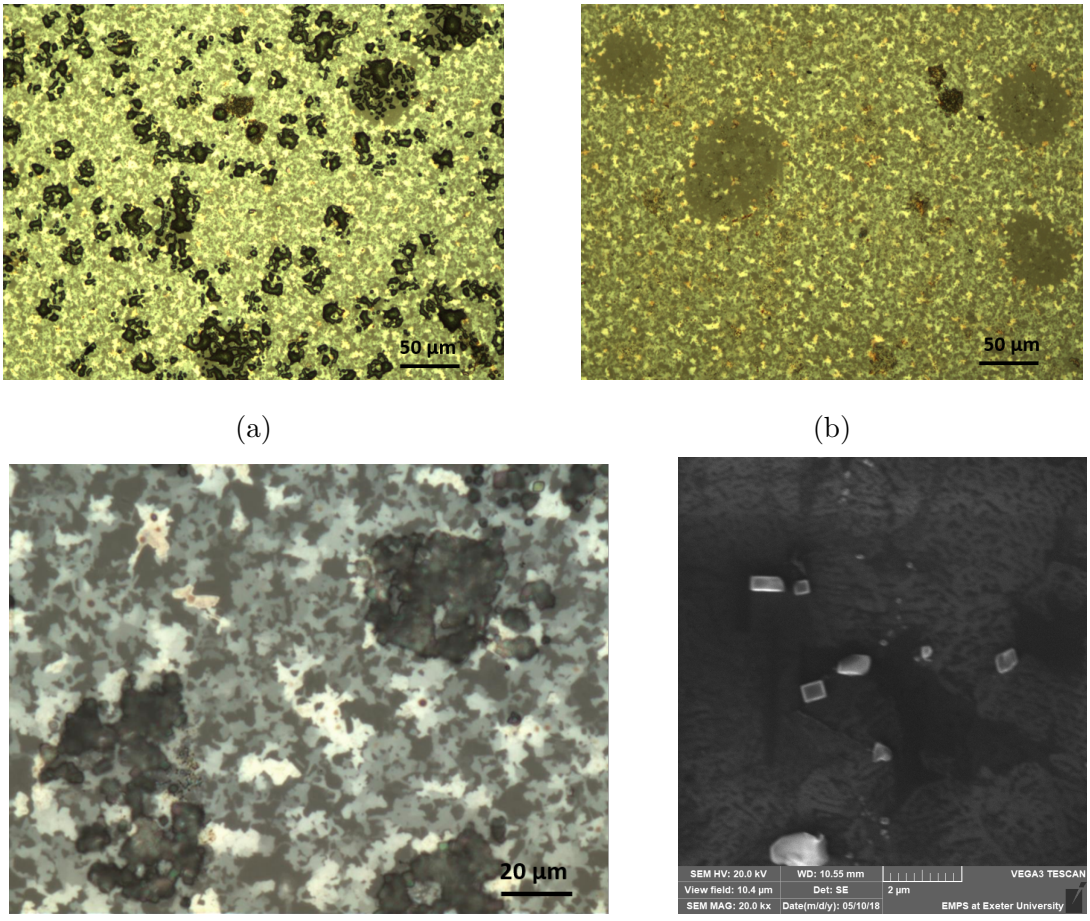

(a) (b)

(c) (d)

Figure 4.10: Optical microscopy images of intercalated graphene samples before (a) and after (b and d) washing with hot IPA. While the IPA can be shown to remove the majority of aggregates from 'dirty' intercalations, small particles of $FeCl_3$ as well as larger aglomerations of particles are still present across the surface of the graphene film. a. and b. are shown at $\times 20$ magnification, c. is shown at $\times 50$ magnification. d. is a Scanning Electron Microscopy (SEM) image of $FeCl_3$ aggregates at $\times 100$ magnification. Scale bars are shown for all images.

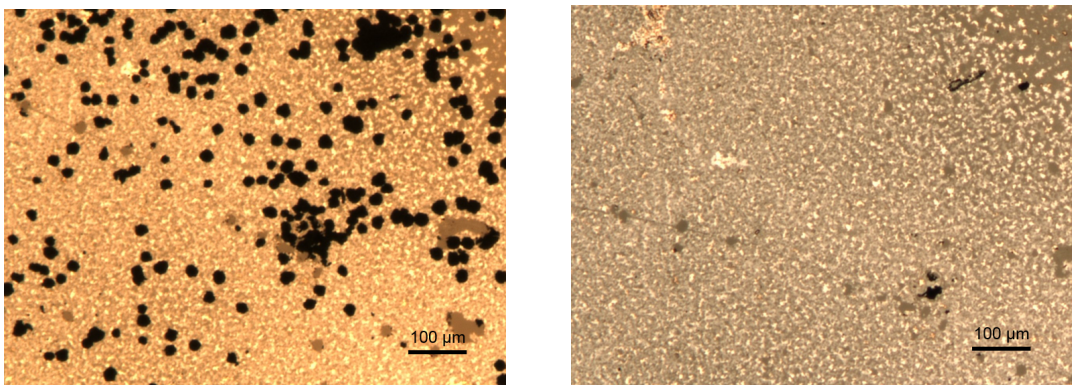

(a) (b)

Figure 4.11: Optical microscope images at 10 × magnification of $FeCl_3$ aggregates covering the surface of an i-FLG sample (a) and the same area of graphene after HCl acid cleaning has been employed (b). 1 M HCl acid was used for 1 hour before the graphene sample was removed. While some small aggregates remain, the vast majority have been removed in the cleaning process. Scale bars are shown on both images (100 μm)

the i-FLG sample from the substrate, as shown in figures 4.11a and 4.11b.

Table 1: Sheet Resistance before/after HCl wash		
Sample	**Sheet Resistance/Ω/sq**	**Sheet Resistance after cleaning/Ω/sq**
1	84600	126
2	386	540
3	261	337
4	84800	98
5	498	879

Although i-FLG samples are normally highly conductive, the presence of aggregates on the surface forms an insulating layer that prevents the accurate measurement of sheet resistance using a 4-point probe setup. Instead, a much higher sheet resistance is measured, as seen in table 4.5 for samples 1 and 4. For these samples, the sheet resistance measured after cleaning in HCl is much lower than that

measured before. However, for samples that were measured as conducting before acid washing (2, 3 and 5) their sheet resistance after acid washing was greater than that measured before. The mean increase in sheet resistance for these samples was $\approx$ 50%, ranging from 30% to 75%. This can be explained through the removal of surface aggregates along with the de-intercalation of the FLG due to the HCl. This is supported by Raman mapping measurements taken from samples before and after cleaning with HCl (displayed in table 4.5). As can be seen from the PosG histograms before and after HCl washing (figure 4.12), there is a notable shift in distributions from one weighted towards higher PosG values of between 1600 – 1610 cm^{-1} before washing, to one that is more evenly spread across all PosG values within the distribution. Additionally, there is a downshift of the centre of the distribution of around 10 cm^{-1} after washing with HCl. However, of the 10 graphene samples used for this study, only half had measurable sheet resistances after washing with HCl. This is likely caused by damage to the sample, either from the removal of $FeCl_3$ aggregates or due to delamination of the i-FLG sample from the substrate.

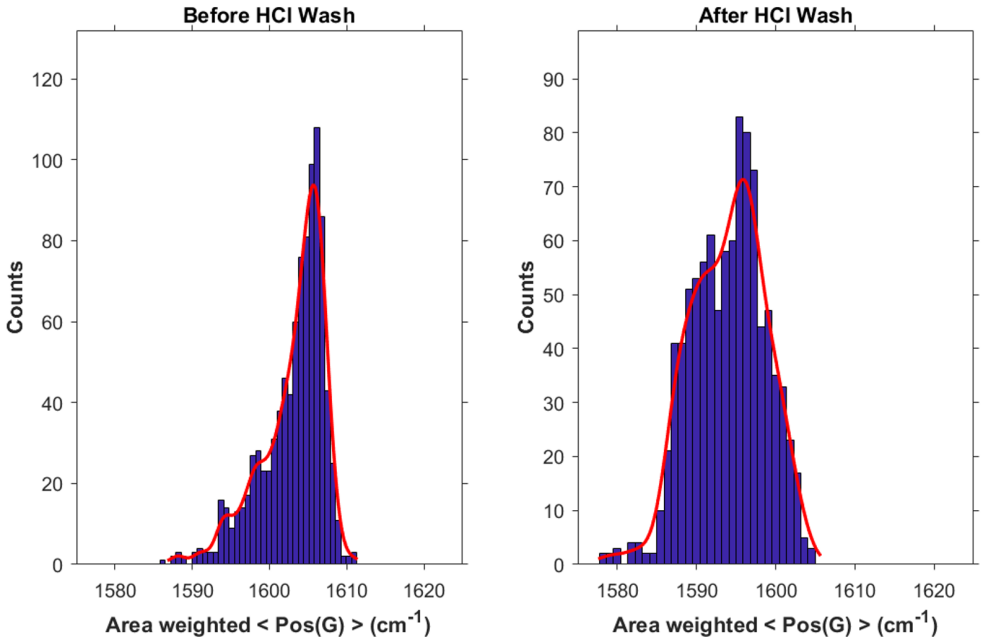

Figure 4.12: Histograms taken from Raman maps before and after washing with 1M HCl for 1 hour. Mean PosG values for each histogram are 1603 cm^{-1} and 1594 cm^{-1} before and after washing with HCl, respectively.

Table 2: ⟨PosG⟩ before/after HCl wash		
Sample	**⟨PosG⟩/cm^{-1} Before**	**⟨PosG⟩/cm^{-1} After**
1	1600	1590
2	1599	1595
3	1597	1592
4	1605	1593
5	1598	1590
6	1603	1594
7	1603	1597
8	1601	1594
9	1604	1589
10	1604	1592

For all samples measured, there is a notable drop in PosG value after washing in HCl. This is evidence for the partial de-intercalation of the i-FLG samples. As the sheet resistance of samples after washing is lower than the sheet resistance of pristine FLG (≈ 1 kΩ) and the PosG values measured are higher than that of pristine graphene, it is clear that there is still some intercalant present between the graphene sheets. However, as can be seen from the PosG values in table 4.5, samples showed a mean drop in PosG of 8.6 cm^{-1} after washing with HCl. This suggests there is a significant degree of de-intercalation which is likely to negatively impact the electrode performance. Limited evidence has been discussed in the literature with regards to i-FLG de-intercalating in the presence of solvents. However, acetone has been noted as a potential cause of de-intercalation when i-FLG samples are washed in heated acetone. It is likely that HCl molecules are small enough to penetrate between graphene sheets to react with the $FeCl_3$ intercalant molecules.

While HCl washing is reasonably successful at removing Iron aggregates from the surface of i-FLG samples, it does not completely remove all contaminants. This leaves the sample with a small number of large particles on the surface, each of which could lead to a short circuited device when fabricated into OPV devices. In

addition, I have provided evidence that this cleaning procedure de-intercalates the i-FLG sample, weakening the doping from $FeCl_3$ and increasing the sheet resistance. As such, the cleaning procedure described above will not be used throughout the remainder of this investigation. Instead, focus will be placed on making sure all elements of the intercalation procedure are carried out carefully in a clean environment, to prevent the Iron aggregates forming in the first place. This involves extended cleaning of samples (3 hours in acetone at 70 °C, followed by 3 hours in IPA at 70 °C) to remove any PMMA residues. The intercalation tube was also washed with acetone and IPA after every intercalation and an annealing cycle run afterwards to ensure all contaminants are removed from the tube. Samples to be intercalated are taken directly from a desiccator to ensure no traces of water are present on the sample. Likewise, the vial used to hold the intercalant is heated to 150 °C prior to intercalation. This ensures any water vapour from the atmosphere evaporates from the vial, drying it and preventing any unwanted reactions with the anhydrous $FeCl_3$. Combined, these precautions enable reproducible intercalation of graphene samples.

4.6 Optical and Electrical Characterization of i-FLG Samples

As was noted in the previous section, intercalation regularly results in the deposition of a layer of iron based aggregates on the surface of the FLG. In addition to the previously noted effects of these aggregates, they also reduce the transmission through the graphene layers. To better understand how this may impact the performance of these electrodes, transmission spectroscopy measurements were made on samples intercalated in both the 3 cm diameter furnace and the 9 cm diameter furnace to compare the transmission achieved after intercalating samples of different sizes, shown in figure 4.13.

While the transmission of i-FLG samples is very similar to that of unintercalated

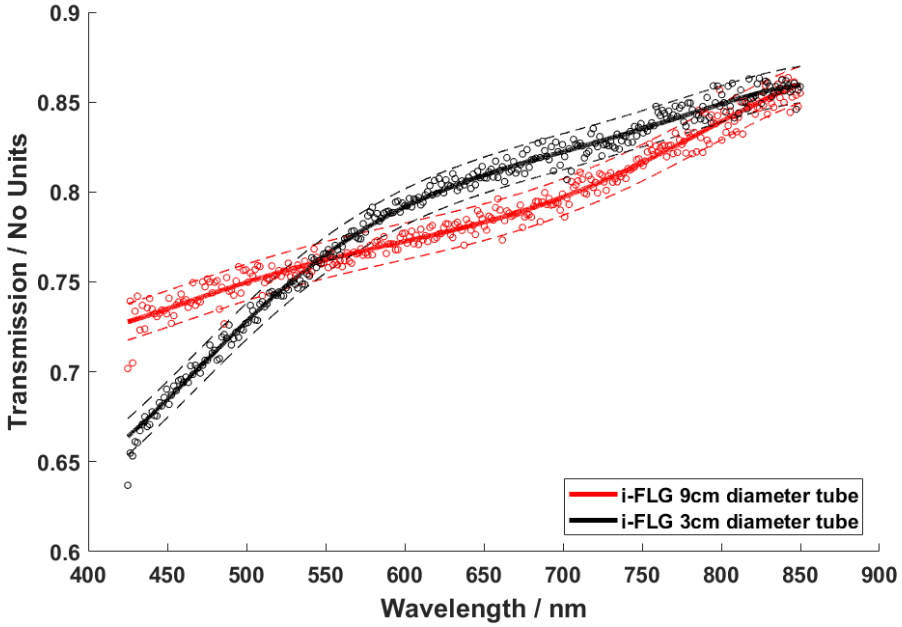

Figure 4.13: Transmission spectra for pristine and i-FLG samples fabricated in the two different furnaces used for medium and large area intercalation respectively. The dashed lines show 95% confidence limits, calculated from the standard deviation for both sets of data.

samples, the presence of aggregates on the surface of the i-FLG causes the results to deviate from that of samples intercalated in the 3 cm diameter furnace. Most notably, there is a drop in transmission at lower wavelengths, causing the spectrum to deviate from the approximately linear nature of pristine samples. However, the primary absorbers in OPV devices tend to have absorption spectra weighted towards larger wavelengths, typically between 600 – 700 nm [171]. This means that the reduced transmission through large area i-FLG samples at low wavelengths may not have a significant impact on the device performance.

4.6.1 Work Function Mapping of Wafer Scale i-FLG Samples

Small ($\approx$ 1 cm $\times$ 1 cm) sections of large area FLG samples were intercalated and mapped using SKPFM to determine the work function of the i-FLG, and to correlate this with the measured $\langle$PosG$\rangle$ values. As has been discussed previously, intercalation with $FeCl_3$ causes a strong p-doping of the graphene sheets, leading to an increased work function as high as 5.1–5.2 eV [60]. However, our measurements show a much smaller adjustment of the work function, reaching values as high as $\approx$ 4.6 eV, as shown in figure 4.14. Of the 5 samples mapped, the mean work function adjustment was just + 0.11 eV, considerably less than the + 0.8 eV increase seen previous samples [60]. This is due to the poorer quality of intercalation that is achieved for samples grown on wafer scale compared to smaller samples, as well as the comparatively poor intercalation achieved in the 9 cm diameter furnace. Examining the work function distributions of the 5 samples studied shows some variation between the samples, most notably in the width of the distributions. Sample i-FLG 1 has the highest work function measured of the large area samples, due to its wide distribution extending up to $\approx$ 4.8 eV, with all other distributions reaching just above 4.6 eV. This can be seen by observing the work function distributions, displayed in figure 4.14. Comparing these measured work functions to those of smaller area i-FLG samples with comparable $\langle$PosG$\rangle$ values, it can be seen that small area samples achieve a much higher work function for similar levels of intercalation. This suggests that the poorer quality of the wafer scale samples negatively impacts the work function values that can be achieved.

These measurements indicate the increase in work function for samples fabricated from large area graphene wafers to be much less than the increase seen in small area graphene samples. Although there is variation within each set of data, it can be seen that the increase in work function approximately correlates with the measured $\langle$PosG$\rangle$ values. Further optimisation of wafer scale FLG growth is required before an equal increase in work function can be seen in wafer scale i-FLG as in smaller

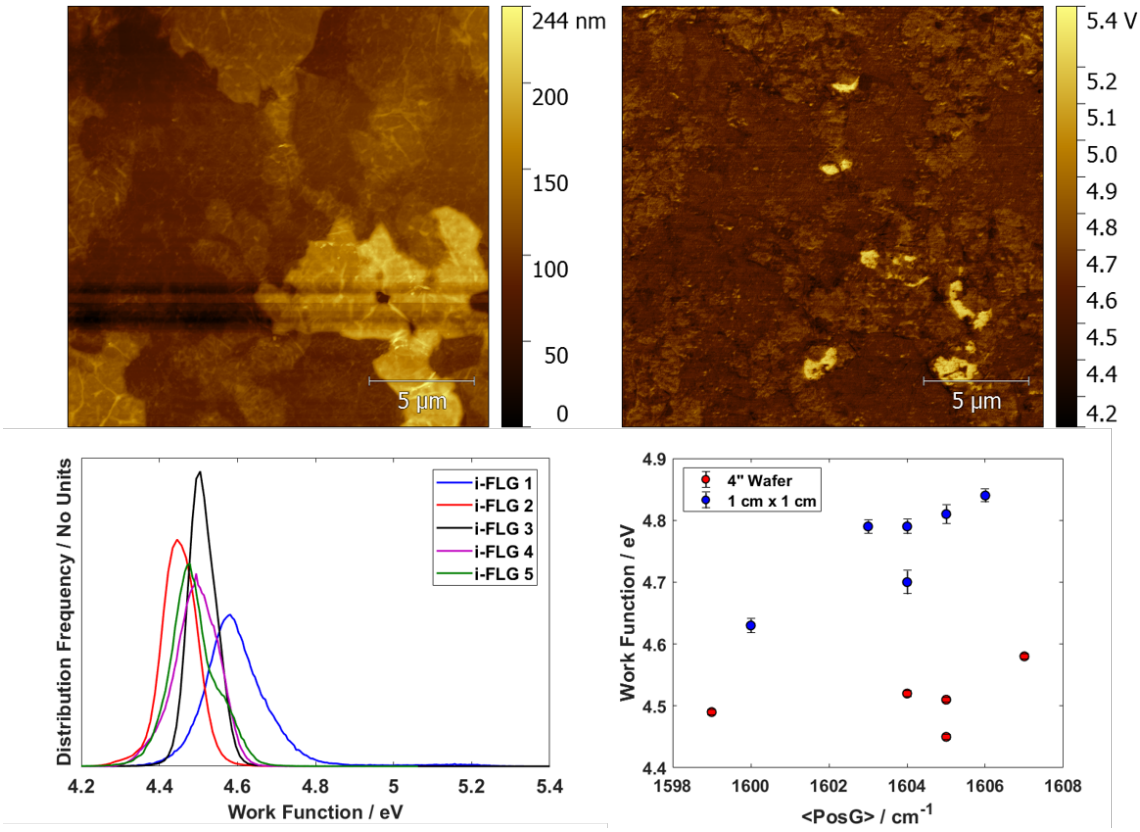

Figure 4.14: Data collected from SKPFM measurements. Top right shows a topographical map of the same area as the top left, which shows the surface potential as measured by SKPFM. Bottom left shows the WF distributions for 5 samples of large area i-FLG. Bottom right plots the ⟨PosG⟩ against the measured work function for the large area samples (4" wafer) compared to small area samples (1 cm × 1 cm). Error bars are calculated from Gaussian fits of the distributions.

samples. There are a number of examples of doped graphene electrodes with modest work function adjustments that have been shown to function well in OPV devices [48, 172, 103]. However, these devices still rely on the use of transport layers to match the work function at the bulk heterojunction interface so the doping of graphene was primarily used as a method to reduce sheet resistance.

4.6.2 Van der Pauw Measurements

Because the samples tested with SKPFM mapping showed much lower work functions than previous i-FLG samples, Van der Pauw measurements were taken to mea-

sure the sheet resistance, charge carrier concentration and carrier mobility. This was carried out for one of the large area samples mapped (i-FLG 3), as well as a number of smaller area samples (S1-4) that all showed higher work functions than the large area sample.

Table 3: Magneto-transport Measurements for i-FLG Samples

Sample	$\langle$**PosG**$\rangle$/**cm**$^{-1}$	**WF (eV)**	**Sheet Resistance** (Ω/**sq**)	**Carrier Density** ($10^{14} cm^{-2}$)	**Carrier Mobility** (cm^2/Vs)
S1	1606	4.84	73.0	9.53	89.9
S2	1603	4.79	87.3	9.02	79.3
S3	1597	4.59	57.2	11.01	99.3
S4	1597	4.66	67.1	9.82	94.7
i-FLG 3	1605	4.51	64.5	7.46	135.6

Measurements of the charge carrier concentration and sheet resistance show that the large area i-FLG sample (i-FLG 3) has successfully undergone intercalation, and has a significantly enhanced doping and sheet resistance as a result. However, the adjustment to work function is much less significant than for i-FLG samples from smaller growth substrates. It should also be noted that the higher carrier mobility of B3 is due to the lower charge carrier concentration, as there are fewer carrier-carrier scattering events. The sheet resistance measured for these samples is lower than that measured by 4 point probe, indicating that the 4 point probe may potentially introduce additional resistance, most likely due to the probes making poor contact with the i-FLG surface because of the particle aggregates covering the samples.

4.6.3 Magneto-transport Measurement in Hall Bar Geometry

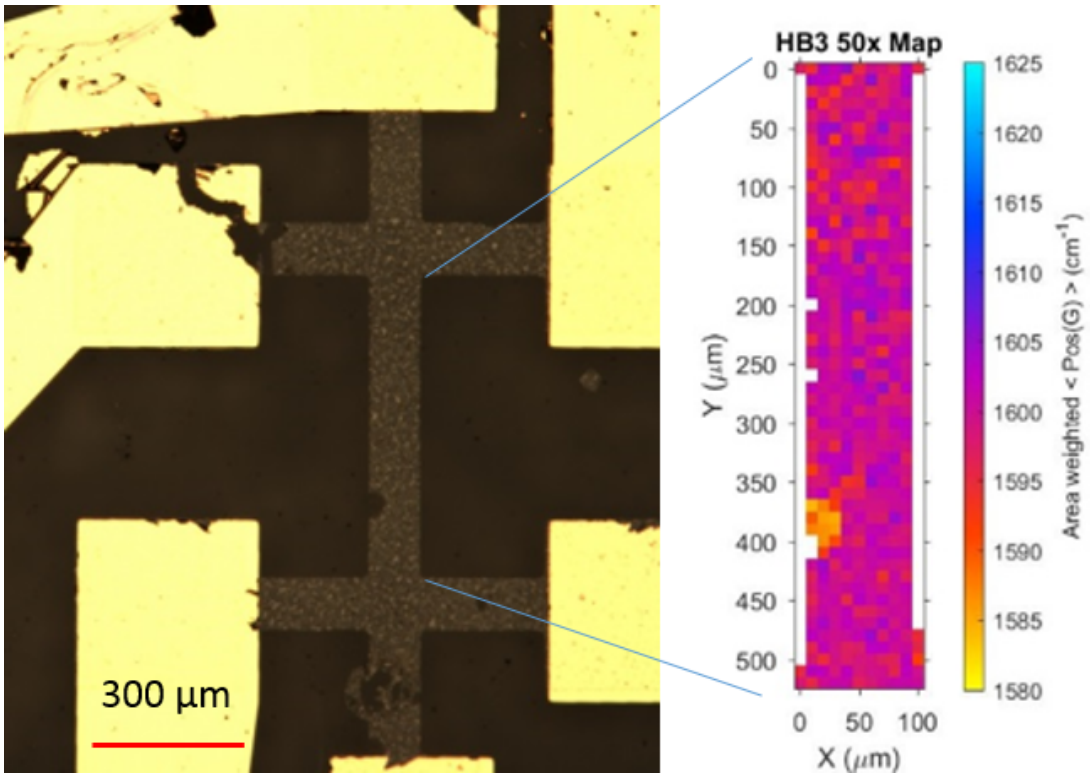

Figure 4.15: Image of i-FLG sample patterned into a Hall bar with Cr/Au contacts applied. Current is sourced in the vertical direction (x-direction) with a magnetic field orientated out of the page (z-direction). The electrons flowing along the graphene channel then experience a Lorentz force, deflecting them transverse to the direction of current flow (y-direction). This allows the measurement of the Hall voltage across the graphene channel. On the right shows the Raman mapping of the PosG value of the i-FLG channel, showing the sample to be intercalated with a mean PosG of 1599 cm^{-1}. Scale bar shown in red at the bottom left corner.

Magneto-transport measurements were also carried out on i-FLG Hall bar devices (figure 4.15). This functions in a similar manner to magneto-transport in Van der Pauw geometry except that current is always sourced along the same channel of the Hall bar. 6 terminal Hall bar devices were fabricated before being intercalated and contacted with Cr/Au contacts and gold wires. 3 Hall bar devices of different

dimensions (channel lengths of 600, 900 and 1050 μm, and channel widths of 100, 150 and 175 μm for samples 1, 2 and 3 respectively) were fabricated from the same sample of i-FLG, and Raman mapping used to characterize the degree of intercalation in each of the devices. All Hall bar devices were measured to have the same mean $\langle \text{PosG} \rangle$ value.

Table 4: Magneto-transport Measurements for i-FLG Hall bars				
Sample	$\langle$**PosG**$\rangle$/**cm**$^{-1}$	**Sheet Resistance** (Ω/sq)	**Carrier Density** ($10^{14} cm^{-2}$)	**Carrier Mobility** (cm^2/Vs)
HB1	1599	134.6	8.21	58.4
HB2	1599	100.3	7.89	78.8
HB3	1599	112.5	9.02	61.5

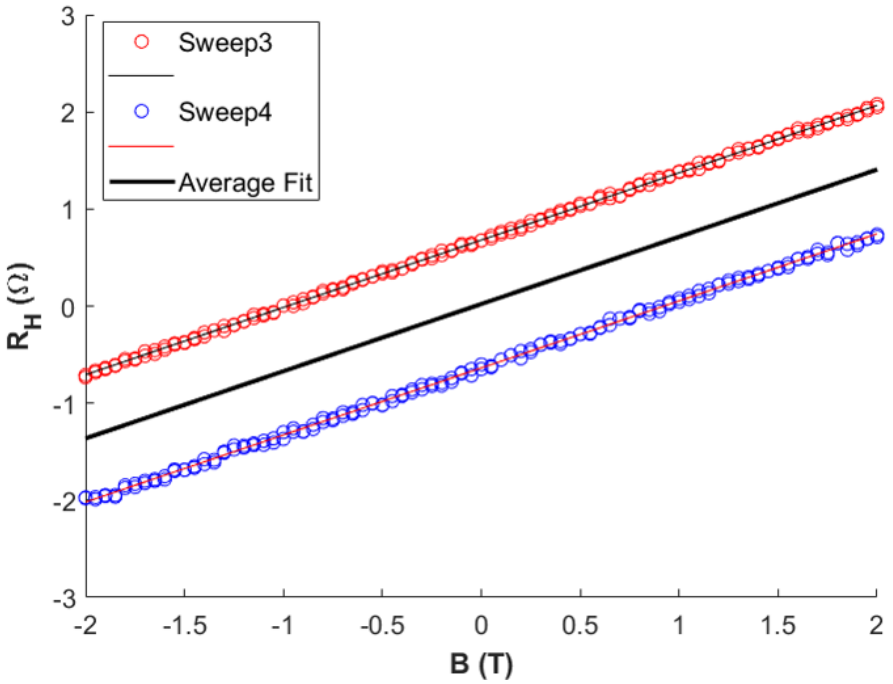

Figure 4.16: Response of measured Hall resistance to applied magnetic field for i-FLG Hall bar device. The gradient is equal to $1/ne$ where n is the charge carrier concentration. The two sets of data are from two sweeps taken with current flowing in forward and reverse directions respectively. For each set of data the non-zero Hall voltage at zero field is due to inhomogeneities in the sample. When the mean of both data sets is taken, they give zero Hall voltage at zero field, shown by the average fit. Results from characterising each Hall bar are shown in the table above.

Figure 4.16 shows the linear increase in Hall resistance with magnetic field for two sweeps of B_{field} for the current applied in two different directions, along and against the channel. Each of these sweeps have a slight offset from the mean fit which is caused by inhomogeneities in the sample. Carrying out these measurements twice, with the current flowing in each direction, allows the averaging of these two measurements and the removal of the offset caused by sample inhomogeneity, fixing R_H as zero when the magnetic field is zero. This is not necessary for calculation of the charge carrier concentration, which is found from the gradient of either sweeps, but is instead carried out for completeness.

Results, displayed in table 4.6.3 show values for sheet resistance and carrier mobility to be lower on average than those measured in Van der Pauw geometry, while charge carrier concentration remains largely unchanged. There also appears to be little change in transport properties with increasing size of Hall bar dimensions. The degree of intercalation as indicated by the PosG metric is relatively low, most likely due to the fabrication process used to produce the Hall bars leaving polymer residues behind on the graphene. These will interfere with the intercalation process and lead to a poor intercalation compared to that of a clean sample. These polymer residues can also cause particles of Iron Chloride to form on the surface of the graphene which can act as scattering sites and hence reduce carrier mobility. Formation of aggregates on the sample can also interfere with the adhesion of the metal contacts applied by thermal evaporation, and lead to a poor contact formed with the i-FLG. Poor contact adhesion can lead to an increase in the measured sheet resistance. In addition, as was shown in the previous section, the removal of these aggregates can cause damage to the sample (seen in Figure 4.15), which is likely to cause the observed increase in sheet resistance. However, high levels of doping are still observed in all samples, confirming the measurements taken in Van der Pauw geometry that suggest very high levels of doping can be reached even with relatively modest intercalation. However, this does not necessarily lead to the same level of work function increase as is seen in smaller samples [60].

4.7 Conclusions

$FeCl_3$ intercalated FLG promises to be a very useful material in the field of flexible transparent electrodes, with potential applications in both flexible display technologies, as well as energy harvesting devices (e.g. Photovoltaics). In this chapter I have demonstrated a reliable method of transferring wafer scale graphene samples for intercalation, as well as providing a new metric by which to characterize the level of doping in the samples. This method was used to demonstrate the drop in carrier concentration across a hole in the graphene, common to large area samples. Methods to improve the quality of intercalated films were discussed, including washing the graphene samples with HCl. While this method was successful at removing Iron Chloride contaminants it was also shown to partially de-intercalate the i-FLG samples. SKPFM was used to map the work function of large area samples, showing much lower values than for the higher quality 1 cm $\times$ 1 cm samples. Magneto-transport measurements were used to confirm that these samples had undergone intercalation and were heavily doped as expected. As the work function of a material is highly dependent on the condition of the surface, this is likely due to a combination of using poorer quality graphene and the further optimisation required for the intercalation conditions used. It should also be noted that possible contamination of the samples from exposure to atmospheric conditions are likely to have a large impact on their measured work functions. These results highlight the need for high-quality CVD graphene films of uniform coverage. This would allow more homogeneous doping of the films, produce samples of lower sheet resistance. As such, 1 cm $\times$ 1 cm Ni CVD graphene will be used throughout the remainder of this investigation, as results indicate these samples achieve lower sheet resistance values after intercalation. This is likely because the samples are higher quality and contain fewer holes and patches of thin graphene, allowing better intercalation and a greater reduction in sheet resistance. Additionally, further optimisation of intercalation conditions in the 9 cm diameter tube could lead to improved sheet resistance values, below 100 Ω/sq. This is required if $FeCl_3$ intercalated FLG is to be used

in flexible or rigid OPV devices and compete with ITO, capable of reaching sheet resistance values of around 15 Ω/sq. This provides a potential route to the fabrication of flexible energy harvesting devices boasting improved efficiencies compared to alternative devices that utilize other flexible, transparent conducting electrodes.

Chapter 5

Effects of Ozone Treatment on $FeCl_3$ Intercalated Graphene for Photovoltaics Applications

5.1 Introduction

Over the past decade, the volume of research dedicated to integrating graphene electrodes into photovoltaic devices has increased dramatically [40, 173, 174]. This is due to the many attractive properties of graphene previously mentioned in this work, such as the low sheet resistance and high transmittance. However, as was discussed in chapter 2, a number of roadblocks to progress have been uncovered, namely the compatibility of graphene with the PEDOT:PSS HTL. Due to graphene's hydrophobic nature, it interacts poorly with aqueous solutions, such as those used in PEDOT:PSS spin coating [175]. This causes uneven or discontinuous coverage of graphene with PEDOT:PSS, as shown in figure 5.1. Uneven coverage can lead to the formation of shunts, while discontinuous coverage has been shown to cause short circuits and lead to device failure. However, this has not deterred researchers, and many strategies have been employed to combat this issue of poor coverage, including the addition of secondary co-solvents such as IPA and MeOH [46, 176], modifying

the solution with MoO_3 [177], or using mixed organic/aqueous PEDOT:PSS solutions [178]. However, perhaps the most promising and applicable method to the fabrication of large area devices is the use of UV/ozone treatment on graphene to reduce its hydrophobicity [179, 180].

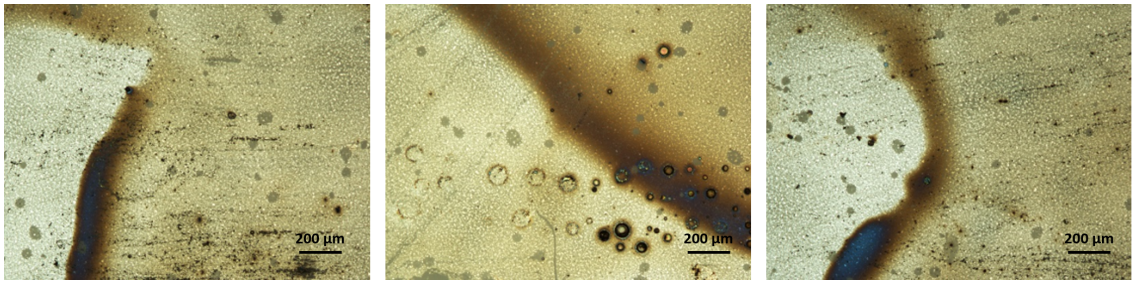

Figure 5.1: Examples of poor PEDOT:PSS coverage on hydrophobic graphene films, taken from three separate regions of the same sample. Optical contrast shows thicker (darker) areas of PEDOT:PSS caused by uneven wetting on the graphene surface. This introduces roughness into the organic layers of OPV devices and can lead to reduced efficiencies and device failures. 200 μm scale bars are shown on each of the images.

UV/ozone treatment has been extensively employed for the cleaning of material surfaces [181], and more recently has been used to successfully reduce the contact angle between graphene films and PEDOT:PSS solutions [46, 180], making the graphene more hydrophilic and improving the success rate of OPV devices made with graphene electrodes. It was found that PEDOT:PSS films spin coated on graphene pretreated with UV/ozone exposure resulted in much smoother and more continuous films. Untreated films show discontinuous PEDOT:PSS coverage, which was highlighted as a source of device failure. The reason UV/ozone treatment is so effective in this instance is due to the chemical modification of the graphene surface it causes. Ozone radicals, produced when air is exposed to strong UV, react with the surface of the graphene film. This forms oxygen containing groups (e.g -OH, -COOH, -HCO and -CO-) on the surface of the graphene film which can favourably interact with water molecules in the PEDOT:PSS solution due to the polar nature of the oxygen containing groups [182]. The creation of these reactive species that in-

teract with the graphene film is also the driving force to UV/ozone treatment being one of the most effective methods of removing polymer residues from the surface of graphene and many other materials [183, 184, 185]. However, the addition of these polar groups disrupts sp^2 hybridised structure of graphene, resulting in an increase in the sheet resistance of the sample. This means the benefits to surface wetting offered by UV/ozone treatment have to be weighed against the negative impact on graphene's sheet resistance. The use of FLG films doped through intercalation with $FeCl_3$ may offer a solution to these two opposing outcomes of ozone treatment.

As UV/ozone treatment only affects the top-most graphene layer, the sheet resistance of FLG samples may be preserved due to the underlying layers of graphene being unaffected. This mitigates some of the negative effects of UV/ozone treatment, while retaining the improvement to surface wetting. i-FLG takes this strategy a step further, as the FLG has already been heavily doped to reduce its sheet resistance. Combining both doping of the graphene and ozone treatment has not been previously tested, as ozone treatment is liable to remove any dopant molecules on the surface layers of graphene. This makes intercalation the perfect choice of doping technique to combine with ozone treatment, as the doping occurs between the graphene layers and not at the surface. In this chapter I will examine the effects of UV/ozone treatment on i-FLG and pristine FLG films grown by CVD on a Ni catalyst. Sheet resistance and contact angle measurements are taken before and after successive UV/ozone treatments to establish the effect of UV/ozone treatment duration, and the treatment time required for the fabrication of OPV devices using graphene electrodes. Raman mapping was used to fully characterize the impact of UV/ozone treatment on the presence of defects in i-FLG samples, as well as the impact on doping in i-FLG films. Lastly, Scanning Kelvin Probe Force Microscopy (SKPFM) is used to demonstrate the elevated work function of both i-FLG, and UV/ozone treated intercalated FLG.

5.2 Methods

Graphene samples were transferred and intercalated as described in chapter 3, before being exposed to UV/ozone treatment, which is known to be a powerful method for cleaning organic residues from material, as well as adjusting the wetting behaviour of many materials. Here, I investigate the use of UV/ozone treatment on FLG and i-FLG samples to improve the wetting of PEDOT:PSS. A UV/ozone cleaner was purchased from Ossila, with a power of 20 μW/cm^2 at a distance of 100 cm. The UV lamp has dominant wavelengths of 185 and 254 nm, which generate ozone molecules from molecular oxygen in the atmosphere. Sheet resistance and contact angle measurements were taken before UV/ozone treatment, after which the sample was dried before again being exposed to UV/ozone treatment. UV/ozone expsoure time was maintained at either 1 or 2 minute increments, before the contact angle and sheet resistance were remeasured. This process was repeated up until 12 minutes, when the sheet resistance of the FLG sample had significantly increased. Measurements of the sheet resistance and contact angle made with water were performed using a 4 point probe measurement setup and goniometer, respectively, as described in Chapter 3: Methods. These measurements were made after each successive treatment in order to determine the optimum treatment time and impact of UV/ozone exposure on sheet resistance.

Atomic Force Microscopy (AFM) and Scanning Electron Microscopy (SEM) were used in conjunction to characterize the surface roughness of i-FLG films coated with PEDOT:PSS. i-FLG films were prepared by myself, first by treating them with UV/ozone for between 0 – 8 minutes, before PEDOT:PSS film was spun at 2400 rpm for a nominal thickness of 40 nm. The characterisation of these samples by AFM and SEM was performed by Miss Kavita Harry under the supervision of Dr Hong Chang.

Raman mapping was performed using the setup described in Chapter 3: Methods [162]. Spectra were taken to allow the measurement of both G and D peak in order to characterize the defect density in the graphene samples. This was performed

using a script prepared by Miss Gabriella Prando, which analyses the intensity of the G and D peaks by peak fitting similar to the method described in section 4.3.1.

Characterisation of the work function of i-FLG samples was carried out by Scanning Kelvin Probe Force Microscopy (SKPFM). This was carried out using a Bruker Dimension XR commercial Scanning Probe Microscope in Peak Force KPFM mode, as opposed to the setup outlined in chapter 3. The characterisation was performed by Dr. Vishan Pashal, using a PFQNE-Al probe tip (doped silicon with a 5 nm radius) allowing both topographical and potential data to be collected simultaneously. Freshly exfoliated Highly Orientated Pyrolitic Graphite (HOPG) was used to calibrate for the tip potential before each measurement. KPFM measurements were taken over a 30 μm $\times$30 μm area to account for variation in sample thickness, and hence intercalation condition.

5.3 Results

5.3.1 Contact Angle and Sheet Resistance

Results presented in figures 5.2c and 5.2d show that for both pristine and intercalated FLG films, increasing the UV/ozone treatment time resulted in increased sheet resistance and decreased contact angle made with DI water. However, the behaviours of these two kinds of graphene film were quite different. The sheet resistance of the pristine FLG film quickly rose to twice its original sheet resistance, from 600 Ω/sq to 1250 Ω/sq after just 10 minutes exposure. Intercalated FLG's sheet resistance only increased by around 50% after the same exposure, from 120 Ω/sq to 200 Ω/sq. As i-FLG samples have a much lower sheet resistance to begin with, it can be seen that UV/ozone treatment has much less of an impact on the film's sheet resistance when compared to pristine graphene.

For both intercalated and pristine graphene films, UV/ozone treatment causes the reduction in contact angle made between the film and DI water, with both films starting as hydrophobic (making a contact angle of 90° or above with water, shown

(a) Untreated graphene

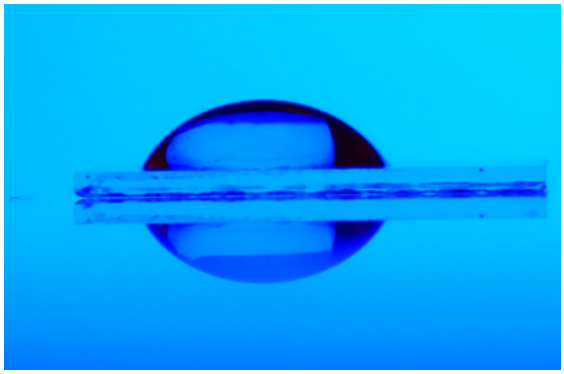

(b) Graphene treated with ozone for 2 minutes

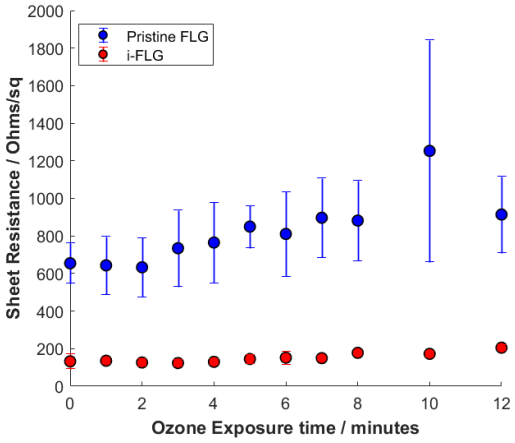

(c) Sheet resistance

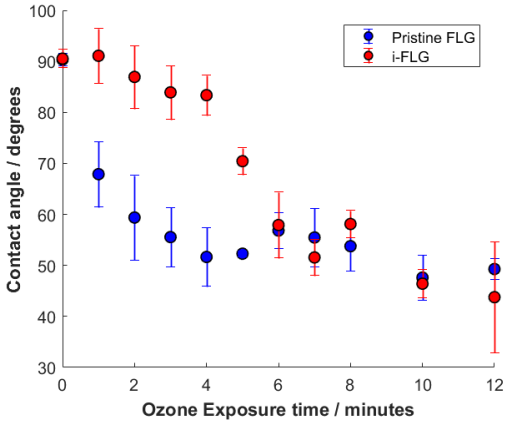

(d) Contact angle made with water

Figure 5.2: Effect of UV/ozone treatment on the wetting behaviour of water on a hydrophobic graphene film, before (a) and after (b) treatment. Result of exposure on sheet resistance (c) and the contact angle (d) for pristine FLG (blue) and $FeCl_3$ intercalated FLG (red) for different exposure times.

in figure 5.2a). However, the contact angle decreases much more quickly in pristine graphene films than for intercalated films. The contact angle between water and pristine graphene decreased to around 50° after just 4 minutes of exposure, however intercalated samples' contact angle only reduced by 5-10° after the same period of exposure. Following further exposure to UV/ozone, the rate of decrease in contact angle accelerates, reaching 50° after 6–8 minutes exposure.

Complete wetting of the graphene films by water, indicated by a contact angle of less than 5° would lead to the best quality films when spin coating PEDOT:PSS. However, this is not required for films of satisfactory quality, so a contact angle of between 60° and 50° is acceptable (shown in figure 5.2b). This provides a guideline for UV/ozone exposure time to use in the fabrication of OPV devices employing a PEDOT:PSS HTL.

5.3.2 Effect of UV/Ozone Treatment on PEDOT:PSS Surface Roughness

As has been mentioned previously, the roughness of a transparent conductive electrode can have a large impact on the performance of any resulting photovoltaic devices. This is because surface recombination is a key mechanism of charge carrier recombination, particularly in OPV devices. As such, it is important to fully characterize and understand any changes to surface roughness that result from treatment of the i-FLG films by UV/ozone exposure. Roughness of the graphene electrode can be caused a number of sources. In addition to the underlying roughness of the Ni grown FLG patchwork film, contaminants on the graphene film surface, such as polymer residues and aggregated particles left over from intercalation, add to the roughness of the film. i-FLG samples previously measured by Atomic Force Microscopy (AFM) showed a mean roughness of 15–20 nm. However, the PEDOT:PSS HTL is applied to the i-FLG prior to the spin coating of the active layers. It is therefore also important to characterize the roughness of the PEDOT:PSS layers covering the i-FLG electrode. The use of UV/ozone treatment has been shown to

improve the spreading quality of PEDOT:PSS films on graphene by improving the adhesive interactions between the graphene and PEDOT:PSS molecules through the introduction of polar Oxygen containing moieties on the surface of the graphene. Different UV/ozone treatment times lead to varying levels of PEDOT:PSS coverage, and hence different roughness values. In this investigation, AFM and Scanning Electron Microscopy (SEM) were used to characterize the smoothness of PEDOT:PSS films on i-FLG electrodes. Scans were taken over length scales of 20, 50 and 100 μm for both SEM and AFM, and were used to examine the different contributions to the surface roughness. UV/ozone treatment was performed in 2 minute increments, ranging from untreated samples to samples treated for 8 minutes with UV/ozone.

i-FLG samples were first treated with UV/ozone exposure for their allotted exposure time (0–8 minutes), before a layer of PEDOT:PSS HTL was spin coated onto the i-FLG surface. This film was then annealed at 150°C for 10 minutes to ensure any residual water in the film had been removed. Each sample was then characterized by AFM and SEM to assess the roughness of the PEDOT:PSS as a result of different treatment times. As can be seen from figures 5.3a–5.3f, untreated i-FLG samples lead to a non-uniform coverage of the PEDOT:PSS, shown by the rough, uncovered $FeCl_3$ aggregates present. After 4 minutes treatment, the SEM images shows a much smoother surface, with much smaller aggregates spread over the scanned area. These may be aggregates on the surface of the i-FLG that penetrate through the PEDOT:PSS, or aggregates that form in the PEDOT:PSS solution over time. This change in film quality is seen in the AFM scans, where the presence of sharp peaks in the untreated sample are replaced by a much more evenly spread film after 4 minutes. The SEM scan after 8 minutes exposure no longer shows large $FeCl_3$, or even polymer aggregates, but instead a very smooth polymer film, with small wrinkles and flakes on the surface. The AFM scan similarly shows a very smooth surface, with the thicker flakes of graphene showing through the PEDOT:PSS film.

Areas of the AFM scans that do not include any of the large surface aggregates were sampled for Root Mean Square (RMS) roughness measurements. These areas

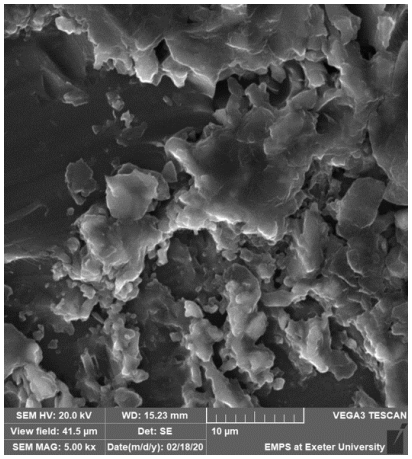

(a) Untreated graphene (SEM)

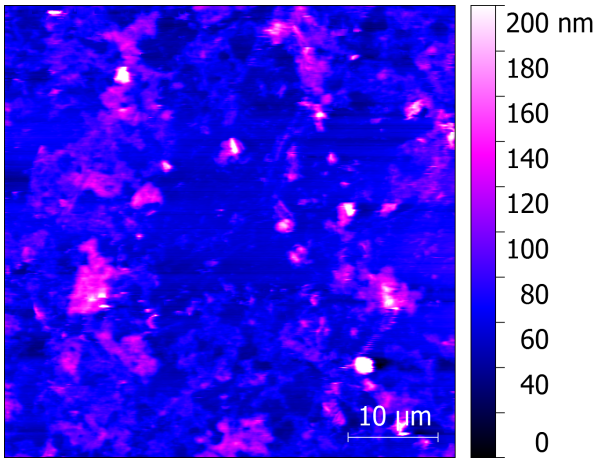

(b) Untreated graphene (AFM)

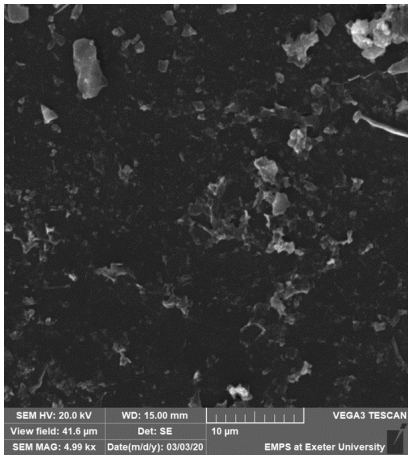

(c) 4 Minutes (SEM)

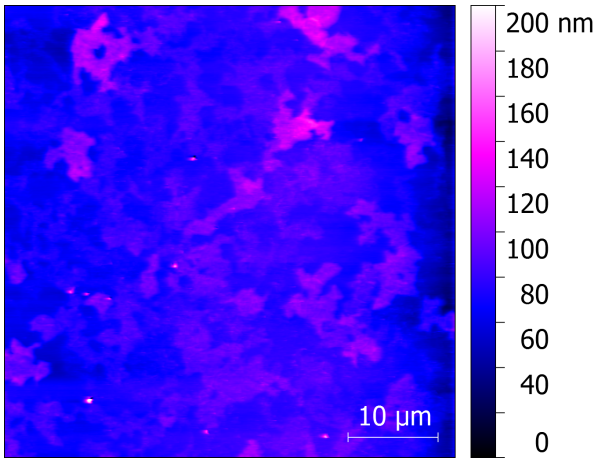

(d) 4 Minutes (AFM)

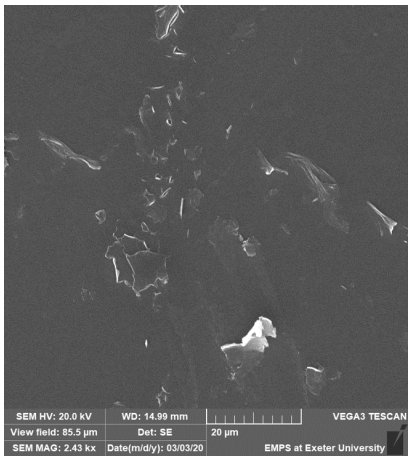

(e) 8 Minute (SEM)

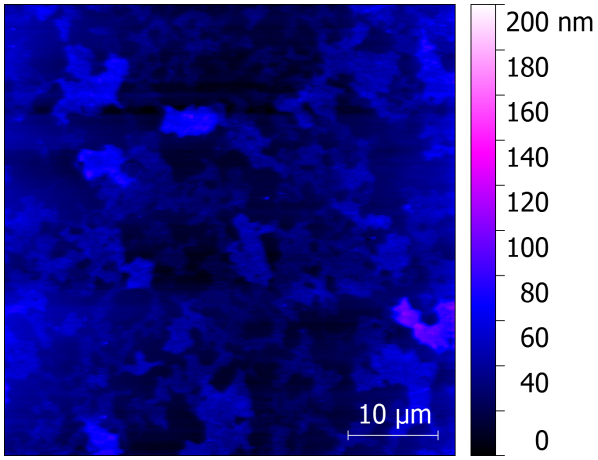

(f) 8 Minute (AFM)

Figure 5.3: Surface roughness characterisation of PEDOT:PSS films on i-FLG electrodes by AFM and SEM measurements. Image captions display the UV/ozone treatment time prior to measurement. Multiple AFM maps were taken over different areas, all maps shown are 50 μm $\times$ 50 μm. Scalebars are shown on all images.

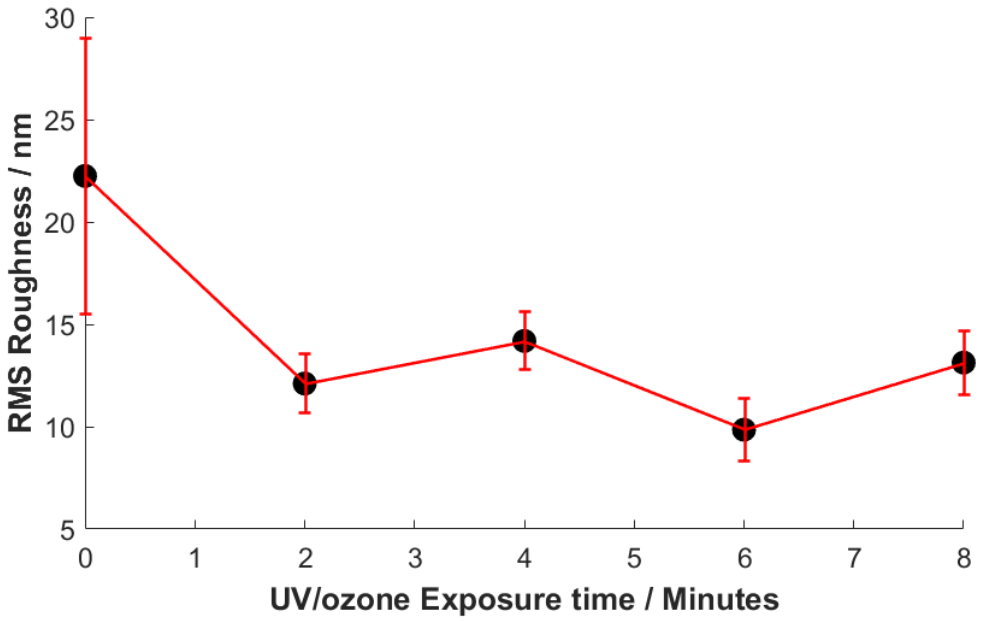

Figure 5.4: Variation in measured RMS roughness from AFM maps over 20, 50 and 100 μm squares. RMS roughness measurements were selected from flat areas of the AFM maps, such that any background present had no affect on the roughness. The mean of these measurements was then calculated, and the standard error used for the error bars shown.

were selected as the peak height of the aggregate may be 10–20 times higher than the roughness of the PEDOT:PSS film, and so dominate the RMS roughness measurement. In this manner, only the roughness of the PEDOT:PSS film is considered.

Figure 5.4 shows the RMS roughness values for PEDOT:PSS films on i-FLG electrodes, across all length scales sampled. After the initial treatment of UV/ozone on the graphene the concomitant roughness drops from $\approx$ 22 nm (greater than the RMS roughness of i-FLG alone), to 12–13 nm. Little improvement is seen after extended UV/ozone treatment, as the roughness remains between 10 and 15 nm. This is likely caused by the underlying roughness of the graphene films impacting the roughness of the PEDOT:PSS layer on top. However, this shows that the PEDOT:PSS does have a smoothing effect on the overall roughness, with the overall roughness experienced by the BHJ layer reducing by 5–10 nm, compared to i-FLG alone. However, it should be noted that just because the roughness does not reduce

after 2 minutes exposure does not mean that the coverage is not improving. Areas sampled that are covered by PEDOT:PSS are likely to have a similar roughness across different exposure times, but the total area covered by PEDOT:PSS is likely to increase up until roughly 6 minutes. Contact angle measurements showed this to be the time required for the contact angle made between i-FLG and water to be reduced to approximately 50°, making PEDOT:PSS spreading significantly more favourable.

One assumption that has been made during this investigation is that the areas that were mapped by AFM were all covered in PEDOT:PSS. As the surface of the film is not smooth, and the topography of the underlying graphene can be seen by the AFM. However, by comparing line profiles taken from the AFM maps across regions where graphene flakes are visible through the PEDOT:PSS, with profiles from an i-FLG sample that has not been coated in PEDOT:PSS, the presence of a polymer film can be determined. This is because the edges of graphene flakes are very sharp, producing a steep profile at the edge of the flake. When covered with PEDOT:PSS, this sharp edge becomes smoothed due to the polymer coating. Such a distinction between the profiles is shown in figure 5.5c, confirming the mapped areas were coated by PEDOT:PSS.

The use of a thicker PEDOT:PSS film would likely further reduce the roughness seen through the PEDOT:PSS film, as a film of only 40 nm was used for all samples. However, altering the thickness of the PEDOT:PSS film will have an impact on the charge transport and absorption properties of the resulting OPV devices that are being developed. As such, the PEDOT:PSS film thickness was held constant and the UV/ozone treatment time was optimised around that. As the total thickness of the BHJ layer is $\approx$ 100 nm, this level of roughness is acceptable but is likely to lead to an increased surface recombination rate at the PEDOT:PSS/BHJ interface when compared to ITO based OPV devices. This is due to RMS roughness for PEDOT:PSS on UV/ozone treated ITO being on the order of 1–2 nm.

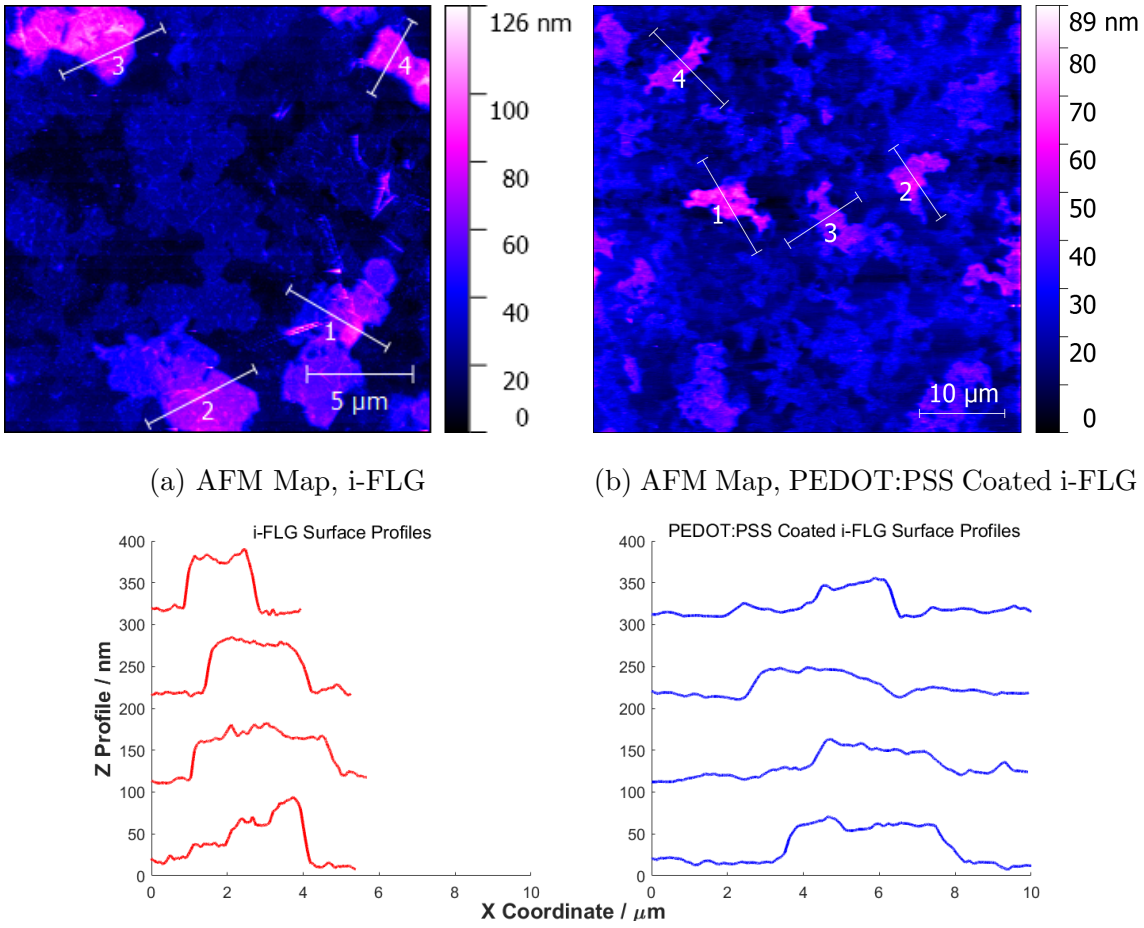

(a) AFM Map, i-FLG

(b) AFM Map, PEDOT:PSS Coated i-FLG

(c) AFM Line Profiles

Figure 5.5: Figures 5.5a and 5.5b show AFM maps taken from i-FLG and PEDOT:PSS coated i-FLG respectively. Annotated line profiles are added to the maps to illustrate the regions selected for profiling. Figure 5.5c plots these line profiles, illustrating the sharp drop at the edge of thicker flakes in the i-FLG sample compared to a similar sample coated with PEDOT:PSS. Although the profiles were taken over different lengths, the X Coordinate is displayed with the same scale, allowing the gradient of the profiles to be compared.

5.3.3 Raman Characterisation of UV/Ozone Treated i-FLG Electrodes

40 μm $\times$ 40 μm Raman maps were collected using a 1 μm step size. The relative intensities of the D and G peaks were calculated through peak fitting, allowing the D/G intensity ratio to be calculated for each point sampled across the area of the sample. This allows the effect of UV/ozone exposure on the defect density in the graphene samples to be investigated, as well as whether this effect varies across the area of the sample. The G peak, appearing around 1580 cm^{-1}, is present for all sp^2 containing carbonaceous materials and gives a measure of the amount of sp^2 carbon present in the material. However, the D peak, appearing around 1350 cm^{-1} is only activated in the presence of defects in the sample, meaning that for graphene, the ratio of integrated intensities of the D and G peaks gives an estimate of the defect density present in the sample [94, 163]. Raman maps were taken for an untreated intercalated sample, an intercalated sample exposed to UV/ozone for 4 minutes, and an intercalated sample exposed to UV/ozone for 12 minutes. These Raman D/G maps, along with an optical image of the area mapped for the 12 min treatment sample are displayed in figures 5.6a–5.6d, with the D/G intensity ratios displayed underneath.

D/G peak ratio maps reveal the untreated sample and the sample treated with 4 minutes of UV/ozone exposure have very similar mean D/G ratios of 0.149 and 0.124 respectively. This indicates that the original films are of high quality, and contain few defects in the areas sampled. The small drop in D/G ratio after 4 minutes could indicate that contaminants are being removed from the graphene surface by the UV/ozone treatment. These act as sources of scattering, and include $FeCl_3$ aggregates, PMMA or other polymer residues, or other surface contaminants that accumulate during the fabrication, transfer and intercalation processes. After 12 minutes exposure the mean D/G ratio rises to 2.372, indicating significant disruption to the sp^2 hybridised graphene structure caused by the introduction of oxygen moieties. This disruption to the structure of graphene gives rise to the increase in

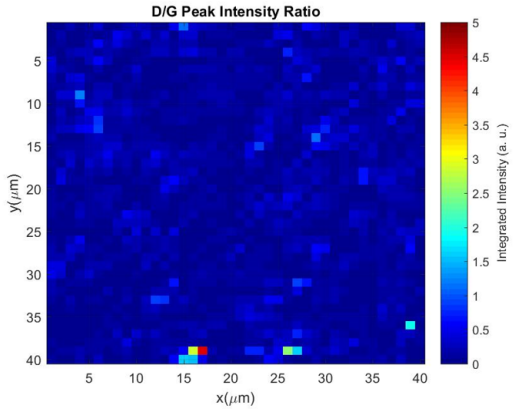

(a) Untreated

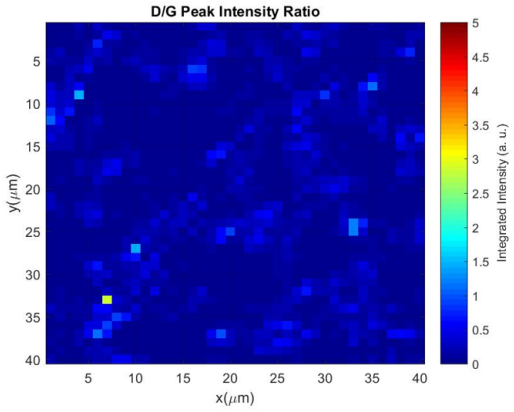

(b) 4 minutes ozone treatment

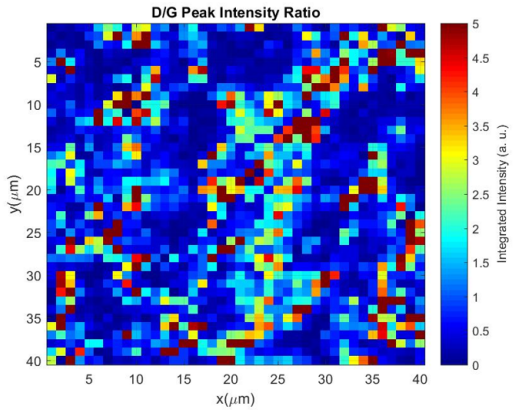

(c) 12 minutes ozone treatment

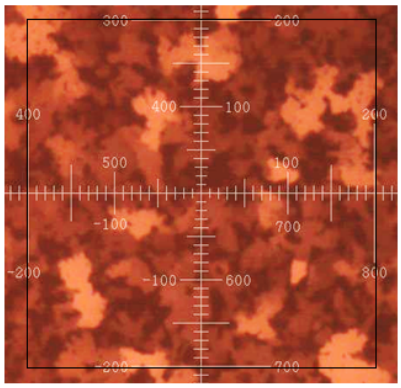

(d) Optical image of mapped area

Exposure time/mins	**D/G Intensity Ratio**
0	0.149
4	0.124
12	2.372

Figure 5.6: D/G intensity maps for graphene samples exposed to UV/ozone for different durations. Table shows mean D/G intensity ratios calculated for the three different samples. Ozone treatment has little effect on the D/G ratio after 4 minutes, but causes a significant increase after 12 minutes. 5.6d shows the optical image of the area mapped (inside black box) after 12 minutes exposure. Relating the optical image to the Raman map shows thicker (brighter) regions to have a much lower D/G ratio than thinner (darker) regions

sheet resistance seen as a result of ozone treatment.

It can be seen from the D/G ratio map that the effect of UV/ozone exposure is not uniform across the graphene film. Instead, particular areas have a far more elevated D/G ratio than others. By examining optical images taken of the same areas we can see that the thinner areas of the graphene film were effected more than the thicker regions. These thinner regions are typically less well intercalated than the thicker regions, as is shown by our mapping of the doping of intercalated samples. This indicates that intercalation may offer some protection to damage caused to the film by exposure to UV/ozone, and would also explain why intercalated samples required greater exposure times to reduce the sheet resistance by an equivalent amount.

5.3.4 UV/Ozone pre-intercalation treatment

One postulate that was considered during this investigation, was the use of UV/ozone treatment to remove contaminants, such as PMMA, from the surface of graphene prior to intercalation. The aim of this investigation was to remove contaminants present during intercalation and thereby improve the quality of the samples produced. Trace contaminants of PMMA and other substances are known to significantly reduce the quality of transferred CVD graphene by introducing unwanted doping, scattering centres, wrinkles and potential tears in the graphene film. This is known to reduce the electrical transport capabilities of the graphene, most notably reducing the charge carrier mobility [186, 187]. Samples of graphene that have first been treated with UV/ozone exposure prior to transfer have shown increased mobilities compared to those that underwent no treatment [188]. These surface polymer contaminants also interfere with the process of intercalation, acting as nucleation points for $FeCl_3$ aggregates. Furthermore, PMMA is documented as producing other contaminants when reacting with $FeCl_3$ during the etching and transfer process [189]. This is likely to also impact the quality of intercalation, and as such it is crucial to develop a method of removing all potential polymer remnants from the graphene film. Graphene samples were transferred to quartz substrates before being cleaned in the method previously outlined. 2 samples were exposed to 4 (sample A) and 12 (sample B) minutes of UV/ozone exposure respectively, prior to intercalation. The two samples were then intercalated together, following the intercalation procedure outlined previously. Raman mapping was carried out on the two samples to assess the impact to intercalation the UV/ozone treatment caused. 30 μm $\times$ 30 μm maps with a 1 μm step size, and 300 μm $\times$ 300 μm with a 10 μm step size were taken and G-peak fitting was carried out as previously described.

Mean $\langle$PosG$\rangle$ values for both the 30 μm$\times$30 μm and 300 μm$\times$300 μm maps showed good agreement for both the 4 minute exposure and 12 minute exposure samples, showing the degree of intercalation to be consistent across the entirety of the sample. Results displayed in figures 5.7a and 5.7c show that 4 minutes of

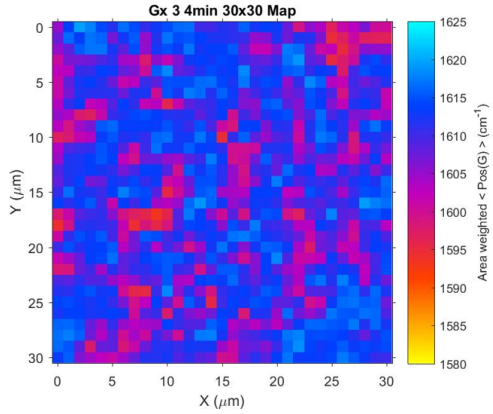

(a) 4 min ozone exposure

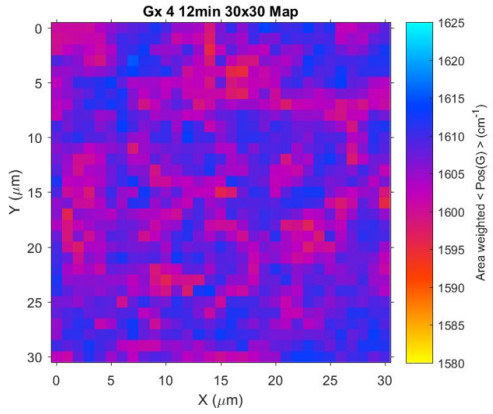

(b) 12 min ozone exposure

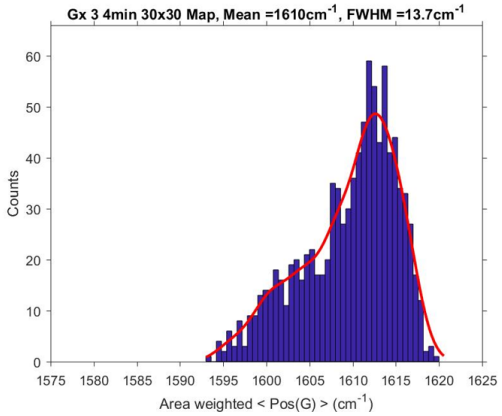

(c) PosG histogram (4 min exposure)

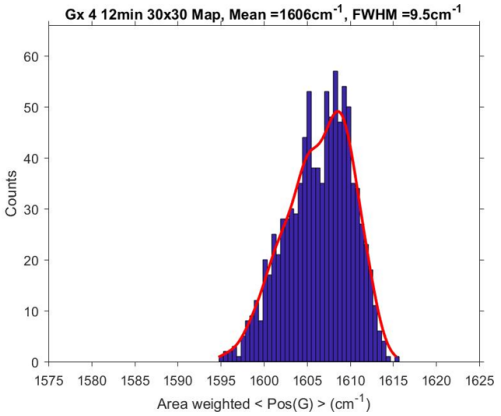

(d) PosG histogram (12 min exposure)

Figure 5.7: (a) and (b) show the ⟨PosG⟩ Raman maps taken over 30 μm×30 μm areas after 4 and 12 minutes UV/ozone exposure respectively. (c) and (d) show the ⟨PosG⟩ histograms for the same data.

exposure to UV/ozone had little impact on the degree of intercalation, with average ⟨PosG⟩ values for sample A being comparable to that of samples characterized in the previous chapter. Sample B (figures 5.7b and 5.7d) showed a marked decrease in ⟨PosG⟩ value of 3–4 cm^{-1} in both the 30 μm×30 μm and 300 μm×300 μm maps. Comparing the histograms of these Raman maps shows sample A to have a much broader spread of ⟨PosG⟩ values (figure 5.7c), ranging from 1593–1620 cm^{-1}, with the histogram heavily weighted towards higher ⟨PosG⟩ values. Sample B, however, had a distribution ranging from 1595–1615 cm^{-1} (figure 5.7d), also weighted towards higher ⟨PosG⟩ values. While the cause of this is as yet undetermined, it is likely that the introduction of oxygen containing groups to the surface of the graphene interferes with the intercalation; either by creating groups that may oxidise the $FeCl_3$ during intercalation, act as points of aggregation for the $FeCl_3$ molecules, or aid in molecules of water adhering to the surface which go on to react with the $FeCl_3$. This indicates that exposure to UV/ozone prior to intercalation does not offer any immediate benefit to the degree of intercalation achieved.

5.3.5 Work Function Measurements of UV/Ozone Treated Samples

The work function of a material is a measure of how much energy is required to remove an electron at the Fermi level from the valence band of a material to vacuum level [190]. In the context of photovoltaics, the work function of the electrode is an extremely important quantity, as poorly matched work functions can present energy barriers to charge extraction at the electrodes. Good alignment of the HOMO of the donor, and LUMO of the acceptor with the work functions of the anode and cathode respectively, leads to the efficient extraction of photoexcited electrons and holes to their respective electrodes. Therefore, the ability to adjust this parameter in the electrodes of photovoltaic devices is key to designing efficient solar cells.

The anode of an organic solar cell must have a low work function to match with that of the PEDOT:PSS HTL. Typically, ITO or gold are used in this place (de-

pending on whether the solar cell is produced with standard or inverted geometry) due to their very high work functions. However, due to the high cost of gold and the aforementioned issues with ITO, these are not ideal materials for this application. Graphene's work function prior to any doping is far too low, sitting at around 4.4 – 4.5 eV, but is susceptible to large changes depending on doping conditions, neighbouring materials and thickness of the graphene sample. Intercalation has previously been shown to be a powerful method of adjusting the doping, and subsequently the work function, in graphene [47, 60, 152]. However, in previous studies these measurements used gold to calibrate for the work function of the AFM probe tip [60]. This can lead to the over estimation of the material's work function. Hence, for this study, HOPG was used to calibrate for the tip potential [164]. The work function of both $FeCl_3$-i-FLG and ozone treated $FeCl_3$-i-FLG were measured to determine any change to the work function that results from the addition of oxygen containing groups to the surface of the $FeCl_3$-i-FLG and to gain knowledge on how this will impact devices.

SKPFM maps were taken from i-FLG samples both before and after ozone treatment for 6 minutes (figures 5.8c and 5.8d, respectively). Topographical AFM maps were also taken (figures 5.8a and 5.8b) in tandem so any variation of work function with sample thickness could be accounted for. The mean work function across the areas scanned was then calculated, showing i-FLG to have an average work function of 5.26 eV, and i-FLG after ozone treatment to have a work function of 5.31 eV. The slightly increased work function is indicative of the addition of oxygen containing groups to the surface of the i-FLG, as is commonly observed in the oxidation of metal electrodes [191]. While the average work function adjustment is rather small, observing the work function distribution for the mapped area reveals the broadening of the work function distribution, leading to a more varied electropoential across the surface of the sample. However, this broadening, displayed in figure 5.9, is largely towards higher work function values, shifting the centre of the distribution up by approximately 0.05 eV. Both distributions could be adequately fitted using Gaussian

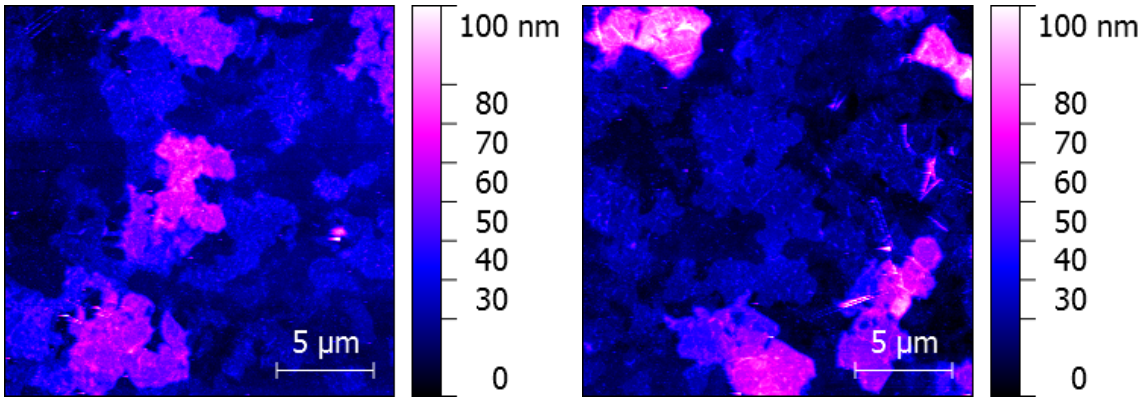

(a) AFM map, i-FLG

(b) AFM map, i-FLG ozone treated

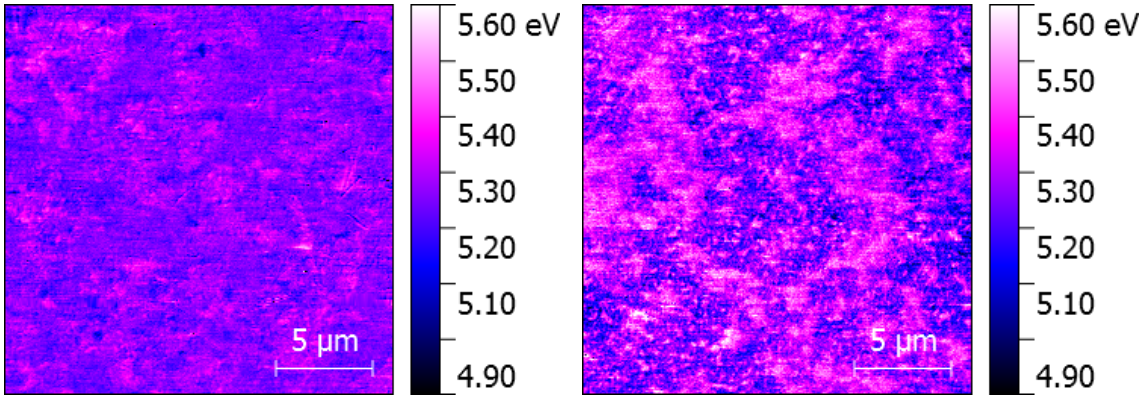

(c) SKPFM map, i-FLG

(d) SKPFM map, i-FLG ozone treated

Figure 5.8: AFM and SKPFM maps of intercalated graphene samples before ((a) and (c)), and after ((b) and (d)) ozone treatment.

functions, revealing a full width half maximum (FWHM) of each distribution to be 0.06 eV pre-ozone treatment and 0.14 eV post ozone treatment respectively.

Topographical maps of the same areas scanned by SKPFM reveal that before treatment the RMS surface roughness was 18.97 nm, while after treatment an RMS roughness of 14.75 nm was measured. As it is extremely challenging to scan the exact same area twice, the difference in measured roughness may simply be due to selecting different areas of graphene to sample. However, 30 μm$\times$ 30 μm areas have been shown to be representative of the graphene sample for Raman and AFM measurements in the past, with properties such as surface roughness varying little across the sampled area, save for any large contaminants on the surface which can be accounted for when calculating the RMS roughness. It can then be seen that

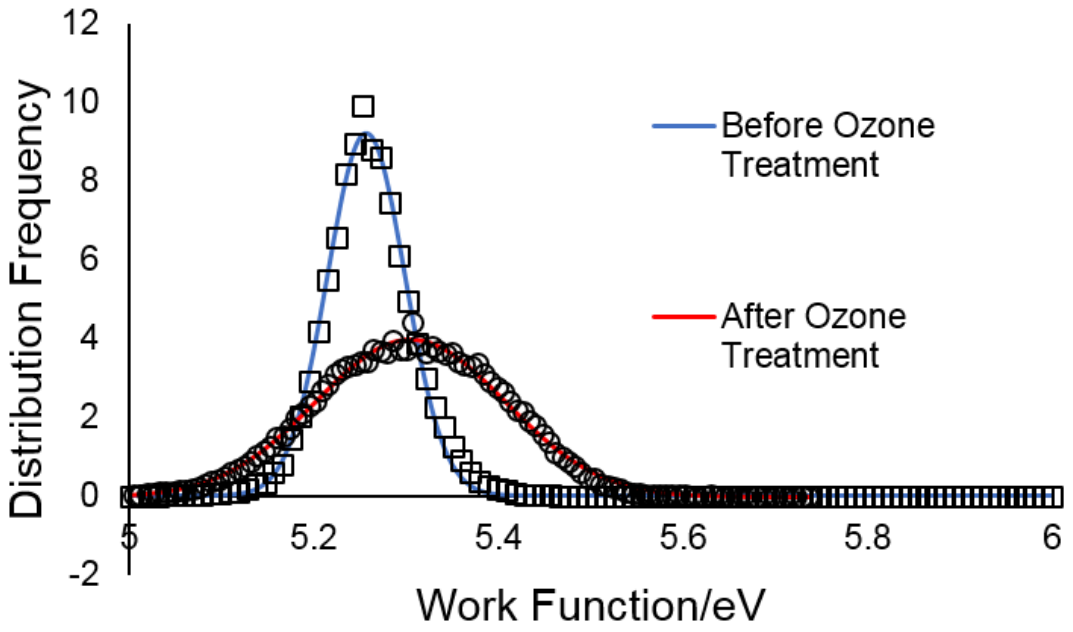

Figure 5.9: Work Function distributions for SKPFM maps showing the effect of ozone treatment on the Work Function of the i-FLG sample.

ozone treatment also reduces the surface roughness of the i-FLG samples, most likely due to the removal of organic/inorganic contaminants on the i-FLG surface, such as PMMA residues and $FeCl_3$ aggregates. This is very useful to the use of ozone treatment in the field of photovoltaics as surface roughness in the BHJ layer induced by roughness in the electrodes is a noted cause of charge carrier recombination, and hence reduced device efficiency.

5.4 Conclusions

In summary, UV/ozone exposure has shown great promise for its use as a treatment in the fabrication of photovoltaic devices with graphene electrodes. The addition of oxygen containing moieties causes the contact angle made between water and graphene to significantly reduce, making graphene significantly more hydrophilic. While this process substantially increases the sheet resistance of pristine FLG, i-FLG is much more robust and maintains a low sheet resistance up to 6 minutes of UV/ozone exposure. Raman mapping was used to demonstrate the increased sheet resistance is due to the disruption of the sp^2 hybridised structure in graphene, as has been reported in other works for undoped graphene. It was also found that exposure to UV/ozone treatment prior to intercalation offered no benefit to the quality of intercalation or the surface wetting of PEDOT:PSS. SKPFM measurements revealed that the enhanced work function of i-FLG is retained, and slightly improved after UV/ozone treatment. This makes UV/ozone treated i-FLG better suited to use in OPV devices than either pristine FLG or untreated i-FLG. This work has provided a viable strategy to fabricating OPV devices with i-FLG electrodes. The next stages of this investigation will see UV/ozone treated i-FLG being successfully employed in OPV devices for the first time.

Chapter 6

Organic Photovoltaics with $FeCl_3$ Intercalated Graphene Electrodes

---

Data contained within this chapter has been subject to publication: *"Improved Stability of Organic Photovoltaic Devices with $FeCl_3$ Intercalated Graphene Electrodes"* K. K. Walsh, C. Murphy, S. Russo, M. F. Craciun. Frontiers in Electronics, published 23^{rd} April 2021 [192]

6.1 Introduction

OPV devices have shown great improvements in recent years, with efficiencies now far exceeding the long held 10% target [193]. However, most devices that show high efficiencies rely on ITO electrodes to achieve the best possible performance [15, 194]. While this is a good strategy for demonstrating the capabilities of the organic materials used, it neglects one of the key drawbacks to using ITO in OPV devices: device stability. Recent studies into the factors effecting the stability of OPVs under different testing conditions have greatly aided the understanding of different degradation mechanisms that can impact OPVs. A number of mechanisms have been identified as contributors to performance degradation in OPV devices, these include the thermal stability of the active layers [195], photo-oxidation[171, 196] and photo-degradation [197] inside the BHJ, the ingress of water into the cell

[198] and atmospheric oxidation [156, 199, 200].

However, while these are present in all OPV devices to some extent, ITO based OPV devices also suffer from degradation caused by the diffusion of indium ions into the active layers of the device, and the deterioration of the ITO electrode by the acidic PEDOT:PSS layer [19, 201]. Improving device stability is an important issue in OPV devices because it greatly increases the total amount of energy produced over the lifetime of the device. Any strategy that prevents rapid device degradation also reduces the device's Energy Pay Back Time (EPBT), which is the time taken for the device to produce the same amount of energy as was required to fabricate it. OPV devices require much less energy to fabricate compared to other types of solar cells, with EPBTs on the order of days [44] instead of years for Si solar cells [202, 203, 204].

It is clear that a suitable replacement electrode for ITO must be found in order to achieve the lowest possible EPBT values. However, selecting a material that can compete with ITO is not a straightforward task. Other electrodes currently under investigation include conductive polymers [205] and metallic nanowire meshes [206, 207]. However, each of these alternatives also introduce their own issues of high sheet resistance and increased surface roughness, respectively. Perhaps the most promising alternative electrode currently under investigation is graphene. Since graphene was first isolated and its electrical properties investigated [32, 33, 34], the research community has highlighted photovoltaics as a promising application of graphene. Many researchers have made excellent progress on this, in the fields of silicon photovoltaics [208], Perovskite Photovoltaics [209] and OPVs [37, 39, 148]. However, there have been a number of roadblocks to progress in using graphene as a transparent conductive electrode in OPV devices. Firstly, the sheet resistance of CVD graphene is too low to compete with ITO [210] with a comparable transmission, requiring strong doping to reach similar sheet resistance values [115, 148, 211]. Secondly, graphene's hydrophobic nature makes it difficult to use in solution processing steps, such as the spin coating of transport and BHJ layers in OPV fabrication stages

[43]. Lastly, the low work function of graphene leads to an energy offset between the LUMO of the acceptor and the graphene electrode, inhibiting charge extraction and reducing device efficiencies [49, 212]. As I have demonstrated in the previous two chapters, a combination of functionalization through intercalation with $FeCl_3$ and subsequent UV/Ozone treatment are effective at tailoring the sheet resistance, work function and hydrophobicity of the i-FLG electrode, providing a solution to each of these problems. As such, this chapter will investigate the use of i-FLG electrodes in OPV devices, characterizing their device performance and stability compared to commercially available ITO based devices.

6.2 Methods

Sheet Resistance Measurements

As was described previously, sheet resistance measurements were carried out using a Signatone S-302-4/SP4 4 point probe measurement system, connected to a Keithley 2400 source measurement unit. 9 separate measurements were taken across the area of the sample and the mean taken. A correction factor is then applied to account for the geometric shape of the sample.

The 4 point probe system used was noted as damaging the i-FLG samples by the probe tips cutting holes through the graphene. As such, the sheet resistance of each i-FLG electrode was not measured to prevent damage and potential device failure. However, enough i-FLG electrode sheet resistance measurements have been taken to be able to estimate the sheet resistance of all samples as falling between 50–100 Ω/sq.

IV Curve Measurement

IV curve measurement was carried out using an Ossila Solar Cell IV Test System by first loading samples into the push fit test board. IV curve sweeps were run between -1 and 1 V, and then 1 and -1 V to assess any hysteresis between the two sweeps.

Voltage step increments of 10 mV and a voltage settle time of 10 ms were used.

A Newport 94011A class ABB solar simulator fitted with an AM1.5G filter was used as a light source, and irradience intensity calibrated using an Oriel model 91150V Calibration Cell connected to a readout meter. The output of the solar simulator was allowed to stabilize for 30 minutes prior to measurements being taken.

For each sample measured, IV curves were measured in both dark conditions and under illumination. For measurement of the dark curve, the shutter on the solar simulator was closed and a cover placed over the opening on the push-fit test board to prevent any ambient light from entering and giving false readings. Measurement of the ambient light intensity was performed using the calibration cell used for measuring light intensity from the solar simulator. While the shutter was closed, ambient light intensity in the room was measured to be ≈ 0.05 Sun, although this value is likely to vary depending on the time of day measurements were taken. A custom built mask was also used during measurements, covering the areas of the solar cell where the contacts do not overlap. This prevents erroneous current generated outside of the solar cell active area from being collected in addition to the current produced by the active area of the cell. Device PCE values are then calculated using equation 2.6 in chapter 2.

Stability Measurements

Two different methods of measuring photovoltaic stability were used in this investigation, the first being continuous light exposure with regular measurement and the other being periodic exposure and measurement. For the first method, devices were continually exposed to light from the solar simulator while IV curves were taken every minute over a period of 60 minutes. This allows for the continual monitoring of photovoltaic parameters such as efficiency, and how they change over time with continuous exposure. The second method was to expose a sets of i-FLG and ITO OPV devices to illumination under the solar simulator and measure the device parameters multiple time over a period of ≈ 10 days. Between each measurement the

devices were returned to a desiccator, out of direct sunlight to prevent degradation of the device from extrinsic factors.

6.3 Results

6.3.1 Optimisation of OPV layers

The first stages of optimising the fabrication of OPV devices was to ensure all solutions used were mixed correctly and could achieve the desired thickness from spin coating. PEDOT:PSS, the BHJ solution (PTB7/PC70BM) and ZnO solutions were all spin coated onto glass substrates and the resulting films inspected for aggregates by optical microscopy. Small crystalline particles were identified in the ZnO films. However, as this layer is the last spun onto the OPV device these aggregates will not impact the BHJ layer and pose little risk of shorting the devices. Aggregates of various sizes were also found in both the PEDOT:PSS and BHJ layers. These are much more likely to cause short-circuits in OPV devices and must be removed from solution before spinning. Several methods were used to reduce the incidence of polymer aggregates in these solutions, including heating the solutions prior to spin coating, sonication and filtering of the solution. Filtering was not used on the BHJ solution as this is liable to impact the phase mixing of the two BHJ components, and could lead to reduced photovoltaic performance. Instead, the BHJ solution was heated and mixed continuously, with mixing temperature being slightly increased before spin coating to encourage the dissolving of polymer aggregates. A combination of heating, sonication and filtration of the PEDOT:PSS solution were found to be most effective at removing aggregates. As this is the first layer applied in the OPV devices, it is also the most crucial to ensure no aggregates are present to short the device.

OPV layer thickness

Control over the thickness of the individual layers in an OPV device is crucial to producing efficient, consistently functioning devices. Values from the supplier's website were taken as the optimum thickness values for PEDOT:PSS, OPV and ZnO layers. However, as the OPV layer is spincoated from a freshly prepared solution of PTB7 and PC70BM, the spin speed required may be different to that listed by the supplier. Similarly, the PEDOT:PSS solution had to be diluted in order to achieve a low enough thickness for the spin speeds attainable by spincoater used, so calibration of the speed required was necessary. As such, the layer thickness of different samples of OPV materials were characterized by surface profiler for different spin speeds.

A common problem in measuring the thickness of polymer layers by surface profiler is that the tip of the profiler will pick up some of the soft polymer underneath and push the displaced polymer into the path of the tip. As the tip moves along the surface, more and more polymer is built up in front of the tip, until the tip finally moves over the mass of polymer. This can lead to the under/over estimation of layer thickness, depending on what section of the surface profile is being measured. As such, polymer layers were baked before profiler measurement to help harden the film. Additionally, the lowest force setting was used for profiler measurements, in order to cause as little damage as possible to the polymer films. Once measured, the background gradient in the profiles was removed and the mean thickness was measured from sections of the profiles that showed a consistent thickness.

A minimum of three surface profiles were taken for each spin speed for both PEDOT:PSS and BHJ films, and the measured thicknesses averaged by taking the mean value. The film thicknesses for these two materials are shown in figures 6.1 and 6.2. Once the spin curves were obtained, estimates of the required spin speeds could be extracted, settling on using a 3:1 dilution of PEDOT:PSS spun at 2400 rpm for a required thickness of 30–40 nm, and spinning the BHJ solution at 1200 rpm for a required thickness of 90–100 nm.

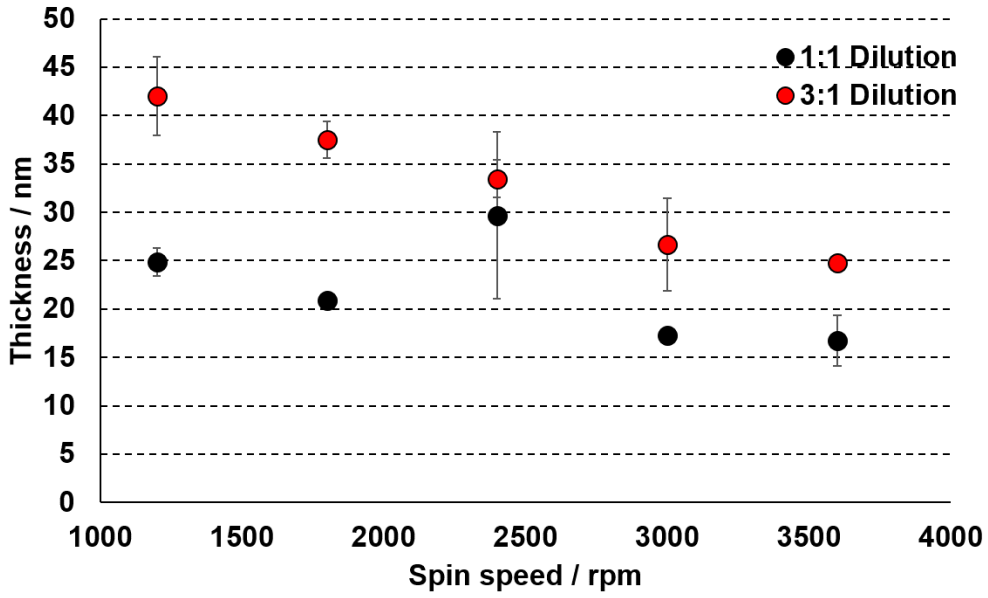

Figure 6.1: PEDOT:PSS Layer thickness measured by surface profiler. Thicknesses for two dilutions of 3:1 and 1:1 ratios of PEDOT:PSS and DI water were measured to achieve the 30–40 nm thickness required.

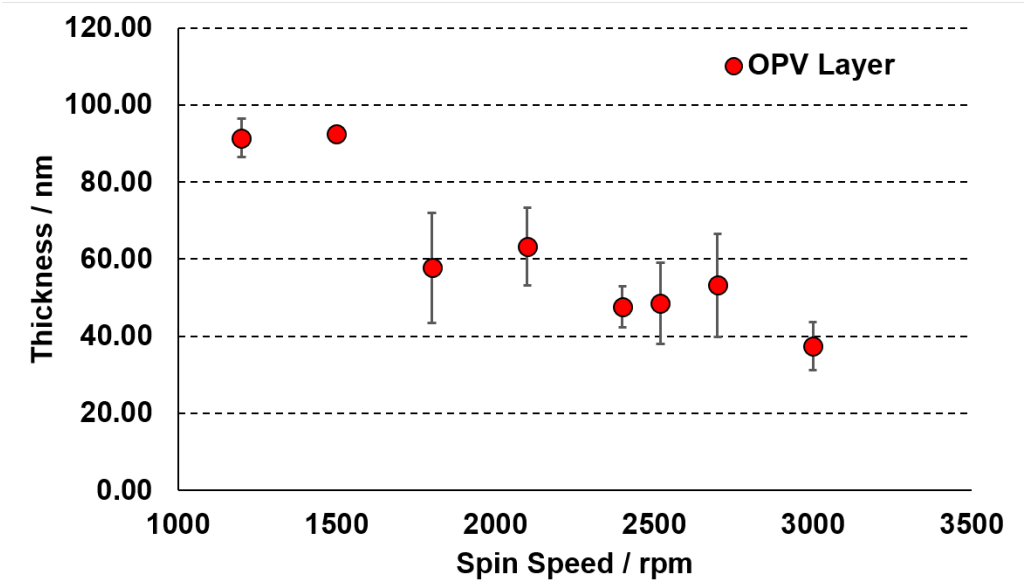

Figure 6.2: Thickness measured from surface profiler of BHJ layers spun at different spin speeds to determine the required speed to achieve a thickness of 90 nm

Characterisation of interlayer roughness by AFM mapping

Another important parameter when spinning thin film devices is the roughness of each layer. The roughness of the BHJ and the underlying layers directly effects

device performance, as increased roughness also increases the surface area of the BHJ, leading to a rise in bimolecular recombination of charge carriers and therefore decreasing the short circuit current [213]. Additionally, excessive roughness in device layers can cause short circuits and lead to faulty devices.

While the surface profiler is capable of measuring the roughness of hard films, the added uncertainty that comes from the profiler damaging the soft polymer film means that a higher precision instrument must be employed. To measure the roughness, therefore, I used an AFM in non-contact mode, to ensure that the roughness of the film was not affected by the measurement. AFM maps were taken of the BHJ layers as well as ZnO ETL.

AFM Maps, displayed in figures 6.3a–6.3f, were taken over multiple areas of each of the OPV device interlayers; ITO and i-FLG electrodes, PTB7:PC70BM BHJ and ZnO elctron transport layer (PEDOT:PSS layers were not mapped as their roughness was characterized by AFM in the previous chapter). This allowed the calculation of root-mean-square (RMS) roughness values, which are displayed in table 1.

As was described in chapter 3, i-FLG electrodes are much more rough than their ITO counterparts. This is caused by two main factors, the roughness of the as prepared CVD graphene, and the added roughness caused by the intercalation process with $FeCl_3$. The ITO, however, has a very smooth surface once it has been carefully cleaned, with the measured roughness being very close to the quoted roughness of 1–2 nm given by the manufacturer. The higher roughness of i-FLG electrodes compared to ITO is a potential source of device failure, and will be investigated by examining device success rates.

ZnO films were prepared from both filtered and unfiltered solutions. Two annealing temperatures (120 and 140°C) were used to anneal the films. Figures 6.3c and 6.3d show the AFM maps taken for both the unfiltered samples annealed at 120 and 140 °C, respectively. The maps show a strong, non-linear background offset, that dominated the data. This is an artifact from what is known as the bowing effect [214], caused by the motion of the cantilever. As such, the RMS roughness

Table 1: OPV Device Interlayer Roughness				
Layer	**RMS Roughness / nm**			
ITO	2.3			
i-FLG	16.0			
ZnO	Unfiltered 120 °C	Unfiltered 140 °C	Filtered 120 °C	Filtered 140 °C
	7.2	7.0	5.4	7.8
PTB7:PC70BM	16.2 (Unfiltered)		11.1 (Filtered)	

(a) ITO Electrode

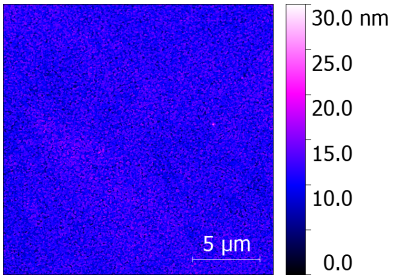

(b) i-FLG Electrode

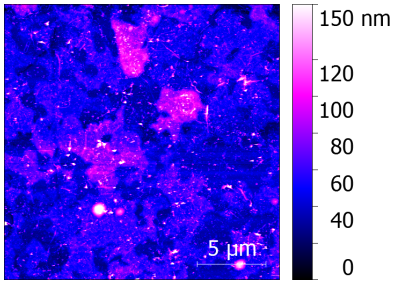

(c) ZnO Unfiltered, 120°C

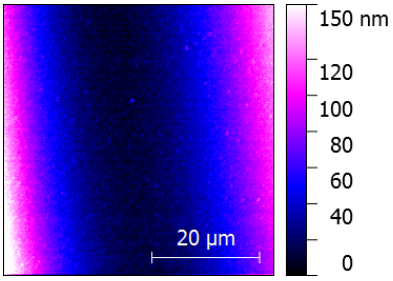

(d) ZnO Unfiltered, 140°C

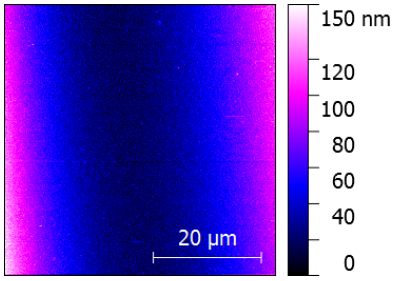

(e) BHJ (unfiltered)

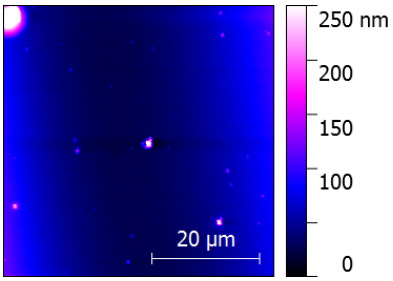

(f) BHJ (filtered)

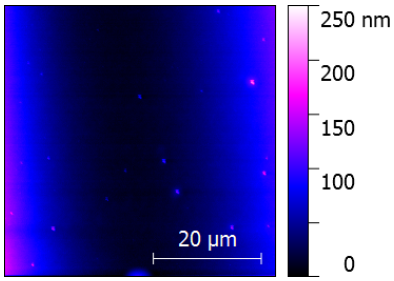

Figure 6.3: AFM maps of device interlayers. Topographical maps of (a) ITO and (b) i-FLG electrodes used in device fabrication. The ZnO ETL was also mapped for both filtered and unfiltered solution treated at different annealing temperatures, 120 °C (c) and 140 °C (d). The BHJ was also mapped, for both unfiltered (e) and filtered (f) solutions.

measurements for these maps were taken over smaller areas in the centre of the sample, where the background had little effect on the data. Average roughness measurements taken from the maps are shown in table 1.

Annealing temperature and filtration have little effect on the roughness of the ZnO layer, which is unsurprising as the solution the layers were prepared from is low concentration and shows no aggregation of ZnO particles, leading to smooth films. Higher annealing temperatures are known to aid in removing remnant DIO from the BHJ, and can lead to improved device efficiencies [158]. As such, the higher annealing temperature of 140 °C was used in device fabrication.

The AFM maps of the BHJ films displayed in figures 6.3e and 6.3f, revealed particle aggregates in the film, causing an increase in surface RMS roughness. This is much more prominent for the unfiltered film than the filtered film, indicating filtration to successfully remove particle aggregates. These aggregates could be accumulations of fullerene molecules that have stuck together, or originate from an impurity, either a contaminant or a polymer of the BHJ that has photodegraded and accumulated other polymers around it. While assessing the origin of these aggregates is beyond the scope of this investigation, developing a method of removing or re-dispersing them was required. Filtration was attempted as a method of removing these particles but was shown to only be effective at removing the largest of aggregates. Instead, a combination of heating and continual stirring was used to ensure particle aggregates in the BHJ solution were kept to a minimum.

A similar, although less pronounced, background was seen in the AFM maps of BHJ films, meaning that care had to be taken when selecting areas to calculate the mean roughness from. This lateral, parabolic background was only seen after subtracting a more dominant background from the maps, so could be a remnant of the previous background subtraction process. The aggregates seen in the AFM maps have a much larger measured height than the background, so it is likely the aggregates will dominate the roughness measurement. Regardless, efforts were still made to ensure the background or any other artifacts of processing the data were

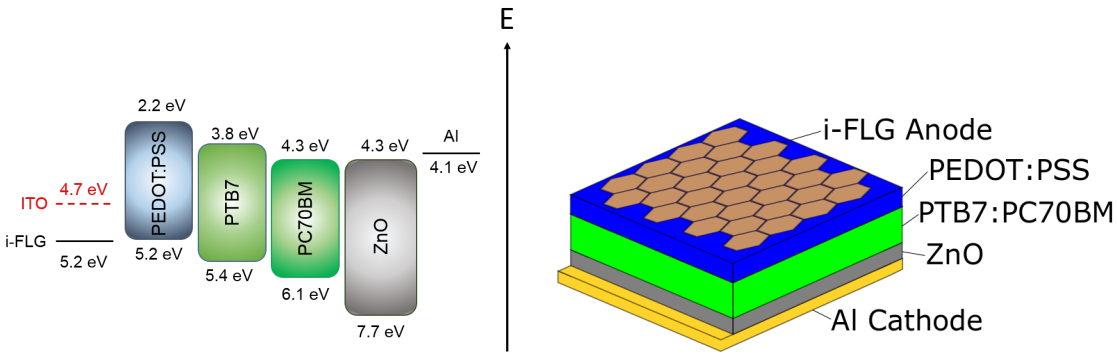

(a) (b)

Figure 6.4: a. Energy level diagram of OPV devices fabricated with i-FLG and ITO transparent conductive electrodes. This diagram shows the work functions of ITO and i-FLG, along with the energy levels of the HOMO and LUMO for both the donor and acceptor. b. Diagram of i-FLG standard device architecture. Light enters the device from the top, through the i-FLG electrode and into the active layers of the device.

not included in the final result.

6.3.2 PTB7:PC70BM Organic Photovoltaic Devices

Organic photovoltaic devices were fabricated to test the effectiveness of i-FLG transparent electrodes against commercially available ITO electrodes. The devices were constructed with i-FLG/ITO transparent anodes, a PEDOT:PSS HTL, PTB7:PC70BM bulk heterojuntion (BHJ), ZnO ETL and an evaporated Aluminium cathode. When under illumination, the absorption of light in the BHJ generates excitons, which are separated at the BHJ interface by the in-built field generated from the difference in electrode work functions. Figure 6.4a shows the work functions of the two electrodes being used, as well as the HOMO and LUMO levels of the OPV materials and transport layers. From there the electrons and holes are transported to the ETL and HTL respectively, before being extracted at the anode and cathode. This allows the generation of current and is characterized by measurement of the OPV device's IV curve.

IV characterisation under illumination

IV curves were collected under 1 Sun illumination and under dark conditions. From the IV curve, one can measure the short circuit current, open circuit voltage, PCE, fill factor, series and shunt resistances; as detailed in chapter 2. These parameters were obtained for both devices and are displayed in table 2.

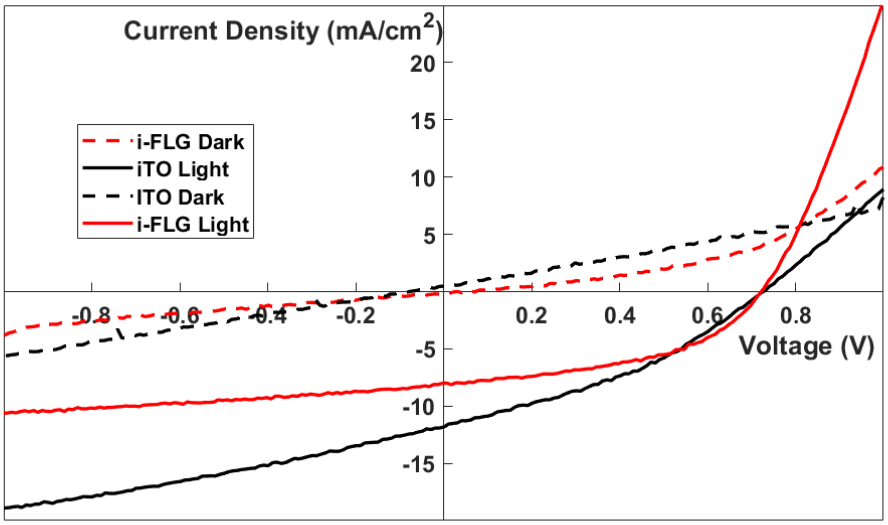

Figure 6.5: IV curve for PTB7:PC70BM Photovoltaic devices fabricated with ITO (black) and i-FLG (red) electrodes respectively. Forward and reverse curves are not shown, as they overlapped significantly. IV curves taken in dark conditions are shown with a dashed line, with curves taken under illumination having solid lines.

Table 2: Photovoltaic Device Parameters

Electrode	$PCE/\%$	J_{sc}/mA.cm^{-2}	V_{oc}/V	FF	$R_{shunt}/\Omega.cm^2$	$R_{series}/\Omega.cm^2$
ITO	3.2	-11.88	0.73	36.4	126	32
i-FLG	2.8	-8.12	0.72	47.5	305	19

Similar efficiencies values were attained for the two best performing devices of each variety. By comparing the shape of the IV curves, values are obtained for the photovoltaic parameters outlined above, which are presented alongside the PCE

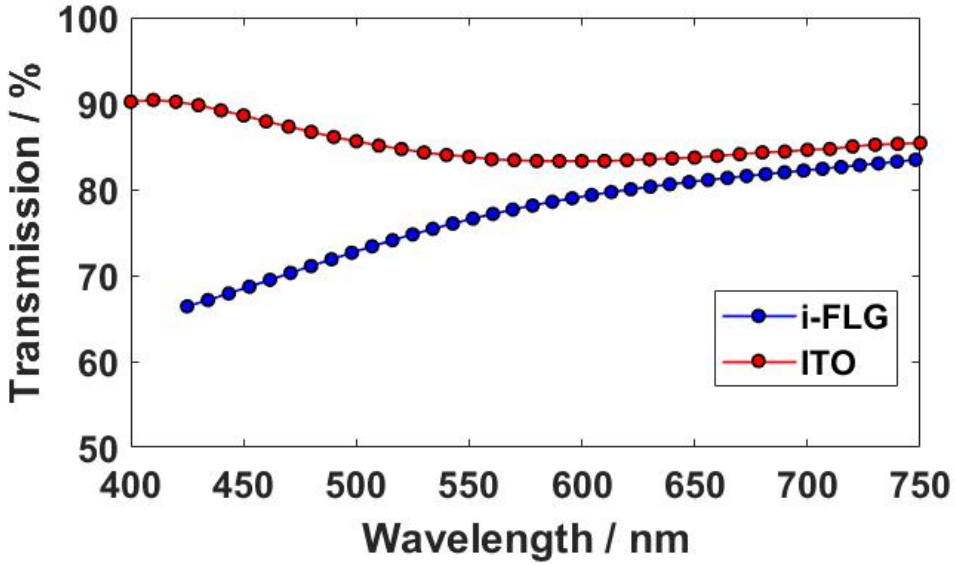

Figure 6.6: The transmission through ITO and i-FLG electrodes over the visible spectrum. ITO possesses a higher overall transmittance, with transmittance values far exceeding that of i-FLG at shorter wavelengths. Reproduced from Frontiers in Electronics under Creative Commons Licence (Walsh KK et al. (2021) Improved Stability of Organic Photovotlaic Devices With FeCl3 Intercalated Graphene Electrodes. Front. Electron. 2:643687).

values in table 2. As can be seen from figure 6.5 the short circuit current produced by the ITO based OPV device was larger than that produced by the i-FLG based device. This is likely due to the ITO having a greater transmission than i-FLG (shown in figure 6.6), allowing more light to enter the solar cell and generate a greater photocurrent. V_{oc} values for both devices are comparable and in line with devices reported in the literature. However, the charge transport shown in the i-FLG based device shows improved behavior when compared to the ITO based device, having greater shunt resistance and lower series resistance. These combine to give the effect of the i-FLG device having a much larger fill factor than the ITO device, despite having a lower efficiency over all. While the series resistance was only slightly lower for the i-FLG device, the shunt resistance was more than twice as much. As the shunt resistance represents the resistance to current flow in the direction opposite to the extraction of current, having a high shunt resistance is

a desired property in photovoltaics. The shunt resistance is largely thought to be dependent on the composition of the BHJ, with defects or a non-ideal mixing causing alternate conductive pathways through the solar cell, reducing the current produced. This parasitic resistance has a particularly high impact at low light levels, making a high shunt resistance particularly important for devices to be used in low light conditions, such as those used for the internet of things.

There was no hysteresis found between the forward and reverse sweeps of the IV curves collected under illumination (only forward sweeps are displayed), but a small current offset for the ITO device's dark curve was observed, indicating a small dark current contribution to be present in the device. Hysteresis is the offset between the current-voltage relation under forward and reverse bias [215]. This can be caused by a number of factors, including a high charge trap density in the organic polymers that make up the BHJ. This effect can be reduced by increasing the transient measurement time but as this effect is not observed in the light curves, the measurement time was held fixed.

As the work function of the ITO used was not experimentally determined, as was done for the i-FLG samples (value in 6.4a taken from literature [191]), I cannot explicitly state whether the poor fill factor of the ITO devices was due to a poorly aligned work function of the ITO or due to problems with the BHJ composition. In reference devices produced in literature, increased efficiencies are seen in devices that also employ a thin Calcium layer before evaporating the Aluminium contact to reduce the interfacial resistance between the electrode and ETL. This improves charge extraction to the electrode and increases efficiency [16]. However, as it was not feasible to evaporate Calcium in the thermal evaporator used, all devices were prepared without this step and efficiencies were reduced as a consequence. It is likely that this effect, combined with a non-ideal BHJ composition/microstructure are responsible for the reduced device efficiency seen in both ITO and i-FLG devices, compared to reference devices from the literature which range between 5–7 % for OPV devices made from the same materials [216, 157, 67, 159].

Another source of the discrepancy between the efficiency of devices produced in this report and those in the literature are the possible sources of degradation that could not be mitigated during fabrication. Although all devices were fabricated in a nitrogen filled glovebox, the content of the atmosphere inside the glovebox could not be controlled over the whole period of fabrication. This meant that the oxygen content of the glovebox would vary from below 50 ppm (the desired level for OPV fabrication) to as high as 500 ppm. This means that devices fabricated under these conditions are likely to have partially degraded before IV curves could be measured. Furthermore, while the thermal evaporation of Al contacts was performed in vacuum, the thermal evaporator was not in an atmospheric controlled environment, meaning careful transport of samples was required to not introduce further possible routes of degradation. Atmospheric induced degradation has been shown to have the ability to generate traps in the BHJ, leading to increased recombination rates and hence a lower J_{sc} value. Further degradation mechanisms include water ingress at the metal contacts [198] and oxdiation of the Aluminium electrode. As such, the stability of OPV devices produced in this investigation is of key interest to understanding how to improve future devices.

6.3.3 Stability testing of OPV devices with ITO and i-FLG electrodes

As is discussed at the beginning of this chapter, one of the key factors that contributes to the loss of device efficiency across many OPV devices is damage to the ITO electrode caused by its proximity to the PEDOT:PSS HTL. The acidic nature of the PSS groups corrodes the ITO and has been held as responsible for the migration of Indium ions from the electrode into the BHJ which leads to further degradation [217, 218]. Here, I will investigate the replacement of the ITO electrode with an i-FLG electrode, which may alleviate this potential degradation pathway. To achieve this, stability tests were performed on both ITO and i-FLG based OPV devices to assess 1: If the ITO electrode devices degraded as quickly as expected, 2:

if the i-FLG electrode devices showed greater stability, 3: what are the estimated lifetimes for the devices.

Two types of stability measurement were carried out, the first being periodic measurements of the device parameters by IV curve measurement under illumination and storing the devices in the dark under vacuum between measurements, the second being measurement of IV curves under continual illumination of the devices. The first method was carried out over a much longer period of time (over 250 hours) compared to the continual illumination, which was only carried out for 1 hour due to the rapid deterioration of the devices. It should be noted that while these measurements are invaluable for characterising the performance of OPV devices over time, they give little insight into the exact mechanisms by which the decay occurs. In many cases, there are multiple decay mechanisms working at one time, making them difficult to separate from one another without extensive testing (e.g. varying atmospheric conditions such as humidity, O_2 content, temperature, etc.).

The stability data in figure 6.7 shows that working devices prepared with i-FLG electrodes operated for more than twice as long as those prepared with ITO electrodes. After 120 hours all ITO devices had failed, while several of the i-FLG devices stayed functioning after 250 hours. A possible reason for this is that damage to the ITO caused by the acidic PEDOT:PSS caused the ITO devices to short [217, 180]. This process will take place regardless of the devices being shielded from atmospheric degradation by being placed in a desiccator in between measurements. i-FLG electrodes are not susceptible to this form of damage and, apart from one of the devices tested, show no degradation over the period of time they were tested for.

While i-FLG devices show a lower average device efficiency by approximately 0.8% at first, this improves over the next 150 hours to a comparable level as the ITO based devices. Over the same time period the ITO devices quickly fail after around 120 hours, indicating a rapid deterioration of performance and greater degree of instability than in i-FLG devices.

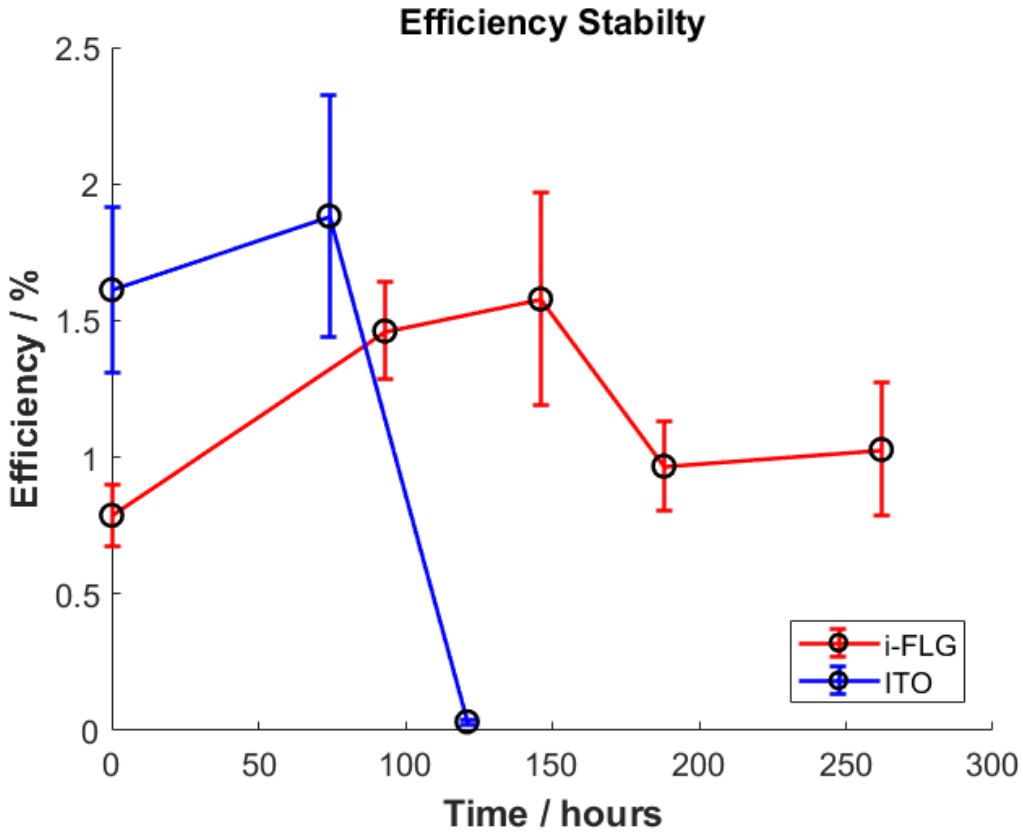

Figure 6.7: ITO and i-FLG device stability with periodic measurement of device parameters under illumination. Devices were prepared with each electrode, two of the ITO devices and one of the i-FLG devices were not functioning and so were not included in calculation of the mean or standard error.

One trend shown in both sets of data was that the efficiency of devices improved after the first measurement. All ITO devices had failed by the third measurement, but i-FLG devices showed consistent improvement up to 150 hours. The solar simulator was calibrated before each set of measurements to ensure the correct level of illumination was being used, so variation in light intensity is not the cause of this rise in efficiency. It can also be seen from figure 6.8a, that the J_{sc} values remained relatively consistent for each device across the set of measurements. This would be expected to increase if the light intensity increased, confirming this is not the origin of the increased efficiency. In the functioning devices produced with both ITO and i-FLG electrodes, a small increase in V_{oc} can be seen (figure 6.8b), as well as a substantial increase in shunt resistance (figure 6.8c) for i-FLG devices. Shunt resistance

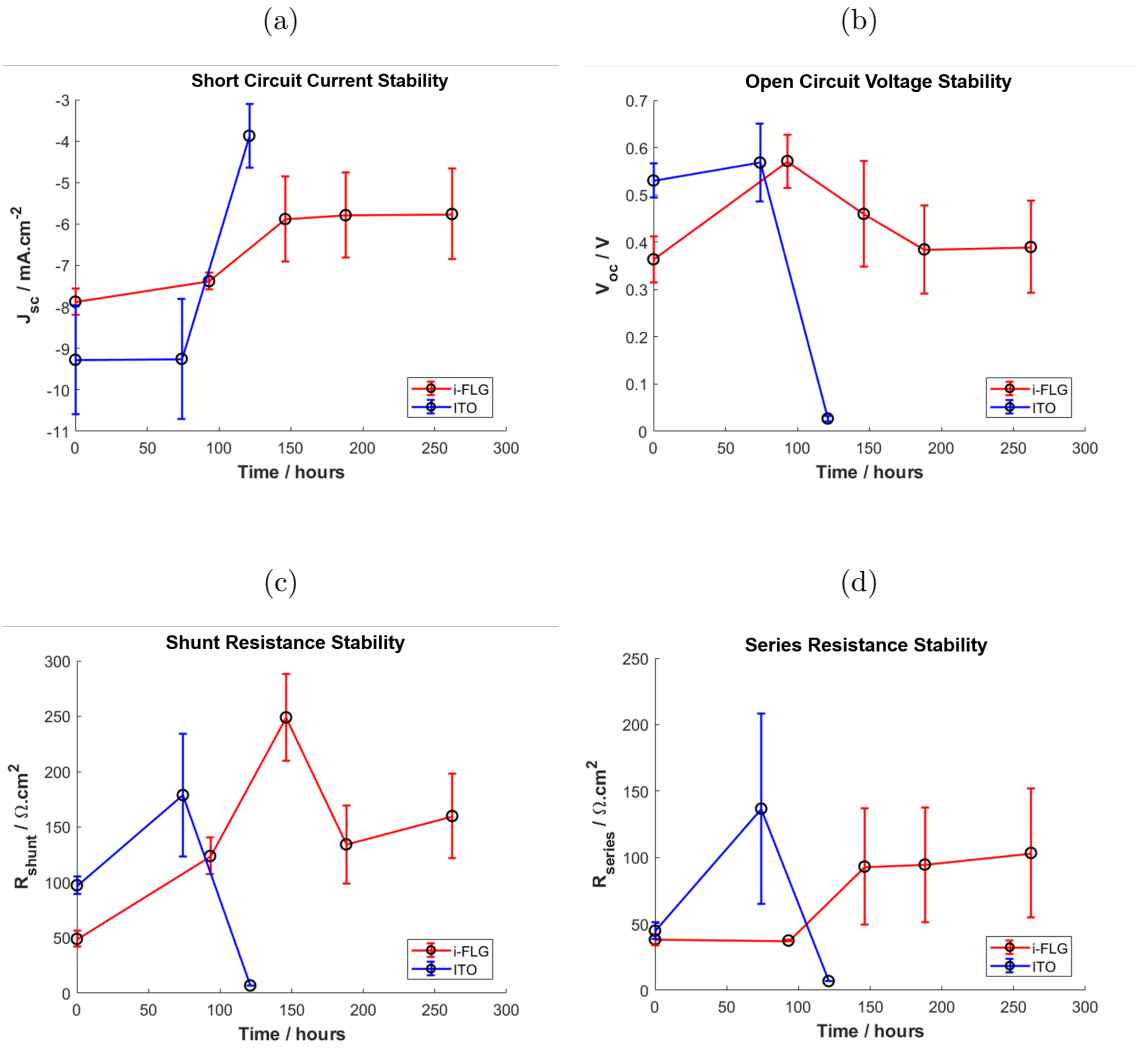

Figure 6.8: Electrical characterisation of ITO and i-FLG device periodic stability, showing the change in (6.8a) short circuit current, (6.8b) open circuit voltage, (6.8c) shunt resistance and (6.8d) series resistance. Understanding how these parameters vary with time gives indications as to the cause of device degradation.

acts against the flow of current into the device from the electrodes, and hence higher shunt resistance prevents this leakage current and mitigates power losses [219]. As this leakage current opposes the flow of the photogenerated current, it is desirable for solar cells to possess a high shunt resistance. This is largely determined by the nanoscale composition of the BHJ, and so an increase in shunt resistance could be caused by a rearrangement of the polymer/fullerene within the BHJ, either by remnant solvent within the device allowing their movement, or by the generation of ions

and impurities due to light exposure causing a rearrangement of polymer/fullerene.

The origin of the increase in V_{oc} is much less clear, as there are many factors that impact the open circuit voltage [215]. While the V_{oc} is largely determined by the HOMO and LUMO levels of the donor and acceptor, the work function of the electrodes can also have an impact, particularly where non-Ohmic contacts are formed at the electrode-transport layer interface. It is possible that processes such as the oxidation of the metal electrode could also have an impact, however this would be expected to lower the open circuit voltage, not improve it. Finally, by observing the series resistance of the devices we can observe changes to the resistance of the device electrodes, this data is shown in figure 6.8d. While series resistance for ITO devices varies significantly before dropping to zero for all devices due to short circuiting, the i-FLG devices show remarkable consistency for all devices apart from one that shorted soon into testing. This indicates that little to no damage is done to the i-FLG electrodes by the acidic PEDOT:PSS layer, demonstrating that i-FLG electrodes may be a potential route to OPV devices with greater long term stability than those with ITO electrodes.

Continuous stability testing

To calculate the device's functional lifetime, another measurement must be carried out to acquire the decay curve of the solar cells. This requires measurement to be made under continuous illumination, with the efficiency at $t = 0$ (E_0) being recorded. Once the decay curve is acquired, the time taken to decay to 80% (t_{80}) of the original efficiency (E_{80}) can be calculated using the equation:

$$E(t) = E_0 e^{-\lambda t} \tag{6.1}$$

where $E(t)$ is the time dependent efficiency, E_0 is the efficiency at $t = 0$ and λ is the exponential decay constant. This is a standard exponential decay equation, commonly used to model the decay of organic solar cells [10, 220, 221, 222]. Some time after E_{80} is measured, the efficiency is measured again and denoted E_{s0}, for the second E_0. A second measurement of t_{s80} and E_{s80} are then made. This char-

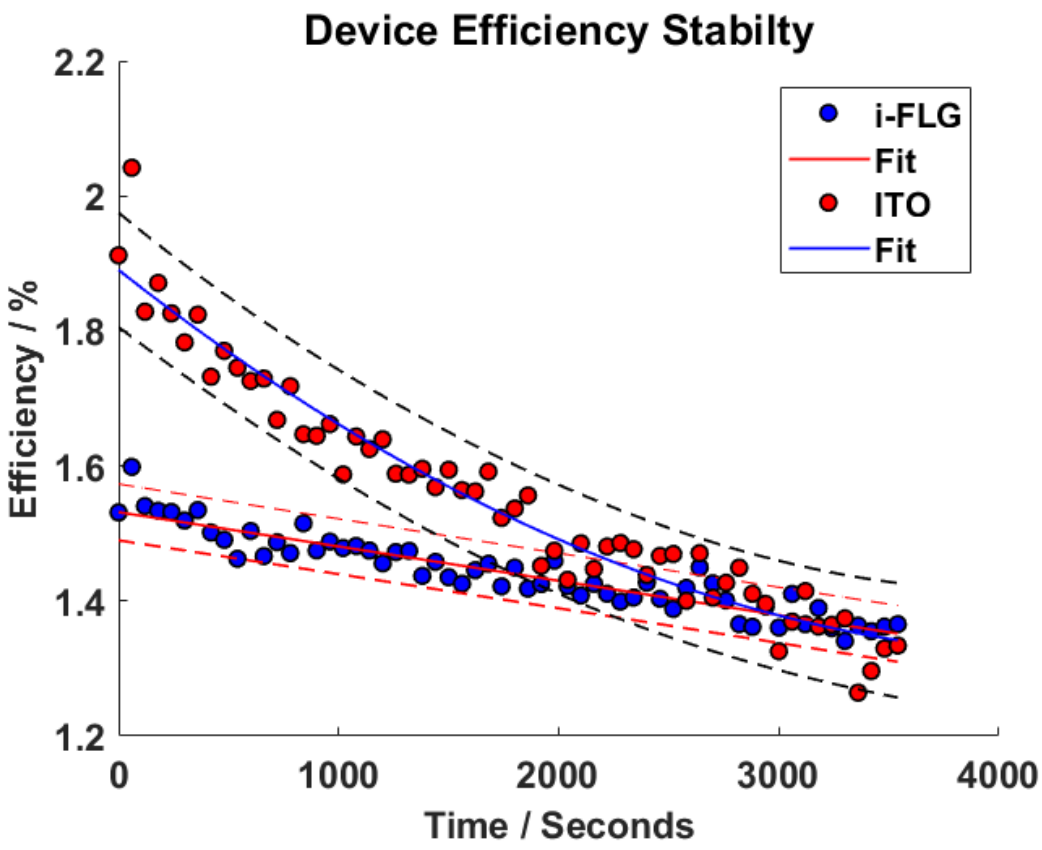

Figure 6.9: Performance decay curves for ITO and i-FLG based devices, showing the decrease in efficiency under continuous illumination over a period of 1 hour. Fitted curves are given confidence bounds (black for ITO, red for i-FLG) representing a 95% confidence of the data being within those bounds, calculated by standard error.

acterizes the decay in device performance across the two common phases in device degradation, the burn in phase and the long term degradation phase [199, 223]. The burn in phase is characterized by a rapid deterioration of device performance immediately after fabrication, this is normally responsible for the first drop of 20% in efficiency. After this phase, the rate of device degradation slows to a lower rate which persists until the device fails. This can usually be characterized by the measurement of t_{s80}. However, due to the rapid deterioration of devices, only the first t_{80} measurement was taken for both devices.

Figure 6.9 shows the efficiency decay behaviour of both ITO and i-FLG devices over the first hour of operation. The i-FLG devices all showed a linear decrease in efficiency over this period of time, while the ITO based devices are better represented

by a quadratic or exponential decrease. Similarly to the periodically measured stability data, the ITO based device begins with a greater efficiency than the i-FLG device, before deteriorating at an accelerated rate. Four i-FLG devices were measured in this way, with all devices behaving in a similar manner as shown in figure 6.10a–6.10d. t_{80} times were calculated and summarized in table 4. Similarly, two ITO devices were characterized in this manner, with efficiency data plotted in figures 6.11a–6.11d and decay parameters summarized in table 5, giving a mean decay time for ITO based devices of between 2000–2500 s, or approximately 30–40 minutes. i-FLG devices showed a greater degree of variability, with two devices possessing t_{80} times of approximately 6000 s (100 minutes), and two approximately 10,000 s (165 minutes). This demonstrates that i-FLG devices are functional for approximately 3-5 times longer than ITO based devices.

While all i-FLG devices showed a linear decrease in efficiency, it is noted that the devices performing at a higher efficiency at $t = 0$ decayed much faster than those with a slightly lower starting efficiency. This is shown by Devices 1 and 2's t_{80} times being almost half that of devices 3 and 4's, as well as the steeper gradient of the fitted data in figures 6.10a and 6.10b. The linear decay in efficiency indicates that these devices instead follow a zeroth order decay equation, meaning the rate of decay is proportional to a constant, but this constant is different for devices with different efficiencies. Such a decay equation is shown here:

$$E(t) = E(0)\lambda t \tag{6.2}$$

while it is possible the duration of the measurement was too short to display an exponential decay, more experiments would need to be taken to confirm this. This data alone suggests that all i-FLG devices are likely to follow this decay pattern.

Table 5: Stability metrics: ITO Devices

Device	E_0 / %	E_{80} / %	t_{80} / s	λ / $\%^{-1}s^{-1}$
1	1.9	1.5	2600	-6.3x10^{-5}
2	1.9	1.5	2100	-5.9x10^{-5}

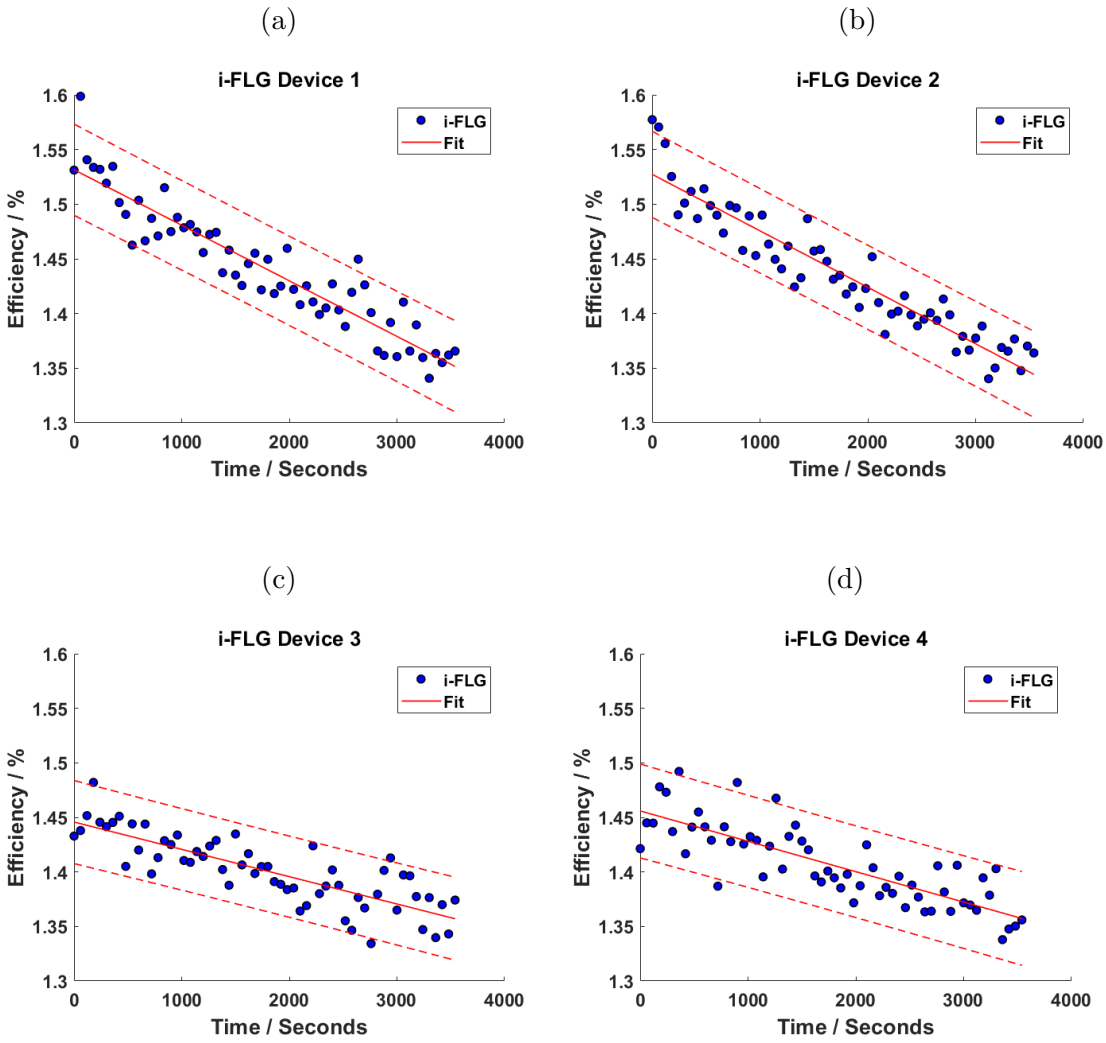

Figure 6.10: Continuous illumination stability data for all i-FLG devices tested. All devices showed a linear decrease in efficiency with consistent efficiency values, displayed in Table 4.

Table 4: Stability metrics: i-FLG Devices

Device	E_0 / %	E_{80} / %	t_{80} / s	λ / s^{-1}
1	1.5	1.2	6000	-5.1x10^{-5}
2	1.5	1.2	5900	-5.2x10^{-5}
3	1.5	1.2	11500	-2.5x10^{-5}
4	1.5	1.2	10500	-2.8x10^{-5}

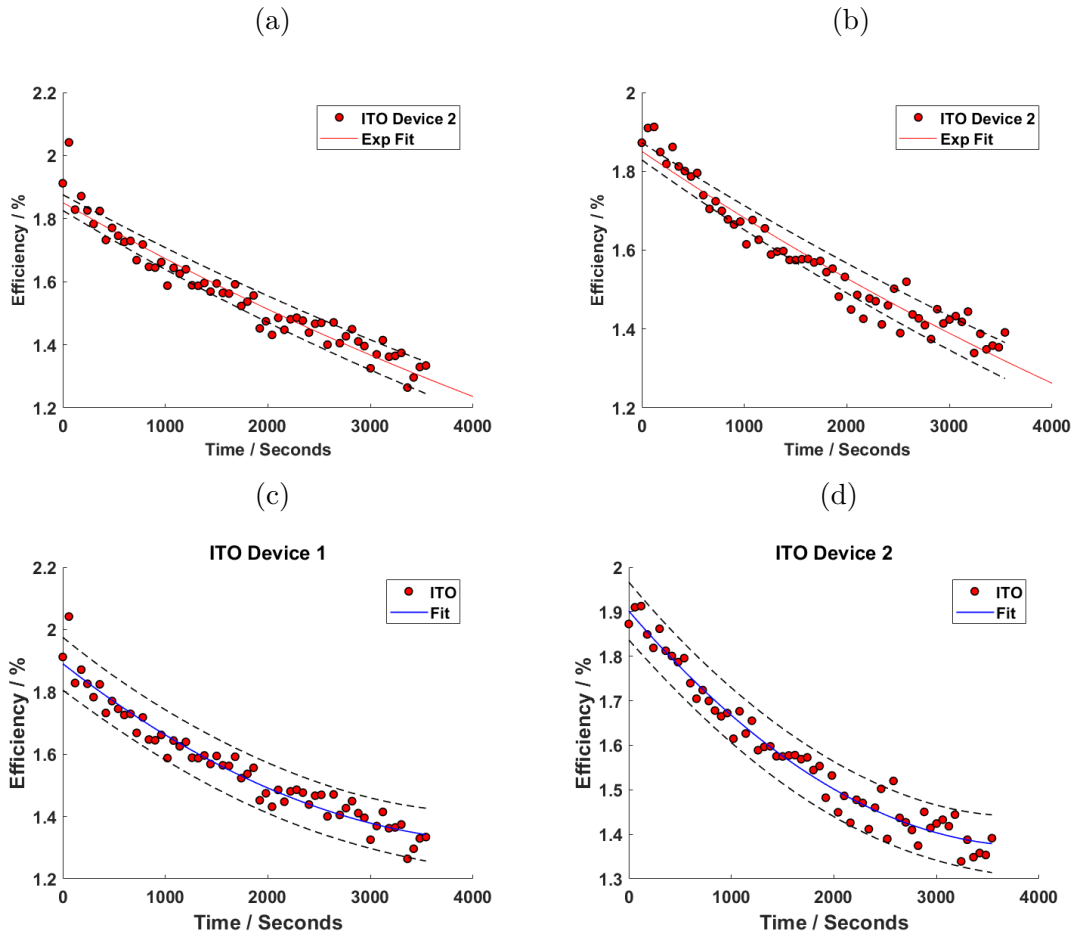

Figure 6.11: Continuous illumination stability data for the two ITO devices tested, fitted with (a and b) exponential and (c and d) quadratic decays. Decay metrics and constants are shown in Table 5, calculated from the quadratic fits to the decay data.

The decay behaviour of ITO devices 1 and 2 were fitted with the expected exponential decay equation, but showed a poor fit (figures 6.11a and 6.11b) indicating the decay behaviour could not be described by a first order decay equation. Instead, this decay behaviour was successfully fitted with quadratic decay curves, indicating this decay behaviour followed a second order decay equation of the form:

$$\frac{1}{E_{(t)}} = -\lambda t + \frac{1}{E_0} \tag{6.3}$$

By plotting $1/E_{(t)}$ against the exposure time, a linear fit can be made for both sets of ITO decay data, plotted in figure 6.12. This shows the data to fit a second order decay law, but that the data begins to deviate from the fit after approximately

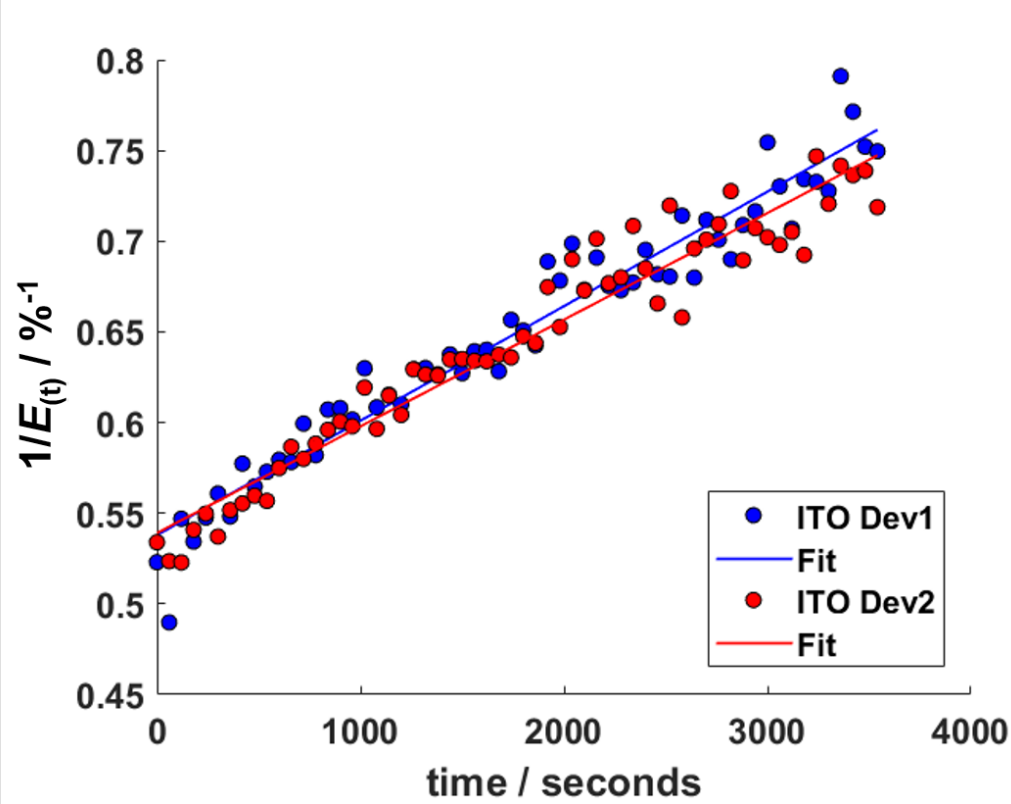

Figure 6.12: Linear plot of $1/E_{(t)}$ against time, showing a linear trend. This indicates the ITO based OPV devices follow a second order decay law, with the gradient of the graph giving the decay constant, λ, and the intercept being equal to $1/E_0$. Error in the decay constant was calculated from the standard error of the fit with the data.

3000 seconds. Using this second order decay equation, the decay constants and t_{80} times for ITO devices can be extracted, giving a decay time for ITO based devices of between 2100–2600 s, or approximately 30–40 minutes.

The data shown in Figure 6.12 do not fit a linear trend exactly, with an error of 2.0×10^{-6} and 1.9×10^{-6} $\%^{-1}s^{-1}$ in the decay constants of devices 1 and 2 respectively, approximately 3% of the total decay rate. Error values were calculated from the standard deviation of the data from the fit. However, this is accounted for by the uncertainty in the efficiency data, as a greater degree of variation can be seen in the ITO efficiency data compared to the i-FLG data (shown in Figure 6.9). It is less clear why ITO based devices follow a second order decay in efficiency, as there are many factors that impact the rate of decay in efficiency of organic solar cells. Di-

rectly comparing the electrical metrics that impact device efficiency reinforce these findings, but also give possible indications for causes of device degradation.

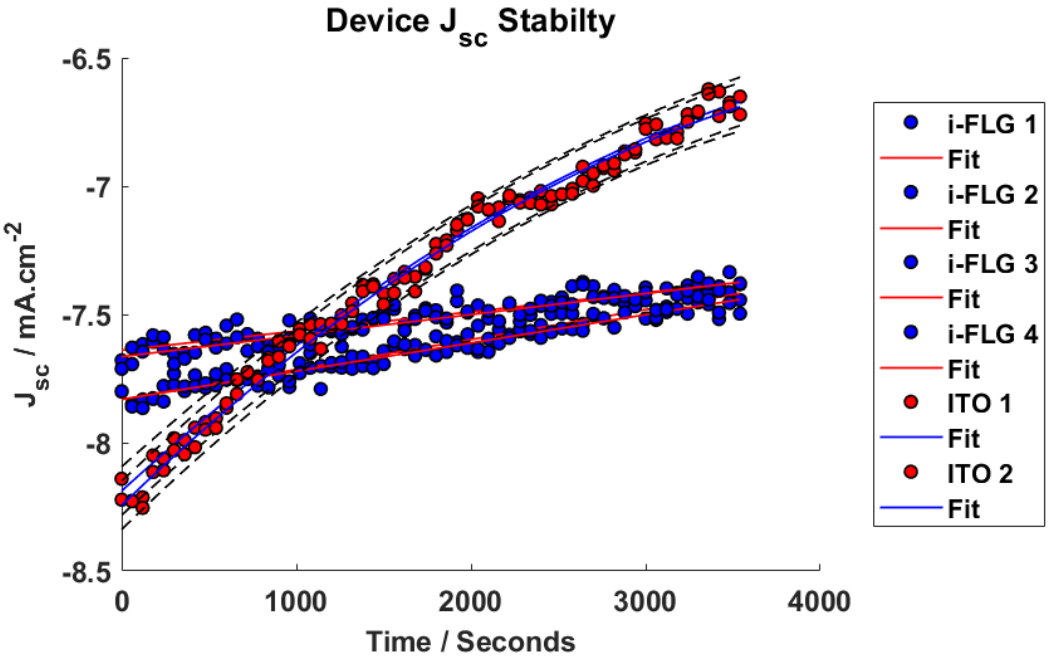

Figure 6.13: Variation of J_{sc} with time under continuous illumination for all i-FLG and ITO devices tested. Error bounds are shown for the ITO devices but not the i-FLG devices for clarity.

Figure 6.13 shows the rapid deterioration of the J_{sc} values for ITO based devices compared to i-FLG devices, with good agreement in J_{sc} values for the sets of 4 i-FLG devices and 2 ITO devices respectively. The rapid decrease in the magnitude of J_{sc} is likely to be one of the main factors causing the higher order decay seen in the ITO based devices.

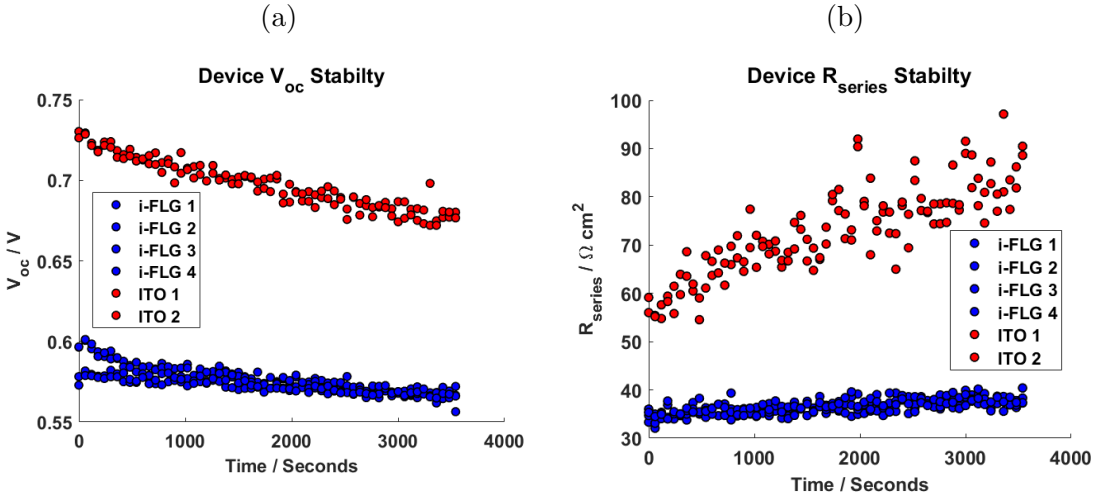

Figure 6.14: Data for all ITO and i-FLG devices showing variation of ***a.*** V_{oc} and ***b.*** series resistance with time. Both ITO and i-FLG devices saw a minor decrease in V_{oc} over the duration of the measurement. ITO device series resistance increased to a much greater degree than was seen in i-FLG devices, indicating damage to the ITO electrode may be the cause of the increased rate of decay in ITO devices.

Figures 6.14a and 6.14b show the continuous illumination stability data for both V_{oc} and R_{series} data. Both ITO and i-FLG devices show a linear decrease in V_{oc} over time, with comparable decay rates between all devices, despite ITO devices possessing a much higher V_{oc} compared to i-FLG devices. However, the variation in series resistance between ITO and i-FLG is in stark contrast. i-FLG devices show a very consistent series resistance, slowly increasing from around 35 – 40 Ωcm^2 for all devices studied. However, ITO devices showed a much greater increase and a greater degree of variability in the series resistance. This is likely to be the source of the greater uncertainty in ITO device efficiency compared to i-FLG devices. In addition, because the series resistance is primarily dependent on the resistance of the

electrodes, this could indicate that progressive damage to the ITO electrode under operation. This is likely caused by the acidic PEDOT:PSS increasing the series resistance of the ITO electrode and accelerating the rate of device degradation in ITO based devices.

No guarantee can be made that both devices were tested at the same point in their decay. As the same materials were used for both types of device, it is likely that the burn in phase would last the same time for ITO and i-FLG devices, but this is not a certainty. It is possible that the rapid decay seen for ITO devices simply indicates they are still in the burn in phase of degradation, while i-FLG devices were measured during their long term stability phase. Without further measurements on both types of device it is difficult to determine at which point each device is in the decay process.

In summary, these results show that i-FLG based OPV devices possess superior stability both under continual operation and after periodic measurement, compared to ITO based devices. This is primarily due to the degradation in ITO electrodes, thought to be caused by their proximity to the highly acidic PEDOT:PSS. i-FLG electrodes are not damaged by the same acidic conditions, as shown by the stability in their series resistance values, and by previous investigations into cleaning contaminants from the i-FLG electrodes using much stronger acids. This indicates i-FLG electrodes are well suited for use in OPV devices, possibly improving their long term stability. A full study into the stability of ITO and i-FLG devices that have been encapsulated in glass by epoxy would have been undertaken, had time permitted the devices to be made and tested. This would give better insight into how devices would perform under standard operating conditions for organic solar cells, and would allow a better comparison between i-FLG and ITO electrodes.

6.3.4 OPV device success rates

When discussing the lifetime of devices, it is important to also note the device fabrication success rates of the different varieties of devices examined. Here I will

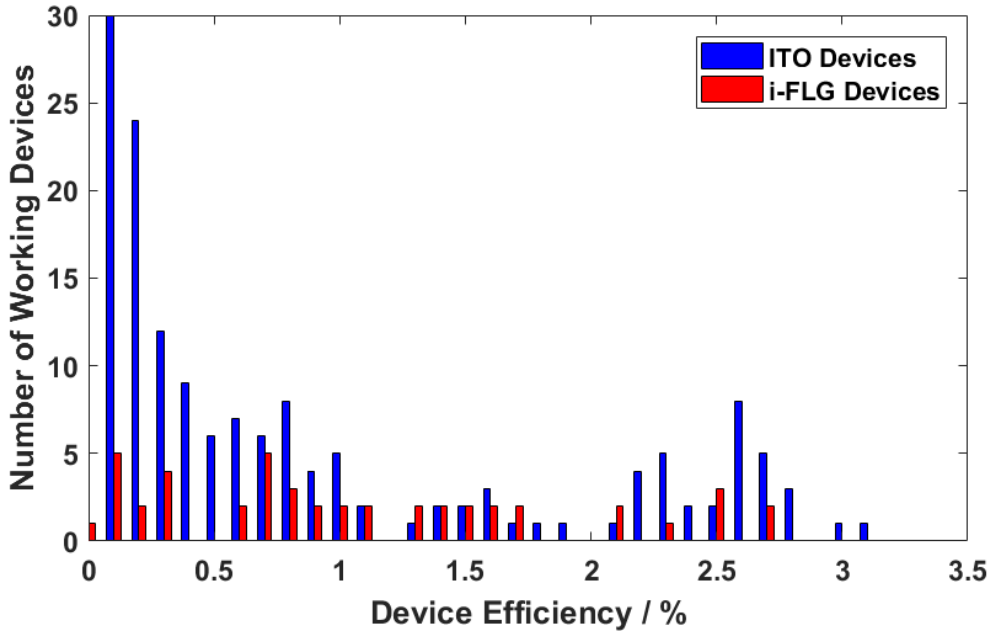

Figure 6.15: Device efficiencies for OPV devices with greater than 0.1% efficiency for ITO and i-FLG electrodes.

discuss the success and failure rates of OPV devices fabricated on i-FLG and ITO on glass (flexible devices fabricated on PET will not be included). Here I will be describing a working device as any device with a measured efficiency of 0.1% or greater.

Figure 6.15 shows the number of working devices produced and the efficiencies they achieved for both ITO and i-FLG based devices. A total of 446 ITO devices and 146 i-FLG devices were tested (between 6–8 devices were made per sample of ITO/i-FLG) producing a total of 156 working ITO devices and 46 working i-FLG devices. This gives the success rates of each type of device to be 35% for ITO devices and 32% for i-FLG devices. While these success rates are rather low, device failures are more heavily weighted towards the beginning the investigation, as it required numerous attempts before working devices were produced. Once successful devices was fabricated, subsequent batches had better success rates. Indicating early device failures are due to poorly optimized fabrication procedures. Given the greater surface roughness of i-FLG electrodes compared to ITO, it is surprising that both types of device had such similar success rates. This could potentially indicate that

short circuited devices were not being caused by the roughness of the electrode but rather a source common to both types of device (such as particulates in the BHJ or PEDOT:PSS layers).

As can be seen from Figure 6.15, i-FLG devices show a fairly even spread across a range of efficiencies, from 0.1–2.8%. ITO based devices have a heavier weighting towards lower efficiencies, as well as a slight increase in the device efficiency distribution between 2–3%. As the device success rates improved as the investigation progressed, it is likely that continuing to fabricate more devices would reveal a more representative device efficiency distribution. This would allow a better comparison to be made between the two types of electrode and their impact on the overall device performance.

6.3.5 Applications of i-FLG electrodes in OPV devices

As has been demonstrated in this chapter, i-FLG electrodes can produce OPV devices with comparable efficiencies to those fabricated from commercially available ITO electrodes. This is rather impressive as the measured sheet resistances for i-FLG electrodes are still greater than those of the ITO electrodes, with the transmittance through i-FLG electrodes also being lower than for ITO. However, the improved work function of i-FLG caused by the strong doping through intercalation leads to improved charge extraction efficiency of the i-FLG electrode.

I have also demonstrated the scalability of the i-FLG manufacturing process in chapter 3, indicating the potential to increase device areas. This would increase the device power output and allow for the powering of small scale sensors, such as those used in IoT applications. Furthermore, development of the fabrication process may allow for i-FLG OPV devices to be fabricated on flexible substrates. Not only would this allow OPV devices to be used in a wider variety of environments and for a broader range of purposes, but it would also potentially improve device lifetimes compared to ITO based devices, as the data I have provided shows i-FLG electrodes to not suffer from the same PEDOT:PSS induced degradation as ITO devices.

Photovoltaic devices produce a great deal of energy compared to other passive energy harvesting strategies, more than triboelectric, thermoelectric and pietzoelectric energy harvesting devices [224]. However, for practical uses, OPV devices still produce limited energy due to their modest efficiencies and low light absorption compared to silicon photovoltaics. But it is these properties that make i-FLG flexible OPV devices perfectly suited for energy harvesting for internet of things (IoT) applications. Here, the OPV devices can be used to power sensor networks that monitor parameters of interest (dependent on the application) and record data that can be used to run a system more efficiently. One such example of this would be using semi-transparent i-FLG OPV devices to line the windows and walls of buildings, and using the energy they harvest to run a network of smoke detectors throughout the building, thereby removing the need for battery operated smoke detectors and hence the need to change batteries. As the IoT gains in popularity for the added efficiency with which it can be used to operate systems, the need for such energy harvesting devices will increase and bridge into wearable electronics for health monitoring, various commercial sensor networks, and even devices to be used around the home such as smart fridges. Such devices will employ energy harvesting in low light environments, where the aforementioned improved shunt resistance of i-FLG OPV devices will allow them to perform better than their ITO counterparts.

6.3.6 Future Work

A number of other additional experiments and investigations were planned to be carried out. However, due to a combination of a lack of materials during the fabrication process and a complete halt to all laboratory work during the COVID-19 epidemic meant that these could not be completed. This work included:

- **Characterisation of pristine FLG electrode based OPV devices.** Multiple devices of this type were attempted but none functioned as working OPV devices. This would allow a direct comparison to be made between pristine graphene and i-FLG OPV devices, and the improvements that result from using i-FLG electrodes to be shown.

- **Characterisation of inverted OPV devices for both ITO and i-FLG electrodes.** A small trial set of inverted devices on ITO were attempted but again, no working devices were produced. Inverted devices are observed to have improved stability, due in part to the PEDOT:PSS layer no longer being in contact with the ITO electrode. Fabrication and characterization of inverted OPV devices would provide further evidence of ITO being the cause of device degradation in this study.

- **Extended stability study (24 hours).** Increasing the duration of the study such that it extends beyond the burn in phase for both encapsulated and unencapsulated ITO and i-FLG OPV devices would allow for a much better assessment of device lifetimes for the different electrodes used. This would allow full determination of the burn in phase period and more accurate measurement of t_{80} times.

- **Large area device study.** Fabrication of a large area (7x7 cm) i-FLG OPV device and demonstration of it powering a small sensor device (e.g humidity sensor). This will demonstrate the functionality of i-FLG OPV devices for IoT applications.

- **Light dependence characterisation.** By varying the height of the solar simulator, the intensity of the incident light can be varied giving information on the performance of the devices at different light levels. This is of particular interest for the i-FLG devices as many IoT applications require operation under low light levels. This measurement is also a useful method of showing the presence of trap assisted recombination in OPV devices [141].

- **Flexible OPV device fabrication with i-FLG electrodes.** By fabricating OPV devices on flexible substrates it would highlight the superior flexibility of graphene materials compared to ITO. Previous flexible devices fabricated with i-FLG [64] showed no deterioration of performance after extended bending cycles. Similar tests could be performed with flexible i-FLG based OPV devices and compared to either ITO electrodes on flexible substrates, or an alternative flexible electrode such as PEDOT:PSS.

These additional experiments would add to the full characterisation of i-FLG as a flexible, transparent electrode for OPV applications and demonstrate the its use in a working device.

6.4 Conclusions

In this chapter I have demonstrated working OPV devices based on i-FLG electrodes with device efficiencies comparable to that of ITO based devices made from the same batch of OPV materials. The best performing ITO and i-FLG devices had efficiencies of 3.2 and 2.8% respectively. Fabrication and characterisation of devices was clearly described and the parameters used to compare devices (J_{sc}, V_{oc}, etc.) were defined. While ITO devices showed slightly higher efficiencies, i-FLG devices had a greater FF, indicating more efficient charge extraction was taking place. i-FLG devices also showed much greater stability when compared to ITO based devices, for both periodic and continuous illumination. While all mechanisms of degradation present were not identified, it is likely that this improvement to stability is caused by the removal of the ITO electrode. PEDOT:PSS has been shown to cause damage to ITO over time, while graphene has an inert surface, giving it improved stability to acidic conditions. Continuous illumination data was analysed and fitted in order to extract the time taken to drop to 80% of the initial device efficiency (t_{80}). For all devices tested, i-FLG devices lasted longer under operation than ITO devices, with t_{80} times between 3 and 5 times larger than those of ITO based devices. Improved device stability is a key step towards the fabrication of low cost OPV devices with low EPBTs. Future work should focus on investigating the flexible properties of i-FLG OPV devices, for use in wearable electronics and IoT applications.

Chapter 7

Triboelectric Energy Harvesting Devices from $FeCl_3$ Intercalated Graphene Electrodes

In this chapter, I will examine the use of i-FLG in triboelectric energy harvesting devices when combined with a range of materials (Nylon, Nitrile rubber, PDMS and PTFE). Triboelectric Nanogenerator (TENG) devices were fabricated with both pristine graphene and i-FLG electrodes. The performance of these devices are characterized against a range of dielectric materials in order to determine the position of i-FLG in the triboelectric series, using the known position of graphene established by previous works on this topic [82]. The performance of the two varieties of device are then compared for both short circuit current and open circuit voltage measurements. Applications of i-FLG TENG devices are then briefly discussed, considering both the performance of i-FLG TENG devices and the specific material properties of i-FLG.

7.1 Introduction

The drive to produce renewable energies on a scale large enough to offset the carbon footprint of the fossil fuels industry has seen incredible achievements in recent years.

Large scale investment in solar, wind and wave energy around the world has seen some of the largest renewable energy projects ever undertaken, which promise to contribute a significant energy output. However, one of the most promising avenues of research for renewable energy harvesting comes on a much smaller scale; the powering of the IoT, including wearable electronics [147, 225].

Wearable electronics have not seen the technological boom that they were originally thought to have when flexible electronic devices were first being investigated. This is due to the lack of flexible energy storage devices to power the electronics, leaving conventional battery packs to supply the required power to the device [146]. While this allows devices to function, it removes the purpose of the flexible electronics in the first place, as the user must still carry around a rigid power supply. This is particularly problematic for medial monitoring devices, as user comfort is often paramount to device function. Using energy harvesting to supply the wearable electronics with a source of power instead presents many potential benefits, such as removing the need to replacement battery packs and the associated reduced cost.

As discussed in chapters 1 and 2, Triboelectric Nanogenerators (TENG) harvest energy from the mechanical motion of two materials being brought into contact, triggering the contact electrification where charge transfer occurs between the materials [226]. TENG have the potential to transform the manner in which wearable technologies are powered due to their performance in terms of power output, low weight and scalability of material and device manufacturing processes. As such, this chapter will focus on the fabrication and characterization of TENG devices fabricated from pristine graphene and i-FLG large area samples for the purposes of assessing the utility of these materials for use in triboelectric energy harvesting for IoT applications.

7.2 Methods

Outlined here are the methods used in the fabrication and characterisation of TENG devices. First, the fabrication and transfer of the graphene/i-FLG electrode is discussed, followed by the preparation of the dielectric materials used in combination with the graphene/i-FLG. Finally, the characterization of pristine graphene and i-FLG as both a triboelectric material and an electrode in TENG devices is discussed. This includes details of the experimental setup designed to carry out the measurements, as well as the methods used to analyse the results.

7.2.1 Fabrication

TENG devices were prepared using two different varieties of graphene, pristine FLG and i-FLG. Ni-CVD graphene was purchased from graphene supermarket as wafer scale samples, before being coated with PMMA (150 nm) and cut to desired sizes using a diamond tipped scriber. For the preparation of i-FLG devices, the samples were then transferred to glass slides using the large area graphene transfer technique developed in house and described in chapter 4. Once transferred, the graphene samples were intercalated following the process for large area intercalation (Chapter 4), and characterised by Raman spectroscopy to map the shift in G-peak of the sample by use of the $\langle \text{PosG} \rangle$ metric. Samples were then transferred to PET substrates using thermal release tape, as described in the section 3.6.2 of the Methods chapter. Once transferred to PET, the i-FLG samples were connected to copper wire by applying a small amount of conductive silver paste to the edge of the sample and placing a copper wire in the silver paste. The sample is then heated at 60°C for 10 minutes to dry the silver paste before covering the area with conductive copper tape to prevent cracks and damage to the contact. Pristine graphene TENG devices followed a similar fabrication procedure, with the graphene being transferred directly to PET substrate without the need to first transfer to a glass substrate. As such, the pristine graphene samples are subject to less damage during the fabrication process than the i-FLG samples. i-FLG TENG devices were measured to be 15 mm $\times$ 25 mm in size,

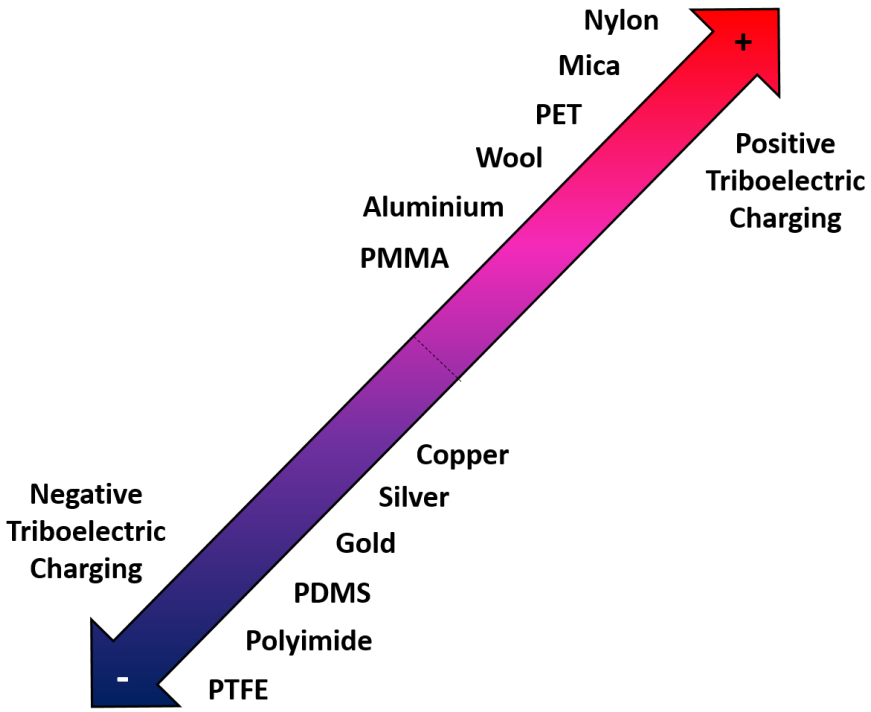

Figure 7.1: The triboelectric series for commonly investigated materials used in TENG devices. Materials towards the top of the series (positive side) will donate electrons when in contact with more negative materials, while materials towards the bottom of the series (negative side) will accept electrons from the more positive materials. The exact positions of materials in this series are difficult to quantify as there are many factors that impact a material's position, as will be explored in Appendix 1: Factors Impacting the Triboelectric Effect.

not including the area covered by the connecting wire. Pristine graphene samples were slightly too small to fit this area, each being approximately 80–90% the total area of the i-FLG samples. The impact of this difference in device area is discussed later in the chapter.

Once the TENG electrode was prepared, a range of dielectric materials were selected to contact the graphene/i-FLG material with. These materials effectively span much of the range of the triboelectric series (shown in figure 7.1), with Nylon being very positive in the triboelectric series and PTFE being very negative. This should allow the characterization of i-FLG's position in the triboelectric series relative to that of pristine graphene. The materials chosen were a thick Nylon weave,

Nitrile rubber from gloves, as prepared PDMS and PTFE from PTFE tape. Nylon, Nitrile rubber, and PTFE samples were cut to shape from much larger areas of their respective materials and were taped to the characterization mount by a conductive copper tape electrode. PDMS was prepared from the base elastomer and curing agent by mixing the two in a 10:1 ratio and stirring for 2 minutes. The polymer mixture is then placed in a desiccator for 20 minutes to remove any air bubbles. A copper tape electrode is then cut to size before being cleaned with IPA to remove the adhesive, this improves PDMS spreading in the next stage. The PDMS mixture is then spincoated on the copper electrode at 1000 rpm for 1 minute, for an approximate thickness of 25 μm. The PDMS film was then cured for 48 hours at 50°C.

7.2.2 Triboelectric device characterization

The characterization setup designed by Dr. Zakria Saadi and described in section 5.2 of Chapter 3 [73, 227], was used to characterize both pristine graphene and i-FLG TENG devices against a range of materials (Nylon, Nitrile rubber, PDMS and PTFE). Initially, both the pristine/i-FLG sample and material being tested are fixed to the sample mounts (graphene based samples by kapton tape and the test materials by conductive copper tape). The mount securing the graphene/i-FLG sample is connected to an electromagnetic actuator, which controls the cycling motion of the setup. The mount securing the dielectric material is connected to a load cell, allowing the force exerted during the contact of the two materials to be monitored. Prior to measurement, the two materials are brought into contact and a set-point overstep is set. This is a small distance (typically set to 21 μm unless otherwise specified) beyond the point of contact of the two materials, that the setup returns to after each cycle. This ensures good contact between the two materials being tested, especially for compressible materials such as the Nylon weave used in this investigation. This stage is also used to ensure that the two sample mounts are aligned properly such that there is planar contact between the two samples to

maximise the electrical response.

A contact cycle is then set to run for 300 cycles at a frequency of 3 Hz. This allows the ground point to settle as it is prone to drift at the beginning of measurements. For most materials tested, this was sufficient. However, certain measurements were still subject to a drift in voltage due to the ground point not being fixed. However, there are many other factors contributing to this effect, as will be discussed later. Measurement cycles for samples that exhibit a voltage drift are then run at a frequency of 1 Hz, running for 30 seconds. Voltage measurements are repeated until 3 satisfactory measurement cycles are recorded without significant voltage drift. As current measurements are unaffected by the voltage drift, the first 3 current measurement cycles were used. In total, 3 i-FLG TENGs and 2 pristine graphene TENGs were each tested against the 4 dielectric materials being tested, with multiple readings being taken for each sample. The best performances for current and voltage are displayed in the results section, with the mean device response against each dielectric being compared at the end of the results section.

7.3 Results

7.3.1 i-FLG as a Material for Triboelectric Power Generation

The low sheet resistance and high level of doping present in i-FLG samples make it an appealing material to study the triboelectric properties of. As a number of studies have already been conducted on the triboelectric properties of graphene, and its applications as an electrode, this study will examine the role of i-FLG and pristine graphene as both the electrode and one of the component triboelectric layers. The doping produced by intercalation is thought to alter the position of i-FLG in the triboelectric series. In addition, the drop in sheet resistance observed in i-FLG samples makes it a much better conductor than pristine graphene, which should lead to an increased triboelectric response. With these predictions in mind, i-FLG samples were characterized as a material for TENG devices by being repeatedly contacted against a range of known triboelectric materials (Nylon, Nitrile rubber, PDMS and PTFE) to allow the position of i-FLG in the triboelectric series to be determined.

To check that the electrical response produced by the TENG devices behaved as was expected, a number of tests were first performed. This involved measuring the TENG devices in both single and double electrode configurations (the schematics for both of which are shown in figure 7.2) and at different contact frequencies. Switching between single and double electrode configurations is expected to produce a doubling of both current and voltage, as both halves of the circuit are being measured. As is shown in figure 7.2, both the current and voltage responses increase under double electrode configuration, with the voltage response doubling and the current increasing by approximately a factor of 4, from 15 nA to 90 nA. This is a greater increase than was expected, and may be accounted for by poor planar contact between the two halves of the TENG device in single electrode configuration. In addition, it can be seen that the background noise and the consistency of the

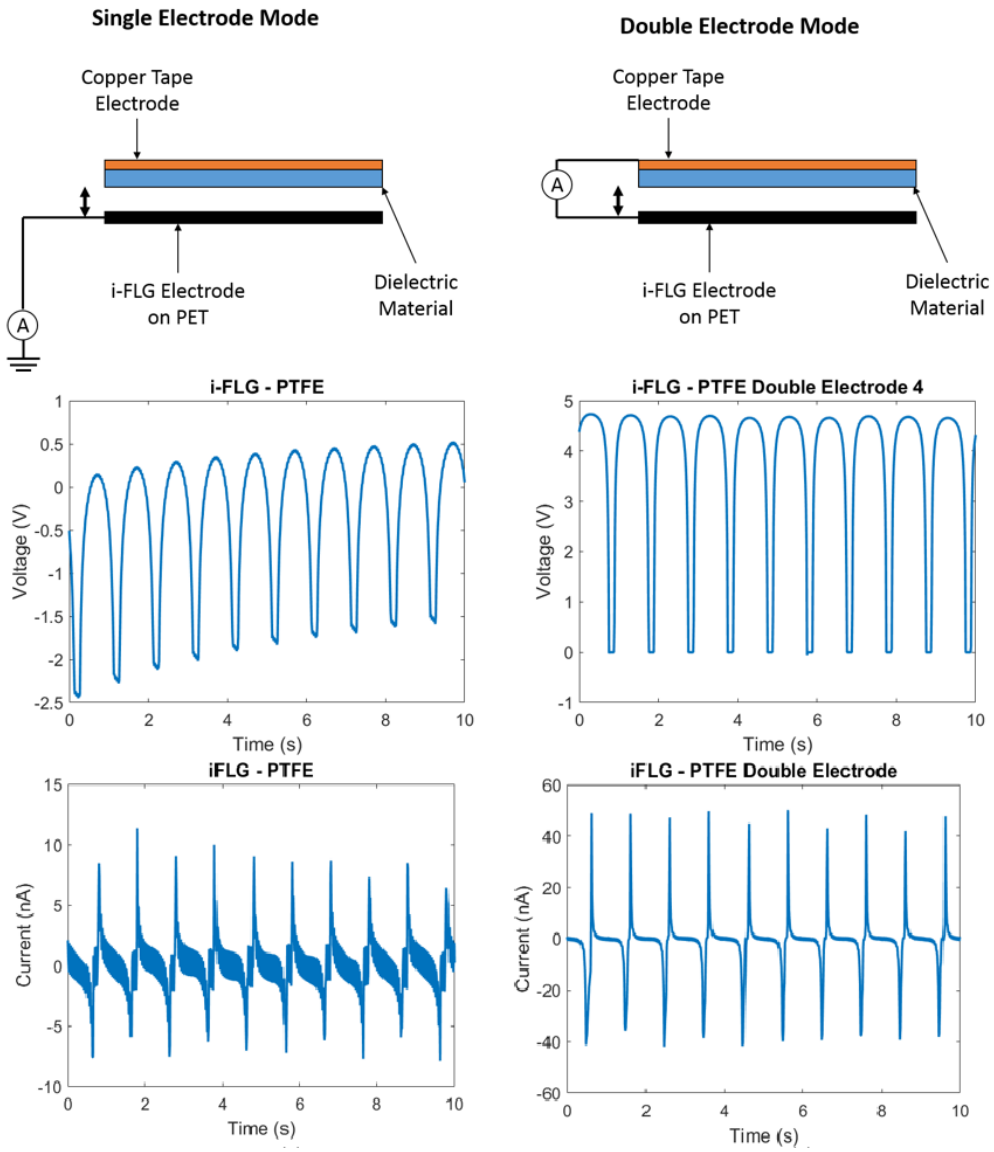

Figure 7.2: (Above) Schematics of TENG devices being measured in both single (Left) and double (Right) electrode configurations. Double headed arrows show where the device would the contacted and separated in order to produce a current. (middle) TENG device voltage response under single and double electrode configurations, and (bottom) current response for single and double electrode configurations.

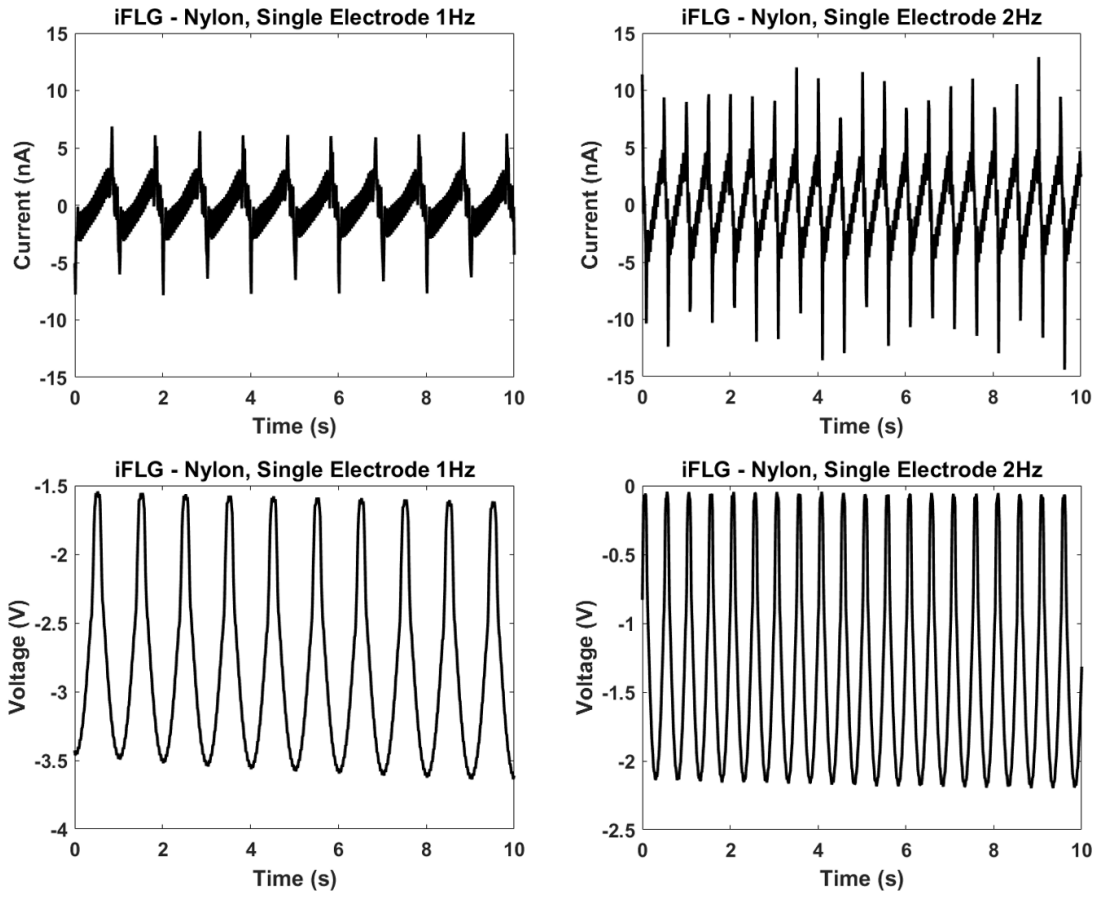

Figure 7.3: Variation of triboelectric response with change of frequency, for both current (above) and voltage (below). Data was collected from and i-FLG/Nylon TENG device, clearly showing an increase in current output with increased frequency but equal voltage output.

measurement have both also improved. In the single electrode current measurements there is a significant level of noise present, that can be seen as very short period oscillations in the current on the order of approximately 1 nA. It should be noted that this noise is still present in the double electrode measurement on PTFE, but due to the large increase in current signal this noise becomes less noticeable.

Increasing the frequency of the contact cycling is expected to produce an increase in current but no effect on the voltage measured. This is because increasing the frequency reduces the time available for charges to be moved from the TENG device surface. Since current is simply measuring the rate of movement of charges, cycling frequency and current have a proportional relationship. However, this does not effect

the voltage produced as the total charge accumulating on the surface is unchanged. This can be seen in figure 7.3, where an i-FLG TENG device was contacted against a sample of Nylon and the current and voltage responses measured for 1 Hz and 2 Hz contact cycling frequencies. Peak to peak current response approximately doubled, from 10 nA to 20 nA with increasing frequency. The magnitude of the voltage response remained the same for both frequencies, with peak to peak voltage being approximately 2 V. These two sets of tests confirmed that the TENG devices produced and the experimental characterization setup were functioning as intended. Unless otherwise specified, all results that follow were taken in double electrode configuration at a frequency of 1 Hz.

To compare the performance of i-FLG as a triboelectric material, compared to graphene, several graphene and i-FLG TENG devices were tested in contact cycles against a range of dielectric materials. These materials included thick Nylon fabric, Nitrile rubber, PDMS and PTFE. The current and voltage responses for the graphene based TENGs are shown in figure 7.4, and the responses for i-FLG based TENGs shown in figure 7.5. Both figures are presented such that the dielectric materials are ordered from positive at the top of the figure (Nylon) to negative at the bottom of the figure (PTFE).

The current and voltage responses for graphene TENG devices, shown in figure 7.4, are comparable to or lower than the response for i-FLG TENG devices, shown in figure 7.5. Before analysing the data, I will first make a number of comments on some notable peculiarities in figures 7.4 and 7.5. Firstly, as can be seen in a number of the voltage responses for graphene devices and the voltage response for i-FLG/Nitrile TENGs, there is a drift in the ground point. This leads the high and low points on each voltage cycle to drift with the ground point. This was observed as a common feature of many measurements, and was minimized through repeated contact cycling before measurements were recorded. Nevertheless, this slight drift remained a feature in a large number of measurements taken. Secondly, measurements of both current and voltage of TENG devices contacted with PDMS

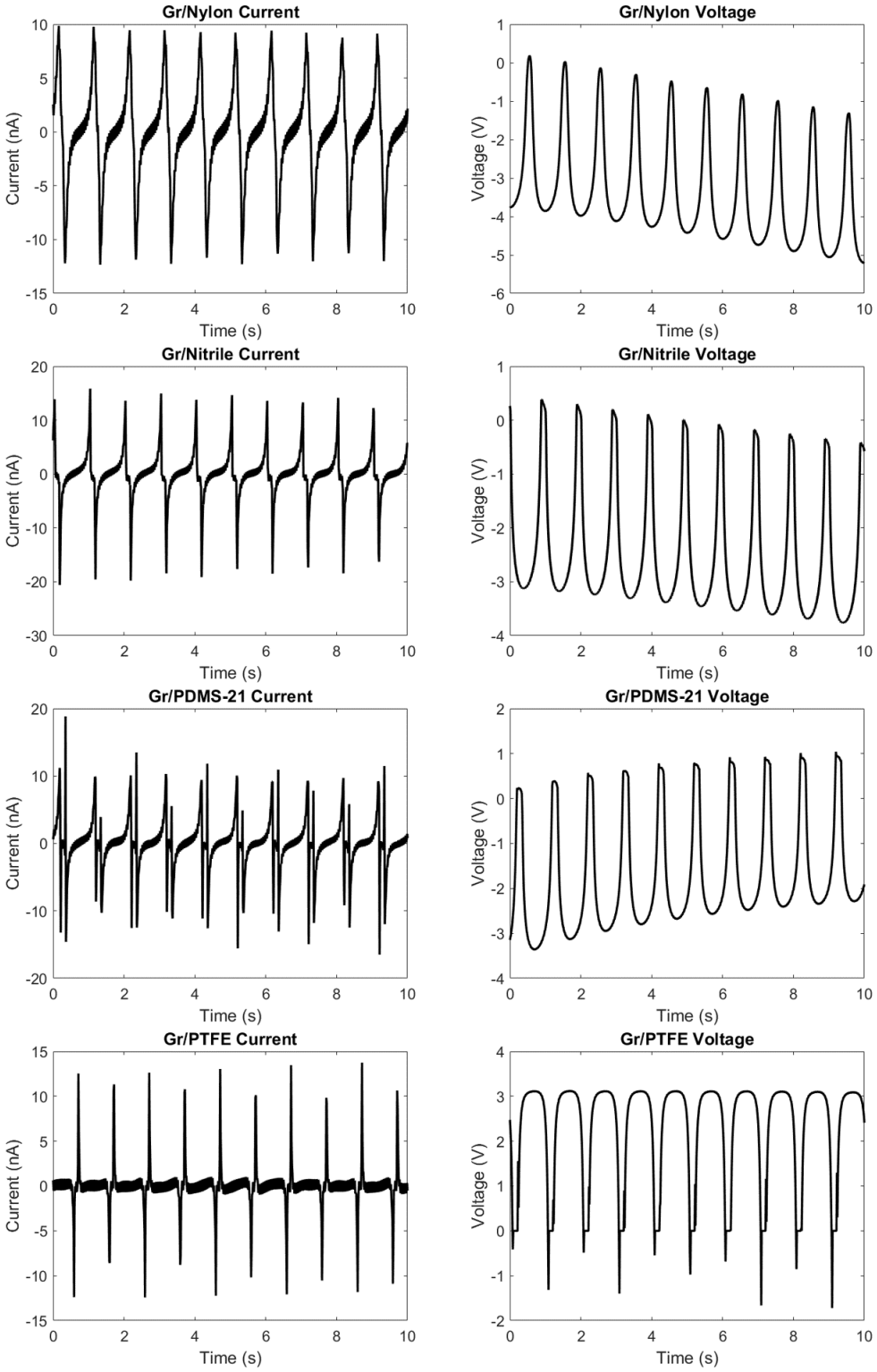

Figure 7.4: Current (Left) and voltage (right) responses for graphene TENG devices against different dielectric materials.

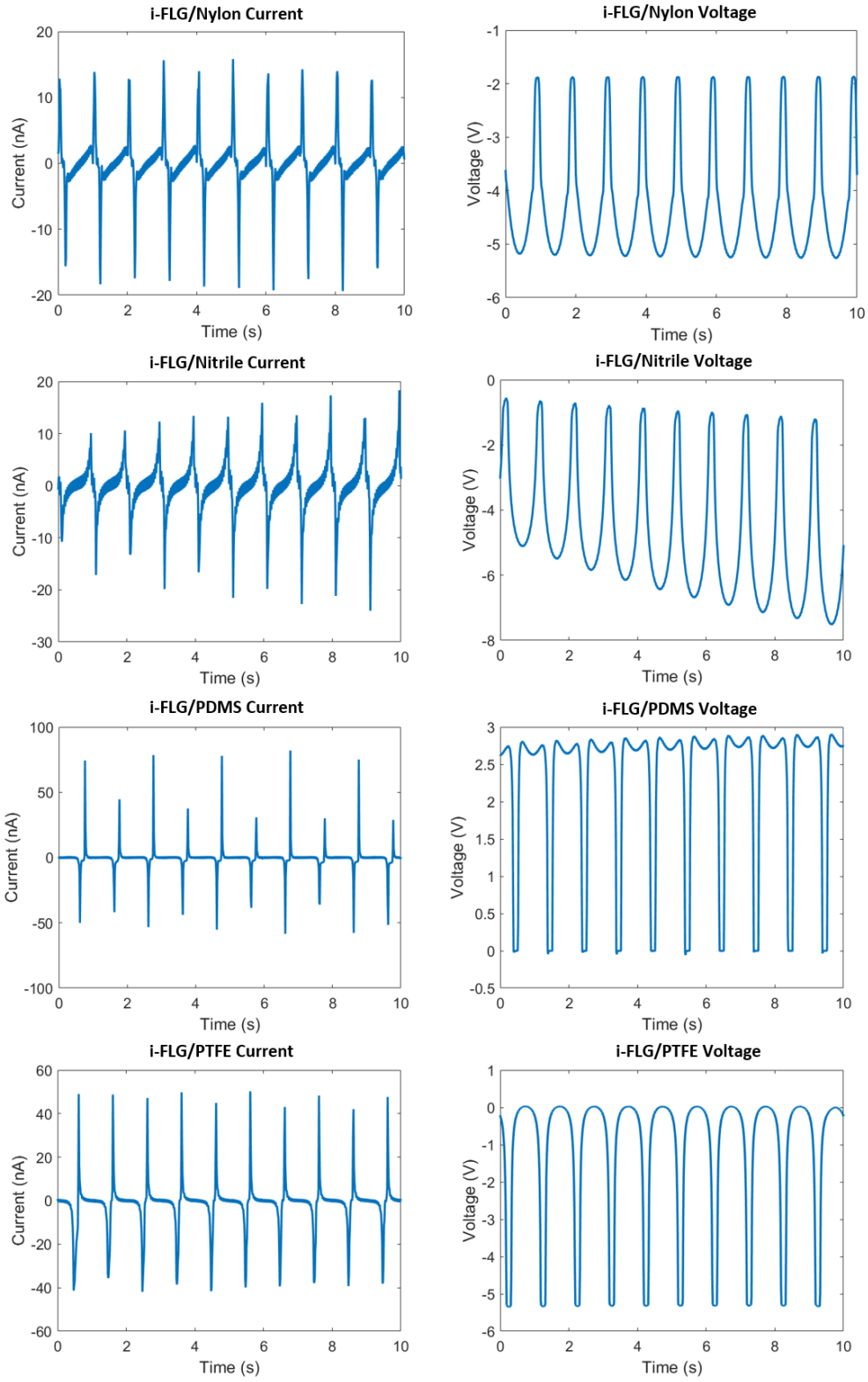

Figure 7.5: Current (Left) and voltage (Right) response for i-FLG TENG devices contacted against different dielectric materials.

saw irregularities in the response, thought to be caused by the PDMS film having slight adhesive properties. This caused the contact between the two materials to be poorly defined as they would stick together, prolonging their contact. The effect of this was inconsistent current measurements for both graphene and i-FLG devices, and small dips in the voltage response seen for i-FLG devices. This appears to have a much greater impact on the current response than the voltage response. This is due to the current pulses being generated just before contact and just after separation of the two materials. Therefore, the materials sticking together will lead to multiple current pulses overlapping (as seen in the Gr/PDMS Current response in figure 7.4) or pulses of varying magnitude (as seen for the i-FLG/PDMS current response in figure 7.5).

The key difference between these two figures is that the sign of the response against different dielectrics is different for the graphene/PDMS TENG and the i-FLG/PDMS TENG. This is significant because the sign of the triboelectric response, for both current and voltage, gives an indication to the position of the materials used in the triboelectric series. Both the current and voltage responses for both sets of TENGs were positive for contact with Nylon and Nitrile, and were both negative for contact with PTFE. However, graphene TENG devices showed a positive response when contacted with PDMS, while i-FLG devices showed a negative response. The sign and magnitude of current and voltage responses for graphene and i-FLG devices is compared in more detail in figure 7.6. In their paper on the characterization of the triboelectric series for 2D materials, Seol et al. [82] showed that the sign of the voltage response of their TENG devices when combined with a range of dielectric materials can be used to determine the position of different 2D layered materials (including graphene, graphene oxide and molybdenum disulphide) in the triboelectric series. They explain their findings by relating the sign of the response to the work function of their materials, as determined by KPFM measurements. Using an alternative doping method to intercalation, they also reveal that the position of a material in the triboelectric series can be altered through the doping of that

material. Observing the change in sign for i-FLG/PDMS TENG devices, we can conclude that i-FLG is shifted towards the positive side of the triboelectric series, compared to pristine graphene.

When comparing these two sets of results, it is clear to see that the form of the voltage response in Seol et al.'s work is very different to that of this work. The form of the triboelectric response can be heavily influenced by the geometry of the sample, along with many other experimental parameters such as form of the contact and separation motion of the experimental apparatus (sinusoidal, square or triangular, for example). As such, I will be using the current measurements to compare between the pristine graphene and i-FLG TENG devices. The form of the current response for both sets of devices is the same when combined with Nylon and Nitrile rubber, showing only slight differences in the magnitude of the response. As the response is positive for both dielectric materials, it can be seen that both Nylon and Nitrile rubber lie to the positive side of the triboelectric series when compared to pristine graphene and i-FLG. The current response for both varieties of graphene electrode against PTFE was negative instead of positive, indicating that PTFE lies to the negative side of the triboelectric series compared to both pristine graphene and i-FLG. The difference in results comes when comparing the response of graphene and i-FLG against PDMS, where a negative response is seen for i-FLG and a positive response seen for pristine graphene. This suggests that i-FLG lies to the positive side of the triboelectric series when compared to pristine graphene. It is known from the SKPFM measurements performed on i-FLG samples in chapters 4 and 5 that intercalation with $FeCl_3$ raises the work function of graphene to 5.2 eV through p-doping of the graphene sheets. Following the analysis performed by Seol et al., this would lead to an expected negative response for PTFE, and a positive response for PDMS, as is seen for MoS_2 and $MoSe_2$ in Seol et al.'s results. However, instead we observe that i-FLG's response is negative for both PTFE and PDMS, and pristine graphene's response is negative for PTFE but positive for PDMS. This would lead us to conclude that graphene sits in between PTFE and PDMS in the

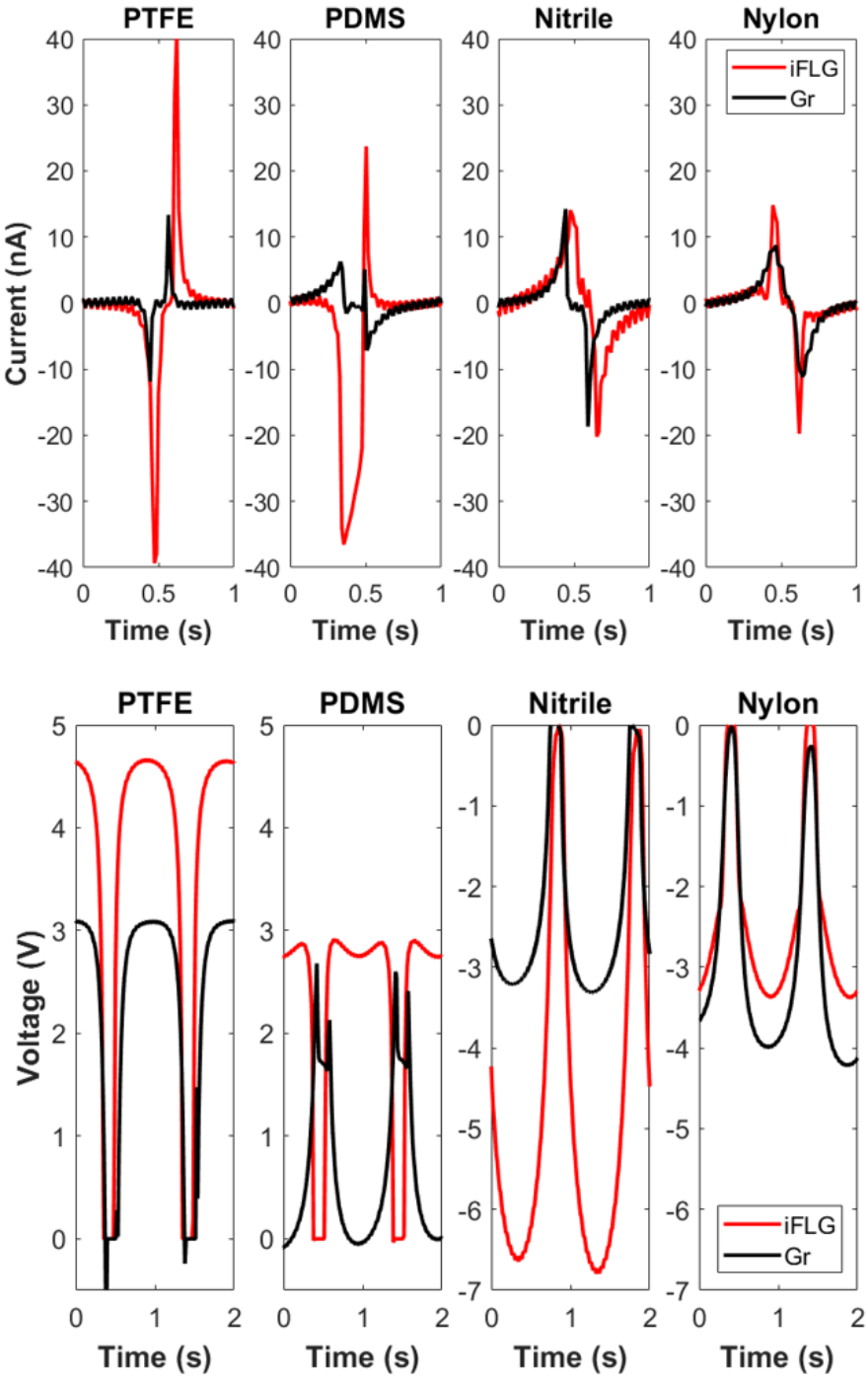

Figure 7.6: The current (above) and voltage (below) responses for pristine graphene and i-FLG TENG devices when contacted with different dielectric materials. The magnitude and sign of the response is discussed in the following section.

triboelectric series, and i-FLG between PDMS and Nitrile.

To explain these results, it should first be noted that the large area i-FLG samples used in TENG devices were over a year old. As was seen in the characterization of i-FLG by SKPFM in chapter 4, the work function increase is much more modest if time is left between intercalation and measurement. This is most likely due to surface contamination by atmospheric water, leading to the oxidation of surface $FeCl_3$ molecules. Secondly, while the same types of materials were used to characterize the positions of pristine graphene and i-FLG in the triboelectric series as in the work of Seol et al., it cannot be ensured that these materials have the exact same properties as those used by Seol et al. This can be caused by slight variations in the material production and handling processes due to using different material suppliers, contamination of dielectric materials or the graphene electrodes, or even variations in the thickness/roughness of the dielectric material chosen. Furthermore, the graphene samples used in the study of Seol et al. were fabricated in solution by exfoliation through ClF_3 intercalation, followed by vacuum filtration. This fabrication method could potentially dope the graphene film and lead to very different and surface properties and work function than the pristine graphene used in this investigation.

This presents a multitude of factors that can influence the triboelectric response seen of these devices. As such, these results would suggest that i-FLG is further towards the positive side of the triboelectric series than pristine graphene. This is the opposite to the adjustment seen in the work of Seol et al., which is ascribed to be caused by differences in the graphene and dielectric materials used. While this method provides a reliable way to determine one material's position in the triboelectric series relative to another, it is difficult to compare results between studies without exact knowledge of all the materials and fabrication methods used.

Finally, it was found that the sign of both the current and voltage responses for both i-FLG and pristine graphene TENG devices could be switched from negative to positive simply by cleaning the PTFE with IPA before measurement, as shown

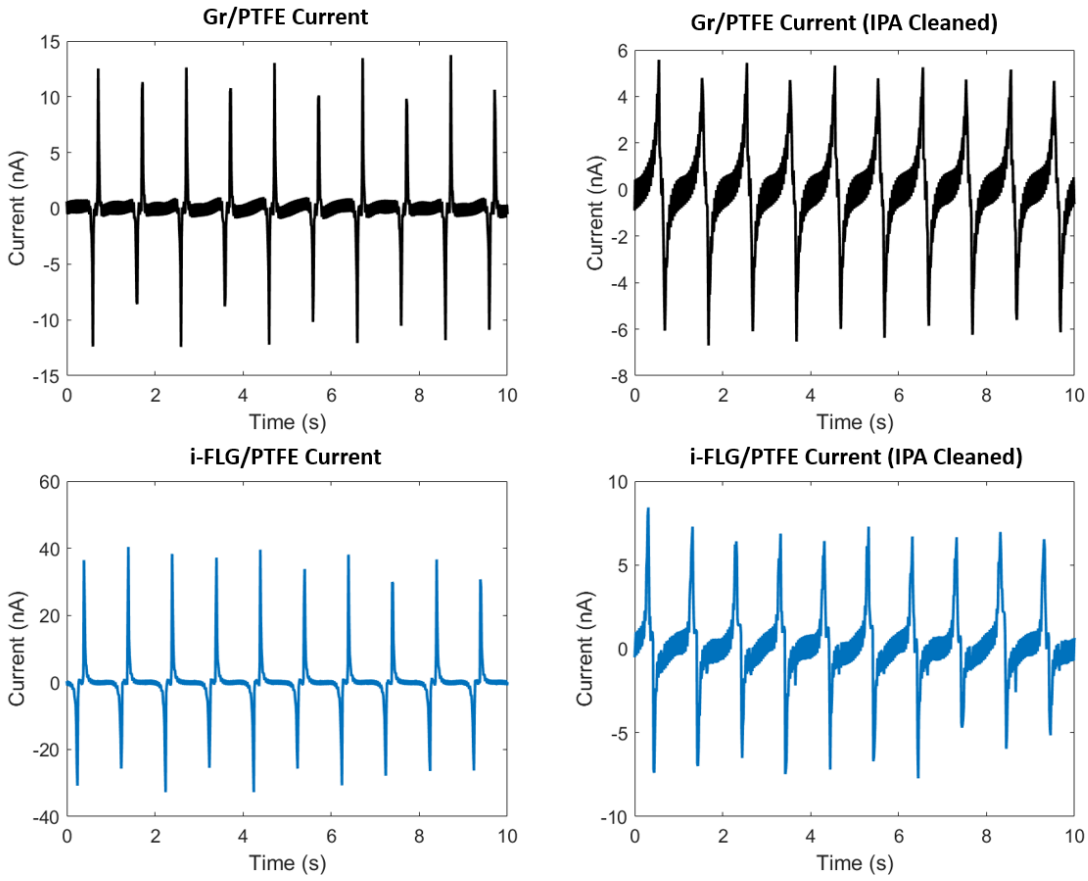

Figure 7.7: Impact of IPA cleaning on the PTFE dielectric on (above) graphene and (below) i-FLG TENG devices. For both sets of devices, the sign of the triboelectric current response switched. This indicates a repositioning of the materials in the triboelectric series.

for the current measurement in figure 7.7. The IPA was sprayed on the PTFE surface, before being allowed to fully dry under heating (70 °C for 5 minutes). It has been previously shown that for accurate triboelectric measurements to be made, the surface charges on the materials being tested must first be neutralized [226]. This is because they will undoubtedly have some built up charge on their surfaces due to handling or past contact with other materials. IPA is particularly effective at neutralizing such surface charges as it is a polar solvent that will rapidly evaporate from the sample leaving behind a charge neutral surface.

Figure 7.7 also shows a significant reduction in the magnitude of the current response for both varieties of TENG device. However, it is not clear if this is a

result of a change in material properties of the PTFE after cleaning, or a result of the cleaning and neutralization of surface charges. One thing this result does make clear is the number of factors affecting the triboelectric response of these devices. Seemingly small changes, such as cleaning the dielectric or moving a connecting wire during measurement can have a significant impact on the resulting triboelectric response. Because of this, it is difficult to conclude the position of i-FLG in the triboelectric series, relative to pristine graphene. For an accurate comparison to be made with the work conducted by Seol et al., the exact same materials, fabrication process and characterization would need to be used.

7.3.2 Graphene/i-FLG TENG Performance Comparison

While the positions of graphene and i-FLG within the triboelectric series cannot be precisely identified through the method trialled, the performance of those devices can be compared through the magnitude of the current and voltage responses. These values are critical in discerning which materials are suitable for use in energy harvesting as it gives an indication of how the materials perform as actual TENG devices. To assess the performance of these two materials, 3 i-FLG TENG devices and two graphene TENG devices were characterized against the range of dielectric materials previously trialled, with at least three measurements being made for both the current and voltage responses of each device. The average response for each type of device, against each dielectric, is then calculated and shown in figure 7.8.

As demonstrated by figure 7.8, in terms of both current and voltage, i-FLG TENG devices perform better on average than pristine graphene devices. This is evidenced by the peak-to-peak short circuit current being greater for every dielectric material trialed against i-FLG devices, as well as the peak open circuit voltage values being greater for i-FLG devices when measured against PTFE, Nitrile rubber and Nylon. Only PDMS showed a greater voltage response when measured with pristine graphene TENG devices. It should be noted however, that this only marginally outperformed i-FLG devices measured against PDMS.

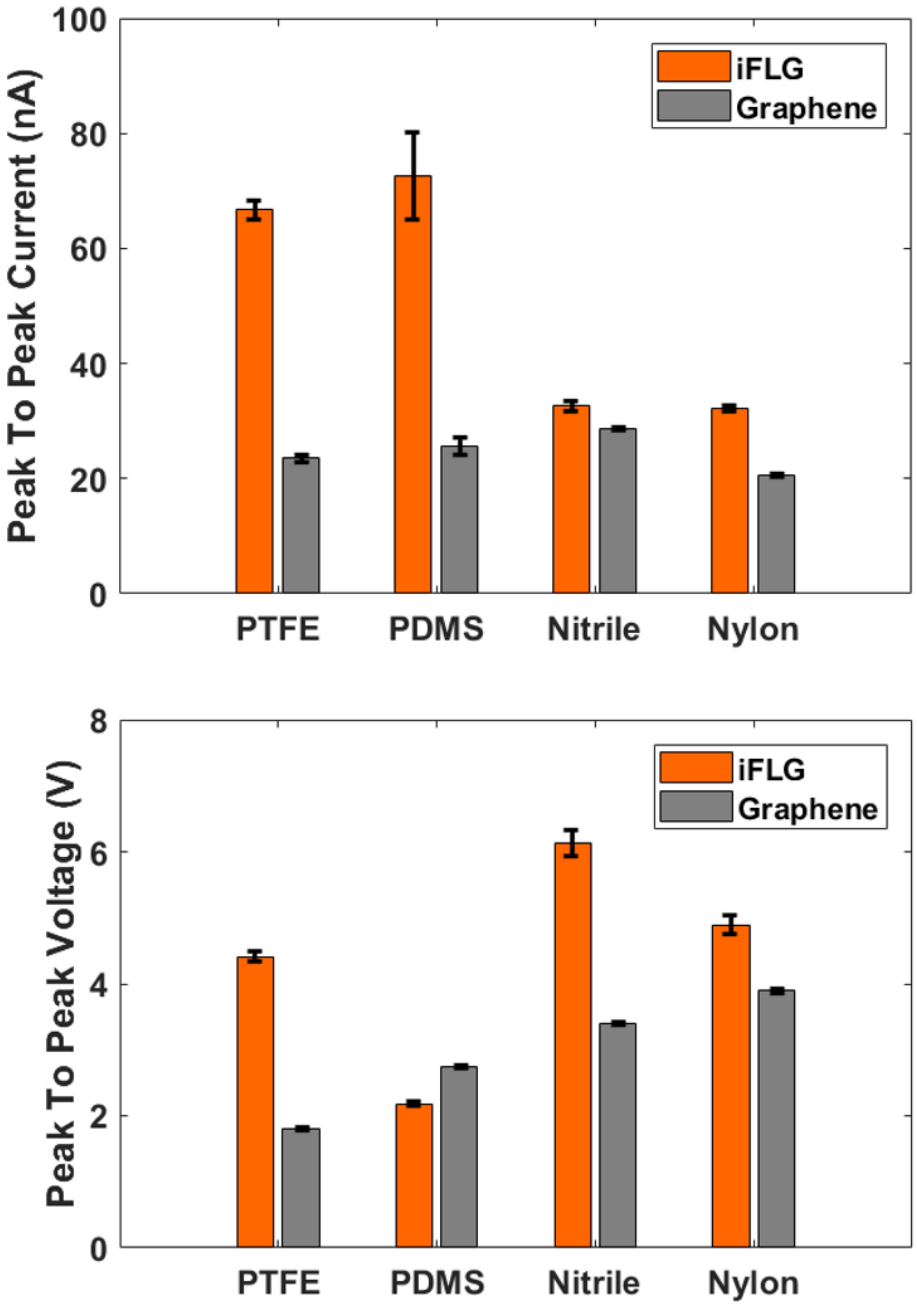

Figure 7.8: Performance summary of i-FLG and pristine graphene TENG devices when static triboelectric measurements were taken with different dielectric materials. The short circuit current (above) and open circuit voltage (below) values are averaged from multiple measurements on several TENG devices, for both i-FLG and pristine graphene devices.

One possible reason for these results is that i-FLG outperforms pristine graphene because of the greatly reduced sheet resistance. This allows for the more efficient extraction of current and the movement of charges in i-FLG devices. Another possible reason is that the high level of p-doping in i-FLG allows it to produce a much larger current than pristine graphene when combined with materials towards the negative end of the triboelectric series. This can be seen for the current response for i-FLG with PTFE and PDMS being more than double that of pristine graphene when combined with the same materials.

Another reason for the greater performance of i-FLG devices is that not all devices were of equal size. Although all devices were intended to be 2.5cm $\times$ 1.5cm, pristine graphene samples were only 70–90% of this area. The current and voltage produced by a TENG device are directly related to the area of the device, therefore it is likely the current produced with both Nitrile and Nylon samples would be comparable for both pristine graphene and i-FLG TENG devices.

Finally, it should be considered that while short circuit current and open circuit voltage measurements give an indication of the performance a TENG device can achieve, the exact performance cannot be concluded until device power output measurements are made. This can be done by connecting the TENG device in series with a variable resistor and measuring the current and voltage response at a range of resistance values. This allows the maximum power output to be calculated for each device. These measurements could not be conducted in the investigation due to not having the correct components to integrate such a measurement into the characterization setup.

Future Work

There are a number of further measurements that, if performed, would allow for the full characterization of i-FLG as a material for use in TENG devices. In this section, I will discuss some of the future work to be conducted, had there been more time/resources to work on this investigation.

- **Power Output Characterization.** By connecting the TENG device under characterization to a variable resistor, the maximum operating power output of the device can be calculated. This would allow the direct comparison of the TENG devices fabricated in this investigation and would provide a definitive answer to which variety of graphene electrode performs better as a triboelectric material. It would also allow a better comparison to be made between the performance of these devices and TENG devices fabricated in previous studies.

- **Device flexibility study.** One of the great advantages of graphene based devices is their inherent flexibility. Although all devices were fabricated on flexible PET substrates, no flexibility tests were conducted. Such tests could include cyclic bending measurements, repeatedly measuring device performance after a number of bends and evaluating if either graphene material is more suitable for flexible TENG device applications. Other measurements could include using a curved sample mount in order to assess device performance under bent conditions. This would allow for the observation of any performance changes under bending conditions, which is crucial information if these materials are to be used in flexible TENG devices.

- **Effect of graphene fabrication of TENG performance.** All varieties of graphene devices used in this study were fabricated from Ni CVD graphene, which has considerably different surface and electrical properties to Cu CVD graphene or solution processed graphene. By comparing the performance similar devices prepared from a selection of graphene materials, the optimum fabrication strategy for graphene based TENG devices can be deduced.

7.4 Conclusions

TENG devices were fabricated from both pristine graphene and highly doped i-FLG samples. These devices were contacted with a range of dielectric materials and the electrical responses measured. The sign of the electrical response was used to characterize the position of i-FLG in the triboelectric series, with it being shifted slightly to the positive side of the series as a result of the strong doping from intercalation. These results, while being in disagreement with the findings of Seol et al. [82] are valid as the graphene samples were prepared using different methods, which is likely to result in different material properties. In addition, any differences in the dielectric materials used, the geometry of the devices, experimental setup or cleaning procedures could also heavily influence the triboelectric response of these devices. Directly comparing the performance of pristine graphene and i-FLG TENG devices showed i-FLG devices to have increased short circuit current and open circuit voltage. This is likely due to the reduced sheet resistance of the i-FLG samples, along with the increased work function that results from intercalation. This indicates that i-FLG is a suitable material for use in TENG devices, particularly those used as power sources in IoT and wearable electronics applications.

Chapter 8

Conclusions

The aim of this thesis has been to investigate the use of i-FLG electrodes in energy harvesting devices, and to assess the potential benefits. The results presented within this thesis are summarized as follows:

In chapter 4, I introduced a method of wafer scale graphene transfer, capable of reliably etching and transferring graphene samples of up to 7 cm $\times$ 7 cm from their Ni/Si/SiO_2 growth substrate to a glass substrate. This allowed for the intercalation of large area samples to examine the scalability of the intercalation process. I first optimized intercalation conditions within a large area intercalation furnace, in order to improve the material qualities of the resulting i-FLG samples. These samples were extensively characterized by Raman mapping to determine the degree of intercalation across the area of the samples. I introduced sample assessment by calculation of the $\langle \text{PosG} \rangle$ metric, calculated from the relative shift in the G-peak, establishing the degree of intercalation present in the sample. Sheet resistance and work function measurements revealed these samples to be limited to a sheet resistance of $\approx$ 100 Ω/sq, and to undergo a much smaller adjustment of work function than has been previously observed for 1 cm $\times$ 1 cm samples. These results were assessed by carrying out magneto-transport measurements in order to confirm that the level of doping in the samples was comparable to previously characterized, 1 cm $\times$ 1 cm samples. Optical images of i-FLG samples revealed large areas of the samples to be covered in holes, originating from the growth process of FLG on Ni.

The presence of these holes was attributed as the cause of the reduced effectiveness of intercalation and the limited reduction in sheet resistance observed.

In chapter 5, I examined how i-FLG samples could be further functionalized for use in OPV devices. The key aspect of graphene that inhibits its use in OPV devices is the surface wetting properties of graphene films. UV/Ozone treatment was used on both pristine graphene and i-FLG samples in order to determine an appropriate treatment time to allow for the wetting of the samples by PEDOT:PSS. Contact angle and sheet resistance measurements were made to monitor the improvement to wetting, as well as any possible damage caused by UV/Ozone exposure. i-FLG samples were shown to be more resistant to damage caused by UV/Ozone exposure, and saw a much smaller increase to sheet resistance compared to pristine graphene samples. An exposure time of 5 minutes was found to give satisfactory wetting while not causing significant damage to the i-FLG samples. Raman mapping was used to monitor the introduction of defects into the i-FLG samples, and to determine whether UV/Ozone treatment could be used as a method of cleaning pristine films prior to intercalation. These results indicated thinner regions of i-FLG to underwent a greater increase in defect content than thicker regions with larger $\langle \mathrm{PosG} \rangle$ values. Finally, SKPFM was used to map the work function of the UV/Ozone treated i-FLG samples, showing a much larger increase in work function than previously observed for large area samples in chapter 4, as well as a small increase caused by the UV/Ozone exposure itself.

In chapter 6, I used the fabrication and functionalization methods developed in the previous two chapters to fabricate functioning OPV devices with i-FLG and ITO anodes. These two types of devices were then compared, with the ITO devices outperforming the i-FLG devices. The best performing devices achieved efficiencies of 3.2% and 2.8% for ITO and i-FLG devices respectively. However, the i-FLG devices proved to have superior device stability over both continuous and periodic long term stability studies. t_{80} times were calculated from continuous efficiency decay curves, revealing i-FLG devices to have device lifetimes of 3–5 times longer

than ITO based devices. This was attributed to i-FLG's superior stability to the acidic conditions created by the PEDOT:PSS layer, as this has been known to cause damage to ITO electrodes in OPV and OLED devices. This was evidenced by the increase in series resistance seen for ITO based devices under continuous illumination. Although the device efficiencies achieved in this study were much lower than those of similar devices in the literature, this was likely caused by a poorly optimized fabrication process. However, as results were consistent between both sets of devices, the improvement to stability offered by i-FLG electrodes will likely also apply to fully optimized devices.

Finally, in chapter 7, I demonstrated the use of i-FLG as a material for triboelectric energy harvesting and compared its performance to that of pristine graphene. The triboelectric response against a selection dielectric materials was then measured for both pristine graphene and i-FLG devices, and was used to determine the position of i-FLG in the triboelectric series. The results indicated that i-FLG was shifted towards the positive side of the triboelectric series compared to pristine graphene. Previous studies had indicated that p-doping leads to a shift towards the negative side of the triboelectric series. However, differences in the position in the triboelectric series could originate from the use of different fabrication methods for the graphene samples, as well as the use of different suppliers for the dielectric materials studied. Furthermore, the sign of the triboelectric response was altered by the application of IPA to clean the dielectric. This indicated that the triboelectric response of these devices was heavily dependent on the composition of the materials used, and the presence of any contaminants. Finally, I compared the performance of a number of i-FLG and pristine graphene devices, with i-FLG devices showing a greater response for both current and voltage measurements. This indicated i-FLG as a superior material for triboelectric energy harvesting compared to pristine graphene.

To conclude, graphene materials have a clear role to play in the field of energy harvesting devices, with i-FLG possessing many advantages over pristine graphene.

However, further optimization of the large area fabrication of i-FLG are required if it is to compete with other transparent electrodes such as ITO. The further development of research areas such as wearable electronics and the IoT is expected to increase the demand for energy harvesting devices capable of powering small electronic devices. i-FLG is perfectly suited for use in such devices, but further research is needed to understand how best to apply it.

Comments on future work

As was highlighted at the end of chapters 6 and 7, there are a number of areas of future work that, if completed, would further the understanding of the results presented in this thesis.

Firstly, the fabrication of flexible OPV devices would allow for a comparison to be made between ITO and i-FLG electrodes in a flexibility study. This would reveal whether replacing the ITO electrode successfully allows for the use of OPV devices in flexible applications or if there are other concerns that would limit the application of OPV devices.

Secondly, extension of the continuous stability study to longer exposure times for a greater number of devices would reveal what stage the devices were in their degradation. If these results confirmed the findings of the stability testing presented in this thesis, then it would give new motivation to the use of graphene materials as electrodes in OPV devices.

Finally, the accurate determination of the power outputs of graphene based TENG devices would allow confirmation that i-FLG is superior to pristine graphene for use in triboelectric energy harvesting. This would also allow i-FLG devices to be compared to other varieties of graphene based TENG devices presented in the literature, such as those fabricated from solution processed graphene, allowing for an accurate assessment of which graphene manufacture method leads to the most cost efficient devices.

Chapter 9

Publications and Conferences

The following is a list of publications I have contributed to throughout my studies, as well as a list of the conferences I have presented work at. The precise relation of the publications and presentations to the work contained in this thesis are made explicit for each item:

9.1 Publications

- *"A New Facile Route to Flexible and Semi-Transparent Electrodes Based on Water Exfoliated Graphene and their Single-Electrode Triboelectric Nanogenerator."*

  S. Dong-Wook, M. D. Barnes, K. K. Walsh, D. Dimov, P. Tian, A. I. S. Neves, C. D. Wright, S. M. Yu, J. Yoo, S. Russo, and M. F. Craciun,

  Adv. Mater. 2018, 30, 1802953. DOI: 10.1002/adma.201802953.

  This paper [72] focuses on a novel transfer method for solution processed graphene films in TENG devices. My contributions to this paper were in the experimental work I performed optimizing the solution processing conditions, as well as transferring graphene films and characterizing their sheet resistance by transfer length measurements.

- *"Wafer scale $FeCl_3$ intercalated graphene electrodes for photovoltaic applications."*

K. K. Walsh, C. Murphy, G. Jones, M. Barnes, A. De Sanctis, S. Dong-Wook, S. Russo, M. F. Craciun

Proc. SPIE 10688, Photonics for Solar Energy Systems VII, 106881C (21 May 2018); DOI: 10.1117/12.2307410.

This paper [117] was published in the proceedings for the SPIE Europe conference. It covers the large area graphene transfer, intercalation and Raman mapping characterization covered in chapter 4. All experimental work carried out for this publication was carried out by myself and Conor Murphy, the text of the paper was written entirely by myself.

- *"Transmission Properties of $FeCl_3$-Intercalated Graphene and WS_2 Thin Films for Terahertz Time-Domain Spectroscopy Applications."*

  M. O. Zhukova, B. T. Hogan, E. N. Oparin, P. S. Shaban, Y. V. Grachev, E. Kovalska, K. K. Walsh, M. F. Craciun, A. Baldycheva & A. N. Tcypkin

  Nanoscale Res Lett 14, 225 (2019).https://DOI.org/10.1186/s11671-019-3062-3.

  My contributions to the work covered in this paper [63] was solely in the preparation of i-FLG samples, as the main body of experimental work covered in this paper was undertaken by collaborators.

- *"Photoexcited terahertz conductivity in multi-layered and intercalated graphene."*

  A. N.Grebenchukov, A. D.Zaitsev, M. G.Novoselov, P. S.Demchenko, E. O.Kovalska, E. Torres Alonso, K. K. Walsh, S. Russo, M. F.Craciun, A. V.Baldycheva, M. K.Khodzitsky

  Optics Communications, Volume 459, 15 March 2020, 124982, DOI:10.1016/j.optcom.2019.124982.

  Similarly to the previous publication, the work covered in this paper [228] was carried out by collaborators. My contribution was the preparation of i-FLG samples.

- *"Improved Stability of Organic Photovoltaic Devices with $FeCl_3$ Intercalated*

Graphene Electrodes"

K. K. Walsh, C. Murphy, S. Russo, M. F. Craciun.

Frontiers in Electronics, accepted for publication 11^{th} March 2021.

This paper described the fabrication and characterization of OPV devices with i-FLG and ITO electrodes, and the improved stability observed for the i-FLG based devices. This is the first example of an OPV device fabricated with i-FLG electrodes.

9.2 Conferences

- Recent Appointees in Materials Science (RAMS), Exeter (2017). Poster Presentation, *"Solvent Assisted Transfer of Solution Processed Graphene Films."*
- SPIE Europe, Strasbourg (2018). Poster Presentation, *"Wafer scale $FeCl_3$ intercalated graphene electrodes for photovoltaic applications."*
- Materials for Clean Energy Conference (MCEC), Teddington (2019). Oral Presentation, *"Graphene Electrodes for Energy Harvesting."*
- Large-area, Organic and Printed Electronics Convention (LOPEC), Munich (2019). Oral Presentation, *"Graphene Electrodes for Energy Harvesting."*
- NanoGE Hybrid Organic Photovoltaics (HOPV), Rome (2019). Oral Presentation, *"Graphene Electrodes for Organic Photovoltaics."*
- Frontiers in Optics (FiO), Online (2020). Poster Presentation, *"Fully Flexible, Transparent Electrodes for Organic Photovoltaic Applications."*

Chapter 10

Appendix

Factors Impacting the Triboelectric Effect

As was discussed in chapter 7, there are many factors that impact the transfer of charge between two materials that are undergoing triboelectric charging. Furthermore, there are additional factors that will impact the performance of Triboelectric energy harvesting devices depending on the materials used, methods of characterisation and the environment the devices are being characterised in. In this section, I will briefly explore what these factors are and how they can be investigated. I will go on to set out a list of potential avenues for further research to be carried out into i-FLG as a material for TENG devices.

There has been much debate in the field of triboelectric energy harvesting as to what the nature of triboelectric charging actually is. Arguments have been made for the effect being driven by the transfer or charge, ions, or material [229]. It may even be a combination of each of these, and potentially different depending on the combination of materials used. For example, fabrics used in triboelectric energy harvesting can leave behind fibres on the material they are being contacted with. Similarly, polymer films can leave polymer residues on the surface of other materials. This transfer of materials can change the triboelectric response being produced by such devices. However, for simplicity I will only consider the effect being driven by the transfer of charge alone, as this has been the most thoroughly investigated and

has shown the most evidence for being the case.

There are a number of experimental factors that will impact the performance of all triboelectric devices that should be considered when undertaking investigations into triboelectric energy harvesting. The device area directly relates to both the short circuit current and the open circuit voltage that can be drawn from the device, giving larger devices much better performance. Similarly, both the force and frequency of contact cycles between the materials can have a large affect (as was shown for frequency in chapter 7). Other experimental parameters which will impact the performance include the neutralization of surface charge prior to experiment (this has a greater impact for thinner materials, so is crucial when investigating TENG devices comprised of 2D material layers), the atmosphere the investigation is carried out under (inert atmospheres comprised of nitrogen or argon should be used where possible, as this prevents the adhesion of charged atmospheric contaminants such as water vapour to the device surface [145]. This commonly has the effect of neutralising surface charge, reducing device performance). The force exerted when contacting the two triboelectric materials is also crucial to device performance. Compressible materials such as fabrics and thick polymer films will behave differently to incompressible 2D materials such as i-FLG or transition metal dichalcogenides. Finally, the device structure and the nature of the tests being performed can have a large effect on the device performance. Devices comprised of multiple stacked dielectric layers are able to produce more power than single layer device comprised of similar materials. These devices will also produce different responses depending on whether they are being tested in a vertical contact structure (as was carried out in this investigation) or a horizontal sliding structure. These different methods of characterising TENG devices lend themselves to different applications, so should both be investigated when characterising a new material or device architecture.

In addition to these experimental considerations, the choice of materials is crucial to ensuring good device performance. As was mentioned previously in chapters 2 and 7, the triboelectric materials selected should be from opposite ends of the

triboelectric series to ensure good charge transfer. However, there are several material properties that impact the triboelectric response of devices. These factors should be more thoroughly investigated in order to gain a better understanding of the triboelectric response of devices, and maximize power generation from this new variety of energy harvesting device.

Each of these factors and material properties should be investigated prior to characterisation of triboelectric devices comprised of new materials so that trends in device performance can be identified. As was seen in this investigation, the source of the material is also a crucial factor. Although a material from two different suppliers may have very similar properties, the manufacturing method used to produce the material, its purity, and even how the material is stored and transported can influence the triboelectric response the material will produce. This can mean that triboelectric devices composed of the same material, but from different manufacturers, may produce different results. This can make it difficult to accurately determine the cause of differences in triboelectric response of similar devices. This is likely to be the reason why many reports on the triboelectric series do not report the exact same order of materials in the triboelectric series. Rigorous control of both the quality of materials used and the experimental parameters investigated are required if meaningful results are to be drawn from triboelectric device characterisation.

Factors Impacting the Triboelectric Effect

Factor	Impact on Triboelectric Effect
Work Function	The work function of a material defines the energy difference between the highest energy electron of a material and the vacuum level. Higher work functions mean a lower energy electron, making the material more likely to withhold electrons than donate them. Materials with lower work functions will transfer electrons more easily. Combining materials with large differences in work function may be an effective method of producing triboelectric charge transfer.
Surface Composition	The chemical composition of a material at its surface can have a large impact on the triboelectric charging of the material, as the presence of electron withdrawing/donating groups will determine the materials position in the triboelectric series. Cleaning procedures such as Reactive Ion Etching or UV/Ozone treatment can alter the composition of a material at the surface, leading to changes in its triboelectric response/position.
Surface Charge Density	The surface charge density of a material impacts the triboelectric effect as the more charge can be stored on the surface of the material, the more can be transferred under contact electrification. This factor is subject to influence from many different contributions, including surface contamination and the environment in which the experiment takes place. As such it should be carefully investigated in future works.
Surface Roughness	Materials with high surface roughness directly increase the area of the material at the surface. This can lead to an increase in the amount of charge that can be stored, and so an increase in total charge available to transfer. It also increases the area of contact between the two materials being used. This has been successfully exploited by a number of groups that create micro/nanostructures on the triboelectric material surface to increase charge transfer.
Charge Injection Depth and Dielectric Constant	The charge injection depth is defined as the distance into a material an electric field produced by a charge will penetrate. This parameter, along with the dielectric constant of the material determine the material's Capacitance. As this key to determining how much charge can be supported by a material, it is also key to understanding the triboelectric response of materials. In the case of nanomaterials, such as graphene, the charge penetration depth may be greater than the thickness of the material. This makes these systems more complicated and requires further investigation to fully understand.

Factors affecting the triboelectric effect. These factors have been selected through a combination of surveying current literature, as well as my experience of characterizing triboelectric devices. Though some sources make reference to the importance of these factors, stringent investigations are still required to fully understand the impact of these factors for different materials. The factors are given in no particular order of importance.

Chapter 11

Bibliography

Bibliography

[1] Bin Li, Liduo Wang, Bonan Kang, Peng Wang, and Yong Qiu. Review of recent progress in solid-state dye-sensitized solar cells. *Solar Energy Materials and Solar Cells*, 90(5):549–573, 2006.

[2] Prashant V. Kamat. Meeting clean energy demand with nanostructure architectures. *ACS National Meeting Book of Abstracts*, pages 2834–2860, 2007.

[3] Corsin Battaglia, Andres Cuevas, and Stefaan De Wolf. High-efficiency crystalline silicon solar cells: Status and perspectives. *Energy and Environmental Science*, 9(5):1552–1576, 2016.

[4] Waheed A. Badawy. A review on solar cells from Si-single crystals to porous materials and Quantum dots. *Journal of Advanced Research*, 6(2):123–132, 2015.

[5] Henry J Snaith, Antonio Abate, James M Ball, Giles E Eperon, Tomas Leijtens, Nakita K Noel, Samuel D Stranks, Jacob Tse-wei Wang, Konrad Wojciechowski, and Wei Zhang. Anomalous Hysteresis in Perovskite Solar Cells. *J. Phys. Chem. Lett*, 5(iii):1511–1515, 2014.

[6] Antonio Agresti, Sara Pescetelli, Alessandro L Palma, Antonio E Del, Rio Castillo, Dimitrios Konios, George Kakavelakis, Stefano Razza, Lucio Cina, Emmanuel Kymakis, Francesco Bonaccorso, and Aldo Di Carlo. Graphene Interface Engineering for Perovskite Solar Modules: 12.6% Power Conversion Efficiency over 50 cm2 Active Area. *ACS Energy Letters*, 2:279–287, 2017.

[7] Woon Seok Yang, Byung-Wook Park, Eui Hyuk Jung, Nam Joong Jeon, Young Chan Kim, Dong Uk Lee, Seong Sik Shin, Jangwon Seo, Eun Kyu Kim, Jun Hong Noh, and Sang Il Seok. Iodide management in formamidinium-lead-halide–based perovskite layers for efficient solar cells. *Science*, 356(6345):1376–1379, 2017.

[8] Cenqi Yan, Stephen Barlow, Zhaohui Wang, He Yan, Alex K.Y. Jen, Seth R. Marder, and Xiaowei Zhan. Non-fullerene acceptors for organic solar cells. *Nature Reviews Materials*, 3(February):1–19, 2018.

[9] Gordon J. Hedley, Alexander J. Ward, Alexander Alekseev, Calvyn T. Howells, Emiliano R. Martins, Luis A. Serrano, Graeme Cooke, Arvydas Ruseckas, and Ifor D.W. Samuel. Determining the optimum morphology in high-performance polymer-fullerene organic photovoltaic cells. *Nature Communications*, 4, 2013.

[10] Wanjung Kim, Jung Kyu Kim, Eunchul Kim, Tae Kyu Ahn, Dong Hwan Wang, and Jong Hyeok Park. Conflicted effects of a solvent additive on PTB7:PC71BM bulk heterojunction solar cells. *Journal of Physical Chemistry C*, 119(11):5954–5961, 2015.

[11] René A. J. Janssen and Jenny Nelson. Factors Limiting Device Efficiency in Organic Photovoltaics. *Advanced Materials*, 25(13):1847–1858, 2013.

[12] David Duche, Philippe Torchio, Ludovic Escoubas, Florent Monestier, Jean Jacques Simon, François Flory, and Gérard Mathian. Improving light absorption in organic solar cells by plasmonic contribution. *Solar Energy Materials and Solar Cells*, 93(8):1377–1382, 2009.

[13] Bernd Ebenhoch, Stuart A.J. Thomson, Kristijonas Genevičius, Gytis Juška, and Ifor D.W. Samuel. Charge carrier mobility of the organic photovoltaic materials PTB7 and PC71BM and its influence on device performance. *Organic Electronics*, 22:62–68, 2015.

[14] Yiwei Zhang, Edward Bovill, James Kingsley, Alastair R. Buckley, Hunan Yi, Ahmed Iraqi, Tao Wang, and David G. Lidzey. PCDTBT based solar cells: One year of operation under real-world conditions. *Scientific Reports*, 6, 2016.

[15] Lingxian Meng, Yamin Zhang, Xiangjian Wan, Chenxi Li, Xin Zhang, Yanbo Wang, Xin Ke, Zuo Xiao, Liming Ding, Ruoxi Xia, Hin-Lap Yip, Yong Cao, and Yongsheng Chen. SI_Organic and solution-processed tandem solar cells with 17.3% efficiency. *Science*, 1098(September):eaat2612, 2018.

[16] Said Karim Shah, Jahangeer Khan, Irfan Ullah, and Yaqoob Khan. Optimization of active-layer thickness, top electrode and annealing temperature for polymeric solar cells. *AIMS Materials Science*, 4(3):789–799, 2017.

[17] Seth B. Darling and Fengqi You. The case for organic photovoltaics. *RSC Advances*, 3(39):17633–17648, 2013.

[18] Hwanjoo Park, Dongkeon Lee, Gimin Park, Sungjin Park, Salman Khan, Jiyong Kim, and Woochul Kim. Energy harvesting using thermoelectricity for IoT (Internet of Things) and E-skin sensors. *Journal of Physics: Energy*, 1(4):042001, 2019.

[19] Anirudh Sharma, Gunther Andersson, and David A. Lewis. Role of humidity on indium and tin migration in organic photovoltaic devices. *Physical Chemistry Chemical Physics*, 13(10):4381–4387, 2011.

[20] Nieves Espinosa, Rafael García-Valverde, Antonio Urbina, and Frederik C. Krebs. A life cycle analysis of polymer solar cell modules prepared using roll-to-roll methods under ambient conditions. *Solar Energy Materials and Solar Cells*, 95(5):1293–1302, 2011.

[21] Yue Wang, Chenxin Zhu, Raphael Pfattner, Hongping Yan, Lihua Jin, Shucheng Chen, Francisco Molina-Lopez, Franziska Lissel, Jia Liu, Noelle I. Rabiah, Zheng Chen, Jong Won Chung, Christian Linder, Michael F. Toney,

Boris Murmann, and Zhenan Bao. A highly stretchable, transparent, and conductive polymer. *Science Advances*, 3(3):1–11, 2017.

[22] Gunel Huseynova, Yong Hyun Kim, Jae Hyun Lee, and Jonghee Lee. Rising advancements in the application of PEDOT:PSS as a prosperous transparent and flexible electrode material for solution-processed organic electronics. *Journal of Information Display*, 21(2):71–91, 2020.

[23] S. K.M. Jönsson, J. Birgerson, X. Crispin, G. Greczynski, W. Osikowicz, A. W. Denier van der Gon, W. R. Salaneck, and M. Fahlman. The effects of solvents on the morphology and sheet resistance in poly(3,4-ethylenedioxythiophene)-polystyrenesulfonic acid (PEDOT-PSS) films. *Synthetic Metals*, 139(1):1–10, 2003.

[24] Pengfei Zhao, Qingxin Tang, Xiaoli Zhao, Yanhong Tong, and Yichun Liu. Highly stable and flexible transparent conductive polymer electrode patterns for large-scale organic transistors. *Journal of Colloid and Interface Science*, 520:58–63, 2018.

[25] Chuan Li, Yi Ting Hsu, and Wei Wen Hu. The regulation of osteogenesis using electroactive polypyrrole films. *Polymers*, 8(7):1–12, 2016.

[26] Pen Cheng Wang, Li Hung Liu, Desalegn Alemu Mengistie, Kuan Hsun Li, Bor Jiunn Wen, Tzong Shi Liu, and Chih Wei Chu. Transparent electrodes based on conducting polymers for display applications. *Displays*, 34(4):301–314, 2013.

[27] Y. Yang and A. J. Heeger. Polyaniline as a transparent electrode for polymer light-emitting diodes: Lower operating voltage and higher efficiency. *Applied Physics Letters*, 64(10):1245–1247, 1994.

[28] Jamshid K. Avlyanov, Jack Y. Josefowicz, and Alan G. MacDiarmid. Atomic force microscopy surface morphology studies of 'in situ' deposited polyaniline thin films. *Synthetic Metals*, 73(3):205–208, 1995.

[29] Jihoon Ahn, Hyewon Hwang, Sunho Jeong, and Jooho Moon. Metal-Nanowire-Electrode-Based Perovskite Solar Cells: Challenging Issues and New Opportunities. *Advanced Energy Materials*, 7(15):1–19, 2017.

[30] Chuan Fei Guo and Zhifeng Ren. Flexible transparent conductors based on metal nanowire networks. *Materials Today*, 18(3):143–154, 2015.

[31] Liangbing Hu, Hui Wu, and Yi Cui. Metal nanogrids, nanowires, and nanofibers for transparent electrodes. *MRS Bulletin*, 36(10):760–765, 2011.

[32] K. S. Novoselov, A. K. Geim, S. V. Morozov, D. Jiang, Y. Zhang, S. V. Dubonos, I. V. Grigorieva, and A. A. Firsov. Electric Field Effect in Atomically Thin Carbon Films. *Science*, 306(5696):666–669, 2004.

[33] K. S. Novoselov, D. Jiang, F. Schedin, T. J. Booth, V. V. Khotkevich, S. V. Morozov, and A. K. Geim. Two-dimensional atomic crystals. *Proceedings of the National Academy of Sciences*, 102(30):10451–10453, 2005.

[34] K S Novoselov, A K Geim, S V Morozov, D Jiang, M I Katsnelson, I V Grigorieva, S V Dubonos, and A A Firsov. Two-dimensional gas of massless Dirac fermions in graphene. *Nature*, 438(7065):197–200, 2005.

[35] R. R. Nair, P. Blake, A. N. Grigorenko, K. S. Novoselov, T. J. Booth, T. Stauber, N. M. R. Peres, and A. K. Geim. Fine Structure Constant Defines Visual Transparency of Graphene. *Science*, 320(5881):1308–1308, 2008.

[36] Zhen-yu Juang, Chih-yu Wu, Ang-yu Lu, Ching-yuan Su, Keh-chyang Leou, Fu-rong Chen, and Chuen-horng Tsai. Graphene synthesis by chemical vapor deposition and transfer by a roll-to-roll process. *Carbon*, 48(11):3169–3174, 2010.

[37] Zhike Liu, Peng You, Shenghua Liu, and Feng Yan. Neutral-Color Semitransparent Organic Solar Cells with All-Graphene Electrodes. *ACS Nano*, 9(12):12026–12034, 2015.

[38] Hyesung Park, Sehoon Chang, Matthew Smith, Silvija Gradečak, and Jing Kong. Interface engineering of graphene for universal applications as both anode and cathode in organic photovoltaics. *Scientific Reports*, 3:1–8, 2013.

[39] Hyesung Park, Sehoon Chang, Xiang Zhou, and Jing Kong. Flexible Graphene Electrode-Based Organic Photovoltaics with Record-High Efficiency. *Nano letters*, 14:5148–5154, 2014.

[40] Hyesung Park, Rachel M Howden, Miles C Barr, Vladimir Bulovi, and Park E T Al. Organic Solar Cells with Graphene Electrodes and Vapor Printed as the Hole Transporting Layers. *ACS nano*, 6(7):6370–6377, 2012.

[41] Junbo Wu, Héctor A. Becerril, Zhenan Bao, Zunfeng Liu, Yongsheng Chen, and Peter Peumans. Organic solar cells with solution-processed graphene transparent electrodes. *Applied Physics Letters*, 92(26), 2008.

[42] Lewis Gomez De Arco, Yi Zhang, Cody W Schlenker, Koungmin Ryu, Mark E Thompson, and Chongwu Zhou. Continuous, Highly Flexible, and Transparent Graphene Films by Chemical Vapor Deposition for Organic Photovoltaics. *Acs Nano*, 4(5):2865–2873, 2010.

[43] Hyesung Park, Yumeng Shi, and Jing Kong. Application of solvent modified PEDOT:PSS to graphene electrodes in organic solar cells. *Nanoscale*, 5(19):8934–8939, 2013.

[44] Nieves Espinosa, Markus Hösel, Dechan Angmo, and Frederik C. Krebs. Solar cells with one-day energy payback for the factories of the future. *Energy and Environmental Science*, 5(1):5117–5132, 2012.

[45] Hui Bi, Fuqiang Huang, Jun Liang, Xiaoming Xie, and Mianheng Jiang. Transparent conductive graphene films synthesized by ambient pressure chemical vapor deposition used as the front electrode of CdTe solar cells. *Advanced Materials*, 23(28):3202–3206, 2011.

[46] Seungon Jung, Junghyun Lee, Yunseong Choi, Sang Myeon Lee, Changduk Yang, and Hyesung Park. Improved interface control for high-performance graphene-based organic solar cells. *2D Materials*, 4(4):aa823b, 2017.

[47] Wei Liu, Jiahao Kang, and Kaustav Banerjee. Characterization of FeCl3 Intercalation Doped CVD Few-Layer Graphene. *IEEE Electron Device Letters*, 37(9):1246–1249, 2016.

[48] Chang-Lung Hsu, Cheng-Te Lin, Jen-Hsien Huang, Chih-Wei Chu, Kung-Hwa Wei, and Lain-Jong Li. Layer-by-Layer Graphene/TCNQ Stacked Films as Conducting Anodes for Organic Solar Cells. *ACS Nano*, 6(6):5031–5039, 6 2012.

[49] Hyesung Park, Jill A. Rowehl, Ki Kang Kim, Vladimir Bulovic, and Jing Kong. Doped graphene electrodes for organic solar cells. *Nanotechnology*, 21(50):0–6, 2010.

[50] Keumok Kim, Sang Hoon Bae, Chee Tat Toh, Hobeom Kim, Jeong Ho Cho, Dongmok Whang, Tae Woo Lee, Barbaros Özyilmaz, and Jong Hyun Ahn. Ultrathin organic solar cells with graphene doped by ferroelectric polarization. *ACS Applied Materials and Interfaces*, 6(5):3299–3304, 2014.

[51] Sangchul Lee, Jun Seok Yeo, Yongsung Ji, Chunhum Cho, Dong Yu Kim, Seok In Na, Byoung Hun Lee, and Takhee Lee. Flexible organic solar cells composed of P3HT:PCBM using chemically doped graphene electrodes. *Nanotechnology*, 23(34), 2012.

[52] Sung Joo Kwon, Tae Hee Han, Taeg Yeoung Ko, Nannan Li, Youngsoo Kim, Dong Jin Kim, Sang Hoon Bae, Yang Yang, Byung Hee Hong, Kwang S. Kim, Sunmin Ryu, and Tae Woo Lee. Extremely stable graphene electrodes doped with macromolecular acid. *Nature Communications*, 9(1):1–9, 2018.

[53] T. P. Kaloni, Y. C. Cheng, M. Upadhyay Kahaly, and U. Schwingenschlögl. Charge carrier density in Li-intercalated graphene. *Chemical Physics Letters*, 534:29–33, 2012.

[54] Lawrence. B. Ebart. Intercalation comounds of graphite. *Annual review of materials science*, 6:181–211, 1976.

[55] M. S. Dresselhaus and G. Dresselhaus. Intercalation compounds of graphite. *Advances in Physics*, 30(2):139–326, 1981.

[56] Tapas Kuila, Saswata Bose, Ananta Kumar Mishra, Partha Khanra, Nam Hoon Kim, and Joong Hee Lee. Chemical functionalization of graphene and its applications. *Progress in Materials Science*, 57(7):1061–1105, 2012.

[57] Xiaochang Miao, Sefaattin Tongay, Maureen K Petterson, Kara Berke, Andrew G Rinzler, Bill R Appleton, and Arthur F Hebard. High E ffi ciency Graphene Solar Cells by Chemical Doping. *Nano Letters*, 12:6–11, 2012.

[58] Philipp Rosenzweig, Hrag Karakachian, Dmitry Marchenko, Kathrin Küster, and Ulrich Starke. Overdoping Graphene beyond the van Hove Singularity. *Physical Review Letters*, 125(17):176403, 2020.

[59] Vasilios Georgakilas, Michal Otyepka, Athanasios B. Bourlinos, Vimlesh Chandra, Namdong Kim, K. Christian Kemp, Pavel Hobza, Radek Zboril, and Kwang S. Kim. Functionalization of graphene: Covalent and non-covalent approaches, derivatives and applications. *Chemical Reviews*, 112(11):6156–6214, 2012.

[60] Thomas H Bointon, Gareth F Jones, Adolfo De Sanctis, Ruth Hill-Pearce, Monica F Craciun, and Saverio Russo. Large-area functionalized CVD graphene for work function matched transparent electrodes. *Scientific reports*, 5:16464, 2015.

[61] Dominique Joseph Wehenkel, Thomas Hardisty Bointon, Monica Felicia Craciun, Saverio Russo, Physical Sciences, and Nanotechnology Engineering.

Unforeseen high temperature and humidity stability of FeCl 3 intercalated few layer graphene. *Scientific reports*, 5:7609, 2015.

[62] Ivan Khrapach, Freddie Withers, Thomas H. Bointon, Dmitry K. Polyushkin, William L. Barnes, Saverio Russo, and Monica F. Craciun. Novel highly conductive and transparent graphene-based conductors. *Advanced Materials*, 24(21):2844–2849, 2012.

[63] Maria O. Zhukova, Benjamin T. Hogan, Egor N. Oparin, Polina S. Shaban, Yaroslav V. Grachev, Evgeniya Kovalska, Kieran K. Walsh, Monica F. Craciun, Anna Baldycheva, and Anton N. Tcypkin. Transmission Properties of FeCl3-Intercalated Graphene and WS2 Thin Films for Terahertz Time-Domain Spectroscopy Applications. *Nanoscale Research Letters*, 14(1), 2019.

[64] Elias Torres Alonso, George Karkera, Gareth F. Jones, Monica F. Craciun, and Saverio Russo. Homogeneously Bright, Flexible, and Foldable Lighting Devices with Functionalized Graphene Electrodes. *ACS Applied Materials and Interfaces*, 8(26):16541–16545, 2016.

[65] Freddie Withers, Thomas Hardisty Bointon, Monica Felicia Craciun, and Saverio Russo. All-graphene photodetectors. *ACS Nano*, 7(6):5052–5057, 2013.

[66] Adolfo de Sanctis, Gareth F. Jones, Dominique J. Wehenkel, Francisco Bezares, Frank H.L. Koppens, Monica F. Craciun, and Saverio Russo. Extraordinary linear dynamic range in laser-defined functionalized graphene photodetectors. *Science Advances*, 3(2017), 2017.

[67] Bernd Ebenhoch, Stuart A.J. Thomson, Kristijonas Genevičius, Gytis Juška, and Ifor D.W. Samuel. Charge carrier mobility of the organic photovoltaic materials PTB7 and PC71BM and its influence on device performance. *Organic Electronics*, 22:62–68, 2015.

[68] Emmanuel Kymakis, Kyriaki Savva, Minas M. Stylianakis, Costas Fotakis, and Emmanuel Stratakis. Flexible organic photovoltaic cells with in situ non-

thermal photoreduction of spin-coated graphene oxide electrodes. *Advanced Functional Materials*, 23(21):2742–2749, 2013.

[69] Holger Spanggaard and Frederik C Krebs. A brief history of the development of organic and polymeric photovoltaics. 83:125–146, 2004.

[70] Daniela Charris, Diego Gomez, Angie Rincon Ortega, Mauricio Carmona, and Mauricio Pardo. A thermoelectric energy harvesting scheme with passive cooling for outdoor IoT sensors. *Energies*, 13(11), 2020.

[71] Feng Ru Fan, Zhong Qun Tian, and Zhong Lin Wang. Flexible triboelectric generator. *Nano Energy*, 1(2):328–334, 2012.

[72] Dong Wook Shin, Matthew D. Barnes, Kieran Walsh, Dimitar Dimov, Peng Tian, Ana I.S. Neves, C. David Wright, Seong Man Yu, Ji Beom Yoo, Saverio Russo, and Monica F. Craciun. A New Facile Route to Flexible and Semi-Transparent Electrodes Based on Water Exfoliated Graphene and their Single-Electrode Triboelectric Nanogenerator. *Advanced Materials*, 30(39):1–7, 2018.

[73] R. D.Ishara G. Dharmasena, Jonathan H.B. Deane, and S. Ravi P. Silva. Nature of Power Generation and Output Optimization Criteria for Triboelectric Nanogenerators. *Advanced Energy Materials*, 8(31), 2018.

[74] R. J. Van De Graaff, K. T. Compton, and L. C. Van Atta. The electrostatic production of high voltage for nuclear investigations. *Physical Review*, 43(3):149–157, 1933.

[75] Johan Carl Wilcke. Disputatio physica experimentalis, de electricitatibus contrariis, 1757.

[76] Guang Zhu, Bai Peng, Jun Chen, Qingshen Jing, and Zhong Lin Wang. Triboelectric nanogenerators as a new energy technology: From fundamentals, devices, to applications. *Nano Energy*, 14:126–138, 2014.

[77] D. A. Barkas, C. S. Psomopoulos, P. Papageorgas, K. Kalkanis, D. Piromalis, and A. Mouratidis. Sustainable energy harvesting through triboelectric nano – Generators: A review of current status and applications. *Energy Procedia*, 157:999–1010, 2019.

[78] Carlos García Núñez, Libu Manjakkal, and Ravinder Dahiya. Energy autonomous electronic skin. *npj Flexible Electronics*, 3(1), 2019.

[79] Huamin Chen, Yun Xu, Jiushuang Zhang, Weitong Wu, and Guofeng Song. Enhanced stretchable graphene-based triboelectric nanogenerator via control of surface nanostructure. *Nano Energy*, 58(January):304–311, 2019.

[80] Faezeh Ejehi, Raheleh Mohammadpour, Elham Asadian, Pezhman Sasanpour, Somayeh Fardindoost, and Omid Akhavan. Graphene Oxide Papers in Nanogenerators for Self-Powered Humidity Sensing by Finger Tapping. *Scientific Reports*, 10(1):1–11, 2020.

[81] Jeong Min Baik and Jin Pyo Lee. Strategies for ultrahigh outputs generation in triboelectric energy harvesting technologies: from fundamentals to devices. *Science and Technology of Advanced Materials*, 20(1):927–936, 2019.

[82] Minsu Seol, Seongsu Kim, Yeonchoo Cho, Kyung Eun Byun, Haeryong Kim, Jihye Kim, Sung Kyun Kim, Sang Woo Kim, Hyeon Jin Shin, and Seongjun Park. Triboelectric Series of 2D Layered Materials. *Advanced Materials*, 30(39):1–8, 2018.

[83] P R Wallace. The Band Theory of Graphite. 71(9):622, 1947.

[84] Kin Fai Mak, Matthew Y. Sfeir, Yang Wu, Chun Hung Lui, James A. Misewich, and Tony F. Heinz. Measurement of the opptical conductivity of graphene. *Physical Review Letters*, 101(19):2–5, 2008.

[85] Xuesong Li, Weiwei Cai, Jinho An, Seyoung Kim, Junghyo Nah, Dongxing Yang, Richard Piner, Aruna Velamakanni, Inhwa Jung, Emanuel Tutuc,

Sanjay K. Banerjee, Luigi Colombo, and Rodney S. Ruoff. Large-area synthesis of high-quality and uniform graphene films on copper foils. *Science*, 324(5932):1312–1314, 2009.

[86] Wei Wei Liu, Bao Yu Xia, Xiao Xia Wang, and Jian Nong Wang. Exfoliation and dispersion of graphene in ethanol-water mixtures. *Frontiers of Materials Science*, 6(2):176–182, 2012.

[87] D. C. Elias, R. V. Gorbachev, A. S. Mayorov, S. V. Morozov, A. A. Zhukov, P. Blake, L. A. Ponomarenko, I. V. Grigorieva, K. S. Novoselov, F. Guinea, and A. K. Geim. Dirac cones reshaped by interaction effects in suspended graphene. *Nature Physics*, 7(9):701–704, 2011.

[88] Junbo Wu, Mukul Agrawal, A Becerril, Zhenan Bao, Zunfeng Liu, Yongsheng Chen, and Peter Peumans. Organic Light-Emitting Diodes on Solution Processed Graphen Transparent Electrodes. 4(1):43–48, 2010.

[89] Alexander A. Green and Mark C. Hersam. Solution phase production of graphene with controlled thickness via density differentiation. *Nano Letters*, 9(12):4031–4036, 2009.

[90] Sim Yumin, Park June, Jin Kim Yu, Seong Maeng-Je, and Hong Seunghun. Synthesis of Graphene Layers Using Graphite Dispersion in Aqueous Surfactant Solutions. *Journal of the Korean Physical Society*, 58(41):938, 2011.

[91] S. V. Morozov, K. S. Novoselov, M. I. Katsnelson, F. Schedin, D. C. Elias, J. A. Jaszczak, and A. K. Geim. Giant intrinsic carrier mobilities in graphene and its bilayer. *Physical Review Letters*, 100(1), 2008.

[92] A C Ferrari, J C Meyer, V Scardaci, C Casiraghi, M Lazzeri, F Mauri, S Piscanec, D Jiang, K S Novoselov, S Roth, and A K Geim. Raman Spectrum of Graphene and Graphene Layers. 187401(NOVEMBER):1–4, 2006.

[93] Andrea C. Ferrari. Raman spectroscopy of graphene and graphite: Disorder, electron-phonon coupling, doping and nonadiabatic effects. *Solid State Communications*, 143(1-2):47–57, 2007.

[94] L. G. Cançado, A. Jorio, E. H Martins Ferreira, F. Stavale, C. A. Achete, R. B. Capaz, M. V O Moutinho, A. Lombardo, T. S. Kulmala, and A. C. Ferrari. Quantifying defects in graphene via Raman spectroscopy at different excitation energies. *Nano Letters*, 11(8):3190–3196, 2011.

[95] Krishnan K.S Raman C.V. A new type of secondary radiation. *Nature*, 121:501–502, 1928.

[96] Robin R. Jones, David C. Hooper, Liwu Zhang, Daniel Wolverson, and Ventsislav K. Valev. Raman Techniques: Fundamentals and Frontiers. *Nanoscale Research Letters*, 14(1), 2019.

[97] D. M. Basko, S. Piscanec, and A. C. Ferrari. Electron-electron interactions and doping dependence of the two-phonon Raman intensity in graphene. *Phys. Rev. B*, 80(16):165413–165423, 2009.

[98] Michele Lazzeri and Francesco Mauri. Nonadiabatic Kohn anomaly in a doped graphene monolayer. *Physical Review Letters*, 97(26):29–32, 2006.

[99] A. Das, S. Pisana, B. Chakraborty, S. Piscanec, S. K. Saha, U. V. Waghmare, K. S. Novoselov, H. R. Krishnamurthy, A. K. Geim, A. C. Ferrari, and A. K. Sood. Monitoring dopants by Raman scattering in an electrochemically top-gated graphene transistor. *Nature Nanotechnology*, 3(4):210–215, 2008.

[100] T. M.G. Mohiuddin, A. Lombardo, R. R. Nair, A. Bonetti, G. Savini, R. Jalil, N. Bonini, D. M. Basko, C. Galiotis, N. Marzari, K. S. Novoselov, A. K. Geim, and A. C. Ferrari. Uniaxial strain in graphene by Raman spectroscopy: G peak splitting, Grüneisen parameters, and sample orientation. *Physical Review B - Condensed Matter and Materials Physics*, 79(20), 2009.

[101] Niclas S. Mueller, Sebastian Heeg, Miriam Peña Alvarez, Patryk Kusch, Sören Wasserroth, Nick Clark, Fredrik Schedin, John Parthenios, Konstantinos Papagelis, Costas Galiotis, Martin Kalbáč, Aravind Vijayaraghavan, Uwe Huebner, Roman Gorbachev, Otakar Frank, and Stephanie Reich. Evaluating arbitrary strain configurations and doping in graphene with Raman spectroscopy. *2D Materials*, 5(1), 2018.

[102] L. M. Malard, M. A. Pimenta, G. Dresselhaus, and M. S. Dresselhaus. Raman spectroscopy in graphene. *Physics Reports*, 473(5-6):51–87, 2009.

[103] Ki Kang Kim, Alfonso Reina, Yumeng Shi, Hyesung Park, Lain Jong Li, Young Hee Lee, and Jing Kong. Enhancing the conductivity of transparent graphene films via doping. *Nanotechnology*, 21(28), 2010.

[104] Lorenzo D'Arsié, Santiago Esconjauregui, Robert S. Weatherup, Xingyi Wu, William E. Arter, Hisashi Sugime, Cinzia Cepek, and John Robertson. Stable, efficient p-type doping of graphene by nitric acid. *RSC Advances*, 6(114):113185–113192, 2016.

[105] Li Zhang 1 Youngki Yoon Peter K. Weber Hailiang Wang Xinran Wang, Xiaolin Li and Hongjie Dai Jing Guo. N-Doping of Graphene Through Electrothermal Reactions With Ammonia. *Science*, 324(September), 2010.

[106] Lengyuan Niu, Zhangpeng Li, Wei Hong, Jinfeng Sun, Zhaofeng Wang, Limin Ma, Jinqing Wang, and Shengrong Yang. Pyrolytic synthesis of boron-doped graphene and its application aselectrode material for supercapacitors. *Electrochimica Acta*, 108:666–673, 2013.

[107] Luis M. Arellano, Sun Yue, Pedro Atienzar, María J. Gómez-Escalonilla, Francisco J. Ortega-Higueruelo, José Luis G. Fierro, Hermenegildo García, and Fernando Langa. Modulating charge carrier density and mobility in doped graphene by covalent functionalization. *Chemical Communications*, 55(67):9999–10002, 2019.

[108] Gianluca Giovannetti, Petr A. Khomyakov, Geert Brocks, Paul J. Kelly, and Jeroen van den Brink. Substrate-induced bandgap in graphene on hexagonal boron nitride. (111):1–5, 2007.

[109] K. S. Subrahmanyam, Arun K. Manna, Swapan K. Pati, and C. N.R. Rao. A study of graphene decorated with metal nanoparticles. *Chemical Physics Letters*, 497(1-3):70–75, 2010.

[110] Xi Yang, Wenqing Liu, Min Xiong, Yingying Zhang, Tao Liang, Jingting Yang, Mingsheng Xu, Jian Ye, and Hongzheng Chen. Au nanoparticles on ultrathin MoS 2 sheets for plasmonic organic solar cells. *J. Mater. Chem. A*, 2(36):14798–14806, 2014.

[111] Yoon Hee Jang, Adila Rani, Li Na Quan, Valerio Adinolfi, Pongsakorn Kanjanaboos, Olivier Ouellette, Taehwang Son, Yu Jin Jang, Kyungwha Chung, Hannah Kwon, Donghyun Kim, Dong Ha Kim, and Edward H. Sargent. Graphene Oxide Shells on Plasmonic Nanostructures Lead to High-Performance Photovoltaics: A Model Study Based on Dye-Sensitized Solar Cells. *ACS Energy Letters*, 2(1):117–123, 2017.

[112] M. S. Dresselhaus and G. Dresselhaus. Advances in Physics Intercalation compounds of graphite. *Advances in Physics*, 51(1):1–186, 1981.

[113] Kemeng Ji, Jiuhui Han, Akihiko Hirata, Takeshi Fujita, Yuhao Shen, Shoucong Ning, Pan Liu, Hamzeh Kashani, Yuan Tian, Yoshikazu Ito, Jun ichi Fujita, and Yutaka Oyama. Lithium intercalation into bilayer graphene. *Nature Communications*, 10(1):1–10, 2019.

[114] Kohei Kanetani, Katsuaki Sugawara, Takafumi Sato, Ryota Shimizu, Katsuya Iwaya, Taro Hitosugi, and Takashi Takahashi. Ca intercalated bilayer graphene as a thinnest limit of superconducting C6Ca. *Proceedings of the National Academy of Sciences of the United States of America*, 109(48):19610–19613, 2012.

[115] T. H. Bointon, I. Khrapach, R. Yakimova, A. V. Shytov, M. F. Craciun, and S. Russo. Approaching magnetic ordering in graphene materials by FeCl3 intercalation. *Nano Letters*, 14:1751–1755, 2014.

[116] J. Hwang, J. P. Carbotte, S. Tongay, A. F. Hebard, and D. B. Tanner. Ultrapure multilayer graphene in bromine-intercalated graphite. *Physical Review B - Condensed Matter and Materials Physics*, 84(4), 2011.

[117] Kieran Walsh, Gareth Jones, Matthew Barnes, Conor Murphy, Adolfo De Sanctis, Saverio Russo, Monica Craciun, and Dong-Wook Shin. Wafer scale FeCl3 intercalated graphene electrodes for photovoltaic applications. *Photonics for Solar Energy Systems VII*, 10688(May):52, 2018.

[118] Ya Ping Hsieh, Wan Yu Chiang, Sun Lin Tsai, and Mario Hofmann. Scalable production of graphene with tunable and stable doping by electrochemical intercalation and exfoliation. *Physical Chemistry Chemical Physics*, 18(1):339–343, 2016.

[119] Ranbir Singh, Sanjay Sandhu, and Jae Joon Lee. Elucidating the effect of shunt losses on the performance of mesoporous perovskite solar cells. *Solar Energy*, 193(September):956–961, 2019.

[120] Kristofer Tvingstedt, Lidón Gil-Escrig, Cristina Momblona, Philipp Rieder, David Kiermasch, Michele Sessolo, Andreas Baumann, Henk J. Bolink, and Vladimir Dyakonov. Removing Leakage and Surface Recombination in Planar Perovskite Solar Cells. *ACS Energy Letters*, 2(2):424–430, 2017.

[121] R. N. Hall. Electron-Hole Recombination in Germanium. *Phys. Rev.*, 87(2):387–387, 1952.

[122] W. Shockley and W. T. Read. Statistics of the Recombinations of Holes and Electrons. *Phys. Rev.*, 87(5):835–842, 1952.

[123] Pierre Auger, Pierre Auger, and J Phys. Sur l ' effet photoélectrique composé To cite this version. *J. Phys. Radium*, 6(6):205–208, 1925.

[124] David Kearns and Melvin Calvin. Photovoltaic effect and photoconductivity in laminated organic systems. *The Journal of Chemical Physics*, 29(4):950–951, 1958.

[125] C. W. Tang. Two-layer organic photovoltaic cell. *Applied Physics Letters*, 48(2):183–185, 1986.

[126] G. Yu, K. Pakbaz, and A. J. Heeger. Semiconducting polymer diodes: Large size, low cost photodetectors with excellent visible-ultraviolet sensitivity. *Applied Physics Letters*, 64(25):3422–3424, 1994.

[127] Yanfei Xu, Guankui Long, Lu Huang, Yi Huang, Xiangjian Wan, Yanfeng Ma, and Yongsheng Chen. Polymer photovoltaic devices with transparent graphene electrodes produced by spin-casting. *Carbon*, 48(11):3308–3311, 2010.

[128] Hyesung Park, Patrick R. Brown, Vladimir Bulović, and Jing Kong. Graphene as transparent conducting electrodes in organic photovoltaics: Studies in graphene morphology, hole transporting layers, and counter electrodes. *Nano Letters*, 12(1):133–140, 2012.

[129] Nikolaos Balis, Emmanuel Stratakis, and Emmanuel Kymakis. Graphene and transition metal dichalcogenide nanosheets as charge transport layers for solution processed solar cells. *Materials Today*, 19(10):580–594, 2016.

[130] Sadok Ben Dkhil, Martin Pfannmöller, Rasmus R. Schröder, Riva Alkarsifi, Meriem Gaceur, Wolfgang Köntges, Hamed Heidari, Sara Bals, Olivier Margeat, Jörg Ackermann, and Christine Videlot-Ackermann. Interplay of Interfacial Layers and Blend Composition to Reduce Thermal Degradation of Polymer Solar Cells at High Temperature. *ACS Applied Materials and Interfaces*, 10(4):3874–3884, 2018.

[131] Brian A. Gregg and Mark C. Hanna. Comparing organic to inorganic photovoltaic cells: Theory, experiment, and simulation. *Journal of Applied Physics*, 93(6):3605–3614, 2003.

[132] Krishna Feron, Warwick J. Belcher, Christopher J. Fell, and Paul C. Dastoor. Organic solar cells: Understanding the role of forster resonance energy transfer. *International Journal of Molecular Sciences*, 13(12):17019–17047, 2012.

[133] Oleksandr V. Mikhnenko, Hamed Azimi, Markus Scharber, Mauro Morana, Paul W.M. Blom, and Maria Antonietta Loi. Exciton diffusion length in narrow bandgap polymers. *Energy and Environmental Science*, 5(5):6960–6965, 2012.

[134] Serap Gu, Helmut Neugebauer, and Niyazi Serdar Sariciftci. Conjugated Polymer-Based Organic Solar Cells. *Chem. Rev.*, 107:1324–1338, 2007.

[135] Th. Förster. Zwischenmolekulare Energiewanderung und Fluoreszenz. *Annalen der Physik*, 1948.

[136] S. Matthew Menke and Russell J. Holmes. Exciton diffusion in organic photovoltaic cells. *Energy and Environmental Science*, 7(2):499–512, 2014.

[137] Xiong Gong, Sang Hyun Lim, Jacek C. Ostrowski, Daniel Moses, Christopher J. Bardeen, and Guillermo C. Bazan. Phosphorescence from iridium complexes doped into polymer blends. *Journal of Applied Physics*, 95(3):948–953, 2004.

[138] Oleksandr V. Mikhnenko, Paul W.M. Blom, and Thuc Quyen Nguyen. Exciton diffusion in organic semiconductors. *Energy and Environmental Science*, 8(7):1867–1888, 2015.

[139] Girish Lakhwani, Akshay Rao, and Richard H. Friend. Bimolecular Recombination in Organic Photovoltaics. *Annual Review of Physical Chemistry*, 65(1):557–581, 2014.

[140] Z. Ding, J. Kettle, M. Horie, S. W. Chang, G. C. Smith, A. I. Shames, and E. A. Katz. Efficient solar cells are more stable: The impact of polymer molecular weight on performance of organic photovoltaics. *Journal of Materials Chemistry A*, 4(19):7274–7280, 2016.

[141] M. Magdalena Mandoc, Welmoed Veurman, L. Jan Anton Koster, Bert De Boer, and Paul W.M. Blom. Origin of the reduced fill factor and photocurrent in MDMO-PPV:IPCNEPV all-polymer solar cells. *Advanced Functional Materials*, 17(13):2167–2173, 2007.

[142] G. A.H. Wetzelaer, M. Kuik, M. Lenes, and P. W.M. Blom. Origin of the dark-current ideality factor in polymer:fullerene bulk heterojunction solar cells. *Applied Physics Letters*, 99(15), 2011.

[143] Cheng Xu, Yunlong Zi, Aurelia Chi Wang, Haiyang Zou, Yejing Dai, Xu He, Peihong Wang, Yi Cheng Wang, Peizhong Feng, Dawei Li, and Zhong Lin Wang. On the Electron-Transfer Mechanism in the Contact-Electrification Effect. *Advanced Materials*, 30(15), 2018.

[144] Dong Wook Kim, Ju Hyun Lee, Jin Kon Kim, and Unyong Jeong. Material aspects of triboelectric energy generation and sensors. *NPG Asia Materials*, 12(1), 2020.

[145] Haiyang Zou, Ying Zhang, Litong Guo, Peihong Wang, Xu He, Guozhang Dai, Haiwu Zheng, Chaoyu Chen, Aurelia Chi Wang, Cheng Xu, and Zhong Lin Wang. Quantifying the triboelectric series. *Nature Communications*, 10(1):1–9, 2019.

[146] Hyenwoo Chu, Houk Jang, Yongjun Lee, Youngcheol Chae, and Jong Hyun Ahn. Conformal, graphene-based triboelectric nanogenerator for self-powered wearable electronics. *Nano Energy*, 27:298–305, 2016.

[147] S. Parandeh, M. Kharaziha, F. Karimzadeh, and F. Hosseinabadi. Triboelectric nanogenerators based on graphene oxide coated nanocomposite fibers for biomedical applications. *Nanotechnology*, 31(38), 2020.

[148] Dong Hee Shin, Chan Wook Jang, Ha Seung Lee, Sang Woo Seo, and Suk Ho Choi. Semitransparent Flexible Organic Solar Cells Employing Doped-

Graphene Layers as Anode and Cathode Electrodes. *ACS Applied Materials and Interfaces*, 10(4):3596–3601, 2018.

[149] C Y Liao and J K Wu. Chemical machining of nickel in ferric chloride solution. *Journal of Material Science Letters*, 11:689–691, 1992.

[150] Xuesong Li, Weiwei Cai, Jinho An, Seyoung Kim, Junghyo Nah, Dongxing Yang, Richard Piner, Aruna Velamakanni, Inhwa Jung, Emanuel Tutuc, Sanjay K Banerjee, Luigi Colombo, and Rodney S Ruoff. Large-area synthesis of high-quality and uniform graphene films on copper foils. *Science*, 324(5932):1312–1314, 2009.

[151] Alfonso Reina, Xiaoting Jia, John Ho, Daniel Nezich, Hyungbin Son, Vladimir Bulovic, Mildred S. Dresselhaus, and Kong Jing. Large area, few-layer graphene films on arbitrary substrates by chemical vapor deposition. *Nano Letters*, 9(1):30–35, 2009.

[152] Keun Soo Kim, Yue Zhao, Houk Jang, Sang Yoon Lee, Jong Min Kim, Kwang S. Kim, Jong Hyun Ahn, Philip Kim, Jae Young Choi, and Byung Hee Hong. Large-scale pattern growth of graphene films for stretchable transparent electrodes. *Nature*, 457(7230):706–710, 2009.

[153] Ji Won Suk, Alexander Kitt, Carl W. Magnuson, Yufeng Hao, Samir Ahmed, Jinho An, Anna K. Swan, Bennett B. Goldberg, and Rodney S. Ruoff. Transfer of CVD-grown monolayer graphene onto arbitrary substrates. *ACS Nano*, 5(9):6916–6924, 2011.

[154] Monica Felicia Craciun, Thomas H. Bointon, and Saverio Russo. Is graphene a good transparent electrode for photovoltaics and display applications? *IET Circuits, Devices & Systems*, 9(6):403–412, 2015.

[155] E H Hall. On a New Action of the Magnet on Electric Currents. *Am. J. Math.*, 2(3):287–292, 1879.

[156] Andreas Weu, Joshua A. Kress, Fabian Paulus, David Becker-Koch, Vincent Lami, Artem A. Bakulin, and Yana Vaynzof. Oxygen-Induced Doping as a Degradation Mechanism in Highly Efficient Organic Solar Cells. *ACS Applied Energy Materials*, 2(3):1943–1950, 2019.

[157] Vytenis Pranculis, Arvydas Ruseckas, Dimali A. Vithanage, Gordon J. Hedley, Ifor D.W. Samuel, and Vidmantas Gulbinas. Influence of blend ratio and processing additive on free carrier yield and mobility in PTB7:PC71bm photovoltaic solar cells. *Journal of Physical Chemistry C*, 120(18):9588–9594, 2016.

[158] Yiwei Zhang, Andrew J. Parnell, Fabio Pontecchiani, Joshaniel F.K. Cooper, Richard L. Thompson, Richard A.L. Jones, Stephen M. King, David G. Lidzey, and Gabriel Bernardo. Understanding and controlling morphology evolution via DIO plasticization in PffBT4T-2OD/PC 71 BM devices. *Scientific Reports*, 7(February):1–12, 2017.

[159] Ikerne Etxebarria, Antonio Guerrero, Josep Albero, Germà Garcia-Belmonte, Emilio Palomares, and Roberto Pacios. Inverted vs standard PTB7:PC70BM organic photovoltaic devices. the benefit of highly selective and extracting contacts in device performance. *Organic Electronics*, 15(11):2756–2762, 2014.

[160] Ying Wang, Zhen Ni, Ting Yu, Ze Xiang Shen, Hao Wang, Yi Wu, Wei Chen, Andrew Thye, and Shen Wee. Raman Studies of Monolayer Graphene : The Substrate Effect. (0001):10637–10640, 2008.

[161] Ryan Beams, Luiz Gustavo Canc, and Lukas Novotny. Raman characterization of defects and dopants in graphene. *J. Phys.: Condens. Matter*, 27, 2015.

[162] Adolfo De Sanctis, Gareth F Jones, Nicola J Townsend, Monica F Craciun, and Saverio Russo. thin optoelectronic devices An integrated and multi-purpose microscope for the characterization of atomically thin optoelectronic devices. *Review of Scientific Instruments*, 88, 2017.

[163] Axel Eckmann, Alexandre Felten, Artem Mishchenko, Liam Britnell, Ralph Krupke, Kostya S. Novoselov, and Cinzia Casiraghi. Probing the nature of defects in graphene by Raman spectroscopy. *Nano Letters*, 12(8):3925–3930, 2012.

[164] Pablo A. Fernández Garrillo, Benjamin Grévin, Nicolas Chevalier, and Lukasz Borowik. Calibrated work function mapping by Kelvin probe force microscopy. *Review of Scientific Instruments*, 89(4), 2018.

[165] Wilhelm Melitz, Jian Shen, Andrew C. Kummel, and Sangyeob Lee. Kelvin probe force microscopy and its application. *Surface Science Reports*, 66(1):1–27, 2011.

[166] Dong Wook Shin, Jong Hak Lee, Yu Hee Kim, Seong Man Yu, Seong Yong Park, and Ji Beom Yoo. A role of HNO3 on transparent conducting film with single-walled carbon nanotubes. *Nanotechnology*, 20(47), 2009.

[167] Yong Un Jung, Seok-In Na, Han-Ki Kim, and Seong Jun Kang. Organic photovoltaic devices with low resistance multilayer graphene transparent electrodes. *Journal of Vacuum Science & Technology A: Vacuum, Surfaces, and Films*, 30(5):050604, 2012.

[168] Da Zhan, Li Sun, Zhen Hua Ni, Lei Liu, Xiao Feng Fan, Yingying Wang, Ting Yu, Yeng Ming Lam, Wei Huang, and Ze Xiang Shen. FeCl3-based few-layer graphene intercalation compounds: Single linear dispersion electronic band structure and strong charge transfer doping. *Advanced Functional Materials*, 20(20):3504–3509, 2010.

[169] Simone Pisana, Michele Lazzeri, Cinzia Casiraghi, Kostya S Novoselov, A K Geim, Andrea C Ferrari, and Francesco Mauri. Breakdown of the adiabatic Born-Oppenheimer approximation in graphene. *Nature materials*, 6(3):198–201, 2007.

[170] Yi Zhang, Lewis Gomez, Fumiaki N. Ishikawa, Anuj Madaria, Koungmin Ryu, Chuan Wang, Alexander Badmaev, and Chongwu Zhou. Comparison of graphene growth on single-crystalline and polycrystalline Ni by chemical vapor deposition. *Journal of Physical Chemistry Letters*, 1(20):3101–3107, 2010.

[171] Joseph Razzell-Hollis, Jessica Wade, Wing Chung Tsoi, Ying Soon, James Durrant, and Ji Seon Kim. Photochemical stability of high efficiency PTB7:PC70BM solar cell blends. *Journal of Materials Chemistry A*, 2(47):20189–20195, 2014.

[172] Yumeng Shi, Ki Kang Kim, Alfonso Reina, Mario Hofmann, Lain-jong Li, and Jing Kong. Work Function Engineering of Graphene Electrode via Chemical Doping. *ACS Nano*, 4(5):2689–2694, 2010.

[173] Zhouying Zhao, John D. Fite, Pradeep Haldar, and Ji Ung Lee. Enhanced ultraviolet response using graphene electrodes in organic solar cells. *Applied Physics Letters*, 101(6):1–5, 2012.

[174] Xiaoqiang Li, Wenchao Chen, Shengjiao Zhang, Zhiqian Wu, Peng Wang, Zhijuan Xu, Hongsheng Chen, Wenyan Yin, Huikai Zhong, and Shisheng Lin. 18 . 5 % ef fi cient graphene / GaAs van der Waals heterostructure solar cell. *Nano Energy*, 16:310–319, 2015.

[175] Hobeom Kim, Sang Hoon Bae, Tae Hee Han, Kyung Geun Lim, Jong Hyun Ahn, and Tae Woo Lee. Organic solar cells using CVD-grown graphene electrodes. *Nanotechnology*, 25(1), 2014.

[176] Hyesung Park, Yumeng Shi, and Jing Kong. Application of solvent modified PEDOT:PSS to graphene electrodes in organic solar cells. *Nanoscale*, 5(19):8934–8939, 2013.

[177] Yiling Wang, Qun Luo, Na Wu, Qiankun Wang, Hongfei Zhu, Liwei Chen, Yan Qing Li, Liqiang Luo, and Chang Qi Ma. Solution-processed

MoO3:PEDOT:PSS hybrid hole transporting layer for inverted polymer solar cells. *ACS Applied Materials and Interfaces*, 7(13):7170–7179, 2015.

[178] J. Y. Kim, J. H. Jung, D. E. Lee, and J. Joo. Enhancement of electrical conductivity of poly(3, 4-ethylenedioxythiophene)/poly(4-styrenesulfonate) by a change of solvents. *Synthetic Metals*, 126(2-3):311–316, 2002.

[179] J. Duch, P. Kubisiak, K. H. Adolfsson, M. Hakkarainen, M. Golda-Cepa, and A. Kotarba. Work function modifications of graphite surface via oxygen plasma treatment. *Applied Surface Science*, 419:439–446, 2017.

[180] Ki Chang Kwon, Wan Jae Dong, Gwan Ho Jung, Juyoung Ham, Jong Lam Lee, and Soo Young Kim. Extension of stability in organic photovoltaic cells using UV/ozone-treated graphene sheets. *Solar Energy Materials and Solar Cells*, 109:148–154, 2013.

[181] J.R. Vig. UV /ozone cleaning of surfaces. *Journal of Vacuum Science & Technology A: Vacuum, Surfaces, and Films*, 5302(September 1984):1027–1034, 1985.

[182] Isaac Childres, Luis A. Jauregui, Jifa Tian, and Yong P. Chen. Effect of oxygen plasma etching on graphene studied using Raman spectroscopy and electronic transport measurements. *New Journal of Physics*, 13:0–12, 2011.

[183] General Electric D.A. Bolon, C.O. Kunz ;Company. Ultraviolet Depolymerization of Photoresist Polymers. 12(2):109–111, 1972.

[184] Xiaojian Yang and Mingdi Yan. Removing contaminants from transferred CVD graphene. *Nano Research*, 13(3):599–610, 2020.

[185] V. S. Prudkovskiy, K. P. Katin, M. M. Maslov, P. Puech, R. Yakimova, and G. Deligeorgis. Efficient cleaning of graphene from residual lithographic polymers by ozone treatment. *Carbon*, 109:221–226, 2016.

[186] Ahmet Avsar, Tsung Yeh Yang, Sukang Bae, Jayakumar Balakrishnan, Frank Volmer, Manu Jaiswal, Zheng Yi, Syed Rizwan Ali, Gernot Guöntherodt, Byung Hee Hong, Bernd Beschoten, and Barbaros Özyilmaz. Toward wafer scale fabrication of graphene based spin valve devices. *Nano Letters*, 11(6):2363–2368, 2011.

[187] A. Pirkle, J. Chan, A. Venugopal, D. Hinojos, C. W. Magnuson, S. McDonnell, L. Colombo, E. M. Vogel, R. S. Ruoff, and R. M. Wallace. The effect of chemical residues on the physical and electrical properties of chemical vapor deposited graphene transferred to SiO2. *Applied Physics Letters*, 99(12):2009–2012, 2011.

[188] Hongyan Sun, Ding Chen, Yuming Wu, Qilong Yuan, Liangchao Guo, Dan Dai, Yang Xu, Pei Zhao, Nan Jiang, and Cheng Te Lin. High quality graphene films with a clean surface prepared by an UV/ozone assisted transfer process. *Journal of Materials Chemistry C*, 5(8):1880–1884, 2017.

[189] Jie Song, Fong Yu Kam, Rui Qi Png, Wei Ling Seah, Jing Mei Zhuo, Geok Kieng Lim, Peter K.H. Ho, and Lay Lay Chua. A general method for transferring graphene onto soft surfaces. *Nature Nanotechnology*, 8(5):356–362, 2013.

[190] Kittel. *Introduction to Solid State Physics, 7th Ed.* Wiley India Pvt. Limited, 7th edition, 2007.

[191] John A. Chaney and Pehr E. Pehrsson. Work function changes and surface chemistry of oxygen, hydrogen, and carbon on indium tin oxide. *Applied Surface Science*, 180(3-4):214–226, 2001.

[192] Kieran K. Walsh, Conor Murphy, Saverio Russo, and Monica F. Craciun. Improved Stability of Organic Photovotlaic Devices With FeCl3 Intercalated Graphene Electrodes. *Frontiers in Electronics*, 2(April):1–9, 2021.

[193] Yong Cui, Huifeng Yao, Jianqi Zhang, Tao Zhang, Yuming Wang, Ling Hong, Kaihu Xian, Bowei Xu, Shaoqing Zhang, Jing Peng, Zhixiang Wei, Feng Gao, and Jianhui Hou. Over 16\% efficiency organic photovoltaic cells enabled by a chlorinated acceptor with increased open-circuit voltages. *Nature Communications*, 10(1):1–8, 2019.

[194] Qishi Liu, Yufan Jiang, Ke Jin, Jianqiang Qin, Jingui Xu, Wenting Li, Ji Xiong, Jinfeng Liu, Zuo Xiao, Kuan Sun, Shangfeng Yang, Xiaotao Zhang, and Liming Ding. 18% Efficiency organic solar cells. *Science Bulletin*, 65(4):272–275, 2020.

[195] Him Cheng Wong, Zhe Li, Ching Hong Tan, Hongliang Zhong, Zhenggang Huang, Hugo Bronstein, Iain McCulloch, João T. Cabral, and James R. Durrant. Morphological stability and performance of polymer-fullerene solar cells under thermal stress: The impact of photoinduced PC60BM oligomerization. *ACS Nano*, 8(2):1297–1308, 2014.

[196] Emily M. Speller, Andrew J. Clarke, Nicholas Aristidou, Mark F. Wyatt, Laia Francàs, George Fish, Hyojung Cha, Harrison Ka Hin Lee, Joel Luke, Andrew Wadsworth, Alex D. Evans, Iain McCulloch, Ji Seon Kim, Saif A. Haque, James R. Durrant, Stoichko D. Dimitrov, Wing C. Tsoi, and Zhe Li. Toward improved environmental stability of polymer: Fullerene and polymer:Nonfullerene organic solar cells: A common energetic origin of light- A nd oxygen-induced degradation. *ACS Energy Letters*, 4(4):846–852, 2019.

[197] Sangjun Kim, Md Al Mamunur Rashid, Taewon Ko, Kyusang Ahn, Yukyung Shin, Sanghee Nah, Myung Hwa Kim, Bong Soo Kim, Kyungwon Kwak, and Minhaeng Cho. New Insights into the Photodegradation Mechanism of the PTB7-Th Film: Photooxidation of π-Conjugated Backbone upon Sunlight Illumination. *Journal of Physical Chemistry C*, 124(5):2762–2770, 2020.

[198] Tom S. Glen, Nicholas W. Scarratt, Hunan Yi, Ahmed Iraqi, Tao Wang, James Kingsley, Alastair R. Buckley, David G. Lidzey, and Athene M. Donald. De-

pendence on material choice of degradation of organic solar cells following exposure to humid air. *Journal of Polymer Science, Part B: Polymer Physics*, 54(2):216–224, 2016.

[199] William R. Mateker and Michael D. McGehee. Progress in Understanding Degradation Mechanisms and Improving Stability in Organic Photovoltaics. *Advanced Materials*, 29(10), 2017.

[200] Pei Cheng and Xiaowei Zhan. Stability of organic solar cells: Challenges and strategies. *Chemical Society Reviews*, 45(9):2544–2582, 2016.

[201] M. Girtan and M. Rusu. Role of ITO and PEDOT:PSS in stability/degradation of polymer:fullerene bulk heterojunctions solar cells. *Solar Energy Materials and Solar Cells*, 94(3):446–450, 2010.

[202] V. M. Fthenakis and H. C. Kim. Photovoltaics: Life-cycle analyses. *Solar Energy*, 85(8):1609–1628, 2011.

[203] Mariusz Malinowski, Jose I. Leon, and Haitham Abu-Rub. Solar Photovoltaic and Thermal Energy Systems: Current Technology and Future Trends. *Proceedings of the IEEE*, 105(11):2132–2146, 2017.

[204] Khagendra P. Bhandari, Jennifer M. Collier, Randy J. Ellingson, and Defne S. Apul. Energy payback time (EPBT) and energy return on energy invested (EROI) of solar photovoltaic systems: A systematic review and meta-analysis. *Renewable and Sustainable Energy Reviews*, 47:133–141, 2015.

[205] Xi Fan, Jinzhao Wang, Hanbin Wang, Xiang Liu, and Hao Wang. Bendable ITO-free Organic Solar Cells with Highly Conductive and Flexible PEDOT:PSS Electrodes on Plastic Substrates. *ACS Applied Materials and Interfaces*, 7(30):16287–16295, 2015.

[206] Haitao Zhai, Yang Li, Liwei Chen, Xiao Wang, Liangjing Shi, Ranran Wang, and Jing Sun. Semi-transparent polymer solar cells with all-copper nanowire electrodes. *Nano Research*, 11(4):1956–1966, 2018.

[207] Yanna Sun, Meijia Chang, Lingxian Meng, Xiangjian Wan, Huanhuan Gao, Yamin Zhang, Kai Zhao, Zhenhe Sun, Chenxi Li, Shuiren Liu, Huike Wang, Jiajie Liang, and Yongsheng Chen. Flexible organic photovoltaics based on water-processed silver nanowire electrodes. *Nature Electronics*, 2(11):513–520, 2019.

[208] V. V. Brus, M. A. Gluba, X. Zhang, K. Hinrichs, J. Rappich, and N. H. Nickel. Stability of graphene-silicon heterostructure solar cells. *Physica Status Solidi (A) Applications and Materials Science*, 211(4):843–847, 2014.

[209] Hung-chieh Cheng, Gongming Wang, Dehui Li, Qiyuan He, Anxiang Yin, Yuan Liu, Hao Wu, Mengning Ding, Yu Huang, and Xiangfeng Duan. van der Waals Heterojunction Devices Based on Organohalide Perovskites and Two-Dimensional Materials. *Nano Lett*, 16:367–373, 2016.

[210] T. Sun, Z. L. Wang, Z. J. Shi, G. Z. Ran, W. J. Xu, Z. Y. Wang, Y. Z. Li, L. Dai, and G. G. Qin. Multilayered graphene used as anode of organic light emitting devices. *Applied Physics Letters*, 96(13):4–7, 2010.

[211] F. Brunetti, G. Ulisse, M. Dianetti, G. Susanna, G. Innaccone, G. Fiori, O. Martin, D. Neumaier, R. Puicervert, D. Lordan, M. Burke, A. Quinn, M. Schimidt, and P. Lugli. Doped and textured graphene as electrode for organic solar cells. *IEEE-NANO 2015 - 15th International Conference on Nanotechnology*, pages 560–563, 2015.

[212] Tae Hee Han, Youngbin Lee, Mi Ri Choi, Seong Hoon Woo, Sang Hoon Bae, Byung Hee Hong, Jong Hyun Ahn, and Tae Woo Lee. Extremely efficient flexible organic light-emitting diodes with modified graphene anode. *Nature Photonics*, 6(2):105–110, 2012.

[213] Michael Zawodzki, Roland Resel, Michele Sferrazza, Olivia Kettner, and Bettina Friedel. Interfacial Morphology and Effects on Device Performance of

Organic Bilayer Heterojunction Solar Cells. *ACS Applied Materials and Interfaces*, 7(30):16161–16168, 2015.

[214] P.C. Braga D. Ricci. Recognizing and avoiding artifacts in AFM imaging. *Methods in Molecular Biology*, 242:25–37, 2004.

[215] Naveen Kumar Elumalai and Ashraf Uddin. Open circuit voltage of organic solar cells: An in-depth review. *Energy and Environmental Science*, 9(2):391–410, 2016.

[216] Brian A. Collins, Zhe Li, John R. Tumbleston, Eliot Gann, Christopher R. Mcneill, and Harald Ade. Absolute measurement of domain composition and nanoscale size distribution explains performance in PTB7:PC71bm solar cells. *Advanced Energy Materials*, 3(1):65–74, 2013.

[217] Xiaojing Wu, Huihua Xu, Yu Wang, Andrey L. Rogach, Yingzhong Shen, and Ni Zhao. General observation of the memory effect in metal-insulator-ITO structures due to indium diffusion. *Advanced Materials*, 19(20):3364–3367, 2007.

[218] A. R. Schlatmann, D. Wilms Floet, A. Hilberer, F. Garten, P. J.M. Smulders, T. M. Klapwijk, and G. Hadziioannou. Indium contamination from the indium-tin-oxide electrode in polymer light-emitting diodes. *Applied Physics Letters*, 69(12):1764–1766, 1996.

[219] Christopher M. Proctor and Thuc Quyen Nguyen. Effect of leakage current and shunt resistance on the light intensity dependence of organic solar cells. *Applied Physics Letters*, 106(8), 2015.

[220] Yiwei Zhang, Ifor D.W. Samuel, Tao Wang, and David G. Lidzey. Current Status of Outdoor Lifetime Testing of Organic Photovoltaics. *Advanced Science*, 5(8), 2018.

[221] Lingpeng Yan, Jinduo Yi, Qi Chen, Junyan Dou, Yongzhen Yang, Xuguang Liu, Liwei Chen, and Chang Qi Ma. External load-dependent degradation of

P3HT:PC61BM solar cells: Behavior, mechanism, and method of suppression. *Journal of Materials Chemistry A*, 5(20):10010–10020, 2017.

[222] Somnath Dey, Paola Vivo, Alexander Efimov, and Helge Lemmetyinen. Enhanced performance and stability of inverted organic solar cells by using novel zinc-benzothiazole complexes as anode buffer layers. *Journal of Materials Chemistry*, 21(39):15587–15592, 2011.

[223] Suren A. Gevorgyan, Nieves Espinosa, Laura Ciammaruchi, Bérenger Roth, Francesco Livi, Stylianos Tsopanidis, Simon Züfle, Sara Queirós, Alberto Gregori, Gisele Alves dos Reis Benatto, Michael Corazza, Morten V. Madsen, Markus Hösel, Michail J. Beliatis, Thue Trofod Larsen-Olsen, Francesco Pastorelli, António Castro, Alba Mingorance, Veniero Lenzi, Daniel Fluhr, Roland Roesch, Marta Maria Duarte Ramos, Achilleas Savva, Harald Hoppe, Luís Silvino Alves Marques, Ignasi Burgués, Efthymios Georgiou, Lucia Serrano-Luján, and Frederik C. Krebs. Baselines for Lifetime of Organic Solar Cells. *Advanced Energy Materials*, 6(22):1–9, 2016.

[224] Borja Pozo, José Ignacio Garate, José Ángel Araujo, and Susana Ferreiro. Energy harvesting technologies and equivalent electronic structural models - review. *Electronics (Switzerland)*, 8(5):1–31, 2019.

[225] Wanchul Seung, Manoj Kumar Gupta, Keun Young Lee, Kyung-sik Shin, Juhyuck Lee, Tae Yun Kim, Sanghyun Kim, Jianjian Lin, Jung Ho Kim, and Sang-woo Kim. Nanopatterned Textile-Based Wearable Triboelectric Nanogenerator. (4):3501–3509, 2015.

[226] J. Lowell and A. C. Rose-Innes. Contact electrification. *Advances in Physics*, 29(6):947–1023, 1980.

[227] R. D.I.G. Dharmasena, K. D.G.I. Jayawardena, C. A. Mills, R. A. Dorey, and S. R.P. Silva. A unified theoretical model for Triboelectric Nanogenerators. *Nano Energy*, 48(March):391–400, 2018.

[228] Alexander N. Grebenchukov, Anton D. Zaitsev, Mikhail G. Novoselov, Petr S. Demchenko, Evgeniya O. Kovalska, Elias Torres Alonso, Kieran Walsh, Saverio Russo, Monica F. Craciun, Anna V. Baldycheva, and Mikhail K. Khodzitsky. Photoexcited terahertz conductivity in multi-layered and intercalated graphene. *Optics Communications*, 459(November 2019):2–6, 2020.

[229] Shuaihang Pan and Zhinan Zhang. Fundamental theories and basic principles of triboelectric effect: A review. *Friction*, 7(1):2–17, 2019.